

# **EXPERIMENTAL AND MODELLING STUDIES OF CORROSION FATIGUE DAMAGE IN A LINEPIPE STEEL**

A thesis submitted to the University of Manchester for the degree of

**Doctor of Philosophy**

in the Faculty of Engineering and Physical Sciences

2015

**Olusegun Fatoba**

School of Materials

# Table of Contents

<b>Chapter 1 Introduction .....</b>	<b>9</b>
1.1 Background .....	10
1.2 Aims and objectives.....	11
1.3 Thesis outline .....	12
<b>Chapter 2 Literature Review .....</b>	<b>13</b>
2.1 Corrosion Damage.....	14
2.2 Fatigue of Metals.....	18
2.3 Fatigue Life Prediction .....	21
2.4 Behaviour of Short Fatigue Cracks.....	26
2.5 Fatigue Limit and Non-Propagating Cracks.....	32
2.6 Kitagawa-Takahashi Diagram .....	33
2.7 Environment Assisted Fatigue.....	37
2.8 Crack Nucleation from Corrosion Pits.....	48
2.9 Corrosion Fatigue Lifetime Modelling.....	52
<b>Chapter 3 Experimental Methods .....</b>	<b>58</b>
3.1 Introduction .....	59
3.2 Material.....	59
3.3 Chemical composition.....	60
3.4 Metallography.....	60
3.5 Micro-hardness .....	61
3.6 Electrochemical Testing.....	61
3.7 Rationale for use of single artificial pits.....	63
3.8 Simulation of pit growth .....	63
3.9 Mechanical Testing.....	71
3.10 Crack growth measurements .....	79
3.11 Image analysis and fractography.....	80
<b>Chapter 4 Modelling Methods .....</b>	<b>81</b>
4.1 Introduction .....	82
4.2 FEA modelling techniques.....	82
4.3 Analysis of stresses and strains around pits.....	88
4.4 Modelling of the interaction between localised corrosion and stress .....	90

<b>Chapter 5 Experimental Results and Discussion .....</b>	<b>98</b>
5.1 Introduction .....	99
5.2 Material Characterisation.....	99
5.3 Stress-strain properties.....	102
5.4 Pit growth behaviour.....	109
5.5 Fatigue and corrosion fatigue behaviour .....	112
5.6 Fracture surface analysis .....	145
5.7 Stress-life (S-N) curves .....	151
<b>Chapter 6 Finite Element Analysis Results and Discussion.....</b>	<b>155</b>
6.1 Introduction .....	156
6.2 Mesh convergence study.....	157
6.3 Model validation.....	157
6.4 Changes in stress and strain distribution due to pit growth.....	159
6.5 Analyses of stress and strain distribution in artificial pits .....	169
6.6 Effect of pit-to-pit proximity on stress and strain distribution .....	173
<b>Chapter 7 CAFE Modelling Results and Discussion .....</b>	<b>179</b>
7.1 Introduction .....	180
7.2 Simulation of the micro-capillary cell .....	181
7.3 Model parameter sensitivity analysis.....	182
7.4 Influence of model parameters .....	186
7.5 Model validation.....	190
7.6 Evolution of pit depth with and without stress .....	195
7.7 Evolution of stress and strain with time .....	197
7.8 Preliminary results from 3-D cellular automata model .....	201
<b>Chapter 8 Fatigue Lifetime Modelling.....</b>	<b>204</b>
8.1 Introduction .....	205
8.2 Multi-stage damage accumulation model .....	205
8.3 Discussion .....	226
<b>Chapter 9 General Discussion .....</b>	<b>229</b>
9.1 Introduction .....	230
9.2 The fatigue limit.....	230
9.3 Influence of pit size on fatigue strength.....	231
9.4 Effect of stress on pit development .....	236
9.5 Pit-to-crack transition behaviour .....	238

9.6 Crack propagation behaviour.....	247
9.7 Re-assessment of pit-to-crack transition criteria .....	252
<b>Chapter 10 Conclusions.....</b>	<b>253</b>
<b>Chapter 11 Future Work .....</b>	<b>256</b>
11.1 Experimental work .....	257
11.2 Modelling work.....	258
<b>References.....</b>	<b>259</b>
<b>Appendix.....</b>	<b>274</b>



## NOMENCLATURE

The frequently used acronyms and symbols are listed below. Those which are rarely used are defined in their context.

$a_{ce}$ : crack extension from pit  
API: American Petroleum Institute  
 $AR_p$ : Pit aspect ratio  
 $AR_{p,avg}$ : Pit aspect ratio  
CA – Cellular automata  
CAFE – Cellular automata finite element  
CF – Corrosion fatigue  
CI – Crack initiation  
CPZ – Crack propagation zone  
 $c_p$ : Half pit width  
 $d_p$ : Pit depth  
 $d_{p,avg}$ : Average pit depth  
 $d_{th}$ : Threshold separation distance between double pits  
 $f$ : Cyclic frequency  
 $F$ : Faraday's constant  
FEA – Finite element analysis  
FFZ – Fast fracture zone  
HSLA: High strength low alloy  
HV: Vickers hardness number  
 $\Delta K$ : Stress intensity factor range  
 $\Delta K_{th}$ : Threshold stress intensity factor range  
KDF: Corrosion fatigue knockdown factor  
LEFM: Linear elastic fracture mechanics  
 $N_f$ : Fatigue lifetime  
 $N_i$ : Crack initiation lifetime  
 $N_{i,double}$ : Crack initiation lifetime for double pits  
 $N_{i,single}$ : Crack initiation lifetime for a single pit  
 $R$ : Stress ratio  
 $s_{cc}$ : Center-to-center distance between double pits  
 $s_{ee}$ : Edge-to-edge distance between double pits  
 $\Delta \epsilon$ : Total strain range  
 $\Delta \sigma$ : Stress range  
 $\sigma_{FL}$ : Fatigue limit

## **ABSTRACT**

The work is concerned with the development of a multi-stage corrosion fatigue lifetime model, with emphasis on pitting as a precursor to cracking. The model is based upon the quantitative evaluation of damage during the overall corrosion fatigue process.

The fatigue response of as-received API 5L X65 linepipe steel has been investigated in terms of the evolution of damage during pit development, pit-to-crack transition and crack propagation. Micro-potentiostatic polarisation was conducted to evaluate role of stress on pit development. Crack growth rate measurements were conducted on pre-pitted specimens, which were tested in air and brine, to evaluate the initiation and propagation behaviour of cracks emanating from artificial pits. Finite element analysis was undertaken to evaluate the stress and strain distribution associated with the pits. A cellular automata finite element model was also developed for predicting corrosion fatigue damage.

Pit growth rate was enhanced under stress. It was considered that the strain localisation effect of the pit facilitated strain-assisted dissolution. In air, cracks initiated predominantly from the pit mouth. FEA results indicated that this was due to localisation of strain towards the pit mouth. In corrosion fatigue, cracks tended to initiate at the pit base at low stress and at the pit mouth at higher stresses. Crack initiation lifetimes were shorter in the aggressive environment compared to air and the effect of the environment on crack initiation lifetime was lower at higher stress levels. Crack initiation lifetime for double pits generally decreased with decreasing pit-to-pit separation distance.

The microstructure was observed to influence crack growth behaviour in air particularly in the early stages when cracks were short. The acceleration and retardation in crack growth were attributed to the resistance of grain boundaries to crack advance. Cracks sometimes arrested at these barriers and became non-propagating. Introduction of the environment for a short period appear to eliminate the resistance of the microstructural barriers thus promoting re-propagation of the previously arrested crack. The continued crack propagation after the removal of the environment suggests that the influence of the environment is more important in the early stages of crack growth. Crack growth rates were higher in the aggressive environment than in air. The degree of environmental enhancement of crack growth was found to be greater at lower stress levels and at short crack lengths. Oxide-induced crack closure and crack coalescence were two mechanisms that also affected crack growth behaviour.

2-D cellular automata finite element simulation results, with and without stress, show good agreement agreed with experiments i.e. pit depth and pit aspect ratio increase with time. Results from 3-D cellular automata simulations of pits are also consistent with experiments.

Fatigue lifetimes were significantly shorter (i) in the brine environment than in air and (ii) for specimens with double pits compared to single pits of similar depth. Fatigue strength in air was found to decrease with increasing pit depth. Corrosion fatigue lifetimes predicted based upon the developed model showed good agreement with the experimental lifetimes.

## DECLARATION

I declare that no portion of the work referred to in this thesis has been submitted in support of an application for another degree or qualification of this or any other university or other institution of learning.

Signature

## COPYRIGHT

- i. The author of this thesis (including any appendices and/or schedules to this thesis) owns any copyright in it (the "Copyright") and s/he has given The University of Manchester the right to use such Copyright for any administrative, promotional, educational and/or teaching purposes.
- ii. Copies of this thesis, either in full or in extracts and whether in hard or electronic copy, may be made only in accordance with the Copyright, Designs and Patents Act 1988 (as amended) and regulations issued under it or, where appropriate, in accordance with licensing agreements which the University has from time to time. This page must form part of any such copies made.
- iii. The ownership of any patents, designs, trademarks and any and all other intellectual property rights except for the Copyright (the "Intellectual Property Rights") and any reproductions of copyright works, for example graphs and tables ("Reproductions"), which may be described in this thesis, may not be owned by the author and may be owned by third parties. Such Intellectual Property Rights and Reproductions cannot and must not be made available for use without the prior written permission of the owner(s) of the relevant Intellectual Property Rights and/or Reproductions.
- iv. Further information on the conditions under which disclosure, publication and exploitation of this thesis, the Copyright and any Intellectual Property Rights and/or Reproductions described in it may take place is available in the University IP Policy, in any relevant Thesis restriction declarations deposited in the University Library, The University Library's regulations and in The University's policy on Presentation of Theses.

## ACKNOWLEDGEMENT

I would like to gratefully acknowledge my supervisor, Professor Robert Akid, whose invaluable guidance, continuous support, kindness, suggestions and constructive criticisms throughout this research work and during thesis writing, have helped me to accomplish my academic goals at this level of study.

I would like to thank the School of Materials, Corrosion Protection Centre and the School of Mechanical, Aerospace and Civil Engineering for the use of laboratory and mechanical testing facilities.

I am indebted to BP for providing me with full sponsorship funding for this research work and for providing the test material.

I would like to thank Dr Rafael Leiva-Garcia for his help in developing the CAFE model and support in using the confocal microscope. I also thank him for his advice and suggestions during my research and availability for discussion.

I would like to thank Christopher Evans for developing the micro-capillary cell that was used in generating corrosion pits on the test samples and for providing DIC results that were used for FEA model validation.

I am thankful to Stuart Morse and David Mortimer for providing technical support during mechanical testing, Mark Harris and Ian Winstanley who manufactured the specimens and Teruo Hashimoto for his support on scanning electron microscopy. Thanks are also due to other staff in the School of Materials and Corrosion Protection Centre, especially Olwen Richert, Paul Jordan, Steve Blatch and Harry Pickford for their support in various forms.

I would like to thank Dr Nicolas Larrosa for his assistance with the use of Abaqus software and with the writing python scripts that were used in the CAFE model.

I am also thankful Dr D. Engelberg and Dr R. Lindsay and Dr Y. Yang for the advice and suggestions they provided.

I am grateful to my mother for her prayers and encouragement, and my siblings – Olawale, Kimberly, Olumuyiwa, Onikepeju, Olanrewaju, Iyanuoluwa and Faith, for their moral support and prayers. I am also grateful to Taiwo Oguntayo, Femi Akanbi and Sheilla Osondu-Iheke, for their immeasurable support in the last twelve months.

Last but not least, I would like to thank my mates in the BP laboratory, Ashley Broughton, Gaurav Joshi, Karen Cooper, Dr Clara Escrivá-Cerdán, Dr David Mortelo, Jake Andrews, Melissa Keogh and Dr Dhinakaran Sampat; it was a privilege working with you all.

---

# Chapter 1

## Introduction

---

## 1.1 Background

Top-tensioned risers are critical structures in deep-water oil and gas exploration and production, which provide a temporary extension of a subsea oil well to a surface facility (Figure 1.1). They may be subjected to corrosion fatigue (CF) damage from simultaneous action of internal corrosion (pitting corrosion) and fatigue during operations, which can lead to a reduction in service lifetime. Managing the structural integrity of these structures is therefore of utmost importance to guaranteeing safe, reliable and efficient operation. Current structural integrity challenges include the lack of robust and accurate methods for lifetime prediction and reliability assessment, as existing methodologies are time-consuming and conservative with some degree of uncertainty.

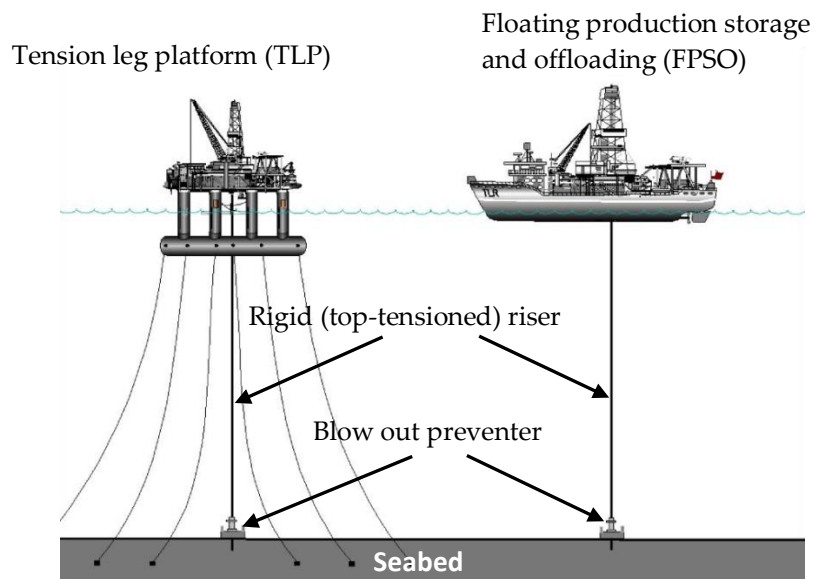


*Figure 1.1 Schematic of a rigid oil riser connecting a subsea oil well to a surface facility.*

In the oil and gas environment, internal pitting corrosion is a significant factor in the degradation of pipelines carrying oil and gas [2, 3]. In contrast to classic pitting corrosion, which involves the breakdown of passive film on metals, pitting corrosion in the oil and gas industry is often associated with the localised breakdown of the iron carbonate and/or iron sulphide scales that are formed on the internal surface of the linepipe. These pits can become the preferred sites for crack nucleation when the risers are subjected to cyclic mechanical loading originating from sources, which include seawater movements, vortex-

induced vibration, downhole vibration, and etc. The cracks then propagate until failure of the structure.

Limited advances have been made concerning corrosion fatigue lifetime prediction. Existing models consider corrosion fatigue as a two-stage process involving pit growth and long crack growth. They also use notch-based modelling to address fatigue crack growth from pits by considering pits as equivalent to cracks and inherently applying the threshold stress intensity factor range,  $\Delta K_{th}$ , a conventional Linear Elastic Fracture Mechanics (LEFM) fracture parameter. However, pitting corrosion fatigue failure is generally regarded as a multi-stage damage process consisting of surface film breakdown, pit development, pit-to-crack transition, short crack growth and long crack growth. Moreover, the prevailing conditions around the pit during and after initiation of short cracks, notably, strain localisation induced plasticity, causes a breakdown of LEFM conditions hence, the appropriateness of using LEFM for addressing crack initiation and growth is questionable. The work presented in this thesis attempts to provide an alternative modelling methodology which accounts for all damage stages, notably from pitting through to long crack growth.

## 1.2 Aims and objectives

This work is part of a broader systematic programme, which has the objectives of formulating a suitable model for corrosion fatigue lifetime prediction and developing the understanding of the corrosion fatigue behaviour of API 5L X-65 linepipe steel. The aims of the present work are to develop a mechanistic understanding of the development of damage during the CF process and to develop a multi-stage damage accumulation model for predicting CF lifetime. In order to achieve these aims, the main objectives are as follows:

1. To evaluate the role of cyclic stress on pit development.
2. To understand the initiation and propagation behaviour of cracks emanating from single corrosion pits in air and aggressive environment.
3. To understand in detail the initiation and propagation behaviour of cracks emanating from double corrosion pits in air.

4. To investigate the mechanics-based conditions that facilitates the transition of pits to cracks by evaluating the distribution of stress and strain around pits.
5. To develop a cellular automata finite element model that offers an alternative method of predicting damage, based upon an understanding of the mechanisms that facilitate the development of a pit and its transition to a crack during CF process.
6. To formulate a multi-stage damage accumulation model that is capable of predicting CF lifetime.

### **1.3 Thesis outline**

This thesis consists of eleven chapters. A literature review on corrosion fatigue damage mechanisms and corrosion fatigue lifetime modelling is presented in Chapter 2. Details of the experimental methods and test procedures are described in Chapter 3. Chapter 4 presents the finite element analysis (FEA) procedure for stress and strain analysis and the development of a cellular automata finite element (CAFE) model for predicting CF damage. In Chapter 5, experimental results are presented and discussed. The results obtained from FEA and CAFE studies are discussed in Chapter 6 and Chapter 7 respectively. In Chapter 8, a multi-stage model for predicting lifetimes for fatigue and corrosion fatigue is presented. Chapter 9 presents a general discussion linking the experimental and modelling parts of this work. Conclusions drawn from the present work and suggestions for future work are presented in Chapter 10 and Chapter 11 respectively.



---

---

# **Chapter 2**

## **Literature Review**

---

---

## **2.1 Corrosion Damage**

### **2.1.1 Introduction**

Corrosion can be generally described as a naturally occurring process which causes degradation of metallic materials when they are exposed to a corrosive environment [4]. The direct and indirect costs associated with corrosion damage have risen over the years and impacts significantly on economies of nations. The cost of corrosion was estimated to be 3 - 4% of the GNP of the USA in 2001 [5]. Corrosion affects industries such as nuclear, aerospace, marine, defence and oil and gas. In the oil and gas industry, corrosion can result in fatal accidents, environmental damage and loss of lives (e.g. Carlsbad pipeline explosion [6], Prudhoe Bay disaster [7], Bhopal gas tragedy [8]).

### **2.1.2 Localised corrosion in passivating metals**

Localised corrosion is associated with high rates of metal penetration at discrete sites. Examples of localised corrosion are crevice corrosion and pitting corrosion. Pitting corrosion is an insidious damage process, which occurs on engineering materials that owe their corrosion resistance to a passive surface film e.g. aluminium alloys and stainless steels. The protective passive film is susceptible to localised breakdown when exposed to specific environments, notably, chloride containing environments, where passive film breakdown results in pitting [9-11]. Under loading, the developed pits can act as initiation sites for cracks. This phenomenon of environment-assisted cracking has been investigated extensively and numerous mechanisms and models have been proposed to explain these damage processes [12-14]. It is worthy of note that the corrosion processes within a pit produce conditions involving the accumulation of chloride ions and pit solution acidification, which further stimulates continuous active dissolution within the pit [15]. A schematic of the processes that take place within an active pit on ferrous alloy in a chloride environment is shown in Figure 2.1. Generally, the redox reactions separate spatially during the process, the anodic dissolution occurring within the pit while the cathodic reactions shift to the exposed surface outside of the pit. The presence of oxidizing agents in the chloride environment can significantly exacerbate the pitting corrosion process. A consequence of the anodic dissolution process is the production of positively charged metal ions, which have to be counterbalanced by cations moving into the pit,

notably  $\text{Cl}^-$ . Consequently, the pit typically contains high concentration of metal anions e.g.  $\text{M}^+\text{Cl}^-$ . Hydrolysis of metal ions also leads to pit acidification. Several factors have been found to influence pitting corrosion of metals and alloys. These include, but not limited to, alloy composition and microstructure [16], temperature [17], chloride concentration and pH [18] and surface condition [19]. Further discussion on pitting corrosion is presented in Section 2.7.5.

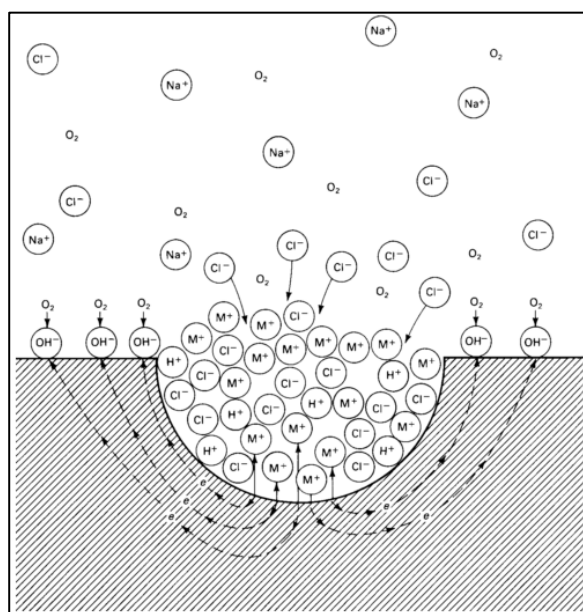


Figure 2.1 Schematic of processes occurring in an active pit in NaCl environment [20].

### 2.1.3 Localised corrosion in oil and gas environment

Internal pitting corrosion is a significant factor in the degradation of pipelines used in the oil and gas industry [2, 3]. Depending on existing conditions, sweet and sour corrosion may result in either uniform or localized attack, the latter in the form of pitting, crevice corrosion, stress corrosion and corrosion fatigue [3, 21]. According to Papavinasam [22], “most of the internal corrosion of oil and gas pipelines is localized attack, characterised by loss of metal at discrete areas of the surface with surrounding areas essentially unaffected or subjected to uniform corrosion”. When the geometrical shapes of the attacked discrete areas are circular depressions with usually smooth and tapered sides, they are referred to as ‘pits’. In the case of stepped depressions with vertical sides and a flat bottom, the attack is referred to as ‘mesa’ attack. Figures 2.2 and 2.3 show schematics of mechanism of pitting and of the types of corrosion that can occur in an oil and gas pipeline respectively. Pitting corrosion has been the subject of several investigations that were directed at

understanding sweet and sour corrosion in linepipe steel. Examples of such studies are Xia *et al.* [3], Papavinasam *et al.* [2, 23] and Nesic *et al.* [24-26]. In contrast to classic pitting corrosion, which involves the breakdown of passive film on metals, pitting corrosion in the oil and gas industry is associated with the localised breakdown of the iron carbonate and/or iron sulphide scales that are formed on the internal surface of the linepipe carrying oil and gas.

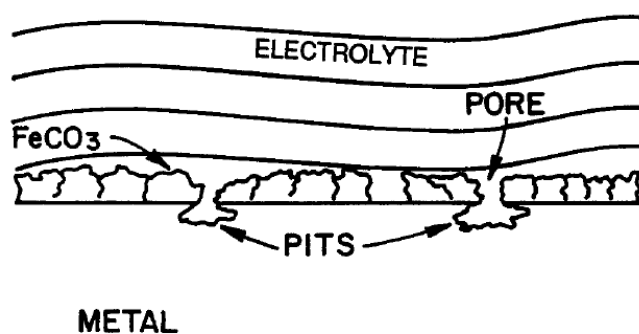


Figure 2.2 Mechanism of pitting corrosion through an iron carbonate scale [27].

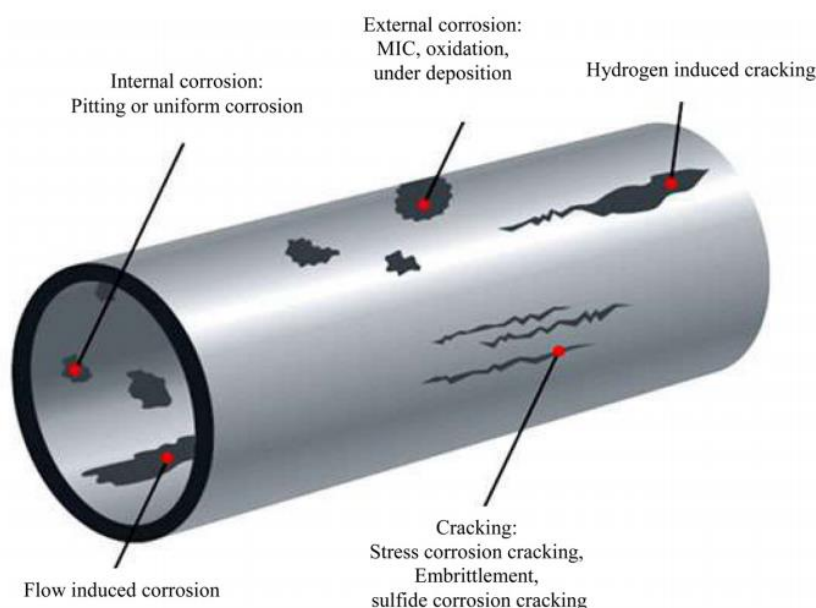


Figure 2.3 Schematic of types of corrosion that can occur in a pipeline [21].

Although the mechanisms that are involved during the pitting process are still being debated, three stages are generally involved: (i) scale formation ( $\text{FeCO}_3$  – siderite and  $\text{FeS}$  – mackinawite in carbon dioxide (sweet) and hydrogen sulphide (sour) environments respectively) on the internal surface of the pipe, (ii) pit initiation resulting from local defects or breakdown of the scale through mechanical or chemical processes and (iii) pit growth stage involving continuous active dissolution of the underlying metal. Some

mechanisms such as differential aeration, pit acidification and point defect mechanism have been invoked from the knowledge of pitting corrosion of passive metals, in order to explain that of a CO<sub>2</sub> environment. However, these have been shown not to apply as discussed by Nesic [25]. Most CO<sub>2</sub> systems are free of oxygen hence, the differential aeration mechanism cannot be considered. The large changes in pH needed to explain the pit acidification mechanism are more difficult to achieve due to the strong buffering capacity of CO<sub>2</sub> solution. In addition, acidification is normally related to the formation of ferric oxides and hydroxides, which are not found in oxygen-free CO<sub>2</sub> systems. The point defect mechanism which is valid for mild steel that passivates in a neutral or alkaline solution does not apply, given the nature of localized corrosion of mild steel in CO<sub>2</sub>-containing chloride environment. An increasingly plausible mechanism is that of galvanic coupling between the pit area exposed to a corrosive environment and the surrounding surface covered by the corrosion scale i.e. a more noble potential on the scaled surface (cathode) compared to that of the pit area (anode) [25, 28, 29]. The difference in open circuit potentials results in an effective polarisation of the pit by the scaled surface and the rate of metal dissolution can be very high due to the large cathode to anode area ratio. A schematic illustration of the galvanic effect is shown in Figure 2.4. In a comprehensive review of pitting corrosion by Nesic [30], factors that can influence internal localised corrosion of oil and gas pipelines include water chemistry (pH, CO<sub>2</sub> partial pressure, acetic acid), temperature, flow conditions, type of steel, inhibition and differential condensation.

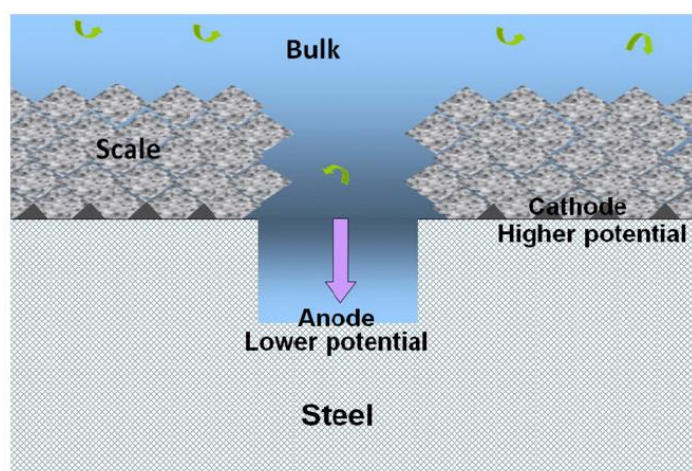


Figure 2.4 Schematic of galvanic mechanistic model for localized CO<sub>2</sub> corrosion [29].

## 2.2 Fatigue of Metals

Fatigue damage is responsible for about 70-80% of the failure cases of mechanical engineering components and structures [31]. An understanding of crack initiation and crack propagation mechanisms is therefore essential for optimum design and maximization of the service life of such components. Generally, pure elastic deformation cannot cause permanent damage because of the reversible nature of the fatigue process. It is therefore accepted that failure due to fatigue is related to localized plastic deformation [32]. Fatigue damage is defined as a process involving the initiation and propagation of cracks under cyclic loading [31].

### 2.2.1 Modes of fatigue crack growth

The three basic modes of fatigue growth are: Mode I, Mode II and Mode III schematically shown in Figure 2.5.

- (A) Mode I is the tensile opening mode in which the crack faces separate in a direction normal to the plane of the crack. Crack propagation is generally by this mode.
- (B) Mode II is the in-plane sliding mode in which the crack faces are mutually sheared in a direction normal to the crack front. Crack initiation is generally by this mode.
- (C) Mode III is the tearing or anti-plane shear mode in which the crack faces are sheared parallel to the crack front.

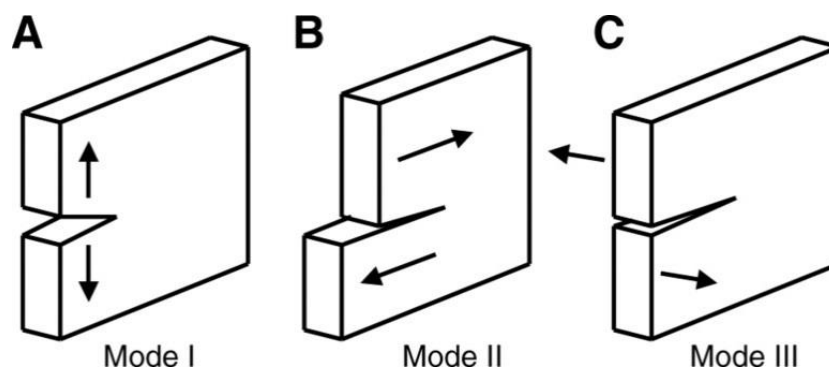


Figure 2.5 Modes of crack growth.

### 2.2.2 Stages of fatigue crack growth

Fatigue in air is a damage accumulation process consisting of two stages:

- Crack initiation
- Crack propagation

The crack propagation stage can be subdivided into three stages [31]:

- Stage I crack propagation
- Stage II crack propagation
- Stage III (Final fracture)

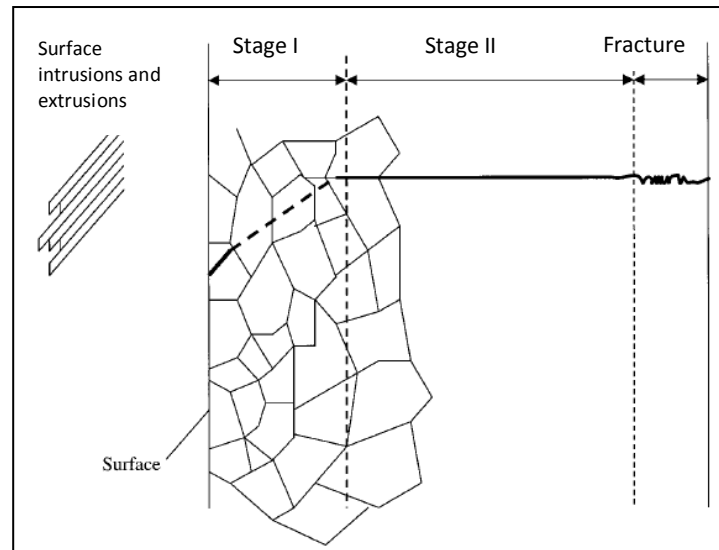


*Figure 2.6 Schematic representation of crack initiation and growth in polycrystalline metals.*

### 2.2.3 Crack Initiation

Fatigue cracks generally initiate in Mode II in the largest surface grains where deformation is largest and there is minimum constraint and are generally oriented along active slip planes, which correspond to the maximum shear planes. In axial loading system, this occurs at  $45^\circ$  to the loading direction [33]. The local stress is determined by factors such as magnitude and type of loading, texture of material, and specimen geometry. In addition, development of intrusions and extrusions resulting from persistent slip bands, local imperfections such as dents, scratches, voids, defects, existing cracks, notches, welds and geometric discontinuities, and other physical/manufacturing flaws can exacerbate local stress concentration and thereby increase the propensity for cracking at these sites [34]. The local strength may reduce to a minimum at features such as grain boundaries, twin boundaries, inclusion-matrix interface and second phase-matrix interfaces [35]. In addition, the fatigue initiation process can be significantly affected by an aggressive environment by increasing the local stress through development of localised

corrosion defects such as corrosion pits and by decreasing the local strength through embrittlement from adsorption of hydrogen. In smooth specimens, the nucleation of short cracks depends on boundary conditions (specimen geometry), loading mode, loading environment and material microstructure (particularly at the free surface of the specimen). Initiation in smooth surfaces often occurs in the largest grains on the surface of the specimen where plasticity is largest and there is minimal. In materials with brittle inclusions, the cracking of the inclusion may result in nucleation of a short crack [36]. Fatigue studies have shown that crack initiation can take up to 90% of the fatigue life in smooth specimens [31].

## **2.2.4 Crack propagation**

### **2.2.4.1.1 Stage I Crack Propagation**

At this stage, microstructural factors influence the propagation mechanics causing the crack to exhibit some anomalous behaviour. This stage is schematically represented in the Figure 2.7. The initiated short cracks propagate until they are decelerated by microstructural factors such as grain and phase boundaries, inclusions and etc. Plasticity induced in the grains drives the crack until a dislocation build-up occurs as the crack tip approaches a grain boundary. Depending on the stress level and orientation of active slip planes in adjacent grains, the crack growth is activated again and then decelerated while for some cracks remain dormant thus becoming non-propagating [37]. The observation of non-propagating cracks gave more insight into the fatigue limit of materials which was thought to be the stress level below which cracks do not initiate. The fatigue limit is now defined as the stress level below which cracks can initiate but do not propagate. Hence the fatigue limit of a material depends on the effective resistance of the microstructural barriers that has to be overcome by the cracks. Having penetrated the bulk of the material, after some few grains, the influence of the microstructure becomes minimal while the crack has become dominant. At this stage, the crack propagation transits to a Stage II propagation [34, 38].



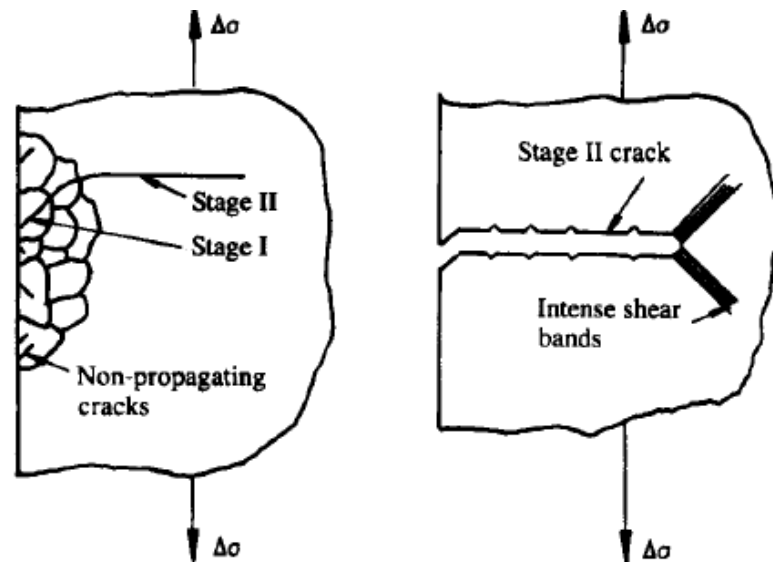


Figure 2.7 Schematic illustration of stage I and stage II fatigue crack growth stages [38].

#### 2.2.4.1.2 Stage II crack propagation

When the stress intensity factor,  $K$  (SIF) increases as a consequence of crack growth or higher applied loads, slip develops in different planes in the reversed plastic zone at the crack tip, initiating Stage II cracks, which are usually Mode I cracks. At this stage, the direction of propagation is perpendicular to the loading direction. An important damage mechanism in this stage is the development of striations by successive blunting and re-sharpening of the crack tip.

#### 2.2.4.1.3 Stage III crack propagation

Stage II crack propagation is related to unstable crack growth as the SIF approaches the critical SIF for fast fracture,  $K_{Ic}$ . At this stage, crack growth is controlled by static modes of failure and is very sensitive to the material microstructure, stress level, stress state and the environment [31, 39, 40]. The material fractures either by brittle or ductile fracture.

### 2.3 Fatigue Life Prediction

In order to develop methods for predicting fatigue lifetime, an understanding of fatigue crack growth behaviour and the mechanisms involved is important. In dealing with this challenge, two basic methodologies are commonly used in fatigue design, namely, 'Total Life' and 'Damage-Tolerance' approaches.

### 2.3.1 Total life methodology

The total life approach involves characterisation of total fatigue life of specimens in inert and aqueous environments. The relationship between the stress or strain range and the fatigue life are presented as Stress-Life (S-N) or Strain-Life (E-N) curves, which can be used for design purposes to estimate the design or residual lives of engineering components. The application of the S-N method is easier in terms of a quantitative assessment of fatigue damage. However, a setback is that experimental data can exhibit significant scatter due to a number of factors including surface finish, flaw distribution and etc., which can have substantial effect on the crack nucleation stage. In addition, because the crack initiation life and propagation life are not separated, it is always difficult to identify the damage mechanisms that govern these two stages of the fatigue life. Hence, it is generally a conservative approach to fatigue design and analysis. A typical S-N curve is shown in Figure 2.8. The horizontal line indicates a fatigue limit for the material and it represents the minimum stress range below which the material will endure infinite fatigue life [31]. The figure also shows the effect of the environment whereby the fatigue limit in air has been reduced. The applicability of the total life approach is dependent on the level of operating stress or strain. These can be classified as low cycle fatigue, high cycle fatigue and giga cycle fatigue.

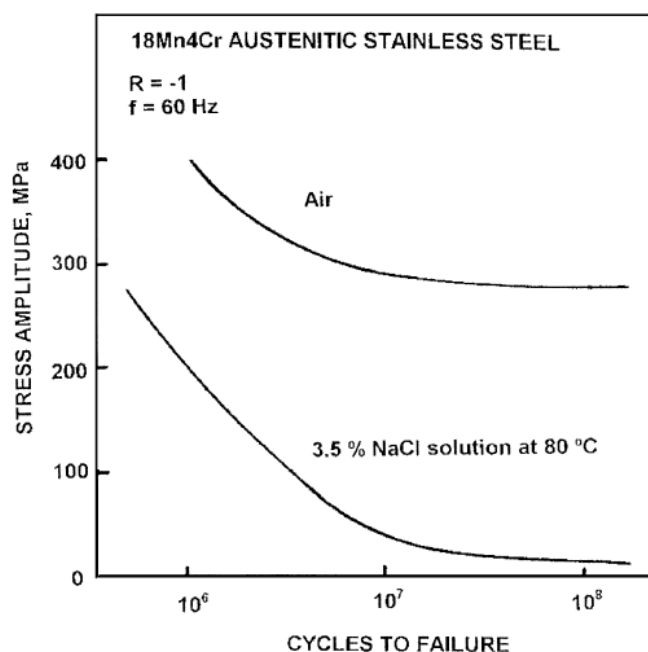


Figure 2.8 Typical S-N curve showing the variation of the stress amplitude with the number of cycles for stainless steel in 2.5% NaCl at 80°C [41].

### High cycle fatigue

At low stress levels, gross deformation in the material is elastic so the material can undergo high number of cycles. Hence, fatigue resistance is usually characterised in terms of the stress range. The S-N curve can be modelled empirically using the Basquin relationship expressed below [42]:

$$\frac{\Delta\sigma}{2} = \sigma'_f (2N_f)^b \quad 2.6$$

where  $\Delta\sigma$  represents the stress range,  $\sigma'_f$ , the fatigue strength coefficient,  $b$ , the fatigue strength exponent and  $N_f$  is the number of cycles to failure.

### Low cycle fatigue

In contrast to high cycle fatigue, low cycle fatigue involves stress levels that are high enough to cause plastic deformation; hence the material can only sustain low number of cycles. Because deformation is no more elastic, the strain range is used to characterise the fatigue behaviour of the material. The Coffin-Manson relationship provides method for modelling the fatigue behaviour of materials [43, 44]:

$$\frac{\Delta\varepsilon_p}{2} = \varepsilon'_f (2N_f)^c \quad 2.7$$

where  $\Delta\varepsilon_p$  represents the plastic strain range,  $\varepsilon'_f$ , the fatigue ductility coefficient,  $c$ , the fatigue ductility exponent and  $N_f$  is the number of cycles to failure.

Since the total strain can be decomposed into the elastic and plastic components (Equation 2.8), both Equations 2.6 and 2.7 can be summed as expressed below:

$$\frac{\Delta\varepsilon}{2} = \frac{\Delta\varepsilon_e}{2} + \frac{\Delta\varepsilon_p}{2} \quad 2.8$$

$$\frac{\Delta\varepsilon}{2} = \frac{\sigma'_f}{E} (2N_f)^b + \varepsilon'_f (2N_f)^c \quad 2.9$$

where  $\Delta\varepsilon$  is the total strain range and  $E$  is the Young's modulus.

#### 2.3.2 Damage tolerance methodology

The relatively recently developed damage tolerance approach invokes LEFM concepts with the premise that all engineering components are inherently flawed with a pre-existing crack size. The LEFM approach has been valuable in the analysis of long crack growth (long crack regime). The fundamental assumptions of LEFM are that a material is

an isotropic continuum and is linearly elastic. Therefore, LEFM is only valid for small-scale yielding conditions where the plastic deformation at the tip of the crack is small compared to the size of the crack. Under LEFM conditions, the driving force is characterised by the SIF range and a similitude concept exists, which links the SIF range to the crack growth rate. According to the similitude concept, two different cracks growing in identical materials and thicknesses with the same SIF range will grow at the same rate [31]. The stress intensity factor is related to the magnitude of the applied nominal stress and the square root of the crack length by [45]:

$$K = Y\sigma\sqrt{\pi a} \quad 2.10$$

where  $\sigma$  is the remote applied stress,  $a$  is the crack length and  $Y$  is a dimensionless geometrical correction factor.

One or all the modes of crack growth (Mode I, Mode II, Mode III) may be prevalent in the vicinity of a crack tip. The associated stress intensity factors are  $K_I$ ,  $K_{II}$  and  $K_{III}$  respectively and the effective SIF can be obtained by summing the prevalent modes (Equation 2.11). However in many practical cases, the predominant case is that of Mode I loading.

$$K = K_I + K_{II} + K_{III} \quad 2.11$$

Paris and Erdogan [46] proposed an empirical relationship (Equation 2.12) that correlates fatigue crack growth rate with the SIF range.

$$da/dN = C(\Delta K)^m \quad 2.12$$

$$\Delta K = K_{max} - K_{min} \quad 2.13$$

where  $C$  and  $m$  are material, temperature and environment dependent constants,  $\Delta K$  is SIF range and  $K_{max}$  and  $K_{min}$  are the maximum and minimum values of the SIF during a fatigue cycle.

With the knowledge of the stress range, threshold and critical values of  $K$  and the constants  $C$  and  $m$ , the fatigue life of engineering structures can be calculated by integrating the equation between the initial and final crack sizes. LEFM uses crack growth rate curves to characterise fatigue life of materials. Fatigue crack growth curves, schematically shown in Figure 2.9, are characteristic plots of  $da/dN$  versus  $\Delta K$ . The plot

has a sigmoidal shape and shows three different regions: Region 1 - Near-threshold region, Region 2 - Paris region and Region 3 - Rapid growth region. In the near-threshold region, the crack growth rate is observed to go asymptotically to zero as  $\Delta K$  approaches a threshold value,  $\Delta K_{th}$ . Below this threshold, there will be no crack extension. At  $\Delta K$  values just beyond the threshold value, cracks grow in both Mode I and Mode II and their growth is strongly affected by microstructure, mean stress, stress ratio and environment hence, the Paris Law is observed to break down. The Paris region is associated with Mode I cracks and growth rate is related to  $\Delta K$  according to the Paris Law (Equation 2.12). The cracks which obey this law are termed long cracks and factors such as mean stress, microstructure and stress ratio have minor influence on their growth rates. However, the environment can influence crack growth. The rapid growth region exhibits unstable crack growth - a rapidly increasing growth rate towards infinity, arising from interactions between cyclic, ductile tearing and/or brittle fracture mechanisms. In this region, cracks grow in Mode I and Mode II and crack growth is strongly accelerated with the value of  $K_{max}$  rapidly approaching the fracture toughness of the material ( $K_{Ic}$ ). Crack extension in this region is dependent on stress ratio. The Paris relationship is only restricted to the linear region hence, integration over the entire lifetime will yield conservative results. The crack growth relationship in the near-threshold region was proposed by Donahue *et al.* [47] as:

$$da/dN = C(\Delta K - \Delta K_{th})^m \quad 2.14$$

Foreman *et al.* [48] proposed the crack growth relationship in the rapid growth region as:

$$da/dN = \frac{C\Delta K^m}{(1-R)K_c - \Delta K} \quad 2.15$$

where  $K_c$  is the plain strain fracture toughness of the material and  $R$  is the stress ratio.

One of the models proposed to describe the entire sigmoidal curve, which has been used extensively in damage assessment is the NASGRO equation [49]:

$$da/dN = A' \left[ \frac{1-f}{1-R} \right]^m \Delta K^m \left[ \frac{1-\Delta K_0}{\Delta K} \right]^p \left[ \frac{1-K_{max}}{K_{mat}} \right]^{-q} \quad 2.16$$

where  $A'$ ,  $m$ ,  $p$ ,  $q$  are material constants and  $f$  is the ratio of the opening and maximum values of stress intensity factor; this in turn is a function of  $R$ . In the Paris region,  $f = R$  and  $p$  and  $q$  are zero.

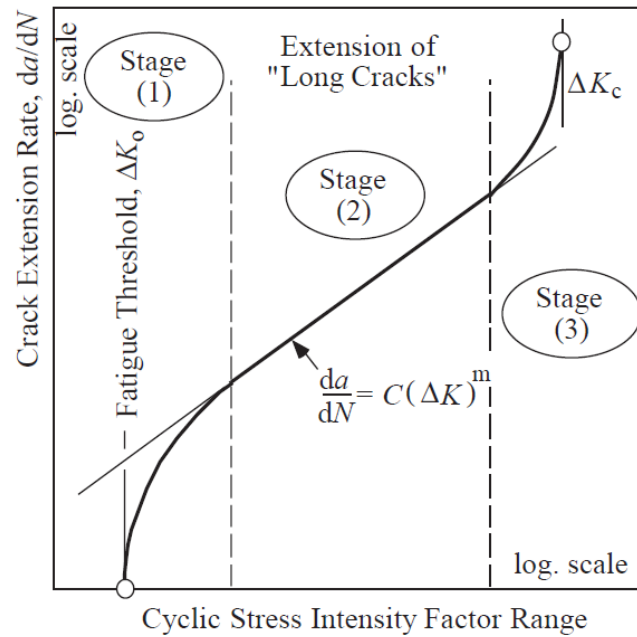


**Figure 2.9** Schematic representation of crack growth rate ( $da/dN$ ) versus range of stress intensity factor [50].

The fracture toughness is a material property which measures resistance to crack extension. In materials with pre-existing flaws, it is an indication of the amount of stress that is required to propagate a pre-existing flaw [51]. In practice, the fracture toughness is an important material property used by engineers in fitness-for-service assessments since the occurrence of flaws such as inclusions, cracks, voids, weld defects, design discontinuities, fabrication defects or a combination of these is not completely avoidable [50].

## 2.4 Behaviour of Short Fatigue Cracks

It is now well established that the behaviour of short fatigue cracks (Stage I cracks) has a considerably influence on the fatigue life of engineering components. Under high cycle fatigue conditions, the propagation of these cracks can take a significant fraction of fatigue life [52, 53]. The behaviour of short fatigue cracks has received wide attention because of the inability of the conventional LEFM to provide accurate models to predict their growth rates [33, 37, 54-59]. It was observed that LEFM only provides more accurate estimates when flaws are above a certain size [60]. However, when the flaws are smaller than this threshold size (typically the size of a few grains), application of LEFM leads to non-conservative predictions. Generally speaking, the reason for this lies in the breakdown of

the similitude concept which results when small-scale yielding conditions are exceeded due to high stress levels and/or when the material is no more homogenous due to the effect of microstructural features in the matrix [35].

Different definitions have been suggested for short fatigue cracks. Suresh and Ritchie [61] suggested that fatigue cracks can be described as being short when:

- i. their sizes are comparable to those of the microstructural features such as grain boundaries. In this case, such cracks can be described as microstructurally short and the material behaviour cannot be described by continuum mechanics,
- ii. when the scale of the local plasticity associated with the crack tip is comparable to or larger than the size of the crack itself. These cracks can be described as mechanically short and they invalidate the small-scale yielding assumption of the LEFM
- iii. when they are merely physically short. These physically short cracks can have lengths typically less than 1 mm.

A short crack was also defined based on the extent of plasticity ahead of the crack tip. A crack is short if the plastic zone size,  $r_p$  is greater than or equal to one fiftieth of the crack length,  $a$  as given in Equation 2.17 [35]. Ritchie and Lankford [52] also defined short cracks as those being less than 0.5 – 1 mm in size.

$$r_p \geq \frac{a}{50} \quad 2.17$$

Three different regimes of short crack growth can be identified based on the behaviour characteristic of each type of crack. These are microstructurally short cracks, physically small cracks and highly stresses cracks [33]. These regimes are schematically shown in Figure 2.13.

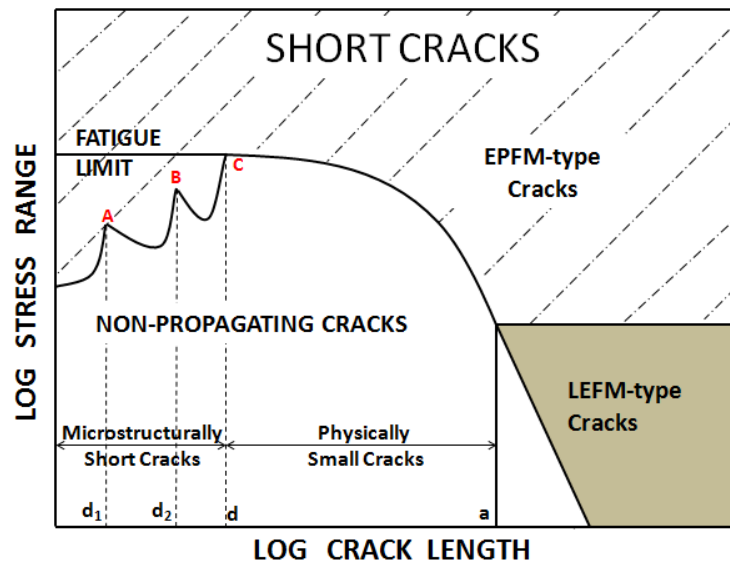


Figure 2.10 Three regimes of short crack behaviour [33].

#### 2.4.1 Microstructurally short crack regime

In general, microstructurally short fatigue cracks are fatigue cracks whose size are in the order or a few times the scale of the microstructural units of the material. They are usually referred to as Stage I-Mode II cracks because they grow in slip planes that have the maximum resolved shear stress. Their lengths are typically less than that of a dominant microstructural barrier,  $d$  (Figures 2.10 and 2.11). The dominant factor in this regime is the surrounding microstructural features such as grain boundaries, twin boundaries, etc., which cause fluctuations in crack growth rates. A retardation of crack growth and possibly crack arrest at these features ( $d_1$ ,  $d_2$ ,  $d$ ) is often observed as the crack tip approaches them (points A, B and C). These types of microstructurally short cracks are referred to as non-propagating cracks. Depending on stress conditions and local conditions, the cracks can cross the grain boundary and re-initiate in adjacent grains. Once this happens, growth accelerates and the retardation and re-initiation may be repeated until the crack size is above a threshold size,  $d$ , whereby it can no more be influenced by the microstructure. Because of the inhomogeneity in the material due to these microstructural features, LEFM is inapplicable and continuum fracture mechanics analysis is considered invalid in this region.

#### 2.4.2 Physically small cracks

Mechanically small cracks are fatigue cracks with lengths that are less than the minimum length for which LEFM is applicable,  $a$ , but greater than that of the dominant



microstructural barrier,  $d$  (Figure 2.10). These cracks are also referred to as Stage II-Mode I cracks since they grow in a direction perpendicular to loading. Since the microstructure has no effect on this type of crack, the expectation is that continuum mechanics approach can be used to analyse crack growth. However, because they need high stress for propagation due to their small sizes, their growth is usually accompanied by considerable plasticity particularly at high growth rates [35]. Consequently, they are normally analysed using elastic-plastic fracture mechanics. In addition, the effect of crack closure on their growth can be considerable [62, 63].

### 2.4.3 Highly stressed cracks

This type of cracks are typically long cracks, hence application of LEFM for their analyses is valid. However, because the applied stress is very high, normally about 66% of the cyclic yield strength of the material, such long cracks can behave as short cracks [35]. Hence, they are considered to be highly stressed cracks for which only EPFM analyses are valid due to the large scale yielding conditions at the crack tip.

The characteristics of short fatigue cracks can be classified generally into three:

- Under the same nominal SIF range, they experience higher growth rates than long cracks [58, 60, 64].
- They propagate below the threshold SIF range where long cracks do not propagate [65].
- They exhibit discontinuous accelerations and decelerations in growth patterns notably in the first stages (Stage I) of fatigue cracking.

Figure 2.11 illustrates the fluctuations due to the effect of grain size. Crack arrest gives rise to non-propagating cracks that are often observed on fractured surfaces. In addition to microstructure, other factors that can affect the behaviour of short crack include mean stress, load ratio, plasticity-induced crack closure and roughness-induced crack closure.

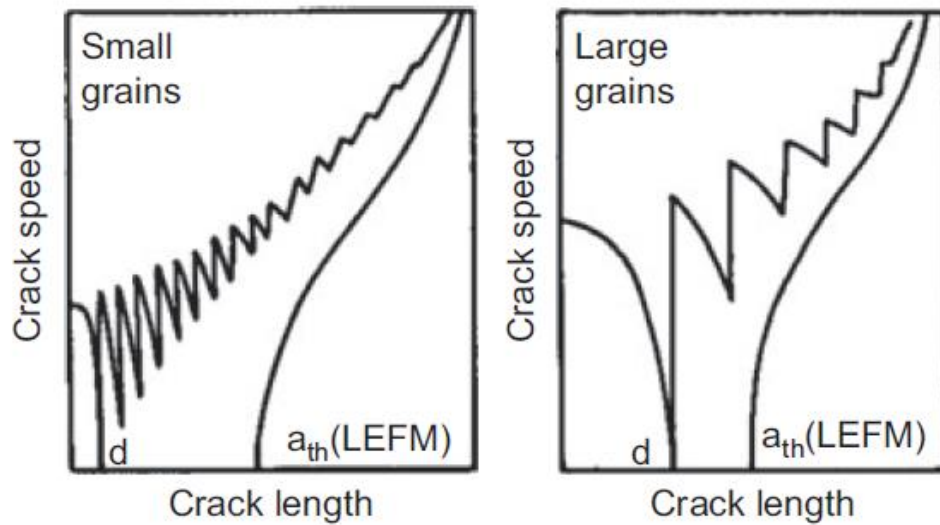


*Figure 2.11 Schematic illustration of fluctuations due to the effect of grain size on growth of microstructurally short cracks [66].*

These characteristic behaviour of short cracks has been extensively studied by a number of researchers. Some of the early works include that of Pearson who first observed accelerated growth rates for short fatigue cracks in two commercial precipitation-hardened aluminium alloys [60]. He reported that the grow rate of short fatigue cracks was as much as hundred times faster than those of long cracks under the same stress intensity factor range. He also reported that when crack size was greater than 0.127 mm, the crack growth curve tended towards that of long cracks. The results of some studies suggest that the higher growth rates observed for short cracks compared to those of long cracks is due to crack tip shielding and closure in long cracks. Detailed discussion by Ganglof and Ritchie [67] suggested that shielding or closure can result from different sources, the most important being plasticity effects, fracture surface roughness and deposits. De les Rois [58] noted that the higher growth rates is due to the size of the plastic zone associated with short cracks, which is significantly larger than that which LEFM predicts.

In the study by Lankford on high strength steel [68], crack growth rate were observed to decelerate for crack lengths which corresponded to the minimum and maximum prior austenite grain size. In another survey of studies on the growth of small fatigue cracks in steels, Lankford showed that the anomalous growth rates are only possible when certain

criteria are met [69]. These include size of microstructure, plastic zone size and the crack size. De los Rios and co-workers have studied the influence of microstructure on the growth behaviour of short cracks in carbon steels [58, 70]. They reported that cracks grew very quickly after initiation but decelerated as they approached microstructural barriers such as at the ferrite and cementite plates and pearlite bands. They pointed out that crack growth rate slowed down when the tip of the crack approached these microstructural barriers and then accelerates again once the crack transverses these barriers. A study on titanium alloy suggested that the orientation between the grains of a material determines the degree of crack retardation [71]. When the orientation of an adjacent grain is not favourable, the crack growth rate would slow down and may possibly arrest. In their study on plain carbon steel, Ray and co-workers reported fluctuations in crack growth rates and also crack arrest at certain crack lengths which corresponded with the transition point between short and long cracks [72]. These fluctuations and crack arrest were observed to be at crack lengths corresponding to microstructural locations of ferrite-pearlite interfaces.

Tokaji and co-workers investigated the influence of grain boundaries on growth rate and the critical length for the applicability of LEFM on a growing short crack in high strength alloy steel [65]. They reported that the effect of grain boundaries depends on the crack length; this effect is limited to three times the size of the prior austenite grain of the material. Above this crack length, the propagation rate of the cracks increased with increase in crack length but the growth rates were still faster than those of long cracks. They concluded that the threshold for the applicability of LEFM was at crack length that is 150  $\mu\text{m}$  above that at which the microstructure was dominant. In a survey of investigations carried out on the behaviour of microstructural short fatigue cracks in seven different types of steels that were tested under rotating bending and axial loading regimes, Tokaji and Ogawa made the following conclusions [73]:

- the behaviour of these cracks was similar in all the materials
- crack growth rates were decreased by grain boundaries, triple points and interface between faces and also due to crack deflection
- crack growth rates were sensitive to grain size; significant deceleration of growth rates in finer grains than in coarse grains, which resulted in increase in fatigue life.

Other studies have also established that short cracks do propagate at SIF levels that are below the threshold value for long cracks. For short cracks, Tokaji and co-workers reported values that were lower than those of long cracks in both fine and coarse grain microstructures in high strength steels [65]. It is worthy of note that microstructural features not only improve fatigue resistance by decreasing the growth of short cracks or arresting them. Another mechanism by which the effective crack growth can also be reduced is through crack deflection. Cracks can be periodically deflected from their original growth path by obstacles in their path which tilt or twist the crack front [31, 74]. The anomalous crack growth behaviour of short cracks, notably higher growth rates, retardation, crack arrest and re-propagation, have been rationalised based on several mechanisms relating to crack-grain boundary interactions, local residual stresses, crack closure effect and the extent of crack deflection. The interaction between microstructural features and the crack tip can lead to: (i) pinning of the slip bands and blocking of dislocation movement which will lead to crack growth retardation or crack arrest [75], (ii) changes in the driving force at the crack tip which can be due to the of the crack deflection resulting from the crystallographic re-orientation of the crack tip during transfer into the adjacent grain across the grain boundary [76-78] and (iii) retardation of crack growth and eventual crack arrest until a significant plastic develops in an adjacent grain [79]. Morris [80], Breat and co-workers [81], and Tokaji and co-workers [65] suggested that the increase in crack closure as a result of increase in length of short cracks was responsible for the observed behaviour. Suresh [76] suggested the behaviour was attributable to crack deflection while Zhai [78] demonstrated that the twist and tilt angles of the crack plane deflection at the grain boundaries is the determining factor controlling the propagation rates and path of short cracks.

## **2.5 Fatigue Limit and Non-Propagating Cracks**

The fatigue limit was previously related to the stress range at which cracks did not initiate and hence, failure will not occur. From observations of the anomalous behaviour of short cracks, it is now generally accepted that a fatigue limit exists in materials not because cracks do not initiate but because of the inability of short cracks to propagate due to the inherent resistance of microstructural features within the material's microstructure [82, 83]. These non-propagating cracks have been observed in both plain [82, 83] notched

components [84-87]. At stress below the fatigue limit, an initiated crack can be arrested at successive microstructural barriers ( $d_1$ ,  $d_2$ ,  $d$  in Figure 2.10) and thus become non-propagating. However, when the barrier is overcome, the crack can re-propagate. This could happen at stresses above the fatigue limit as a result of increase in the size of the local crack tip plastic zone, which was insufficient to cause further crack advance (crack arrest) at lower stress level, but now sufficient to cause slip within adjacent grains.

Under CF conditions, the fraction of the fatigue life a crack spends crossing microstructural barriers can reduce significantly and the feature of non-propagating cracks can be mitigated through the process of strain-assisted dissolution [88, 89]. Investigations by Akid and Murtaza [53, 88-90] showed that the fatigue limit, which is a threshold length scale for crack propagation in air, may be eliminated by the intermittent introduction of a corrosive environment. Their explanation is that below this threshold length, cracks may initiate in air but will arrest at a microstructural barrier. This barrier is eliminated as the crack is allowed to progress through anodic dissolution, and thus propagates to a length that will result in failure.

## 2.6 Kitagawa-Takahashi Diagram

As previously described, two approaches are generally used in fatigue damage assessment of engineering materials – total life (S-N) approach and damage tolerant approach ( $da/dN-\Delta K$ ). Although the total life method is simpler, it can involve excessive scatter in the data and does not provide any information on the different stages of fatigue damage. Conversely, the damage tolerance approach provides a more accurate way for characterising fatigue damage when pre-existing flaws are present, however it is only valid for cases where there is small-scale yielding. Under these circumstances, the use of an assessment method that links the different stages of crack growth whether cracks initiated at a surface, defect, or pit is important. The Kitagawa-Takahashi (K-T) diagram affords this methodology [91]. The K-T diagram is based on the fatigue limit of a plain material and the threshold stress intensity factor range. Typical K-T diagrams are shown in Figures 2.12 and 2.13. The K-T diagram consists generally of three components:

- A threshold line which has a slope of -0.5 representing the threshold stress intensity factor range function,  $\Delta K_{th}$ , below which a crack should not grow if LEFM conditions are valid. This is given by

$$\Delta\sigma_{th} = \frac{\Delta K_{th}}{Y\sqrt{\pi a}} \quad 2.24$$

where  $Y$  is the geometric correction factor,  $\Delta\sigma_{th}$  is the threshold stress range and  $a$  is the crack length.

- A horizontal line which represents the smooth specimen fatigue limit,  $\Delta\sigma_0$ ; and
- The El Haddad line which is an asymptotic matching between the fatigue limit and the threshold line. The equation for this line is given by [92]:

$$\Delta\sigma = \frac{\Delta K_{th}}{Y\sqrt{\pi(a_0 + a)}} \quad 2.25$$

An additional parameter in this equation is the El Haddad parameter,  $a_0$ , which is an intrinsic defect size defined at the intersection of the threshold line and plain specimen fatigue limit line. This intrinsic defect size can be evaluated from Equation 2.32.

$$a_0 = \frac{1}{\pi} \left( \frac{\Delta K_{th}}{Y\Delta\sigma_0} \right)^2 \quad 2.26$$

In Figure 2.12, the K-T diagram is described as a failure envelope of crack size/stress range combinations that will result in fatigue failure of engineering materials [93]. For stresses above this curve, finite life is expected because cracks can propagate to final failure while the region below it is a safe region where initiated cracks will not propagate. It follows from this figure that the difference between fatigue failure (finite life) and no failure (infinite life) is the ability of cracks to propagate.

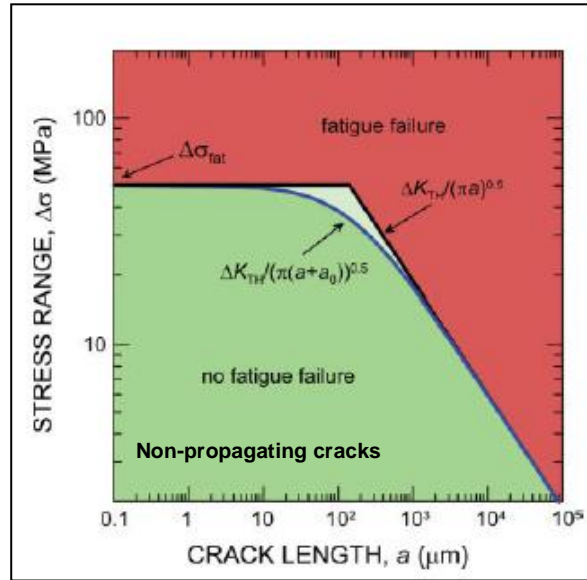


Figure 2.12 Schematic showing the Kitagawa-Takahashi diagram and the limiting conditions for fatigue failure [93].

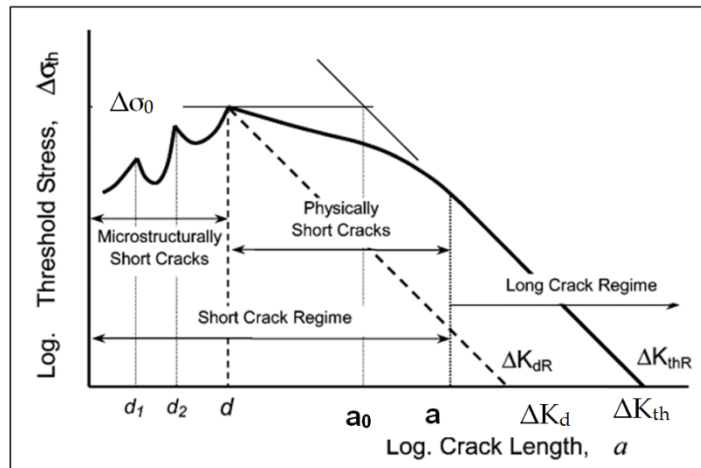


Figure 2.13 Schematic showing the relationship between the limiting threshold stress and crack size and the short crack growth and long crack growth regimes of the Kitagawa-Takahashi diagram [94].

Figure 2.13 describes the K-T diagram based on different types and regimes of crack growth. These include the microstructurally short crack, physically short crack and long crack regimes [94]. In the microstructurally short crack regime, where the crack length is typically of the order of microstructural dimensions, there is an influence of the microstructure on whether cracks will be arrested or continue to propagate [33, 58, 95]. As shown in the diagram, a crack with length less than the strongest microstructural barrier (microstructural threshold), which is at a given distance  $d$ , will result in no failure with respect to the plain fatigue limit,  $\Delta\sigma_0$ . Also, cracks with lengths  $d_1$  and  $d_2$ , shorter than the

size of the strongest microstructural barrier,  $d$ , will be arrested (non-propagating cracks) if the applied stress range is smaller than the plain fatigue limit [95]. In the long crack growth regime, the threshold stress intensity factor range defines a limiting condition for long crack propagation and is independent of crack size for crack lengths greater than a limiting crack length,  $l$  (mechanical threshold). However, above this threshold length, the stress range required to achieve the limiting stress intensity factor (threshold stress range) decreases with increase in crack size [37, 69, 95]. This implies that for a given size of long crack that is greater than the threshold length, crack growth will occur if the applied stress range is greater than the threshold stress range [95]. The regime between that of microstructurally short cracks and long cracks represents the physically short cracks and is the transition between the microstructural,  $d$ , and mechanical,  $l$  thresholds. In this region, below the mechanical threshold, the curve deviates from the threshold stress intensity range line thus indicating that the threshold stress intensity factor for this crack regime cannot be predicted using LEFM analysis. The curve also approaches the plain fatigue limit at the microstructural threshold. The physically short crack region is important because if the defect size is greater than the mechanical threshold, LEFM is applicable for explaining crack propagation. The ability of the K-T diagram to successfully define the combination of crack size (microstructural and mechanical thresholds) and stress range that will lead to failure has given rise to various generalized diagrams, which can be used for design and residual life assessment purposes. These diagrams, which are usually in the form of fatigue damage maps, have been generated for different materials and also applied for fatigue assessments. Venkateswaran *et al.* [96] generated stress versus crack length plots at different stress ratios for a ferritic steel weld metal, based on the K-T diagram. From the generated plots, the limiting stress range required to achieve a desired fatigue life for the components made from the steel and containing different crack sizes was determined. Peters *et al.* [97] examined the effect of applied and residual stresses due to foreign-object damage and stress ratio on high cycle fatigue failures in a titanium alloy. In their study, a modified K-T diagram, which describes the limiting conditions for high cycle fatigue failure, was presented. Various generalised diagrams have also been proposed for design purposes [98-101].



## 2.7 Environment Assisted Fatigue

It is generally accepted that the effect of the interaction between the environmental time-dependent electrochemical processes (corrosion) and applied stress can lead to a significant reduction in the design life of engineering structures and components. For instance, materials with good corrosion resistance in the absence of applied stress and those with superior fatigue strength in air, can exhibit poor behaviour under the conjoint action of stress and corrosion [102]. Environment assisted cracking (EAC) can generally be classified into three forms [103]:

- Stress corrosion cracking (SCC)
- Hydrogen-assisted cracking (HAC)
- Corrosion fatigue (CF).

### 2.7.1 Hydrogen-assisted Cracking (HAC)

HAC involves the diffusion of and build-up of hydrogen in the metal when exposed to hydrogen-rich environments thus, assisting the initiation and propagation of cracks. This could be through reduction of surface energy by hydrogen adsorption, reduction in the inter-atomic bond strength or hydrogen molecules exerting pressure against the wall of the crack. Effects of hydrogen damage include hydrogen embrittlement, loss of tensile strength, blistering, hydride formation, micro-perforation and degradation in flow properties. HAC may also contribute to the failure of materials by SCC and CF. For instance, in some metal-environment systems under cathodic protection, SCC has been found to result from hydrogen-induced subcritical crack growth [104].

### 2.7.2 Stress Corrosion Cracking (SCC)

SCC occurs when a metal is simultaneously subjected to a static stress of sufficient magnitude and a corrosive environment [105]. Usually, a specific environment and metallurgical condition, in terms of the composition and structure of the alloy is also a requirement. For example, the SCC of copper alloys is usually due to the presence of ammonia in the environment while for stainless steels and aluminium, the presence of chloride ions is the main cause [106, 107]. In SCC, crack propagates within the material through the internal structure usually living the outer surface unarmed. Different mechanisms have been proposed to explain the interaction between stress and corrosion

at the crack tip during SCC damage. They include active path intergranular cracking [108], film rupture/anodic dissolution [109], and adsorption-related mechanisms [106, 110]. In SCC, the threshold SIF below which cracks will not propagate,  $K_{Isc}$ , is typically below the threshold SIF implying that cracking can occur at far lower SIF values than when there is no corrosion. SCC is influenced by factors such as material (microstructure, composition, grain size) [111], mechanical (stress, strain rate) [112], and environment (temperature, pH, solute concentration, solute species) [113].

### 2.7.3 Corrosion Fatigue

Historically, corrosion fatigue damage has been recognized as a major cause of failure of engineering structures hence, it is a major concern for design engineers. CF is a material degradation process involving the synergistic damage actions of an aggressive environment and mechanical cyclic loading [114-116]. Generally, the effect of this synergy on the damage process is more severe than the sum of their individual effects when acting separately i.e. corrosion or fatigue [31, 102]. Investigations on the fatigue behaviour of these structures in aggressive environments revealed significant reduction in fatigue strength in these environments far below that observed in air. In some cases, the fatigue limit is completely eliminated. Under CF conditions, no matter how low the stress amplitude is, fracture can eventually occur in the engineering structure [117-120]. This is in contrast to fatigue in air where crack can nucleate but do not grow (crack arrest) at stress levels below the fatigue limit. A thorough understanding of the stages of corrosion fatigue and associated mechanisms is essential in order to optimise design and maximise the lifetime of structures operating in aggressive environments.

The influence of the environment can be related to the crack initiation and crack growth processes especially in the early stages of corrosion fatigue damage. In the initiation stage, the environment can accelerate the nucleation of cracks by creating localised defects such as corrosion pits. Corrosion pits can act as stress intensifiers and also provide a pit chemistry that is favourable for crack nucleation [121-124]. After the nucleation of cracks, the environment can influence crack growth rate through strain-assisted anodic dissolution. Here, the environment can influence Stage I crack growth by overcoming the microstructural barriers that retard crack growth or lead to crack arrest. Furthermore, it can lead to reduction in the Stage I to Stage II transition crack length [36, 88, 89]. A

schematic of the influence of environment on defect size at different stages of fatigue damage in comparison with that of air is shown in Figure 2.14. The figure highlights a reduction in the number of cycles at stage I-to-Stage II transition size in the environment. The environment usually accelerates crack growth rates through anodic dissolution but in some cases, crack growth rates may be reduced through crack tip blunting and corrosion product-induced crack closure [122]. Akid [88, 125, 126] reported that the major effect of the environment is in the early stages of corrosion fatigue crack growth when crack size is below a critical value. When the crack size is greater than this value, the damage process is dominated by mechanical factors and the environment has less effect. Consequently, the air and corrosion fatigue crack growth rates merge since the growth rate is now controlled by the stress intensity at the crack tip with limited contribution from environment-assisted growth.

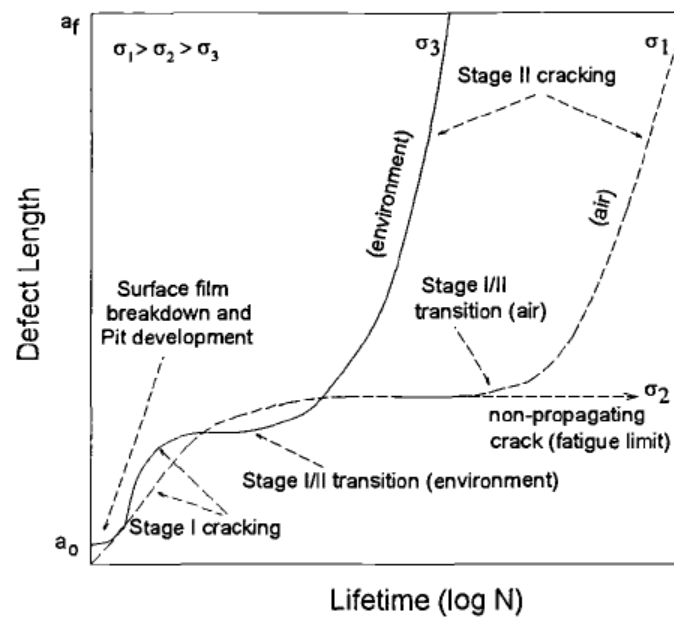


Figure 2.14 Schematic of defect development stages in air and aggressive environment [127].

Results from studies [123, 127, 128] on systems where pits are precursors to cracking have led to the conclusion that corrosion fatigue can be considered as a multi-stage damage accumulation process consisting of the following stages: surfaces include surface film breakdown, pit development, pit-to-crack transition, short crack growth and long crack growth.

## 2.7.4 Corrosion Fatigue Mechanisms

The rate of crack growth in CF is governed by the interaction between the chemical and mechanical mechanisms occurring at the crack tip [103, 129]. CF is such a complex process that no one mechanism can describe all cases. Generally, the mechanisms that contribute to CF crack advancement are stress-assisted dissolution (slip dissolution) [110, 130], corrosion-product-induced crack closure [131] and hydrogen-induced cracking [132, 133] or combination of any [53, 103, 129, 134, 135].

### 2.7.4.1 Anodic Dissolution Mechanism

In fatigue cracking, it is known that the crack tip becomes anodic relative to the rest of the material surface. In this model, the protective film is ruptured either by the applied stress or halide attack near the crack tip. The exposed base metal is then attacked by the corrosive media causing dissolution and consequently sharpening of the crack tip depending on the rate of re-passivation. The re-passivation reaction competes with the dissolution reaction, and when the rate of the former exceeds that of the latter, the passive film is repaired and the anodic dissolution process stops. The crack growth rate is dependent on the rate of anodic dissolution and rate of re-passivation amongst others [103, 135]. The process then begins all over again with the rupture of the passive film thereby exposing the metal at the crack tip to the corrosive media. A schematic illustration of stress-assisted dissolution mechanism is shown in Figure 2.15. Ford [130] verified the slip dissolution and hydrogen embrittlement mechanisms in Al-Mg alloy and concluded that crack growth was controlled by slip dissolution. The environment may also decelerate crack growth rates. This can occur in two ways. The increase of width of cracks by anodic dissolution effectively decreases the stress intensity factor thereby resulting in lower SIF available for crack extension. The second is oxide-induced crack closure, where the corrosion products cause a wedge effect thereby decrease the effective SIF range. Figure 2.16 shows a schematic of the wedge effect mechanism induced by corrosion products.

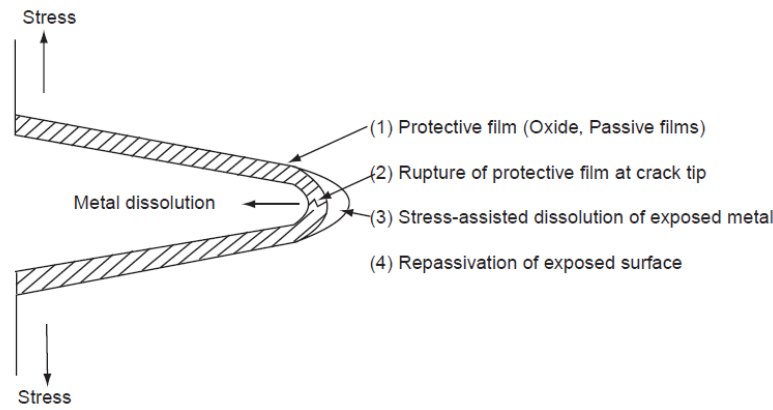


Figure 2.15 Schematic illustration of stress-assisted dissolution mechanism [136].

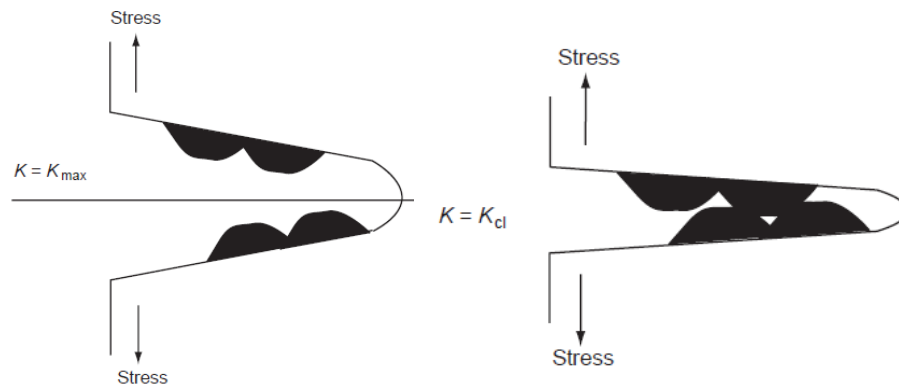


Figure 2.16 Schematic illustration of the wedge effect mechanism induced by corrosion products [136].

#### 2.7.4.2 Hydrogen-induced Mechanism

The presence of hydrogen at the crack tip can aid the propagation of cracks under cyclic loading thereby accelerating the crack growth rate [129]. Gaseous hydrogen environments can aid in crack growth as the relatively high pressure from diatomic hydrogen gas act as a localized force in the crack region supplementing the stress on the metal and consequently accelerate the crack growth rate. Cathodic reactions associated with the corrosion of the metal release hydrogen ions that combine to form gaseous hydrogen ( $H_2$ ) within the metal lattice, which results in a pressure build-up in the crack void space [103]. Atomic hydrogen dissolved in a metal can also lead to an increased crack growth rates.

Hydrogen atoms within a metallic crystalline structure can lower the bond strength between the individual atoms [137, 138]. Moreover, hydrogen atoms generated during the corrosion process can diffuse through a metallic structure under an applied stress, and collect near the point of maximum stress [135]. The consequence of dissolved hydrogen in a metal is that it can reduce the strength of the metal, and if a crack exists, it will

propagate with less resistance where there is a concentration of hydrogen atoms [103, 135]. Adsorbed hydrogen lowers the surface energy of the metal, which facilitates crack growth. Figure 2.17 shows a schematic of the hydrogen-induced mechanism. In an electrolyte, the critical steps involve the diffusion of water molecules and hydrogen ions between the crack walls and the crack tip; production of adsorbable hydrogen atoms at the crack tip; and diffusion to and adsorption of the hydrogen atoms at preferential locations ahead of the crack tip [31]. The preferential locations can be grain boundaries or regions of high stress triaxiality. In situations involving the formation of a passive oxide film on the freshly created surface, the reaction at the crack tip which influences dissolution, hydrogen ion reduction, or crack growth is controlled (at a given electrochemical potential) by three factors: the oxide rupture rate, the solution renewal rate to the crack tip, and the re-passivation rate [31].

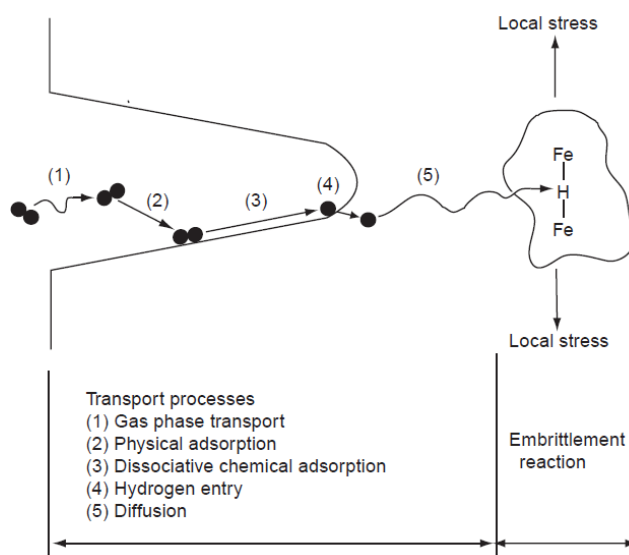


Figure 2.17 Schematic illustration of hydrogen embrittlement mechanism [136].

### 2.7.5 Corrosion Fatigue Stages

When pits are precursors to corrosion fatigue cracking, the fundamental stages in the overall crack development process includes surface film breakdown leading to pit initiation, pit growth, pit-to-crack transition, short crack growth and long crack growth [139]. These stages are shown schematically in Figure 2.18. A reliable prediction of the complete corrosion fatigue process in engineering components would require a quantitative understanding of each stage.

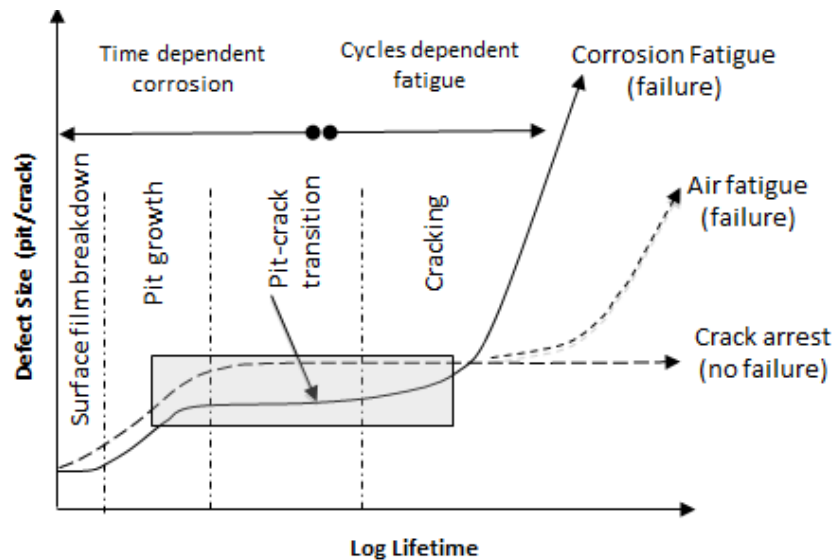


Figure 2.18 Schematic showing the behaviour of fatigue cracks under and corrosion fatigue conditions [119].

#### 2.7.5.1 Surface Film Breakdown

Most engineering metals and alloy, with the exception of the noble metals, develop, to some degree, a passive film on the surface as a result of oxidation in air. Depending on alloy composition, temperature, environment, potential, magnitude of applied stress and exposure history, this film can vary in structure, composition, electronic conduction, porosity thickness and protectiveness [140]. These properties of the surface film determine the inherent resistance of a material to electrochemical damage. The most important criterion for pitting is the pitting potential below which pitting does not occur and above which pits nucleate and develop [141]. However, in some type of systems such as mild steel in chloride-containing solution, no pitting potential is observed. Most metal surfaces have physical or chemical inhomogeneities that can be more susceptible to attack and hence, become the favourable sites for pit initiation.

Preferential attack is due to the difference in the properties of the passive film at these sites from that of other parts of the metal matrix [139]. In steels, these inhomogeneities include sulphide inclusions, oxide inclusions, second phase precipitates, grain boundaries, exit points of dislocations and mechanical flaws [142-144]. During pit initiation, in the presence of depassivating agents like chloride ions, this passive film breaks down and allows the environment to be in contact with metal surface thereby allowing active dissolution of the exposed surface (pitting). Mechanisms of passive film

breakdown and pit initiation can be classified into three: passive film penetration [145], passive film breaking [146] and adsorption [147].

#### **2.7.5.2 Pit Growth**

The breakdown of the surface film leads to dissolution (pitting) of the underlying bulk metal. Pit growth is a time-dependent process that involves two stages: metastable pitting and pit growth. Metastable pits are pits, which initiate and grow for a limited period of time before repassivating. Metastable pits have been reported for stainless steel [148-151], mild steel [152] and aluminium [153, 154]. Pits that survive the metastable stage are referred to as stable pits and they will continue to grow under favourable environmental conditions. Frankel [140] and Szklarska [141] both considered pitting to be autocatalytic in nature; once a pit starts to grow, the conditions developed are such that further pit growth is promoted. Due to the time-dependent nature of metal dissolution, pit sizes are also generally time-dependent [155, 156]. Pit growth can be controlled by the same factors that can limit any electrochemical reaction namely charge transfer (activation), ohmic effects, mass transport or combination of these factors. The rate of pit growth depends on several factors including potential [141, 157], temperature [17, 158], chloride ion concentration [159, 160], alloy effects [161, 162], applied stress [118, 143] and inhibition [163].

#### **2.7.5.3 Pit-to-crack Transition**

The pit-to-crack transition stage is an important stage of the CF process. After initiation, corrosion pits grow under the influence of cyclic stress and create conditions which facilitate cracking. These conditions are generally related to local electrochemical and mechanical factors. When prevailing conditions are favourable, cracks will initiate from the pits. To model the CF process accurately, it is important to consider this stage.

#### **2.7.5.4 Corrosion Fatigue Cracking**

The crack growth stage starts when cracks have initiated from pits. During this stage, the environment can have varying influence on the growth behaviour.

#### **2.7.5.5 Corrosion Fatigue Long Cracks**

As in-air tests, the growth of corrosion fatigue cracks can be characterised using the LEFM approach but in a simulated operating environment. The propagation rates of long cracks



can be greater than in air. A number of relationships between crack growth rates and stress intensity factor have been observed in different metal-environment systems. These may be broadly classified by three patterns of behaviour [31, 164].

- True corrosion fatigue (Figure 2.19a) – this type of behaviour is often observed in materials which are resistant to stress corrosion cracking, thus characterises the synergistic effects of cyclic loads and aggressive environment. Features of this type of behaviour are the lower threshold SIF range and increase rate of crack growth compared to in air. Thus it is possible to predict the extent to which crack growth is affected by the environment.
- Stress corrosion fatigue (Figure 2.19b) – this is typical of where there is a substantial environment-enhanced sustained-load crack growth component. Because the effects of stress corrosion and fatigue are additive and can be superimposed, it is possible to predict corrosion fatigue behaviour when stress corrosion data in the same environment and fatigue data in air are available. Above the threshold  $K_{ISCC}$  for stress corrosion cracking, environment effects are significant but are negligible below this level.
- Combined behaviour (Figure 2.19c) – a complex combination of true corrosion fatigue and stress corrosion fatigue may also be obtained.

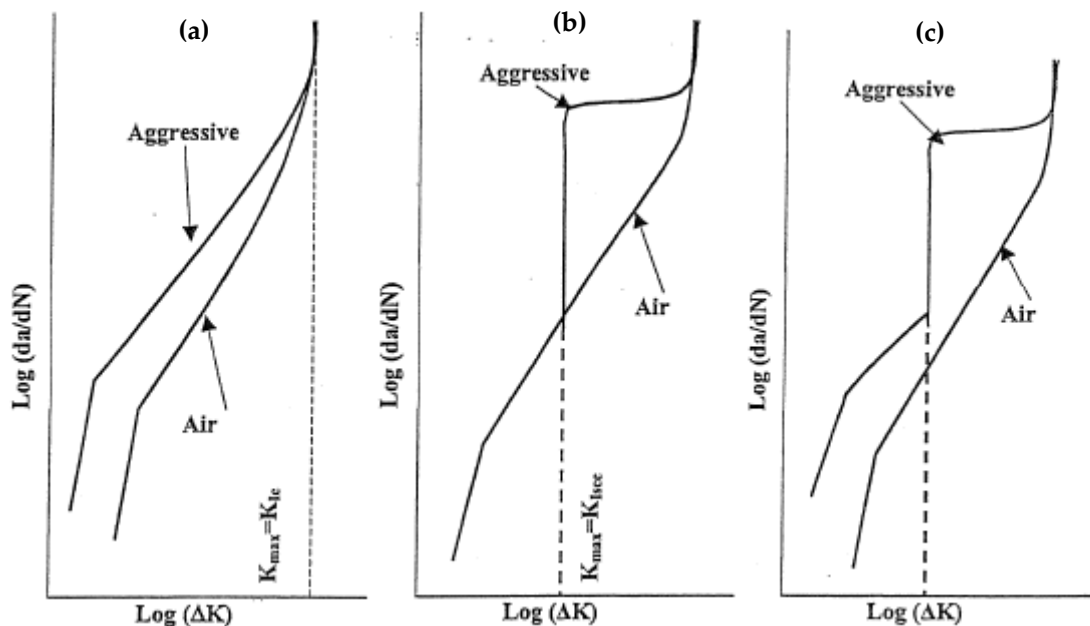


Figure 2.19 Schematic of three types of corrosion fatigue crack growth behaviour (a) true corrosion fatigue (b) Stress corrosion fatigue (c) combined behaviour [164].

### **Corrosion Fatigue Short Cracks**

Under corrosion fatigue conditions, the aggressive environment can have significant effect on the propagation rate of short cracks. Corrosion tends to weaken the resistance of microstructural barriers such as grain and phase boundaries through metal dissolution and crack tip expansion and thus enable cracks to re-initiate in the adjacent grains. At later stages, the effect of corrosion is somewhat hidden by the mechanical driving force, which would have increased due to crack length increase and therefore, becomes the controlling parameter. Previous studies have reported higher propagation rates than long cracks under the same stress intensity factor range [131, 132, 165]. A typical behaviour of short fatigue cracks under corrosion fatigue conditions was reported by Akid [166] where crack growth rate in the presence of the environment was plotted as a ratio to that in air (Figure 2.20). Not only were crack growth rates observed to be retarded by microstructural features, in this case prior austenite grain boundaries, they were significantly higher than in air. In addition, the important effect of the environment is highlighted whereby the ratio increases when the crack approaches a barrier to its growth and subsequently decreases after crossing the barrier. Previous investigations by Akid and co-workers [36, 53, 88-90, 125, 126, 128, 166] can be summarised as follows:

- aggressive environment influences short fatigue crack growth depending on stress level and crack size,
- microstructural features such as the grain boundaries can cause partial retardation of propagation of short cracks but growth rates still remain higher than in air,
- the influence of microstructure is significant in the short crack growth regime but less in the long crack regime,
- aggressive environment, through strain-assisted dissolution, can eliminate the microstructural barriers and allow re-propagation of non-propagating cracks, and
- strain-assisted anodic dissolution reduces the critical length for Stage I to Stage II transition thereby reducing the physically small crack regime compared to air fatigue. The transition crack length can be as low as one to two units of microstructural dimensions.

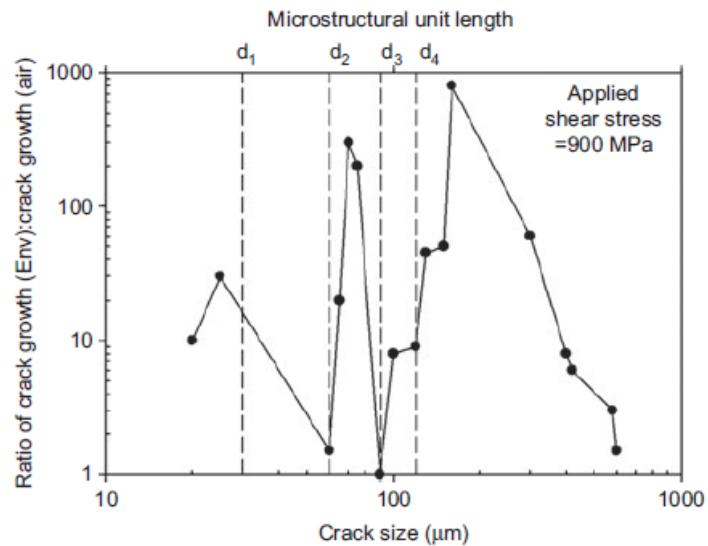


Figure 2.20 Ratio of fatigue crack growth rate in 3.5 % NaCl to fatigue crack growth rate in air as a function of surface crack length [166].

Gangloff [133] reported that the growth of short fatigue cracks in aqueous environments was faster than long cracks. Piascik and Williard [167] and Tanaka *et al.* [165, 168] investigated the growth characteristics of short cracks and reported that the test environment accelerated the growth rates of short cracks faster than in air. Kondo [169] also observed in two low alloy steels that short cracks from pits propagated at  $\Delta K$  values well below the  $\Delta K_{th}$  for a long crack for these materials. Corrosion can also influence short crack growth through oxide-induced crack closure. Suresh *et al.* [170] reported that at low stress ratios, near-threshold short crack growth rates were significantly reduced in aqueous compared to dry environments due to the formation of corrosion deposits on the crack surfaces, which enhanced crack closure. Gangloff and co-workers suggested that the higher growth rates of short cracks was due to differences in the local crack tip environment, which is a consequence of the differences in the electrochemically active surface-to-volume ratios, which is due to crack size [67, 132, 133, 171]. In a recent review, Turnbull [172] discussed different electrochemical mechanisms that may determine the effect of the environment on corrosion fatigue short crack growth. These factors include:

- mass transport of reactive species into and out of cracks through pumping action of opening and closing of cracks due to cyclic loading
- changes in crack tip potential which may result from potential drop in the crack (between the crack tip and crack mouth) and outside the crack (between the crack mouth and the metal surface away from the crack), both of which affect the extent

crack tip polarisation, and the effect of bulk flow whereby mixing of crack and bulk solutions can prevent the development of solution chemistry that promotes crack growth.

#### **2.7.5.6 Factors affecting corrosion fatigue crack growth**

Several variables can influence corrosion fatigue behaviour of metals and alloys. These may be divided into three main groups: mechanical, metallurgical and environmental.

- Metallurgical factors – These include alloy composition [140], distribution of alloying elements and impurities [140, 173], microstructure [89, 174], welding defects [116] and heat treatment [175].
- Environmental factors – Because corrosion fatigue is a damage process involving an aggressive environment, factors that influence the concentration of damaging species will affect the process. These include concentration of damaging species [176], electrochemical potential [177], pH [177], temperature [178, 179] and inhibitors [180-182].
- Mechanical factors – As corrosion fatigue involves cyclic loading, variables that influence the loading spectrum will affect corrosion fatigue behaviour. These include stress range [118, 183, 184], cycle frequency [122, 174, 179, 185], stress ratio [9, 186], load waveform [134], and residual stresses [187].

### **2.8 Crack Nucleation from Corrosion Pits**

Although corrosion fatigue cracks can initiate from features such as inclusions and grain boundaries, corrosion pits are generally the preferred sites for crack nucleation in metal-environment systems where pits are precursors to cracking [9, 16, 117, 121, 123, 167, 169, 188-199]. Figure 2.21 shows an example of the transition from pitting to cracking in turbine blade steel in chloride environment. The transition represents a stage when damage transitions from that of a time-dependent corrosion phenomenon to that of a mechanical cycles-dependent phenomenon [139, 200]. From current understanding, the growth of corrosion pits under cyclic loading is thought to create conditions, which facilitate crack nucleation. These conditions are generally thought to be a complex combination of metallurgical, electrochemical, mechanical and in-service factors [105].

Generally, models for crack initiation in aqueous environment have been based on the following events:

1. preferential attack at sites where the protective film on the surface of an alloy under cyclic load has been ruptured.
2. stress concentration at the roots of corrosion pits thus making them crack nucleation sites.
3. preferential dissolution at regions where plastic deformation is localised, with the less deformed surrounding regions acting as cathodes.
4. reduction in surface energy of the metal due to the adsorption of environmental species such as hydrogen.

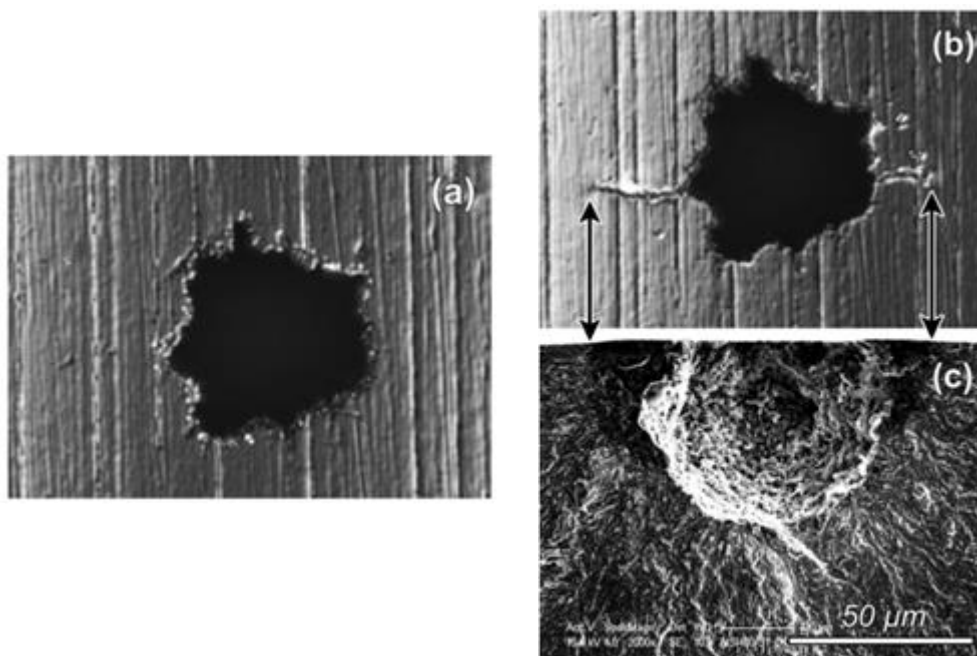


*Figure 2.21 Typical pit-to-crack transition observed on pre-pitted specimen in corrosion fatigue (a) pit before and (b) after transition [9].*

From a mechanical perspective, the presence of geometric discontinuities interrupt the stress pattern in engineering components and tend to make it non-uniform, and consequently resulting in an increase in local stress level around the discontinuities. Hence, corrosion pits can lead to localisation of stress and strain [1, 121, 201-204]. The magnitude of the increase in local stress and strain can be determined using the theoretical elastic concentration factor, defined as the ratio of maximum local stress to the nominal stress. The nominal stress is taken as a reference stress value and is dependent on geometry of specimen and load type while the local stress is dependent on the geometry

of the discontinuity and applied stress. The stress concentration factor depends only on the geometry of the discontinuity. It is worthy of note that the stress concentration factor is an elastic parameter and therefore can only be used as an approximation of the prevailing stress and strain around the pit. In reality, components containing pits may be subjected to elastic-plastic conditions depending on pit size and applied stress. In contrast to elastic conditions where applied stress and strain are linearly related and stresses can reach unrealistic values, stresses typically do not increase beyond the yield limit of the material when plastic conditions are employed. This can result in a redistribution of stresses and strains around a pit and therefore has implications when conducting mechanics based studies on understanding how corrosion pits facilitate crack nucleation. For instance, whereas purely plastic analysis of stress and strain around pits showed similar stress and strain patterns, which is concentrated at the pit bottom, elastic-plastic analysis of the same pits showed that increase in plastic deformation with increasing stress resulted in redistribution of stresses and localisation of strain towards the pit mouth [121, 202]. This also undermines current pit-to-crack transition models, which are based on the  $\Delta K_{th}$ , a parameter that is based small-scale yielding.

Ahn [122] observed a dependence between fatigue limit and pit depth, but only at pit depths above 150  $\mu\text{m}$ . They also reported a decrease in the number of cycles required to initiate a surface crack with increasing pit depth and increasing applied stress range. In-air tests only provide information on the mechanical effect of pits on fatigue life. The influence of corrosion on fatigue life requires the presence of an aggressive environment. Anh [122] observed a further reduction in the number of cycles to initiate a crack in 1M NaCl solution compared to those in air. For the HSLA steel tested, the crack initiation life in air varied between 65% to 94% compared to 35% to 75%, in the chloride environment. They concluded that the presence of the environment changed the fatigue behaviour from being initiation-dominant to propagation-dominant. Pao [205] investigated the influence of corrosion pits on the fatigue strength of an aluminium alloy and reported that both the threshold stress intensity and fatigue crack initiation life of polished specimens in air were reduced by half when pre-existing corrosion pits were present. Wang [206] reported that the presence of pre-existing corrosion pits produced by immersion in 3.5% NaCl, over different exposure times, accelerated crack nucleation stage and consequently reducing fatigue life by up to a factor of 100, compared to smooth specimens. Jones and Hoeppner

[156] investigated the transition of corrosion pits to cracks during corrosion fatigue in aluminium alloys. They observed that the crack nucleation stage accounted for a large fraction of the fatigue life. They also reported that pit surface area, pit geometry, proximity to other surrounding pits and pit depth are quantities which play an important role in determining when a crack will nucleate from a pit.

There is experimental and in-service evidence indicating that multiple corrosion pits can initiate and develop close to each other on engineering components [121, 207]. Multiple pits can coalesce and form larger pits, while the stress fields around those pits that do not coalesce can interact to influence crack nucleation, leading to crack coalescing into a single crack [156, 207]. Horner *et al.* [121] also observed development of multiple pits in high strength disc steel in a chloride environment. Their observation identified coalescence of cracks that initiated from adjacent pits as the key factor in crack propagation behaviour.

Although the nucleation of cracks from pits has been correlated with strain localisation, the location around a pit where a crack will preferably initiate still remains unclear. In some systems, cracks have been observed to nucleate at the bottom of pits [195, 207, 208] while in others crack initiation was observed at the pit mouth [9, 121, 202, 209]. From their tests on stainless steel containing artificial corrosion pits, Masaki [195] observed fatigue cracks initiated at the bottom of the pits even at nominal stress amplitudes below plain specimen fatigue limit. The phenomenon of initiation of cracks at the pit bottom was explained on the basis of the differences in crack initiation stress of the material at the bottom of the pit compared to the pit mouth. Initiation is favoured at a point where the local stress is larger than the crack initiation stress of the material (assumed to be equal to the fatigue strength of an electrochemically polished plain specimen). In Figure 2.22, the favourable points are Points A and C. However, because the specimens were mechanically polished, the surface layer will be work-hardened thereby resulting in increase in the crack initiation stress compared to the bottom. Hence, cracking is favoured at the pit bottom. Using X-Ray tomography, Turnbull and co-workers [105, 121, 202] observed crack nucleation at the mouth of pits in high strength steel in corrosion fatigue (Figure 2.23).

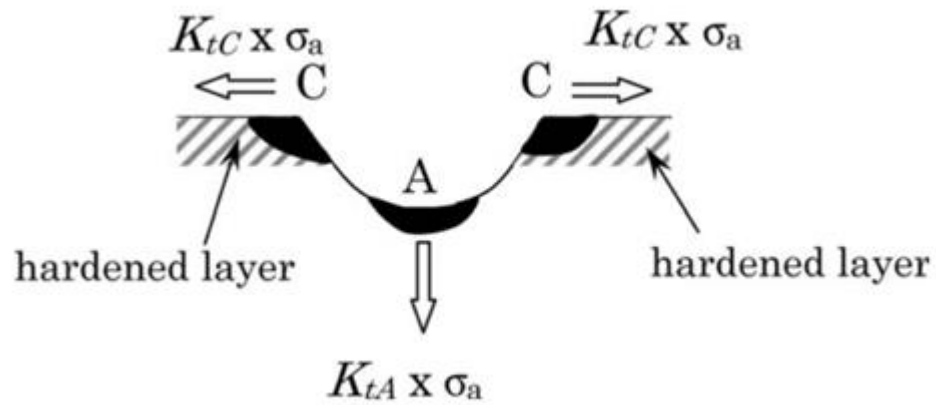


Figure 2.22 Fatigue crack initiation model [195].

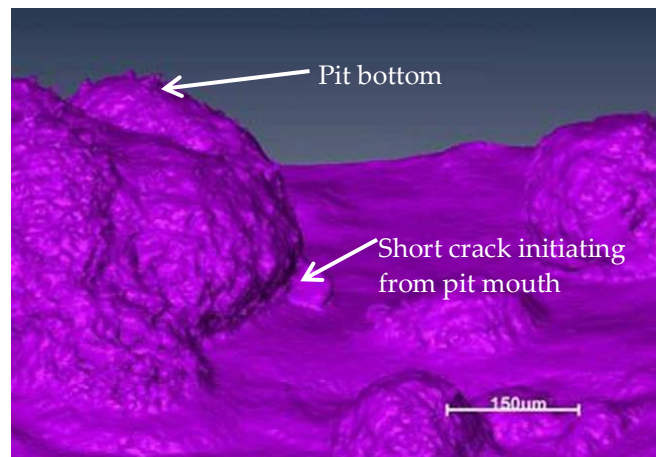


Figure 2.23 Example of crack emerging from the pit mouth as observed by X-ray tomography. The image is best considered as being viewed from inside the steel [202].

## 2.9 Corrosion Fatigue Lifetime Modelling

There are established methodologies and industry standards for predicting the fatigue life of engineering structures in air (e.g. R6 [164] and BS 7910 [210]) all of which are based upon the application of the Paris law, and its various modifications, derived from data generated from pre-cracked specimens. Likewise, under corrosion fatigue conditions, a similar approach is employed, although tests are carried out in a simulated aggressive environment. Since CF is a synergistic process involving mechanical fatigue and aggressive environment, several models have been proposed to describe the effect of the latter on fatigue. A brief review of these models is discussed below.



### 2.9.1 The Superposition Model

A superposition model was first used to describe corrosion fatigue crack propagation by Wei and co-workers [211, 212] who considered the total corrosion fatigue crack growth rate to be the superposition of a plasticity-driven crack extension component with a second component representing the interaction between plastic deformation and chemical reactions.

$$\left(\frac{da}{dN}\right)_e = \left(\frac{da}{dN}\right)_m + \left(\frac{da}{dN}\right)_{cf} \quad 2.27$$

where  $(da/dN)_e$  is the crack growth rate in aggressive environment,  $(da/dN)_m$  is the rate of plasticity-driven fatigue crack propagation in an inert environment and  $(da/dN)_{cf}$  is the difference between the total growth rate and 'pure' fatigue growth rate representing the effect of interaction between chemical reactions and plastic deformation.

### 2.9.2 The Competition Model

In this model [213], corrosion fatigue crack propagation is considered as a competition between mechanical fatigue and cycle-time dependent corrosion fatigue. The measured corrosion fatigue growth rate is taken as the fastest (dominant) process.

$$\left(\frac{da}{dN}\right)_e = \left(\frac{da}{dN}\right)_m (\theta) + \left(\frac{da}{dN}\right)_{cf} (\phi) \quad 2.28$$

where  $\theta = 1 - \phi$  (both measured by fractographic analysis).

In an environment dominant cracking process,  $\phi = 1$  and the  $(da/dN)_m \ll (da/dN)_{cf}$ . Therefore,

$$\left(\frac{da}{dN}\right)_e = \left(\frac{da}{dN}\right)_{cf} \quad 2.29$$

### 2.9.3 Modified Short Crack Growth Model

The Hobson-Brown and Navarro-de les Rios models, previously discussed, were modified by Akid and Miller [125, 126] to account for environmental effects on both short and long cracks. In this model, corrosion fatigue crack growth rate incorporates the summation of crack growth rate in air (representing the mechanical driving force) and growth rate as a result of dissolution in the environment (representing the chemical driving force based on anodic dissolution current).

$$\left(\frac{da}{dN}\right)_{env} = \left(\frac{da}{dN}\right)_{air} + \left(\frac{da}{dN}\right)_{diss} \quad 2.30$$

$$\left(\frac{da}{dN}\right)_{diss} = \left(\frac{Mi_a}{ZF\rho}\right)\frac{1}{w} \quad 2.31$$

where  $M$  is the atomic weight of the corroding metal,  $i_a$  is the anodic dissolution current,  $Z$  is the valency,  $F$  is the Faraday's constant,  $\rho$  is density and  $w$  is the cyclic frequency.

### 2.9.4 Pitting Corrosion Fatigue Models

In material-environment systems where pitting is a precursor to cracking, CF lifetime prediction is a complex procedure because of the need to account for pit initiation, pit growth, crack initiation, short crack growth and long crack growth. Current models proposed to address this [124, 169, 188, 214-217] are based on two-stage process involving pit growth and long crack growth. The pit growth stage is modelled using the pit growth theory while the crack growth is modelled using conventional  $da/dN$ - $\Delta K$  test data. The point of transition is defined by the threshold SIF range. These models are summarised below.

#### 2.9.4.1 Hoepfner Model

This mechanistic model [216] was proposed for predicting the critical pit depth to nucleate a crack under pitting corrosion fatigue conditions. The pit size at a given stress condition at which a Mode I crack develops was determined from the fatigue crack growth threshold. The number of cycles required to generate a pit large enough to develop a Mode I crack, i.e. the time taken to attain the pit depth that satisfies the threshold condition was determined using pit growth theory while the number of cycles to propagate the crack to fracture was then determined using SIF range. The total life is then given by a summation of the two. The model is given by:

$$K = 1.1\sigma\sqrt{\pi\left(\frac{a}{Q}\right)} \quad 2.32$$

$$d = Ct^3 \quad 2.33$$

where  $K$ ,  $\sigma$ ,  $a$ ,  $Q$ ,  $t$ ,  $d$  and  $C$  are stress intensity factor, applied stress, pit length, a function based on crack shape, time taken to attain pit depth for corresponding threshold value, pit depth and constant dependent upon material and environment respectively.

### 2.9.4.2 Lindely Model

Lindely *et al.* [214] proposed a model for determining the threshold stress intensity factor at which a crack would initiate from a pit by considering corrosion pits as semi-elliptical sharp cracks. The model was given as:

$$K_{th} = \frac{\Delta\sigma \sqrt{(\pi a) \left[ 1.13 - 0.07 \left( \frac{a}{c} \right)^{0.5} \right]}}{\left[ 1 + 1.47 \left( \frac{a}{c} \right)^{1.64} \right]^{0.5}} \quad 2.34$$

where  $\Delta K_{th}$ ,  $a$  and  $c$  and  $\Delta\sigma$  are threshold stress intensity factor, minor axis of semi-elliptical crack, major axis of semi-elliptical crack and applied stress range respectively.

### 2.9.4.3 Kawai and Kasai Model

In this model [215], LEFM approach was employed to determine the critical depth from a fatigue crack would grow by estimating the allowable stress intensity threshold under corrosion fatigue conditions. The model, which considered corrosion pits as elliptical cracks, is given as

$$\Delta K_{all} = \Delta\sigma_{all} \sqrt{\pi h_{max}} \quad 2.35$$

where  $\Delta K_{all}$ ,  $\Delta\sigma_{all}$ ,  $F$  and  $h_{max}$  are allowable stress intensity threshold, allowable stress range, geometric factor and maximum pit depth respectively.

### 2.9.4.4 Kondo Model

Kondo [169] proposed a model by estimating the critical pit condition using both stress intensity and pit growth relations. The model considered corrosion pits as sharp hemispherical cracks and proposed that the critical condition for transition is that crack growth rate must exceed pit growth rate. The model was given as:

$$\Delta K_p = 2.24\sigma_a \sqrt{\pi c \frac{\alpha}{Q}} \quad 2.36$$

$$c = C_p t^{1/3} = C_p (N/f)^{1/3} \quad 2.37$$

where  $\sigma_a$ ,  $Q$ ,  $c$ ,  $t$ ,  $N$  and  $f$  represent the stress amplitude, pit aspect ratio, shape factor, pit radius, number of fatigue cycles and cyclic frequency respectively.

### 2.9.4.5 Chen Model

Chen *et al.* [188] proposed a model for predicting crack initiation based on concepts of fatigue crack growth thresholds and a competing pitting/cracking rate. The transition criteria from pitting to cracking was proposed as (i) the equivalent stress intensity factor range must be greater than  $\Delta K_{th}$  for long crack growth and (ii) the fatigue crack growth rate must exceed the pit growth rate. The transition SIF,  $\Delta K_{tr}$ , crack growth rate and pit growth rate were given by

$$\Delta K_{tr} = \frac{1.12K_t\Delta\sigma\sqrt{\pi C_{tr}}}{\Phi} \quad 2.38$$

$$\left(\frac{da}{dN}\right)_{pit} = \frac{C_p}{2\pi} \cdot \beta^2 c^{-2} \quad 2.39$$

$$\left(\frac{da}{dN}\right)_{crack} = C_F(k_t\Delta\sigma)^n\Phi^{-n}c^{0.5n}f \quad 2.40$$

where  $\Delta K_{tr}$  is SIF for transition,  $K_t$  is elastic stress concentration factor,  $c$  is half-pit diameter,  $\Delta\sigma$  is applied stress range,  $\Phi$  is shape factor determined by the pit diameter,  $\beta$  is pit aspect ratio,  $f$  is cyclic frequency, and  $C_F$ ,  $C_p$  and  $n$  are constants.

### 2.9.5 Multi-stage Modelling

CF lifetime prediction is a complex procedure because of the need to account for pit initiation, pit growth, crack initiation, short crack growth and long crack growth. Hence, the pitting corrosion fatigue models enumerated above are simplified into a two-stage process consisting of pit growth and long crack growth. The criteria for transitioning from a pitting to cracking is also defined phenomenologically in that the threshold SIF associated with a pit must exceed that of the pit and the crack growth rate is greater than the pit growth rate. Following initiation, the crack is considered to behave as a long fatigue crack hence crack growth rates can be predicted based on LEFM. Whilst correlations between model predictions and experiments have been made, a major concern surrounds the underlying assumptions of these models.

In the pitting corrosion fatigue models, corrosion pits are considered to be effective cracks, thereby allowing the calculation of a SIF range using LEFM concepts. Therefore, the threshold SIF is assumed to control the transition of pits to cracks. It is considered that cracks will not initiate or propagate when the pit depth is lower than a threshold depth. However, the questions are whether corrosion pits are truly effective cracks and whether

cracks will initiate from pits with depths less than the threshold pit depth. Other concerns are whether the use of a fracture mechanics parameter,  $\Delta K_{th}$ , which is obtained from pre-cracked specimens is applicable to pits growing on smooth specimens or components. From the point of view of LEFM, corrosion pits may also induce significant local plasticity hence, resulting in a breakdown of small-scale yielding condition required for LEFM analysis. Moreover, the conditions governing pit-to-crack transition will most likely depend on both mechanical and electrochemical factors rather than the LEFM threshold fracture parameter presumed in these models. It is also assumed implicitly that, at the point of crack-pit transition, cracks must have the same depth as the nucleating pit and that crack initiation will occur at the bottom of a pit. However, recent studies have shown that cracks can initiate from pit mouth and can have depths that are far smaller than that of the pit.

Since CF involves the accumulation of damage through different stages, it is considered that a more realistic approach towards more accurate prediction of CF lifetime would be that of the formulation of a multi-stage model that accounts for the development of damage throughout all the corrosion fatigue stages namely surface film breakdown, pit growth, pit-to-crack transition, short crack growth and long crack growth. This proposed model is given as

$$N_{cf} = N_{sf} + N_{pg} + N_{ptc} + N_{cfsc} + N_{cflc} \quad 2.41$$

where  $N_{cf}$  is the corrosion fatigue life,  $N_{sf}$ , number of cycles to scale break down,  $N_{pg}$ , the number of cycles for pit growth,  $N_{ptc}$ , the number of cycles to pit-to-crack transition,  $N_{cfsc}$ , the number of cycles for corrosion fatigue short crack growth and  $N_{cflc}$  is the number of cycles to corrosion fatigue long crack growth.

The work reported in this thesis devoted to formulating a multi-stage damage accumulation model for corrosion fatigue damage and lifetime prediction based upon observed controlling damage mechanisms and the time-dependent interactions occurring between corrosion and mechanical loading.

---

---

# **Chapter 3**

## **Experimental Methods**

---

---

### 3.1 Introduction

The objective of this chapter is to describe the experimental procedures and the materials that were used throughout this research. It will also describe the techniques that were applied to analyse the data obtained from the experimental procedures. A detailed structure of this research programme is outlined in Figure 3.1. This chapter is concerned only with experimental work while the modelling work is described in Chapter 4.

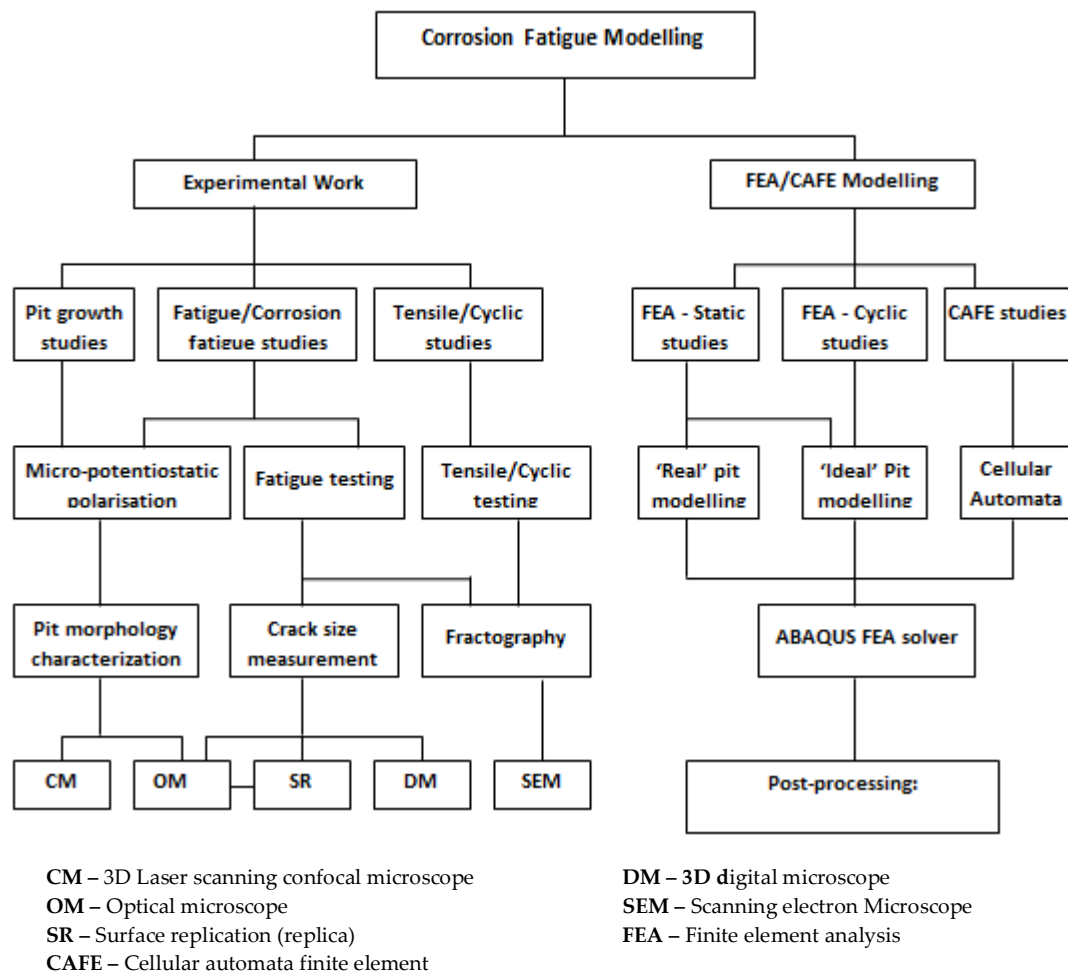


Figure 3.1 Overall outline of research programme.

### 3.2 Material

The material used for this study was API 5L X-65 grade steel, which is a high strength low alloy steel used for linepipe and riser applications in the oil and gas industry. The material was provided by BP as welded seamless pipe sections which have an internal

diameter and wall thickness of 273 mm and 40 mm respectively. Figure 3.2 shows the as-received pipe sections. The specimens used for all the electrochemical and fatigue testing carried out in this work were obtained from the parent plate region of the pipe sections. The material was tested in the 'as-received' (quenched and tempered) condition with no further treatment.



*Figure 3.2 As-received sections of the linepipe from which test samples were manufactured.*

### 3.3 Chemical composition

The actual chemical composition for this material as specified in the material specification data sheet provided by BP is given in Table 3.1.

*Table 3.1 Chemical composition of API 5L X65 steel (wt%\*).*

C	Si	Mn	P	Mo	V	Cr	Ni	Cu	Nb	Ti	Al	S
0.05	0.28	1.08	0.01	0.13	0.06	0.07	0.37	0.16	0.027	0.03	0.037	0.001

### 3.4 Metallography

Metallographic examination was carried out on the welded cross-section to obtain information about the microstructure of the material. The metallographic specimen was



cut from a section of the girth weld; the section was cut such that it contained the weld, heat affected zone and parent plate regions. Specimen was hot mounted in conductive bakelite, ground and polished with SiC paper up to 4,000 grit surface finish and then to 1  $\mu\text{m}$  using diamond paste. It was then etched at room temperature by immersion in 2% Nital for 15 seconds after which it was rinsed in deionized water and dried in hot air. Image analysis was carried out using an optical microscope.

### 3.5 Micro-hardness

The hardness across the weld cross-section was measured on the Vickers scale by following the ASTM E384 procedure [218]. Hardness testing was carried out on a Struers Duramin 2 micro-hardness testing machine. Four rows of indentation were made across the weld cross-section in longitudinal direction of the pipe. The distance between each row of indentation and that between each indentation along rows was 1 mm and 0.25 mm respectively. The Vickers hardness numbers reported herein are of the form xxHVyy where xx and yy represent the hardness number and test force (kgf).

### 3.6 Electrochemical Testing

The electrochemical characteristics of materials in a given environment of interest play an important role in their behaviour under corrosion fatigue conditions. Therefore, understanding the corrosion behaviour of the given metal-environment system is important. In this present study, micro-electrochemical tests including potential monitoring and potentiostatic polarization were carried out in a micro-electrochemical cell in order to determine the basic local electrochemical and pit growth behaviour of the steel in a brine environment. Tests were carried out using a Uniscan Electrochemical Station which consisted of model SCV370 control unit, model PG580R Potentiostat-Galvanostat and model M370 software. In micro-electrochemical testing, measurements were restricted to an area that is equivalent to 0.5 mm in diameter.

### 3.6.1 Electrodes

The working electrode is the specimen obtained from the parent plate region of the pipe. All stated potential measurements are with respect to silver-silver chloride reference electrode while the auxiliary electrode is platinum.

### 3.6.2 Test Solution

Electrochemical and corrosion fatigue tests were carried out in a brine environment. The composition of brine is given in Table 3.2. The solution was prepared by weighing the components in required proportions and then dissolving them in deionized water. Fatigue specimens were pre-pitted using 0.6 M NaCl instead of the brine. This was because of the high concentration of salts in the brine solution, which always results in crystallization at the tip of the microcell, which in turn made the pit generation procedure non-repeatable.

*Table 3.2 Composition of Forties Brine test solution*

Composition	Concentration (mol/L)
NaCl	1.4784
KCl	0.005
CaCl <sub>2</sub> .2H <sub>2</sub> O	0.052
MgCl <sub>2</sub> .6H <sub>2</sub> O	0.0115
SrCl <sub>2</sub> .6H <sub>2</sub> O	0.00157
NaHCO <sub>3</sub>	0.00762
Sodium Acetate	0.029

### 3.6.3 Electrochemical measurements

Two types of electrochemical measurement were carried out in this work. They include potential monitoring and potentiostatic polarization. In the former, the evolution of the OCP of the steel in the test environment over time was monitored under static and flow conditions. Potentiostatic polarization involves the application of a constant potential to the surface of the working electrode for a specified duration. The potential difference between the working electrode and reference electrode is controlled while the current between the working electrode and auxiliary electrode is measured. In all potentiostatic measurements carried out in the present work, an anodic potential above the OCP was applied to the test samples.

### 3.7 Rationale for use of single artificial pits

In metal-environment systems where pits are precursors to cracking, the breakdown of the passive film can result in development of multiple corrosion pits from which multiple cracks can initiate [121, 156, 207]. Under this circumstance, the observed deterioration in fatigue strength will most likely be due to the effect of multiple cracks that resulted from several corrosion pits. Multiple pits can also interact with each other and influence crack initiation behaviour. The nucleated cracks can interact with adjacent cracks through crack coalescence and crack shielding all of which affect the overall fatigue life of the component. Not only are the complexities involved in lifetime prediction increased due to the need to account for all these variables, it is also difficult to isolate and evaluate the individual behaviour of the cracks that may emanate from the pits. By focusing studies on single pits as precursors for characterising corrosion fatigue crack development, it is possible to isolate, assess and study the crack initiation and propagation mechanisms that influence the overall fatigue behaviour of engineering materials. For these reasons, there is considerable virtue in isolating single corrosion pits and studying the behaviour of the cracks that nucleate from them. The popularity of this approach is now increasing and has been employed in several studies [9, 122, 123, 196, 198, 209, 219].

Recently, studies have been carried out using the single corrosion pit approach, where only one corrosion pit is generated on test specimen. Conventional mechanical methods include spark erosion [196] and drilling [198], which have the advantage of controlling the density, size and depth of the pits. However, these methods can introduce additional experimental variables such as residual stresses and, changes in local microstructure, which may influence the damage mechanisms and thereby undermine the results obtained from such investigations. Employing an electrochemical procedure will eliminate these factors and increase confidence in results. Several studies have been carried out by generating single pits using electrochemical methods [9, 122, 123, 219].

### 3.8 Simulation of pit growth

In the present study, the active dissolution (pit growth) stage was simulated using the microcell. The size of the droplet is deemed to be comparable to the sizes of corrosion pits observed in-service on components to which this study is focused. Because this work

involves the study of pits of pre-determined size, shape and morphology, an electrochemical procedure was established for pit development. Two groups of pitting experiments were carried out: the first involved investigating the pit growth behaviour of the steel in brine environment under the influence of cyclic stress while the second involved generating artificial pits of specific sizes on fatigue specimens. In both studies, pit growth was simulated by polarising potentiostatically in the anodic region. In this method, a fixed anodic potential was applied for a predetermined length of time.

### 3.8.1 Micro-electrochemical methods

Conventional electrochemical methods are based on carrying out electrochemical measurements on metallic specimens, whose sizes are usually within a range of the order of square centimetres, immersed in a specified test solution in a corrosion cell. These methods have been applied for studying localised corrosion mechanisms including pitting corrosion. The limitation of these methods is that electrochemical processes on the surface of the working electrode are assumed to be homogenous hence, electrochemical data is often averaged over the entire exposed surface area. For instance, in a case where there are several corrosion pits on the surface of a specimen, measured pitting current density is derived from all the active corrosion pits. This leads to problems in determining the current from single pits, assumptions regarding the active pit surface area and complications associated with hydrogen evolution within pits that can consume a reasonable fraction of the anodic pit current density. The use of micro-electrochemical techniques helps eliminate these problems by focusing the electrochemical study to a small area, thus enabling the study of corrosion processes within the micrometer range. Micro-electrochemical techniques can be classified as follows: scanning techniques and small area techniques. Scanning techniques involve scanning a small area on the surface of an immersed specimen using microelectrodes. However, polarisation of small areas of the sample and measurement of local corrosion currents is difficult. In small area techniques, the exposed area for localised corrosion study is decreased and the polarisation and measurement of local current transients is possible. Examples of small area techniques are small glass capillary, photoresist and droplet cell (Figure 3.3). In the present study, the droplet cell and micro-capillary methods were used. Localised

electrochemical measurements (micro-potential monitoring, micro-potentiostatic polarization) were carried out using the Uniscan M370 SDS module.

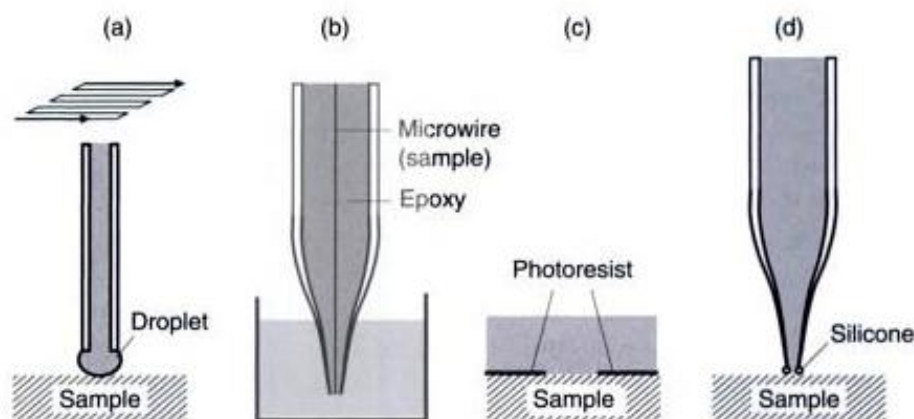


*Figure 3.3 Small area techniques used to study localized corrosion: (a) droplet cell (b) embedded thin wire technique (c) photoresist technique, and (d) microcapillary cell [220].*

### 3.8.1.1 Scanning Droplet System (SDS)

The SDS was employed for studying the effect of cyclic stress on pit growth. The SDS (Figure 3.4) is a three-electrode micro-cell used for localized corrosion studies. It works by constraining a liquid in contact with a sample surface over a small wetted area in form of a droplet in order to measure electrochemical characteristics at the site of the droplet in contact with the sample. This offers the ability to spatially resolve electrochemical activity and to confine it exclusively to a selected quantifiable area of the sample. An additional feature of the SDS is the inclusion of a pumped liquid handling system to vary the flow rate of electrolyte over the surface of the sample. This allows the measurements to be made in relation to flow-rate, whereby reaction product is removed from the corrosion site, resulting in constantly refreshed solution in the microcell. The wetted surface area of the sample under investigation acts as the working electrode and the PTFE head contains the auxiliary and reference electrodes. These are electrically connected to the surface through the droplet (Figure 3.4c). The capillary radius determines the wetted area (in this case, the width of the pit). The small distance between the counter electrode and the sample allows high current densities due to the limited ohmic resistance. As shown in Figure 3.4a, a precision peristaltic pump controls the flow of electrolyte through the cell thus ensuring a constant supply of fresh electrolyte. Through the pump, the SDS routes

the electrolyte from the reservoir to the SDS tip. The electrolyte is then routed back to the reservoir for recirculation or disposed.

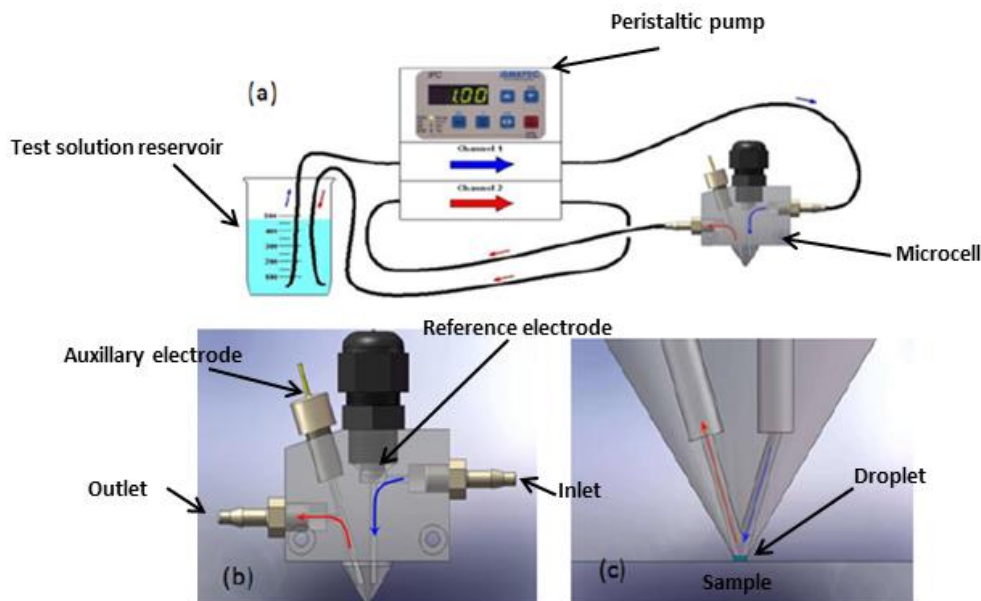


Figure 3.4 Schematic of the scanning droplet system.

### 3.8.1.2 Micro-capillary cell

Pre-pitting of fatigue specimens was carried out on a micro-capillary cell (Figure 3.5) that was developed in-house<sup>1</sup>. It is essentially a three-electrode system with a capillary containing the electrolyte, the reference electrode and counter electrode. The tip of the capillary has a diameter of 500  $\mu\text{m}$ .

### 3.8.2 Pit growth under stress

To investigate the influence of stress on pit growth, anodic dissolution was simulated under cyclic loading. This was achieved by simultaneously polarising the test samples while under cyclic loading. Flat samples dog-bone samples (Figure 3.5), which had their longitudinal axes parallel to the longitudinal direction of the pipes, were polished using a series of successively finer grades of SiC abrasive papers up to a 4,000 grit surface finish. After polishing, the samples were cleaned with de-ionized water, dried in hot air and then stored in a dry chamber. Prior to testing, a piece of copper wire was spot-welded to the samples for electrical contact and then degreased using acetone.

<sup>1</sup> Micro-capillary cell was developed by Mr. C. Evans.

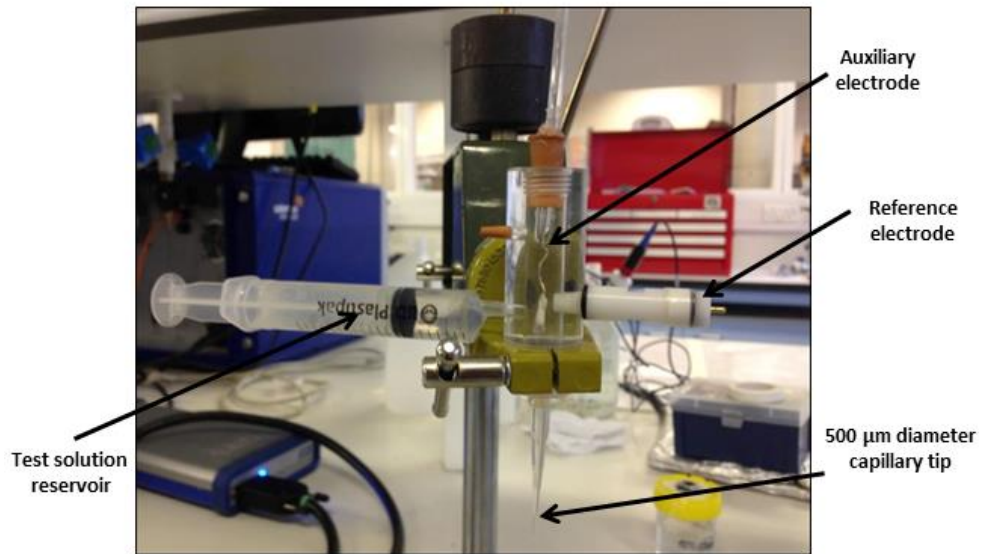


Figure 3.5 Schematic of the micro-capillary cell.

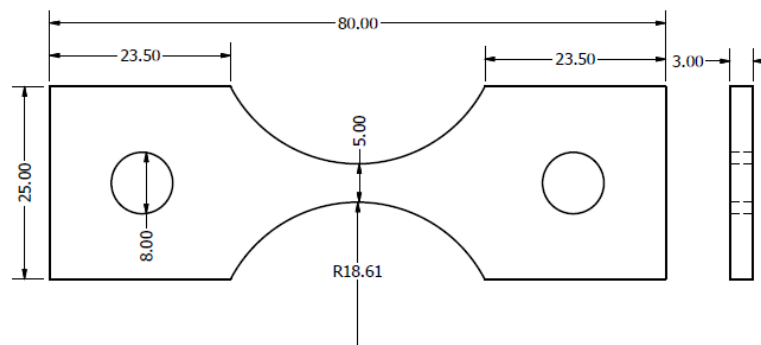


Figure 3.6 Fatigue specimen used to study pit growth under stress.

Fatigue loading of specimens was carried out on a 5 kN computer-controlled hydraulic machine under load control. The test set-up is shown in Figure 3.7. The test conditions were stress range: 180 MPa, stress ratio: 0.1, frequency: 2 Hz and temperature:  $25 \pm 4$  °C. Prior to loading, the gauge section of the specimen was first marked to aid location of the droplet in its centre. The intersection of the marker lines was carefully cleaned with acetone and then installed on the fatigue machine. Electrical contact between the specimen and the grips of fatigue machine was avoided by using a cardboard as a spacer between the two surfaces. The tip of the microcell was then lowered carefully by moving the Uniscan Z-axis control until a stable droplet is formed on the sample. The open circuit potential (OCP) was allowed to reach steady state before starting each test. A potential of 0.2 Volts above the OCP was applied to the sample for a duration ranging between 1 and

30 hours while the current was measured and recorded. At specified intervals, the testing was stopped, the specimen was removed and morphology (depth, width, volume) of the resulting pit characterised. The experimental values were also compared with their corresponding theoretical values obtained from electrochemical data using Faraday's law (Equation 3.1) [221]. The resulting charge was calculated by integrating the area under the Current-Time (I-t) plots (Equations 3.2 and 3.3). By assuming hemispherical pit shapes (pit depth = half pit width), the pit depth can be calculated by determining the cube root of the theoretical volume. However, the pit depth will be overestimated if the pits are not truly hemispherical. To obtain realistic values, Equation 3.4 was used instead, where  $d_p$  the pit depth and  $c$  is half the pit width. For the electrochemical data,  $h$  was set as 4 seconds.

$$V_{theor} = \left(\frac{Q}{F}\right) \left(\frac{M}{z}\right) \left(\frac{1}{\rho}\right) \quad (3.1)$$

$$Q = \int_0^t I(t) dt \quad (3.2)$$

$$Q = \sum_{t=0}^n \left\{ \frac{h}{2} (i_t + i_{t+1}) \right\} \quad (3.3)$$

$$V_{theor} = \frac{2}{3} \pi d_p c^2 \quad (3.4)$$

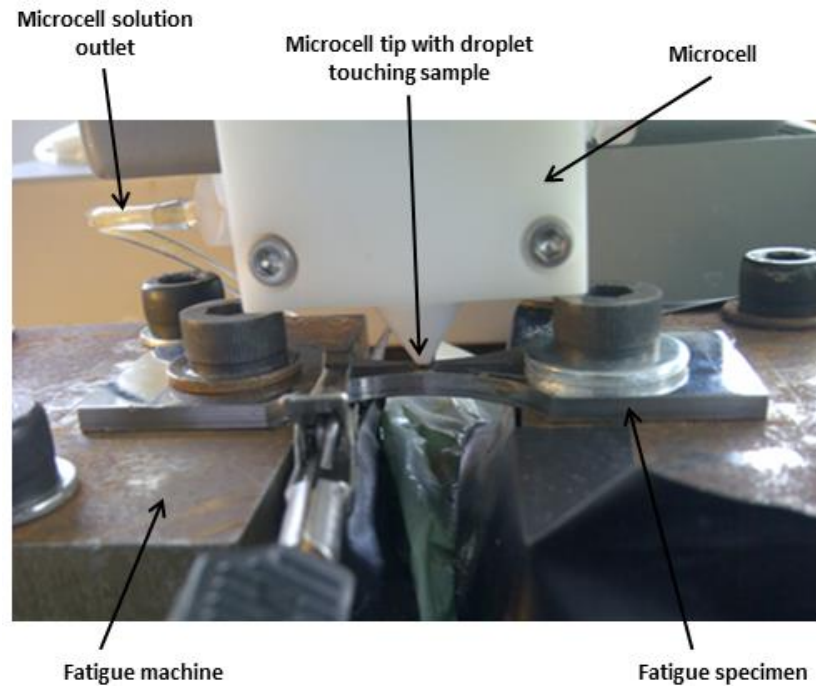


Figure 3.7 Experimental set-up for investigating effect of stress on pit growth.



### 3.8.3 Pre-pitting of fatigue specimens

Artificial corrosion pits having various sizes were generated on plain specimens before fatigue testing. In the pre-pitting procedure, specimens were first polished to a 4,000 grit surface finish in order to avoid reduction of the initial pit depth, which results from the reduction in the thickness of the specimen due to material removal from polishing. The intersection of the marker lines (the centre of the specimen) was then carefully cleaned with acetone and the specimen installed on a holder and levelled using a spirit level. The tip of the microcell was then lowered manually until a droplet contact is established. The specimen was then polarised potentiostatically in the anodic region by applying a potential of 0.5 Volts above the OCP for different durations depending on the target pit depth. Figure 3.7a shows the tip of the capillary placed at the centre of a fatigue specimen, while Figure 3.7b shows the generated pit. After pre-pitting, the specimens that were used for in-air tests were lightly re-polished to 4,000 grit surface finish to remove corrosion products around the pit mouth so that short cracks can be easily observed when they are initiated. Those used for corrosion fatigue tests were not re-polished because it was unnecessary. After pit generation, the pit morphology was characterised using a 3D confocal laser scanning microscope (CLSM).

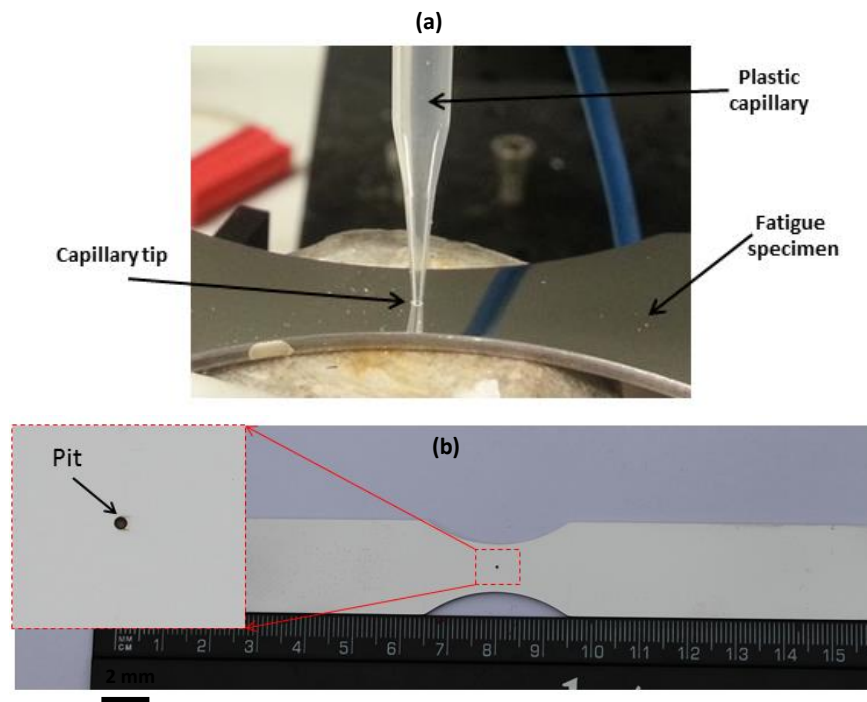
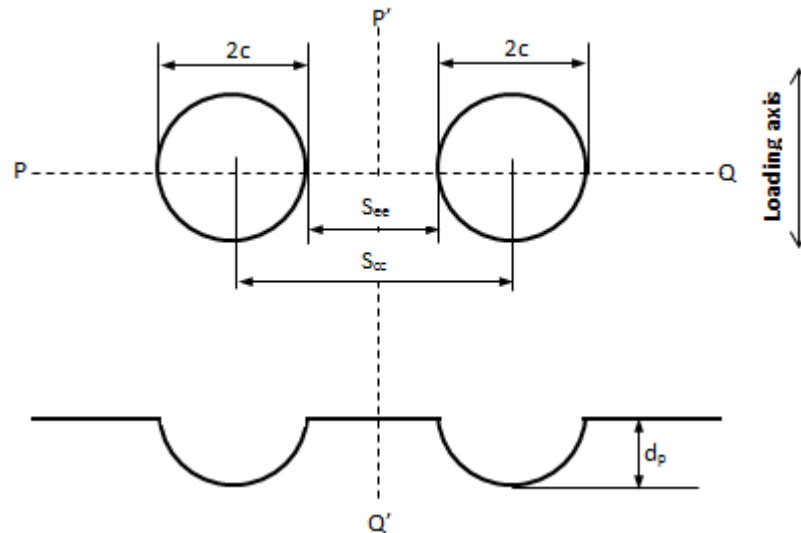


Figure 3.8 Typical pre-pitted fatigue specimen after re-polishing (Inset: a pit in the gauge section)

The experimental values were also compared with theoretical values, which were obtained as described in the previous section. The above procedure was also followed when generating double pits with various separation distances. Figure 3.8 shows a schematic of two single pits generated close to each other. The pits were aligned such that they both lie on the mid-axis (P-Q) of the test specimen equidistant from the longitudinal axis (P'-Q') of the specimen. The parameters defining the relative position of the double pits are:

- $c$ , half-width of a single corrosion pit ( $\mu\text{m}$ )
- $d_p$ , pit depth ( $\mu\text{m}$ )
- $s_{cc}$ , centre-to-centre distance between two pits ( $\mu\text{m}$ )
- $s_{ee}$ , edge-to-edge distance between two pits ( $\mu\text{m}$ )



**Figure 3.9** Schematic showing two pits located close to each other, both on a mid-axis (P-Q) and also positioned equidistant from the longitudinal axis (P'-Q') of the specimen.

Accurate positioning of the pits was achieved by carrying out the procedure on a Uniscan Scanning electrochemical workstation [222] which allowed position control in the x-axis, y-axis and z-axis. Pits were positioned by varying their centre-to-centre distances,  $d'$ . This was achieved by moving the scanning stage along the x-axis (P-Q in Figure 3.8). The values of  $d'$  employed varied slightly from those measured,  $d$ , after the pit generation procedure. The measured value of  $d$  is the summation of the half-width,  $c$ , of the two pits and edge-to-edge distance,  $s$ , between them. For this work programme, the three groups of pits were investigated in order to assess the effect of pit depth and pit geometry (aspect

ratio) on fatigue behaviour. Details of each group are listed in **Table 3.3**. The mean deviation in the pit depth (target parameter), pit width and aspect ratio was found to be less than 5%, 3% and 3% respectively. Before fatigue testing, polished specimens were rinsed in acetone and then kept in a desiccator until fatigue testing.

*Table 3.3 Three groups of corrosion pits generated on fatigue specimens. The given mean values of pit depth are the target values.*

	Pit depth ( $\mu\text{m}$ )	Pit Width ( $\mu\text{m}$ )	Aspect ratio	Polarisation time (s)
Group 1	$140 \pm 6$	$540 \pm 9$	$0.52 \pm 0.01$	7400
Group 2	$200 \pm 6$	$590 \pm 13$	$0.68 \pm 0.01$	15000
Group 3	$270 \pm 8$	$662 \pm 15$	$0.82 \pm 0.02$	31000

### 3.9 Mechanical Testing

In the course of this research, different types of mechanical tests were carried out. These included monotonic tensile tests, cyclic strain-controlled tests, in-air fatigue tests and corrosion fatigue tests. In all of these, test specimens were machined from the parent plate region using electric discharge machining (EDM).

#### 3.9.1 Monotonic tensile testing

Triplicate tensile tests were carried out to characterise the response of the material to monotonic loading. Apart from the mechanical properties of the material from this test, data of the yield stress-plastic strain relationship representing the hardening behaviour of the material was also obtained. The latter, in a digitised form, was used for all finite element analyses work carried out under static loading. ASTM standardised flat dog-bone samples were used for this test (Figure 3.9). The longitudinal axis of the specimens is parallel to the longitudinal direction of the pipes. This test was carried out on a computer-controlled 50 kN Instron 5569 universal testing machine under displacement control at room temperature at a strain rate of  $1 \text{ mm.min}^{-1}$ . Strain was measured using an MTS 634.31F-24 axial extensometer which has a gauge length of 40 mm. Triplicate tests were carried out following the ASTM E6 procedure [223]. Engineering stress, true stress, true strain and plastic strain were obtained from the load-strain data recorded on a computer using Equations 3.5 – 3.8.

$$\sigma = P/A \quad (3.5)$$

$$\sigma_{true} = \sigma (1 + \varepsilon) \quad (3.6)$$

$$\varepsilon_{true} = \ln (1 + \varepsilon) \quad (3.7)$$

$$\varepsilon_p = \varepsilon_{true} - (\sigma_{true}/E) \quad (3.8)$$

where  $\sigma$  is engineering stress (MPa),  $A$  is cross-sectional area (mm<sup>2</sup>),  $P$  is load (N),  $\varepsilon$  is engineering strain,  $\sigma_{true}$  is true stress (MPa),  $\varepsilon_{true}$  is true strain,  $\varepsilon_p$  is plastic strain and  $E$  is Young's modulus.

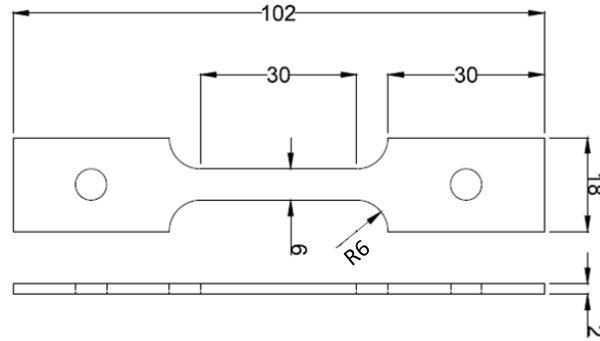


Figure 3.10 Geometry of flat tensile test specimen. All dimensions are in 'mm'.

### 3.9.2 Cyclic strain-controlled testing

Strain-controlled tests were carried out to characterise the cyclic stress-strain behaviour of the material at room temperature using ASTM standardised cylindrical hour-glass specimens (Figure 3.10). Fully reversed push-pull companion cyclic tests were carried out under total strain control on a computer controlled closed-loop 100 kN Instron 8501 servo-hydraulic testing machine with total strain amplitude ranging between 0.3% and 1.2%. Duplicate tests were carried out for each of the six strain amplitudes that were investigated. A triangular waveform with zero mean strain and constant strain rate of  $1.33 \times 10^{-3} \text{ s}^{-1}$  was used. To maintain this strain rate, the frequency was varied between 0.11 - 0.028 Hz depending on total strain amplitude (Table 3.4). A uniaxial dynamic extensometer with a gauge length of 10 mm and strain range of  $\pm 10\%$  was used to measure and control the strain. Data of load and strain for each cycle during each test was recorded at a sampling rate of 200 Hz. The true stress was obtained from Equation 3.5 after dividing the measured load by the cross-sectional area of the test specimen. For this series of test, fatigue life was defined as the number of cycles corresponding to a 2% drop in the value of the load that was measured at half-life [224]. The half-life is defined as the

number of cycles at which the measure load reaches steady state. The experimental set-up for this test is shown in Figure 3.11. Before testing, the gauge section of test specimens were carefully ground and polished with a succession of finer grade SiC paper up to 4,000 grit surface finish and then to 1  $\mu\text{m}$  using diamond paste.

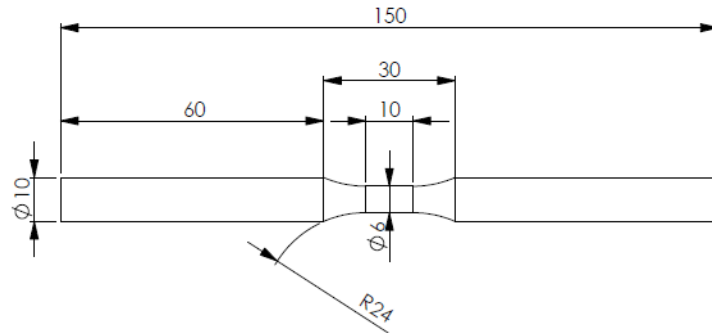


Figure 3.11 Geometry of hourglass cyclic test specimen. All dimensions are in 'mm'.

Table 3.4 Strain-controlled loading frequencies at different strain amplitudes for strain rate of  $1.33 \times 10^{-3} \text{s}^{-1}$ .

Strain amplitude (%)	Frequency (Hz)
0.30	0.1111
0.50	0.0667
0.65	0.0513
0.80	0.0417
1.00	0.0333
1.20	0.0278



Figure 3.12 Experimental set-up for cyclic strain-controlled fatigue testing. Inset: configuration showing grips, specimen and extensometer.

### 3.9.3 Fatigue/Corrosion Fatigue Testing

Flat dog-bone test specimens (Figure 3.12) were used for this test programme. The longitudinal axis of the specimens was parallel to the longitudinal direction of the pipes. Before testing, the gauge section and edges of all test specimens were carefully ground and polished with a succession of finer grade SiC paper up to 4,000 grit surface finish. Special care was taken in polishing the edges of the specimens so as to eliminate all notches or scratches which may act as false crack initiation sites.. Subsequently, the specimens fatigue loaded, in air or corrosion fatigue, depending upon the test programme. Constant amplitude uniaxial fatigue testing was performed on plain and pre-pitted specimens under load control in accordance with ASTM E466 [225]. Tests were carried out on a computer-controlled closed loop 10 kN Instron EletroPuls E1000 testing machine. Specimens were secured to the machine by means of pneumatic grips with serrated flat faces.

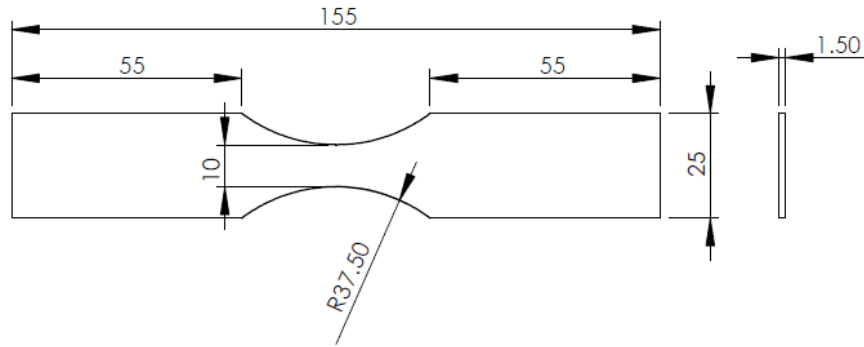


Figure 3.13 Geometry of dog-bone fatigue test specimen. All dimensions are in 'mm'.

#### 3.9.3.1 In-air fatigue tests

In-air tests were conducted on plain and pre-pitted specimens in laboratory air. The pre-pitted samples had two classes of pits, viz single and double pits. Tests were carried at various load levels with each test specimen subjected to constant amplitude cyclic loading until the specimen broke or reached a stage close to fracture. The stress range was obtained from Equations 3.5 and 3.9.

$$\Delta\sigma = \sigma_{max} - \sigma_{min} \quad (3.9)$$

$$\sigma_a = \left( \frac{\sigma_{max} - \sigma_{min}}{2} \right) \quad (3.10)$$

$$R = \frac{\sigma_{min}}{\sigma_{max}} \quad (3.11)$$

where  $\sigma_{max}$  is the maximum stress,  $\sigma_{min}$  is minimum stress,  $\sigma_a$  is stress amplitude and  $R$  represents stress ratio.

The maximum stress that was applied during testing of the pre-pitted specimens was chosen to correspond to the fatigue limit observed for plain specimens. The fatigue limit is defined as the stress range at which a specimen would be expected to survive a given number of cycles with a stated probability [226]. In this work, it is the stress range below which the specimen survived at least  $10^7$  cycles without failure. The specimens that did not fail are indicated as run-outs on S-N plots. Table 3.5 and Table 3.6 show the test matrix for the type of specimen, pit geometry and applied stress range for specimens containing single and double pits. The experimental set-up is shown in Figure 3.13.



*Figure 3.14 Experimental set-up for in-air fatigue testing. Inset: gauge section of fatigue specimen containing a corrosion pit.*

The standard in-air testing conditions are: stress ratio, R: 0.1, frequency, f: 15 Hz, temperature: room temperature ( $25 \pm 2$  °C) and sinusoidal waveform are as follows Stress ratio, R: 0.1

**Table 3.5 Test matrix for in-air testing of fatigue specimens containing single pits.**

Stress range (MPa)	Pre-pitted*			
	Plain	$AR_p = 0.52$	$AR_p = 0.68$	AR = 0.82
495.0	Y	-	-	-
486.0	Y	-	-	-
477.0	Y	-	-	-
463.0	Y	-	-	-
450.0	Y	Y	Y	Y
427.5	Y	Y	Y	Y
405.0	-	-	Y	Y
382.5	-	-	Y	Y
360.0	-	-	-	Y

$AR_p$  – Pit aspect ratio

Y – Tested

(-) – Not tested

\* The variation in the mean values of aspect ratio is always less than 3%

**Table 3.6 Test matrix for in-air testing of fatigue specimens containing double pits.**

Stress range (MPa)	Pre-pitted*	
	$AR_p = 0.68$	$AR_p = 0.82$
405.0	Y	Y
427.5	Y	Y

$AR_p$  – Pit aspect ratio

Y – Tested

\* The variation in the mean values of aspect ratio is always less than 3%

### 3.9.3.2 Corrosion fatigue tests

Corrosion fatigue tests were carried only on pre-pitted specimens in a brine environment. A test solution circulation loop, which consists of a reservoir, corrosion cell, peristaltic pump, tubing connections and stop valves for flow control, was used. A schematic of the three-electrode corrosion cell-specimen assembly is shown in Figures 3.14a and 3.14b. The corrosion cell has an inlet and outlet for the test solution, individual slots for the reference and auxiliary electrodes, an inlet and outlet for the circulation loop and glass windows on the front and back faces (Figure 3.14c). The latter allows for *in situ* optical measurements on the specimen surface during testing without disassembling the cell. The naturally aerated test solution was circulated through the cell at a constant flow rate of 0.3L/hr. This



optimum flow rate was chosen to minimise the effect of flow on corrosion fatigue data and also eliminate the effect of changes in pH which can result from hydrolysis of metal ions during the test. The test solution in the reservoir was renewed at intervals. All corrosion fatigue tests were carried out under freely corroding conditions. The maximum stress that was applied during testing was chosen to correspond to the fatigue limit observed for plain specimens.

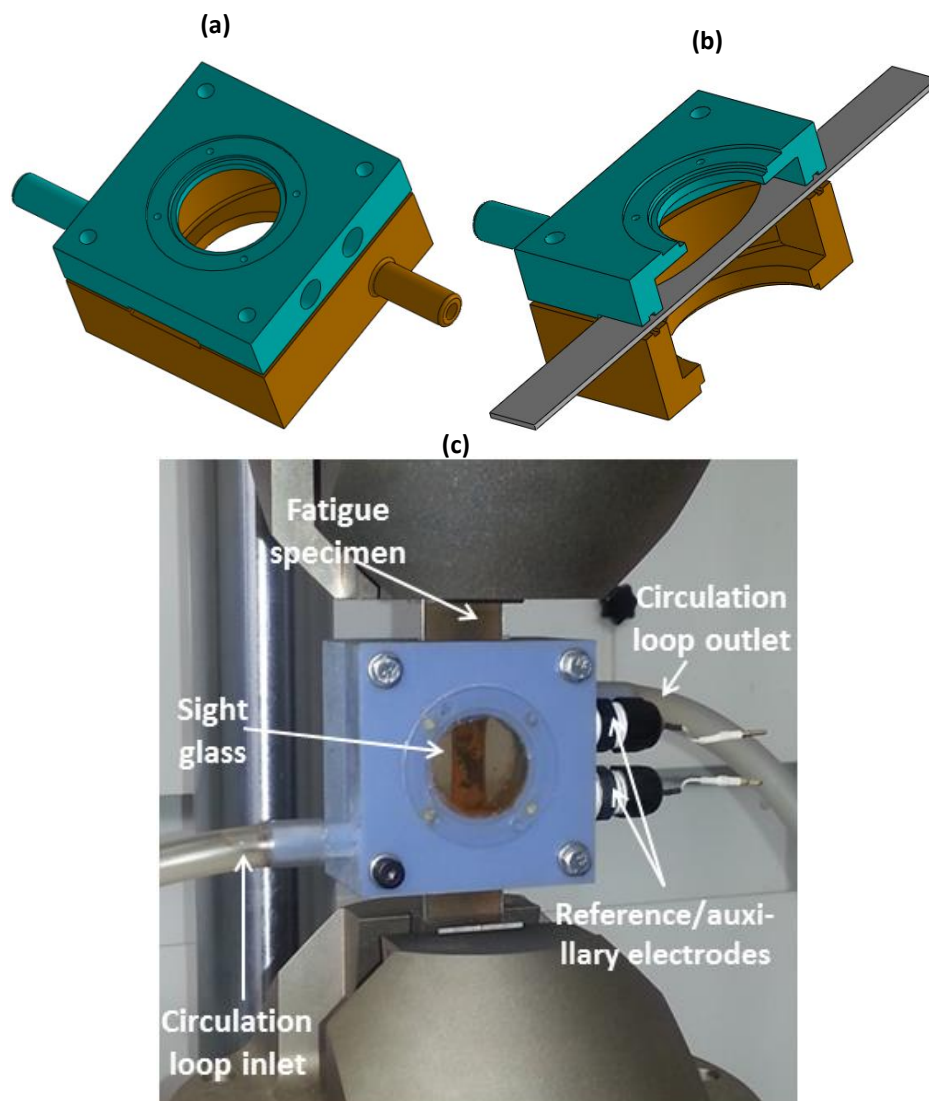


**Figure 3.15** Schematic of (a) corrosion cell used for corrosion fatigue testing and (b) corrosion cell-specimen assembly (c) Test set-up showing corrosion cell-specimen assembly.

The standard corrosion fatigue testing conditions are: stress ratio,  $R$ : 0.1, frequency,  $f$ : 2 Hz, temperature: room temperature ( $25 \pm 2$  °C) and sinusoidal waveform. The experimental set-up is shown in Figure 3.15. Table 3.7 shows the test matrix for corrosion fatigue experiments.

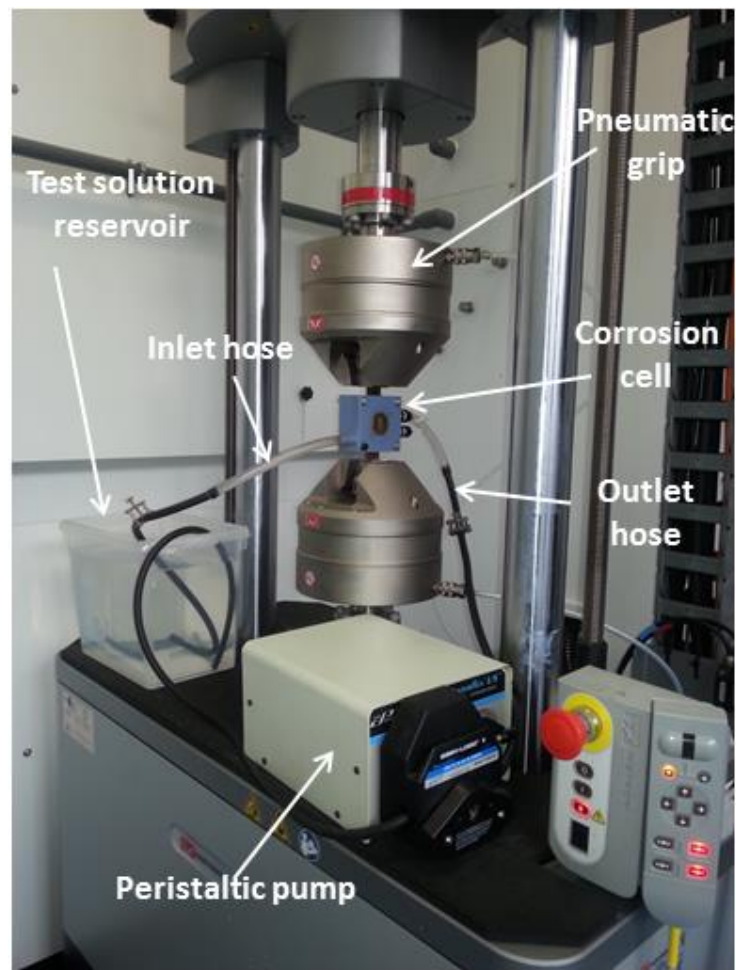


Figure 3.16 Experimental set-up for corrosion fatigue testing.

Table 3.7 Test matrix for corrosion fatigue testing.

Stress range (MPa)	Pre-pitted*		
	$AR_p = 0.52$	$AR_p = 0.68$	$AR_p = 0.82$
450.0	Y	Y	Y
427.5	Y	Y	Y
405.0	Y	Y	Y
382.5	-	-	Y
360.0	Y	Y	-
315.0	-	Y	Y

$AR_p$  – Pit aspect ratio      Y – Tested      (-) – Not test

\* The variation in the mean values of aspect ratio is always less than 3%.

### 3.10 Crack growth measurements

In the present study, a combination of replication technique and direct observation on optical and 3D digital microscopes were used to obtain information on fatigue crack initiation and propagation in air and corrosion environments.

For in-air tests, direction observation on an optical microscope was combined with the replication technique to aid detection of crack initiation and propagation. The direct observation method was more helpful in observing crack initiation on fatigue specimens with double pits. In both methods, fatigue tests were stopped at intervals to detect and to measure the length of cracks. The direct observation involved uninstalling the specimen and analysing the cracks in the region around the pit on the optical microscope. Precaution was taken to ensure that specimens are uninstalled and re-installed correctly. The replica technique involved cutting a sheet of cellulose acetate material into small pieces of approximately 20 mm x 10 mm. This size was chosen to eliminate wrapping of the acetate around the edges of the specimen, which usually results in replicas not lying flat on the specimen surface. At the time of surface replication, the test was paused, the specimen was loaded up to the mean load to cause crack opening, acetone was sprayed on the pit region using an atomiser and the acetate sheet was immediately placed on the pit region using a tweezer. Duplicate replicas were obtained to ensure consistency. After drying, the acetate sheet was removed and fixed on a microscope glass slide using cellotape. The crack lengths were obtained by analysing the replicas on the optical microscope. Advantages of the replication technique include its effectiveness and its economy, its ability to detect cracks that are few microns in length and no need for sophisticated equipment. However, its disadvantage is that only information on crack length on the surface can be obtained. Crack cannot be measured and has to be obtained through an alternative method. In this study, specimens that were fractured and those that cracked but didn't fracture were both used to determine the shape and aspect ratio of the cracks. Specimens that did not fail were fractured in liquid nitrogen.

In corrosion fatigue testing, crack initiation and propagation was studied by direct in-situ observation on a 3D digital microscope. The advantage of this method over the replication technique is that crack initiation and propagation can be detected and monitored in-situ

without removing the specimen from the test solution, which may result in changes in the chemistry of the bulk solution and solution within the pit and crack. In addition it was possible to obtain images with a depth of field, which aids observation. In the direct observation method, the test was stopped at pre-defined intervals, the inlet and outlet of the corrosion cell was locked using valves and the corrosion cell-specimen assembly uninstalled. The sealed corrosion cell assembly was then placed in an ultrasonic bath for 10 – 20 minutes to remove corrosion products from the surface, so that cracks can be readily observed. The assembly was then removed and dried. Crack lengths were then analysed in the region around the pit, by focusing through the glass window on the corrosion cell. After analysis, the assembly was re-installed on the fatigue machine, the valves unlocked and the test re-started.

### **3.11 Image analysis and fractography**

In the course of this research, image analysis was carried out using a combination of optical, digital, and confocal laser scanning microscopy and scanning electron microscopy. A Zeiss Axio Vert. A1 optical microscope was used for analysing replicas, analyses of cracks observed on fatigue specimens that were tested in air and for metallographic investigation. Corrosion fatigue crack growth analysis was carried out on a Keyence VKH 5000 Series 3D digital microscope. Both microscopes consist of a computer-controlled image analysis system incorporating observation, image capture and measurement capabilities. A Keyence VK-X200K 3D laser scanning microscope was used to characterize the morphology (width, depth, volume and 3-D profile) of the pits. This microscope also has the capability for exporting the scanned pit geometry as 3-D CAD files, which can be used for further finite element analysis. This file export capability was employed in the finite element modelling part of this research. Two scanning electron microscope (SEM) instruments, Philips XL-30 FEG/SEM and Zeiss EVO 60 VP/SEM, were used for crack initiation and fracture surface analysis.

---

# **Chapter 4**

## **Modelling Methods**

---

## 4.1 Introduction

For engineering applications where materials are subjected to fatigue, crack initiation is often the life-limiting stage. Once a crack initiates, it will propagate under favourable service conditions. When pits are precursors to these cracks, understanding the conditions that facilitate the evolution of cracks from this type of defect is critical for accurate lifetime prediction. It has been reported that, apart from electrochemical and metallurgical factors, the extent of strain localisation can play an important role in determining crack nucleation behaviour [121, 202, 227-229]. Therefore, detailed understanding of the evolution and distribution of stress and strain around pits is necessary in order to elucidate the conditions that facilitate the pit-to-crack transition. The overall goal of the modelling studies carried out in this research is to obtain more insight into the mechanics-based conditions and mechanisms that can facilitate crack nucleation from corrosion pits. The present study was divided into the following categories, which are described in more detail in the later sections of this chapter:

1. Evaluation of stress and strain distribution due to changes in pit size as a result of pit growth.
2. Assessment of the influence of stress and strain localisation around corrosion pits on pit-to-crack transition behaviour.
3. Study of the interaction between localised corrosion and stress.

The following are described in this chapter:

- Modelling techniques
- Analysis of stresses and strains around pits
- Modelling of the interaction between localised corrosion stress

## 4.2 FEA modelling techniques

### 4.2.1 Material model

An elastic-plastic material model with isotropic hardening isotropic hardening model was employed for FEA. This model is a reasonable assumption for remote tension loading and is characterised by a uniform expansion (hardening) in the size of the yield surface (yield stress) in all principal directions in the stress space, as plastic straining occurs. For a

monotonically increasing load, the current plastic strain increment is history independent although the preceding yield stress must be exceeded for further plastic flow to occur. Isotropic hardening data for the material was obtained from tensile stress-strain data. The yield stress was specified as a tabular function of accumulated plastic strain (see Appendix A).

#### **4.2.2 Robust modelling of real corrosion pits**

Several studies have employed FEA to evaluate stress and strain around pits. In these studies [1, 121, 194, 201, 202, 230], pits are normally idealized as regular shaped (hemispherical, cylindrical and ellipsoidal) defects with smooth surface profiles. However, in reality, corrosion pits seldom have such characteristics. Therefore, the accuracy of the information acquired from these studies may be open to debate. It is suggested that a more realistic and accurate approach is to model the actual morphology of the pits. In the present study, the actual 3-dimensional morphologies of pits were modelled and analysed in parallel with their idealized counterparts (assuming a hemispherical shape).

#### **4.2.3 FEA software**

All simulations and analyses were conducted on ABAQUS 6.13, which is a general purpose finite element program [231]. Models of pre-pitted specimens were developed and submitted as jobs to the in-built ABAQUS Standard Solver using ABAQUS/CAE pre-processor. Results from the analysis were post-processed using the ABAQUS Viewer. Further analysis of the results was carried out by writing additional scripts using the Python scripting language [232], which can communicate directly with the ABAQUS kernel.

#### **4.2.4 Model development**

The procedure involved in the FEA analysis of corrosion pits is enumerated in this section. Figure 4.1 shows a flow diagram of the steps in the procedure employed for model development in this study.

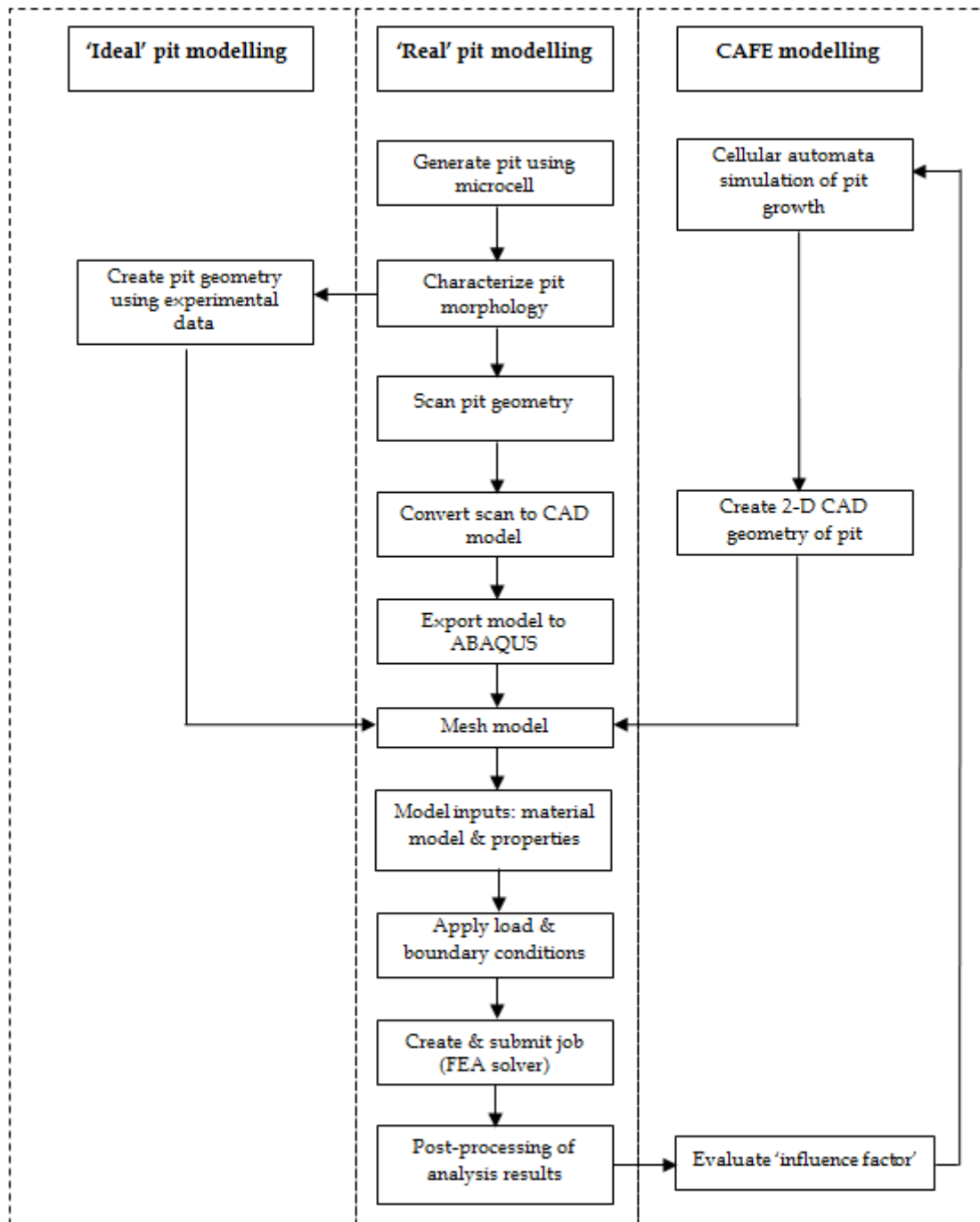


*Figure 4.1 Flow diagram of steps in the procedures employed for model development.*

The steps are briefly described below for double pits, but the same procedure also applies for single pits.

- Generation of pits – Figure 4.2a shows example of double pits that were generated using the pit generation procedure described in Section 3.8.
- Characterise pit morphology – the morphology of the generated pits were characterised using the confocal microscope.



- Scan pit geometry – the 3-D geometry of the generated pit was obtained by scanning on the CLSM (Figure 4.2b). The resolution of the scans was 1  $\mu\text{m}$  in x, y and z – axes. This resolution was necessary to capture the features on the surface of the pit.
- Convert scan to 3-D CAD model – the scanned geometry of the pit was converted into solid model (Figure 4.2c). In the case of ‘ideal’ pits, experimental data (depth, width) obtained from the pit morphology characterisation step was used to create 3-D geometry by employing the ABAQUS pre-processor.
- Export model to ABAQUS – the solid model of the pit region was exported as a ‘.stp’ file into ABAQUS. A preliminary study showed that the ‘as-is’ CAD file required very high computing resources - the models could not mesh (with a 128 GB RAM, 48-core processor PC). Hence it was necessary to reduce the size of the model. Down-sampling by reducing the resolution of the scan data (filtering) was found not to be a good approach because it eliminated the roughness features (which are of interest) on the pit surface. The choice approach was to reduce the size of the model by exporting only the region around the pits (Figure 4.2d). By using the ‘Merge Instances’ command in ABAQUS, the pit region was then merged with the full specimen, which had a pre-cut profile similar to that of the external profile of the exported pit geometry (Figure 4.3).
- Mesh model – The accuracy of the predictive ability of a finite element model depends on accuracy of the mesh model. Generally, a finer mesh results in a more accurate solution in finite element modelling. However, this usually leads to increase in computation time and the computing resources required. Balancing accuracy, computation time and resources satisfactorily requires a mesh convergence study [233]. Prior to meshing of the model, mesh convergence studies were carried out to determine the type and optimum sizes of elements that will be used for meshing. A combination of 3-D 20-node quadratic hexahedral with reduced integration (C3D20R) and 3-D 10-node quadratic tetrahedral (C3D10) solid continuum elements were used for 3D analyses. In the CAFE studies, 2-D 4-node bilinear plane strain quadrilateral (CPE4) elements were used. A higher density of elements was used in the region around the pit for improved accuracy

of results (Figure 4.4). Results of mesh convergence studies are reported in Chapter 6.

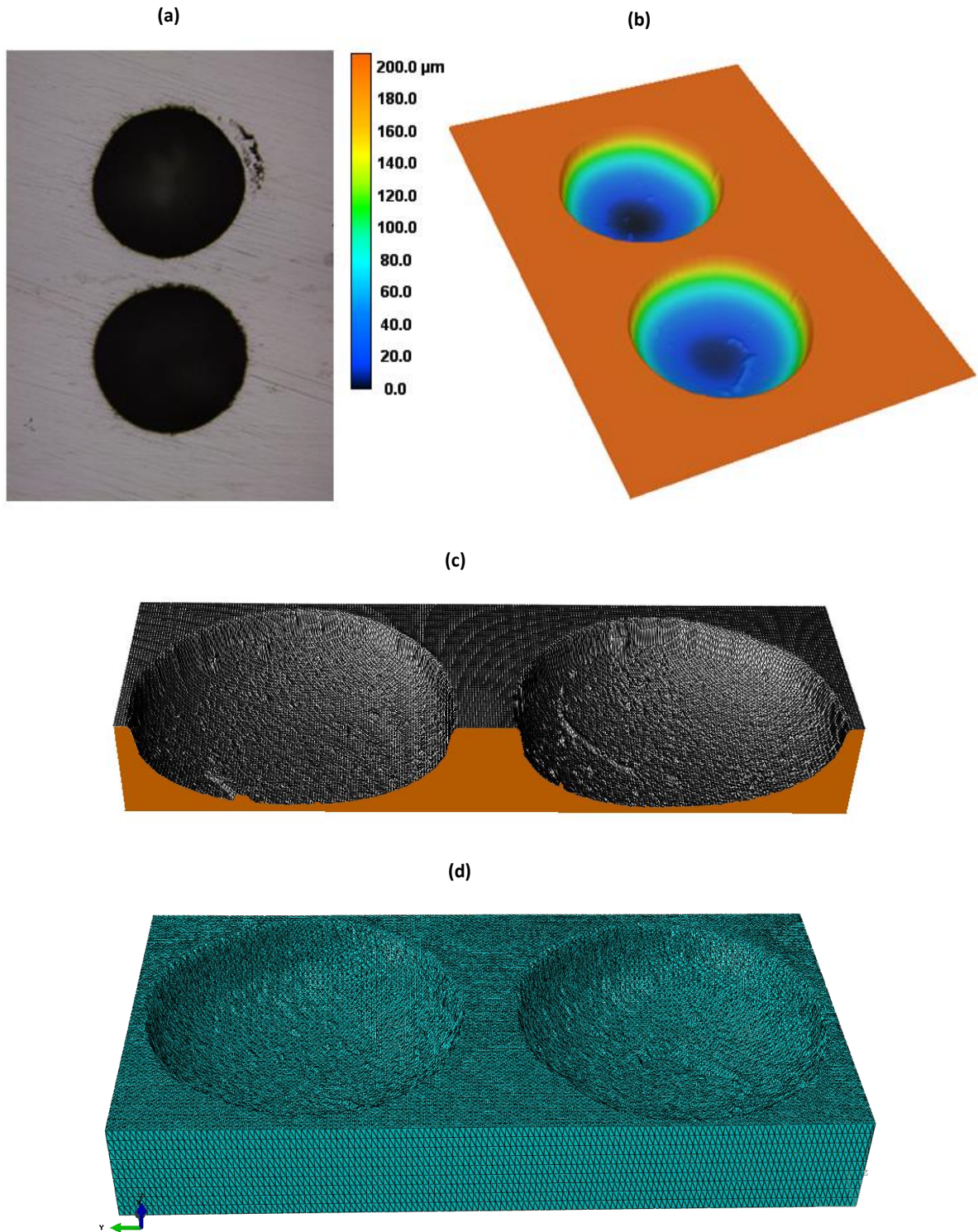


*Figure 4.2 Procedure for model development of pre-pitted specimens containing double pits (a) optical image (b) pit geometries after scanning (c) cross-section of solid CAD model of scan (d) fine mesh around the pits.*

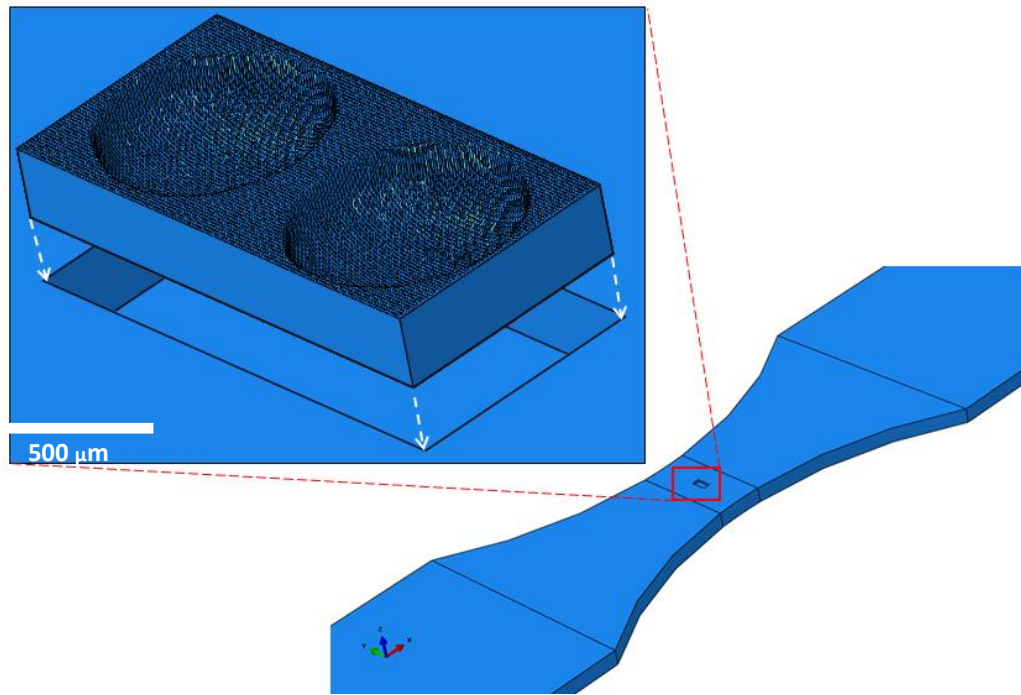


Figure 4.3 Assembly of 3-D models of pit region and specimen.

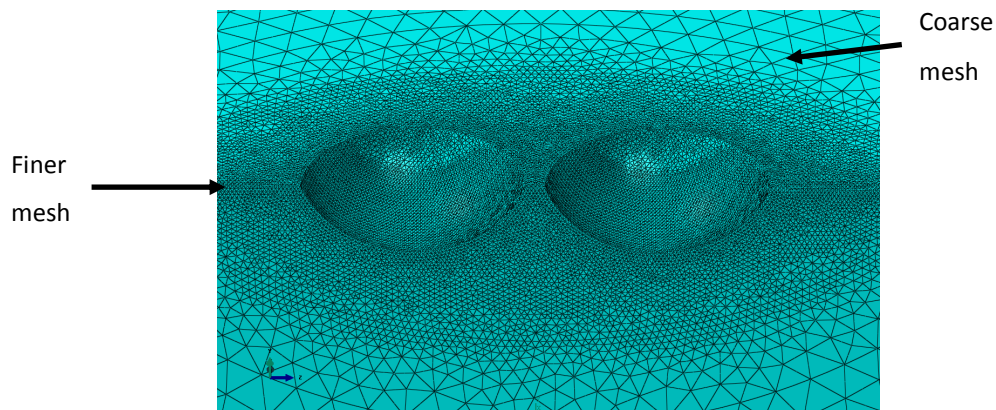


Figure 4.4. Finer mesh around pits and coarse mesh in other regions.

- Specify model inputs – Yield stress and a tabular form of plastic strain and a Poisson's ratio of 0.3 were specified as material properties.
- Apply loads and boundary conditions – in this step, uniaxial loads and appropriate boundary conditions were applied to appropriate regions of the models.
- Create and submit job – in this step, the job was created, submitted and solved using the ABAQUS's in-built solver.

- Post-processing of results – the results from the analysis was plotted into contour maps, time history plots, etc. In some cases, for instance CAFE studies, further analysis of various output variables was carried out.

#### 4.2.5 Mesh convergence

To enhance accuracy of prediction, mesh convergence studies were carried out for both artificial and ideal 3-D pit models. This ensures that the quantities of interest (stresses and strains) in the vicinity of the pit are not affected by changing the size of mesh. Employing an elastic material model, the stress concentration factor (ratio of maximum principal stress to nominal applied stress) was evaluated for ideal and artificial pits with aspect ratios (ratio of pit depth to half pit width) of 0.5 and 0.68 respectively. It was not necessary to consider the strain because of the direct relationship between stress and strain in an elastic material. The models were partitioned in order to create a finer mesh around and within the pit and a coarse mesh in other regions. The size of the coarse mesh was fixed (100  $\mu\text{m}$ ) while only the size of the finer mesh was varied for this study.

#### 4.2.6 Model validation

The 3-D FEA model was validated by comparing the values of the predicted elastic stress concentration factor with results obtained empirically [234] for an ideal pit and with the surface strain obtained from digital image correlation (DIC)<sup>2</sup> analysis of artificial pits. All model validation results are reported in Chapter 6.

### 4.3 Analysis of stresses and strains around pits

Understanding the conditions that facilitate the evolution of cracks from corrosion pits is critical for accurate lifetime prediction. From experiments carried out in the present work, pits were found to be the precursors to cracking in air and corrosion fatigue. In addition, the pit-to-crack transition lifetimes depended on pit characteristics, notably pit depth and pit aspect ratio. The overall goal of this present study is to elucidate the mechanics-based conditions and mechanisms that can facilitate crack nucleation from these pits. To achieve

---

<sup>2</sup>DIC experiment was carried out by Mr. C. Evans as part of his PhD project titled: 'Understanding Pit-to-Crack Transition'.

this, the evolution and distribution of stress and strain around pits were evaluated under three sub-headings.

#### 4.3.1 Changes in stress and strain distribution due to pit growth

In this study, a quasi-static analysis was carried out to simulate the changes in distribution of stress and strains as a result of the changes in pit depth and pit aspect ratio. The artificial pits were modelled by following the procedure described in Section 4.2.4. A corresponding ideal pit was modelled using the experimental characteristics (depth, width, aspect ratio) of each real artificial pit. Figure 4.5 shows (a) a typical real artificial pit and (b) its corresponding ideal model. The dimensions of the flat specimen containing the pits was  $20 \times 10 \times 1.5$  mm. Uniaxial stress in tension, equivalent to the maximum applied during fatigue experiments, was applied to one end of the specimen. The depth and aspect ratios of the pits were the same as those observed for the pit growth rate experiments. An isotropic elastic-plastic material model was used for this analysis.

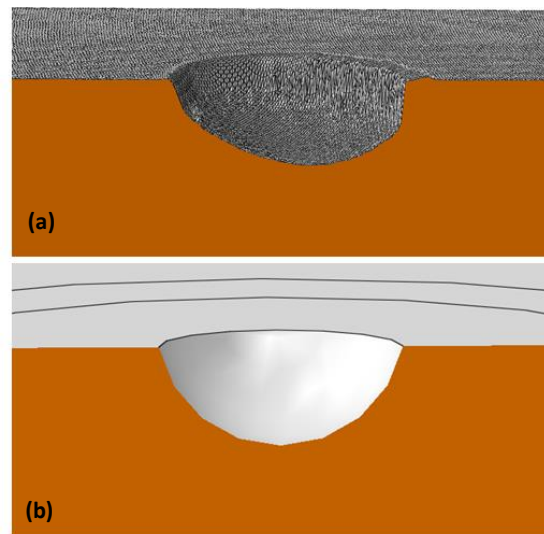


Figure 4.5 Solid models of (a) real and (b) ideal pit (pit depth =  $267 \mu\text{m}$ ; aspect ratio = 0.81)

#### 4.3.2 Assessment of the influence stress and strain localisation around corrosion pits on pit-to-crack transition behaviour.

In this study, a quasi-static analysis was carried out to evaluate the distribution of stress and strain around real and ideal pits under different conditions in order to understand the pit-to-crack transition behaviour. The modelling conditions, which involved a combination of different pit geometries (depth, pit aspect ratio) and levels of loading,

were selected to simulate those employed in the experiments. In addition to single pits, double pits were also investigated to understand how the presence of neighbouring pits can affect stress and strain localisation and consequently the crack initiation site and crack initiation life. A series of real artificial pits were modelled on fatigue specimens by following the procedure described in Section 4.2.4. A corresponding ideal pit was modelled using experimental characteristics (depth, width, aspect ratio, centre-to-centre distance) of each real artificial pit (Figures 4.2c and 4.4). These pits were modelled on the full fatigue specimens (Figure 3.13). The depth, aspect ratios, centre-to-centre distances and applied uniaxial tensile stresses employed in this study are given in Tables 3.5 - 3.7.

#### **4.4 Modelling of the interaction between localised corrosion and stress**

Despite the numerous studies that have been reported in the literature, modelling localised corrosion still presents significant challenges, especially when the complex processes that are involved such as metal dissolution, passivation and re-passivation, IR drop, mass transport, hydrolysis and salt precipitation, all of which, have non-linear behaviour, have to be accounted for. Adding to this challenge is the need to account for the interaction between corrosion and applied stress. The resulting geometric defects, notably corrosion pits, can lead to localisation of stress and strain. When evolution of damage over time is considered, the changing pit geometry (pit development) can induce dynamic local stress and strain distribution around the pit, which can facilitate crack nucleation. Given the complicated nature of the physical electrochemical processes involved, coupled with the dynamic nature of the distribution of stress and strain, a computational approach to modelling the interaction between localised corrosion and stress can prove valuable in the understanding of the damage processes and mechanisms involving pit development and the pit-to-crack transition.

One possible approach for addressing this problem is that of cellular automata (CA). CAs have proved to be a very powerful tool for simulating a variety of real physical system, chemical and biological systems [235-237]. They can be used to describe the discrete space and evolution of systems by applying local deterministic or probabilistic transformation rules. In contrast to partial differential equations in which space, state and time are continuous, these three are discrete in CAs [238, 239]. In a CA, the evolution of the state of



each cell in the modelling space is determined by the current state of a cell at a discrete time step and that of its neighbourhood cells [240]. All cells have access to the same set of states at any time and can assume only a finite number of states. Based on the local transformation rules, which apply to all the cells in the automaton, all cells are updated synchronously.

The nature of electrochemical processes, whereby the state of the species in corrosion reactions changes as a result of interaction with other species around it, makes CA a potent method for modelling electrochemical damage i.e. metal dissolution. In this method, the physical metal-environment system is discretised into a metal/film/electrolyte cellular lattice of sites (also referred to as ‘cells’), where each of the cells in the lattice can represent different species taking part in the corrosion process. Previous investigations using CA in corrosion studies include those on uniform corrosion [241-243], pitting corrosion [240, 244-246] and intergranular corrosion [247]. Historically, the FEM has been employed for evaluating the local stress and strain distribution around corrosion pits [1, 121, 248]. For a growing pit under static loading conditions, the changes in size and geometry induce dynamic distributions of local strain around the pit, which can subsequently influence the rate of pit growth through strain-assisted anodic dissolution mechanism and facilitate crack nucleation. The damage process is more complicated in corrosion fatigue because the growing pit with its dynamic strain is now in a cyclic loading regime. The FEM can be used for re-computation of dynamic stress and strain distribution associated with a pit geometry corresponding to each time interval. In addition, appropriate criteria can be specified for crack initiation in FEM.

As previously discussed, FEA can be employed for analysing local stresses and strains around corrosion pits [1, 121, 248]. Therefore one modelling option is to combine both CA and FE in the cellular automata finite element (CAFE) approach. In this approach pitting damage is induced by corrosion, the geometrical output of the CA model is then introduced to the FE software. By introducing an applied stress, the FE software determines the local stress and strain associated with the pit geometry. The mesh, with its associated stress/strain distribution around the pit is returned to the CA where upon corrosion continues, but taking into account the different stress/strain states of the mesh (cells). Consequently, the effect of mechanical factors on future corrosion damage can be

evaluated by: (i) changing the dissolution kinetics of cells in the CA model subject to local strains determined by FE; and (ii) changing the geometry of the cellular structure in the FE model subject to dissolving cells determined by CA. Consecutive execution of the two analyses with sufficiently small cell size provides a good approximation for the interaction between corrosion and deformation effects on the development and localisation of damage.

#### 4.4.1 Configuration of cellular automata modelling space

##### 4.4.1.1 Electrochemical system

Figure 4.8 illustrates the Pourbaix diagram for iron in the presence of water or humid environments at 25°C. This diagram was calculated by considering all possible reactions associated with iron in wet or aqueous conditions listed in the Table 4.1 and excluding drier forms of corrosion products such as magnetite ( $\text{Fe}_3\text{O}_4$ ) or iron (ferric) oxide ( $\text{Fe}_2\text{O}_3$ ). In Figure 4.6, it can be observed that there are four species which have a stable area in the Pourbaix diagram; they are Fe,  $\text{Fe}^{2+}$ ,  $\text{Fe}^{3+}$ ,  $\text{Fe}(\text{OH})_2$  and  $\text{Fe}(\text{OH})_3$ . These species will be considered in the selection of the states that the cells can have in the cellular automata system. The states considered in the CA model are indicated in Table 4.2. Each state is represented by a numerical value in the CA matrix.

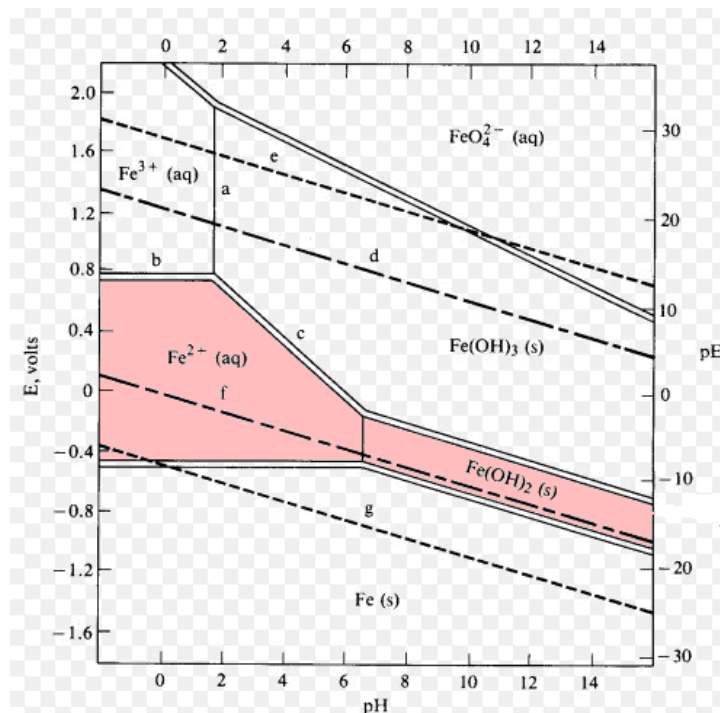


Figure 4.6 Pourbaix diagram of iron or steel with four concentrations of soluble species, three soluble species and two wet corrosion products (25°C).



**Table 4.1 Summary of the possible reactions in the Fe-water system between the species most stable in wet conditions, aerated at 25°C.**

Equilibria	
1.	$2 e^- + 2 H^+ \leftrightarrow 1 H_2$
2.	$4 e^- + 1 O_2 + 4 H^+ \leftrightarrow 2 H_2O$
3.	$2 e^- + Fe(OH)_2 + 2 H^+ \leftrightarrow 1 Fe + 2 H_2O$
4.	$2 e^- + 1 Fe^{2+} \leftrightarrow 1 Fe$
5.	$2 e^- + 1 Fe(OH)_3 + 3 H^+ \leftrightarrow 1 Fe + 3 H_2O$
6.	$1 e^- + 1 Fe(OH)_3 + 1 H^+ \leftrightarrow 1 Fe(OH)_2 + 1 H_2O$
7.	$1 e^- + 1 Fe(OH)_3 + 3 H^+ \leftrightarrow 1 Fe^{2+} + 3 H_2O$
8.	$1 Fe(OH)_3 + 1 H^+ \leftrightarrow 1 Fe(OH)_2 + 1 H_2O$
9.	$1 e^- + 1 Fe(OH)_3 \leftrightarrow 1 Fe(OH)_3^-$
10.	$1 Fe^{3+} + 3 H_2O \leftrightarrow 1 Fe(OH)_3 + 3 H^+$
11.	$1 Fe^{2+} + 2 H_2O \leftrightarrow 1 Fe(OH)_2 + 2 H^+$
12.	$1 e^- + 1 Fe^{3+} \leftrightarrow 1 Fe^{2+}$
13.	$1 Fe^{2+} + 1 H_2O \leftrightarrow 1 Fe(OH)^+ + 1 H^+$
14.	$1 FeOH^+ + 1 H_2O \leftrightarrow 1 Fe(OH)_{2(sln)} + 1 H^+$
15.	$1 Fe(OH)_{2(sln)} + 1 H_2O \leftrightarrow 1 Fe(OH)_3^- + 1 H^+$
16.	$1 Fe^{3+} + 1 H_2O \leftrightarrow 1 FeOH^{2+} + 1 H^+$
17.	$1 FeOH^{2+} + 1 H_2O \leftrightarrow 1 Fe(OH)_2^+ + 1 H^+$
18.	$1 Fe(OH)_2^+ + 1 H_2O \leftrightarrow 1 Fe(OH)_{3(sln)} + 1 H^+$
19.	$1 FeOH^+ + 1 H^+ \leftrightarrow 1 Fe^{2+} + 1 H_2O$
20.	$1 e^- + 1 Fe(OH)_2 + 2 H^+ \leftrightarrow 1 Fe^{2+} + 2 H_2O$
21.	$1 e^- + Fe(OH)_{3(sln)} + 1 H^+ \leftrightarrow 1 Fe(OH)_{2(sln)} + 1 H_2O$
22.	$1 e^- + Fe(OH)_{3(sln)} + 2 H^+ \leftrightarrow 1 Fe(OH)^+ + 2 H_2O$
23.	$1 e^- + Fe(OH)_{3(sln)} + 3 H^+ \leftrightarrow 1 Fe^{2+} + 3 H_2O$

**Table 4.2. States of the cells in the cellular automata model.**

Reaction No	Specie	Symbol	Number
1	Neutral site	W	0
2	Acidic site	H	1
3	Iron (Fe)	M	2
4	Iron (II) ion, $Fe^{2+}$	R	3
5	Iron (III) ion, $Fe^{3+}$	D	4
6	Iron (II) Hydroxide $Fe(OH)_2$	P1	5
7	Iron (III) Hydroxide $Fe(OH)_3$	P2	6
8	Capillary wall	C	7

In the simulations, a 2-D lattice space of 2000 x 1000 (rows x columns) was normally used. A CA with Moore neighbourhood was used in this simulation. In the Moore neighbourhood (Figure 4.8a), all eight neighbours of a particular cell are considered in contrast to the Neumann neighbourhood which considers only four neighbours (Figure 4.8b). The Moore neighbourhood was adopted because it is a more realistic representation of electrochemical processes by considering all the neighbours of the objective cell.



Figure 4.7 Schematic of cellular space for cellular automata modelling.

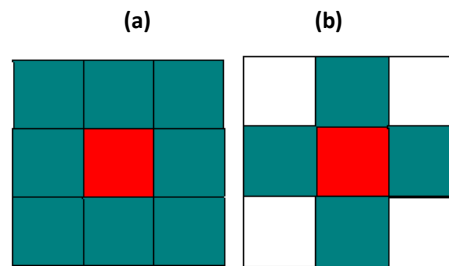


Figure 4.8 Schematic of types of neighbourhood (a) Moore (b) Neumann.

#### 4.4.1.2 Evolution rules of cellular automata

The algorithm for the CA model was written in Matlab ® [249]. The model was formulated into two parts: a corrosion section, which simulates the electrochemical reactions and a diffusion section, which simulates the diffusion of species into the solution during the electrochemical damage process. For implementation in the CA, these two were modelled as two loops.

##### Rules for corrosion reactions

The first rule represents the forward reaction for dissolution of Fe to  $\text{Fe}^{2+}$  considering the *Reaction 4* in Table 4.1. This reaction takes place with a probability  $P_{corr}$  when at least one acidic site (H) is in contact (the neighbourhood) of the metal site, M (Figure 4.9a). The second rule is the oxidation of  $\text{Fe}^{2+}$  to  $\text{Fe}^{3+}$  (*Reaction 12* in Table 4.1). This reaction takes place with probability  $P_{ox}$  and is triggered by the presence of at least one acidic site in

the neighbourhood of  $\text{Fe}^{2+}$  (Figure 4.9b). The third rule involves the hydrolysis of  $\text{Fe}^{2+}$  to give  $\text{Fe}(\text{OH})_2$  taking place with probability  $P_{\text{Hyd1}}$  (Reaction 11 in Table 4.1). For this reaction to proceed, at least two of the neighbours must be neutral sites (Figure 4.9c). The final reaction involves the hydrolysis of  $\text{Fe}^{3+}$  to  $\text{Fe}(\text{OH})_3$  (Reaction 10 in Table 4.1). In this case, at least three neighbours of a  $\text{Fe}^{3+}$  site must be neutral sites. The reaction will be take place with a probability of  $P_{\text{Hyd2}}$  (Figure 4.9d).

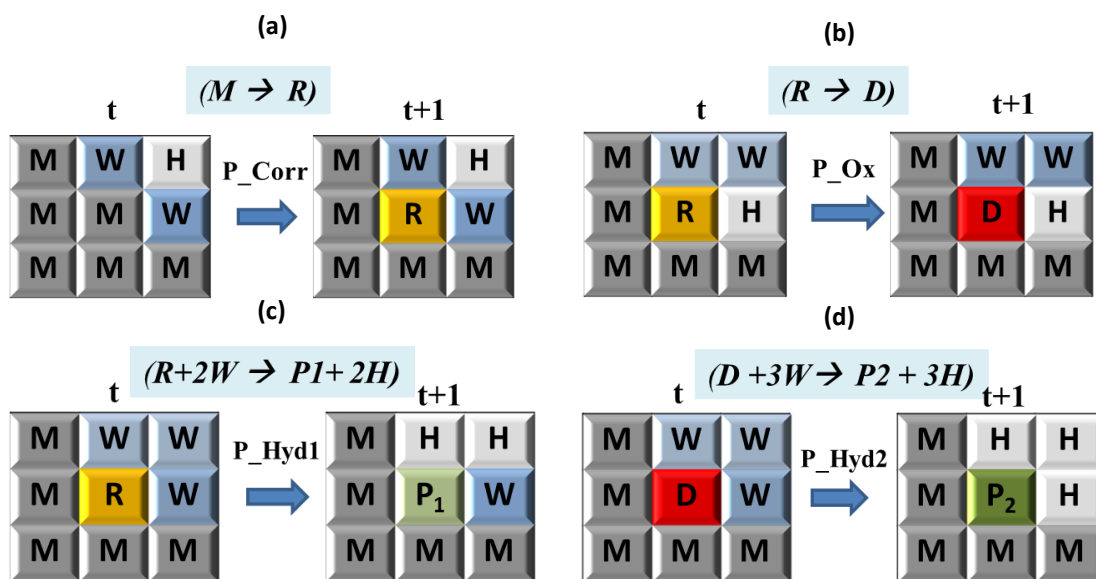


Figure 4.9 Corrosion rules used in CA to simulate (a) oxidation of Fe to  $\text{Fe}^{2+}$ , (b) oxidation of  $\text{Fe}^{2+}$  to  $\text{Fe}^{3+}$ , (c) hydrolysis of  $\text{Fe}^{2+}$  to  $\text{Fe}(\text{OH})_2$  and (d) hydrolysis of  $\text{Fe}^{3+}$  to  $\text{Fe}(\text{OH})_3$ .

### Rules for diffusion

The diffusion of some species is considered in the CA model. These species and their associated probabilities are:  $\text{Fe}^{2+}$  [ $P_{\text{diffFeII}}$ ],  $\text{Fe}^{3+}$  [ $P_{\text{diffFeIII}}$ ],  $\text{Fe}(\text{OH})_2$  [ $P_{\text{diffFeHyII}}$ ],  $\text{Fe}(\text{OH})_3$  [ $P_{\text{diffFeHyIII}}$ ] and  $\text{H}^+$  [ $P_{\text{diffH}}$ ]. Each of these species will diffuse according to their corresponding probabilities. The diffusion of species except the hydroxides is assumed to be isotropic, which means that they can move in any direction with the same probability (Figure 4.10a). In the case of the hydroxides, due to their lower solubility, they will tend to move in the downward direction with greater probability than in any other direction (Figure 4.10b). Therefore, a sedimentation factor,  $Sed$ , was added in the case of the hydroxides in order to take account for the precipitation effect.

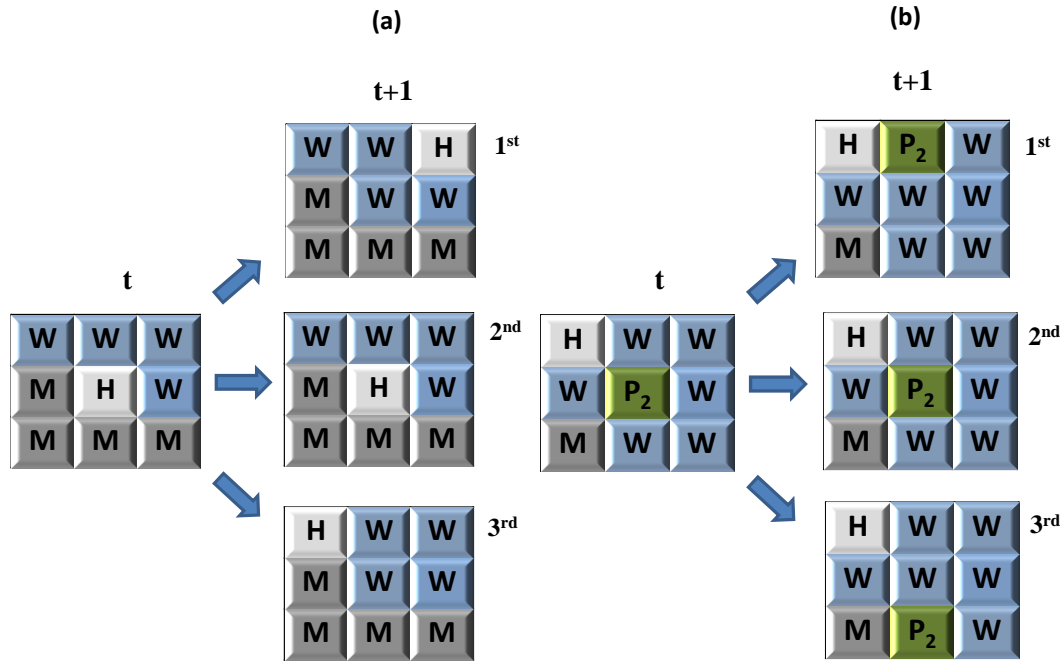


Figure 4.10 Representative diffusion rules used in CA to simulate (a) isotropy (same probability in all the directions for a H site) and (b) precipitation (3<sup>rd</sup> option most likely).

### Rules for mechanical-electrochemical effect

Anodic dissolution of metals and alloys can be promoted by both elastic and plastic deformation [127, 250]. This mechanical-electrochemical interaction has been modelled based on bulk thermodynamic analysis of metals [251, 252]. From this model, away from equilibrium and during strain hardening, the kinetic equation of the anodic dissolution due to deformation can be determined from

$$\frac{I}{I_n} = \exp\left(\frac{\Delta P V_m}{RT}\right) \quad \text{Elastic deformation} \quad 4.3$$

$$\frac{I}{I_n} = \left(\frac{\Delta \varepsilon}{\varepsilon_0} + 1\right) \exp\left(\frac{\sigma_m V_m}{RT}\right) \quad \text{Plastic deformation} \quad 4.4$$

where  $I$  is the anodic current of deformation,  $I_n$  is the anodic current for no deformation,  $\Delta P$  is the hydrostatic pressure,  $V_m$  is the molar volume,  $\Delta \varepsilon$  is the equivalent plastic strain,  $\varepsilon_0$  is strain at onset of strain hardening,  $\sigma_m$  is the hydrostatic stress,  $R$  is the gas constant and  $T$  is the temperature.

According to this model, a mechanical-electrochemical effect exists in areas of localised stress and strain. This effect, defined as an *influence factor*,  $I/I_n$ , can be obtained from Equations 4.3 and 4.4, and is determined by elastic and plastic strain, hydrostatic stress

and pressure stress all of which are obtained from FEA. The magnitude of this factor is used to specify a probability for changing a metal site from a base state to a reactive state.

#### 4.4.2 Finite element analysis of pit geometry

The dynamic localised stress and strain induced by the growing pit were computed after five CA time steps using plain strain FEA. Matlab® [249] scripting language was also used to develop the algorithm that (i) exports the output matrix from the CA, (ii) automates the relevant parts of the procedure described in Section 4.3.4, (iii) creates an ABAQUS input file, (iv) creates and submits the job to the ABAQUS standard solver, (v) uses a python script to output stress and strain tensors from each element, (vi) evaluates the influence factor based on information on stress and strains, and (vii) modifies the CA matrix (geometry) accordingly based on the influence factor. Because boundary conditions and stresses must be applied to continuous surfaces during FE analysis, it was necessary to ensure that the cells in the boundaries of the metal space do not corrode. This was achieved by excluding the boundary cells in the metal space from the corrosion process. Tensile load was applied to evaluate the effect of stress on localised corrosion and the dynamic strains resulting from a growing pit. The ABAQUS input file is given in Appendices E1. Because the CAFE model requires the outputs of the FEA as inputs for the CA, the FEA results were processed further using a subroutine, written in Python scripting language (Appendix E2), that accesses the ABAQUS output database (.odb file) and exports the components of the stress, total strain and principal plastic strain tensors in each element. The parameters in Equation 4.3 and Equation 4.4 were then evaluated from the stress and strain tensors. The model constants are:  $V_m = 7.0923 \times 10^{-6} \text{ m}^3 \cdot \text{mol}^{-1}$  (for iron),  $T = 298 \text{ K}$  and  $R = 8.314 \text{ m}^2 \text{ kg s}^{-2} \text{ K}^{-1} \text{ mol}^{-1}$ . The strain at on-set of strain hardening is taken as 2%.

---

# **Chapter 5**

## **Experimental Results and Discussion**

---

## 5.1 Introduction

This chapter presents the results obtained from the present investigations carried out on API 5L X65 linepipe steel in the as-received condition. The results are presented based on the main objectives of the experimental part of this research, which include:

1. To characterise the microstructural properties of the material.
2. To establish the baseline mechanical (tensile and fatigue) properties of the material in air.
3. To establish the basic electrochemical properties of the material.
4. To evaluate pit growth behaviour with and without stress.
5. To evaluate the initiation and propagation behaviour of cracks emanating from pits in air and aggressive environment.
6. To evaluate the effect of proximity between pits on the initiation and propagation behaviour of cracks emanating from them.
7. To evaluate the effect of aggressive environment on fatigue endurance behaviour when corrosion pits are present.

## 5.2 Material Characterisation

### 5.2.1 Microstructure

The material was composed mainly of polygonal ferrite grains and equiaxed ferrite grains (Figure 5.1). Because carbon is present in the material, some amounts of pearlite microstructure will be expected. However, as can be seen in these micrographs, none was observed optically, probably due to the very low carbon content (0.05% maximum). From the analyses of the grain sizes using the linear intercept method [253] and electron backscattered diffraction (EBSD)<sup>3</sup>, an average grain size of 15  $\mu\text{m}$  was adopted for the material. Figure 5.1 also shows that the shapes and sizes of grains in both longitudinal and long transverse directions are similar but different in the short transverse direction. The orientation of the longitudinal axis of all the samples used for tensile, cyclic and fatigue tests was along the longitudinal direction of the pipe.

---

<sup>3</sup> EBSD analysis was carried out by Dr. Yuan Feng Yang of School of Materials, University of Manchester.

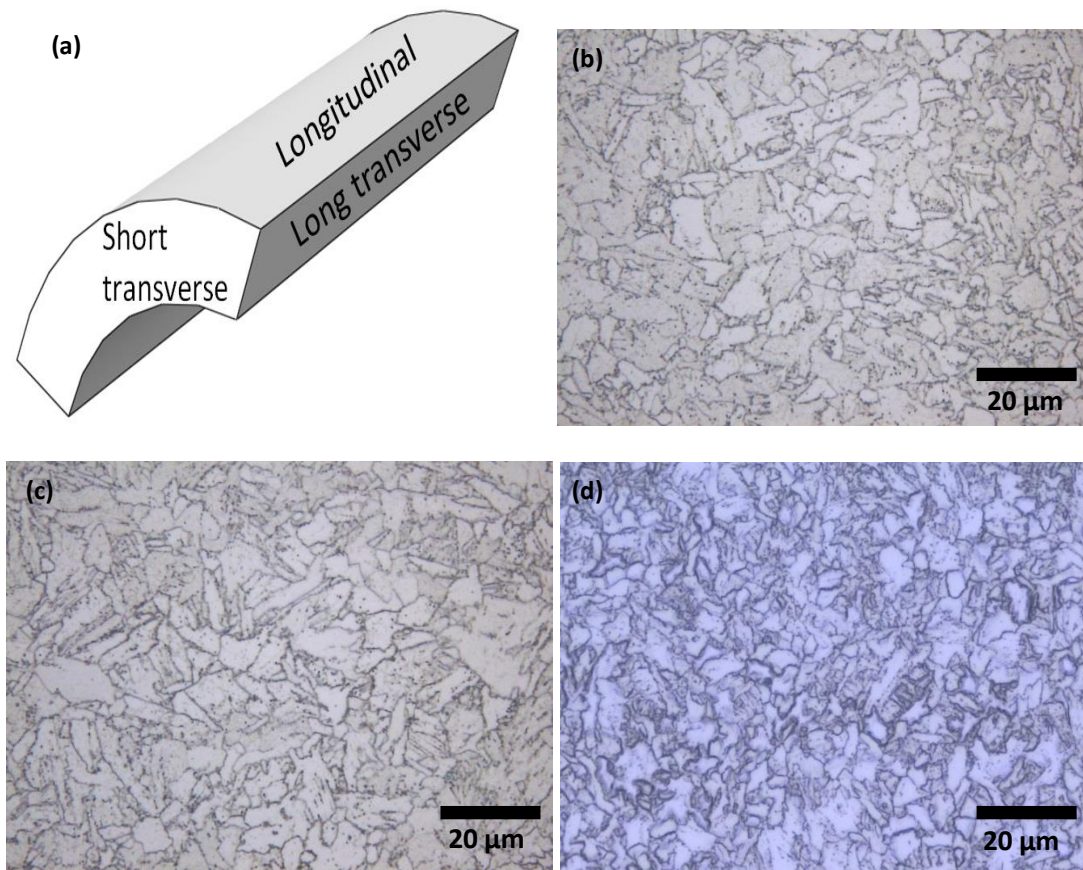


Figure 5.1 (a) Schematic of the three directions in a pipe section; and optical micrographs showing microstructure of the parent plate region of X65 linepipe steel in (b) longitudinal (c) long transverse and (d) short transverse directions.

### 5.2.2 Micro-hardness

Figure 5.2 shows the micro-hardness profile in two randomly chosen regions in material.

The average micro-hardness is  $206 \pm 8 \text{ Hv}_{1.0}$ .

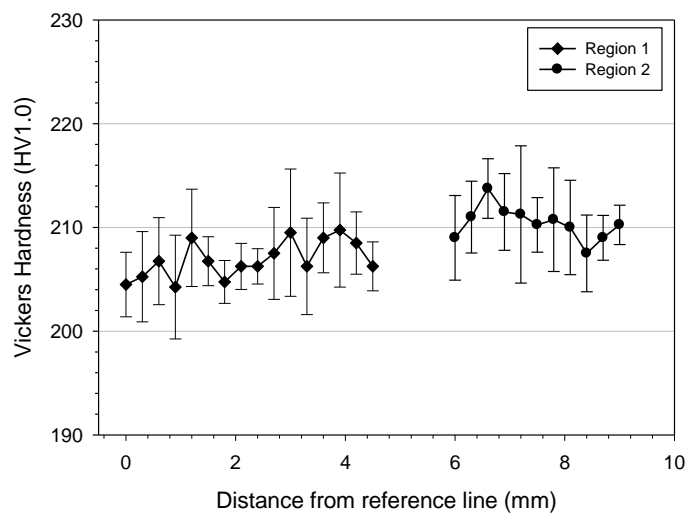


Figure 5.2 Micro-hardness measurements on X65 steel.



### 5.2.3 Open circuit potential

In the pit generation procedure and pit growth studies, an anodic potential was applied with reference to the open circuit potential (OCP) while for corrosion fatigue experiments, tests were carried out at the free corrosion potential. It was therefore important to establish this basic electrochemical characteristic of the material in the test environments. The OCP was monitored in naturally aerated 0.6 M NaCl and brine. The former was chosen as the test solution for generating pits on fatigue samples and for pit growth studies in order to overcome the salt crystallisation issue, which was associated with using the brine ( $\approx 1.48$  M NaCl). Figure 5.3 shows that the free corrosion potential shifted to more negative values but eventually stabilized with immersion time. The shift towards the negative direction can be attributed to the progressive degradation of the poor oxide film on the surface of the steel coupled with the static nature of the test, which limits the transport of oxygen (cathodic reactant in aerated solution) to the electrolyte-material interface [15, 254]. This in turn decreases the resistance to the transfer of electrons across and increases electrochemical activity at the electrolyte-material interface. The stabilized OCP value was more positive in 0.6 M NaCl ( $-600 \pm 6$  mV) than in the Forties brine ( $-667 \pm 5$  mV) indicating that the brine is more aggressive (reflecting the higher chloride concentration) and corrosion rates are more likely to be higher than in 0.6 M NaCl under the same conditions.

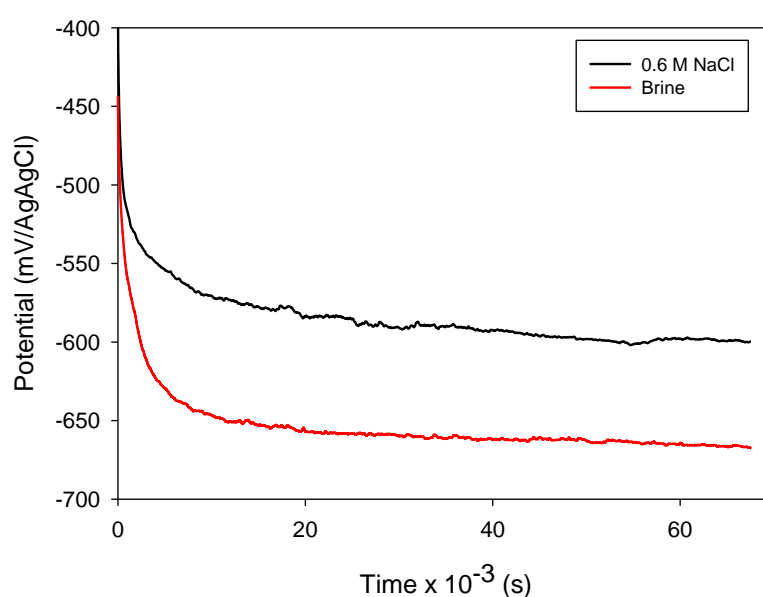


Figure 5.3 OCP measurements in naturally-aerated environments at room temperature.

### 5.3 Stress-strain properties

#### 5.3.1 Tensile stress-strain behaviour

The deformation response of the material under monotonic loading was evaluated in air at room temperature. A total of four tests were carried out to establish this. Figure 5.4 shows the representative true and engineering tensile stress-strain curve (MSSC) for the steel. The material shows discontinuous yielding phenomenon that is peculiar to bcc (body-centred cubic) materials containing carbon and nitrogen as interstitial atoms [255]. The evaluated tensile properties together with the parameters that define the hardening behaviour (assumed to be isotropic) are listed in Table 5.1. Some of these properties were used to define the elastic-plastic material model used for finite element analysis of stress and strain in Chapter 6.

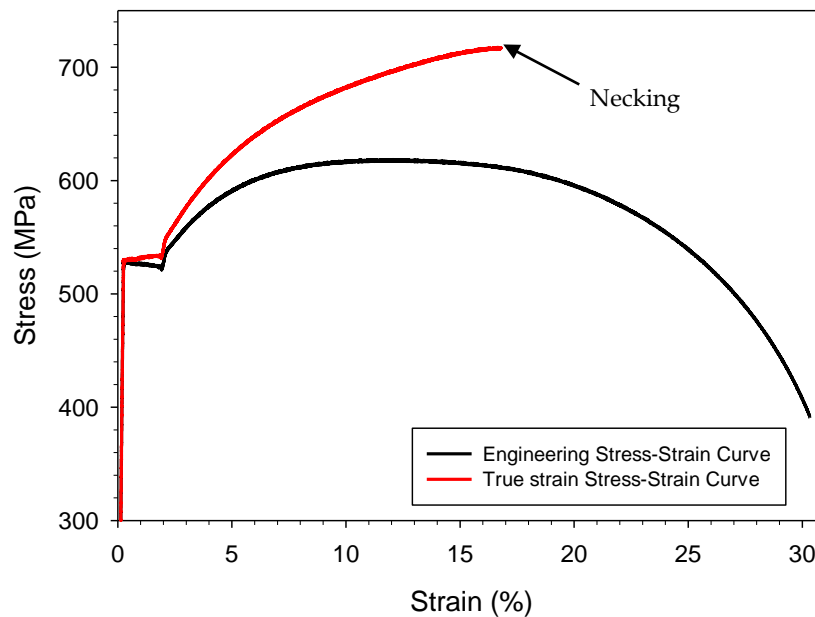


Figure 5.4 Monotonic stress-strain curve for X65 steel at room temperature.

#### 5.3.2 Cyclic stress-strain behaviour

This investigation was carried out to understand the cyclic deformation behaviour i.e. the evolution and mechanisms of damage when this material is subjected to inelastic cyclic loading. The cyclic mechanical properties were evaluated from the cyclic stress-strain curve (CSSC), which was obtained by joining the locus of the tips of the stabilized hysteresis loops that were obtained at different applied strain ranges. The plastic portion of the CSSC can be written in the form [256]

$$\frac{\Delta\sigma}{2} = K' \left( \frac{\Delta\varepsilon_p}{2} \right)^{n'} \quad 5.1$$

where  $K'$  is the cyclic hardening coefficient,  $\Delta\sigma$  is stress range,  $\Delta\varepsilon_p$  is plastic strain range and  $n'$  is the cyclic hardening exponent.

*Table 5.1 Tensile properties of X65 linepipe steel at room temperature.*

Property	Value
Elastic modulus, E (GPa)	211 ± 1
Upper yield strength, Y <sub>U</sub> (MPa)	520 ± 2
Lower yield strength, Y <sub>L</sub> (MPa)	516 ± 4
Ultimate tensile strength, UTS (MPa)	614 ± 3
Percentage elongation, %El	15.72 ± 1
Percentage reduction area, %RA	84.11 ± 5
Strength coefficient, K (MPa)	910 ± 8
Strain hardening exponent, n	0.127 ± 0.02
True fracture strength, $\sigma_f$ (MPa)	1034 ± 25
True fracture ductility, $\varepsilon_f$ (%)	91.63 ± 3

Figure 5.5 shows the CSSC with the tensile curve (MSSC) superposed on it. An intersection can be observed between the MSSC and CSSC in the hardening region. This indicates that in the range of strain that was studied, the material exhibits both hardening and softening (mixed-type) behaviour. The cyclic mechanical properties obtained from the CSSC are given in Table 5.2. The cyclic yield strength was evaluated at 0.2% offset. Similar responses have been observed for carbon steel [257-261]. In the region of the CSSC that lies below the MSSC, cyclic softening occurs while above it, cyclic hardening takes place. This shows that the cyclic behaviour of the material depends on the applied or prevailing strain level. Furthermore, the cyclic yield strength is smaller than the tensile yield strength.

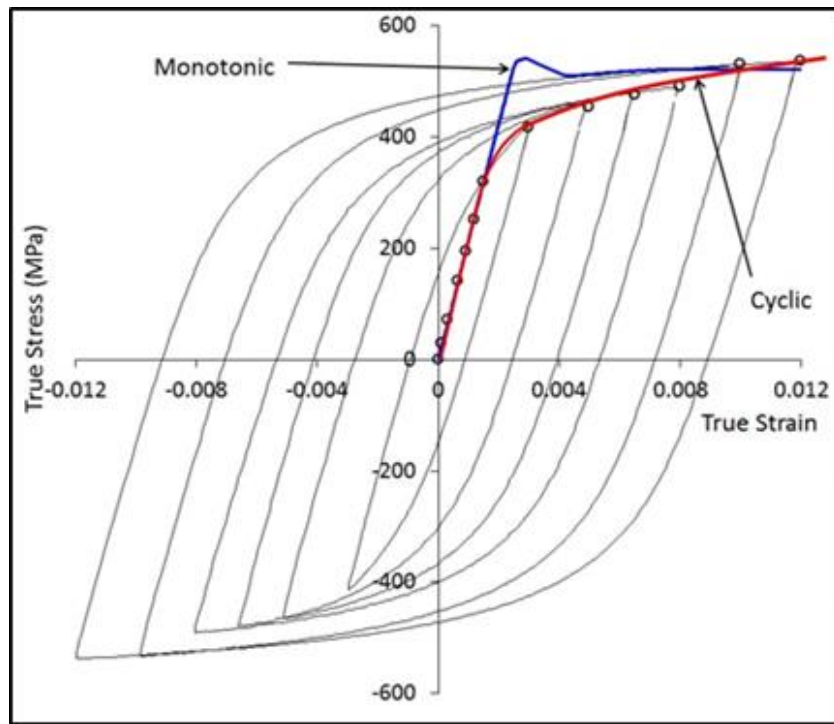


Figure 5.5 Cyclic stress-strain curve for X65 linepipe steel at room temperature.

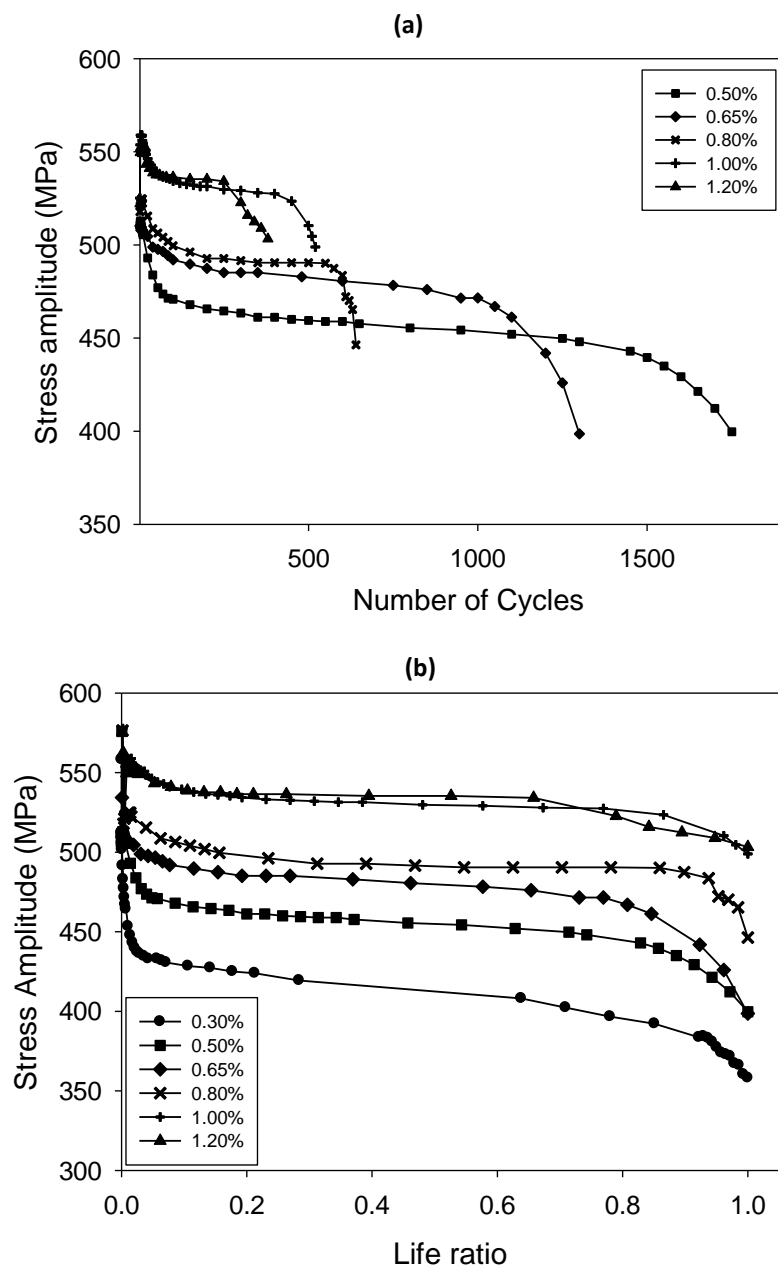
Table 5.2 Cyclic properties of X65 linepipe steel at room temperature.

Property	Value
Cyclic yield strength, $YS'$ (MPa)	$420 \pm 13$
Fatigue strength coefficient, $\sigma'_f$ (MPa)	$802 \pm 12$
Fatigue strength exponent, $b$	$-0.068 \pm 0.004$
Fatigue ductility coefficient, $\epsilon'_f$	$0.372 \pm 0.031$
Fatigue ductility exponent, $c$	$-0.584 \pm 0.022$
Cyclic strength coefficient, $K'$ (MPa)	$923 \pm 8$
Cyclic strain hardening exponent, $n'$	$0.118 \pm 0.012$
Transition life, $N_T$ (cycles)	7000

### 5.3.2.1 Evolution of stress and strain

Evolution of the cyclic stress as a function of cycles and as a function of life ratio (ratio of cycle number to the fatigue life –  $N/N_f$ ) at different strain amplitudes, is shown in Figure 5.6a and Figure 5.6b respectively. All the curves exhibit three different regions, namely: a transient region where the stress amplitude changes rapidly with the number of cycles (up to 10% of fatigue life); a cyclic saturation region where there is little or no change in stress amplitude (up to 80% of fatigue life); and a region with a rapid decrease in stress which can be correlated to the crack propagation process because of the reduction in area available to support the stress. During cyclic loading of the material, an increase or

decrease in the stress amplitude with increase in number of cycle, indicates cyclic hardening and softening respectively [262]. Figure 5.6a and Figure 5.6b appears to show only a general decrease in stress amplitude with number of cycles at all strain amplitudes. However, observations made in the first few cycles (Figure 5.6c) show that at relatively high strain amplitudes ( $> 0.8\%$ ), the stress amplitude increases before progressively decreasing. At total strain amplitudes between  $0.3\%$  and  $0.65\%$ , only cyclic softening can be observed since the stress amplitude decreased continuously starting from the first cycle. In contrast, at  $0.8\%$ ,  $1\%$  and  $1.2\%$ , cyclic softening was preceded by an initial period of cyclic hardening.



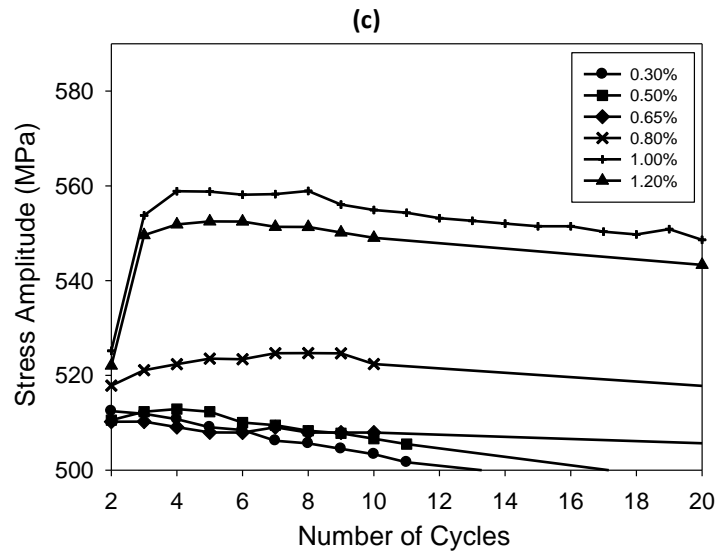


Figure 5.6 Evolution of the stress amplitude (a) with number of cycles; (b) with life ratio; (c) in the first 20 cycles for different values of strain amplitudes.

This result is consistent with Figure 5.5 and shows that the material exhibits a cyclic deformation behaviour (hardening and softening) that is dependent on strain amplitude.

Figure 5.7 shows that, in the strain ranges tested, the plastic strain amplitude increases with increase in number of cycles and with total strain. In terms of plastic strain amplitude, a decrease with number of cycles indicates cyclic hardening while an increase indicates softening behaviour [255, 262]. From studies on the cyclic deformation behaviour of steels, it has been shown that cyclic plastic strain is accompanied by evolution and modification of the internal structure of the material [260, 261, 263]. The internal substructure is modified through creation and rearrangement of dislocation structures, which may involve changes in dislocation density and formation of microstructures with different substructures depending on level of loading. These ultimately lead to the observed macroscopic stress-strain response behaviour i.e. cyclic hardening and cyclic softening. However, the accompanying changes are limited to the initial period of cycling. Beyond this initial period i.e. in the stabilised region, and for the majority of the fatigue life, persistent slip bands (PSBs), in which the cyclic plastic strain is concentrated and redistributed, are formed. As a result of this redistribution, the cyclic stress-strain response is stabilized and the internal structure of the PSBs is modified [264]. The PSBs lead to the formation of extrusions and intrusions from which cracks are initiated [255, 264].

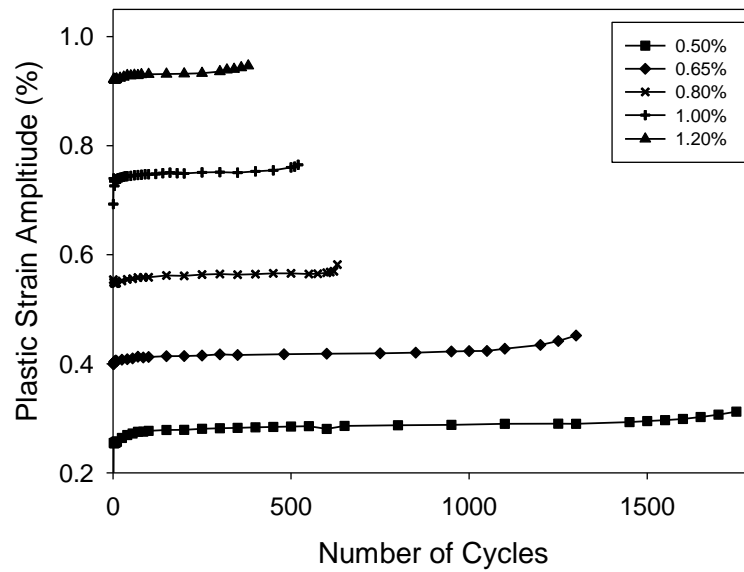


Figure 5.7 Evolution of plastic strain amplitude with number of cycles.

Figure 5.8 presents an example of the surface of a specimen tested at 1% strain amplitude; showing evidence of multiple crack initiation sites, which can be correlated with the relatively large level of plasticity ( $\epsilon_p \approx 0.75\%$ ) occurring at this strain level (see Figure 5.7). It can also be observed that one of the cracks appears to be dominant compared to the others. The location and orientation of the cracks (parallel to loading direction) suggest that crack coalescence is a likely crack propagation mechanism.

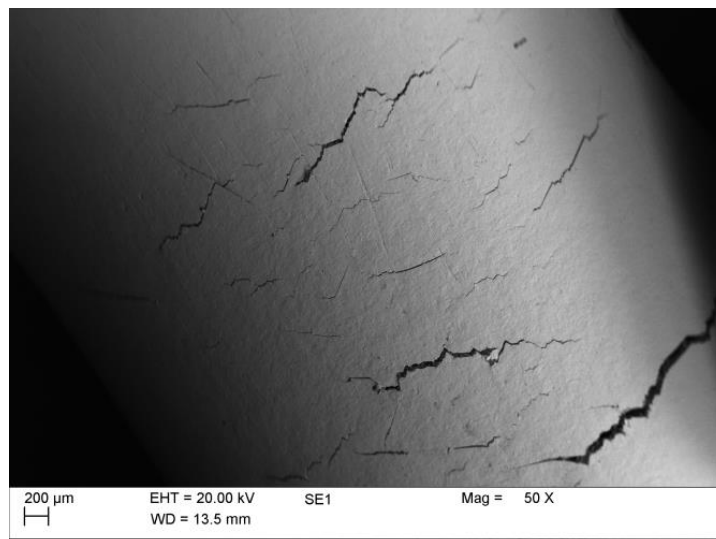


Figure 5.8 Typical surface of a specimen after testing showing dominant crack and several other smaller cracks. (Total strain amplitude = 1%; Plastic strain amplitude = 0.75%).

### 5.3.2.2 Stress-life and strain-life relationships

The results for the low cycle fatigue (LCF) life, notably stress amplitude and the plastic strain amplitude at half-life, are given in Table 5.3. The table illustrates that an increase in total strain amplitude resulted in increases in stress amplitude and plastic strain amplitude and a corresponding decrease in fatigue life. The higher plastic strain magnitudes observed as the total strain increases suggest that an increase in plasticity resulted in shorter crack initiation lifetimes; hence the observed shorter LCF lives. The parameters for the Basquin [42] and Coffin-Manson [43, 44] relationships, which are both combined into Equations 5.2, were also obtained for this material by separating the total strain into its elastic and plastic components, as shown in Figure 5.9.

$$\frac{\Delta \varepsilon}{2} = \frac{\sigma'_f}{E} (2N_f)^b + \varepsilon'_f (2N_f)^c \quad 5.2$$

where  $\sigma'_f$  is the fatigue strength coefficient,  $\varepsilon'_f$  fatigue ductility coefficient,  $N_f$  is number of cycles to failure,  $b$  is fatigue strength exponent and  $c$  is fatigue ductility exponent. These parameters are also given in Table 5.2. It should be noted that the elastic strain values have been multiplied by the elastic modulus ( $E$ ) to obtain values of stress.

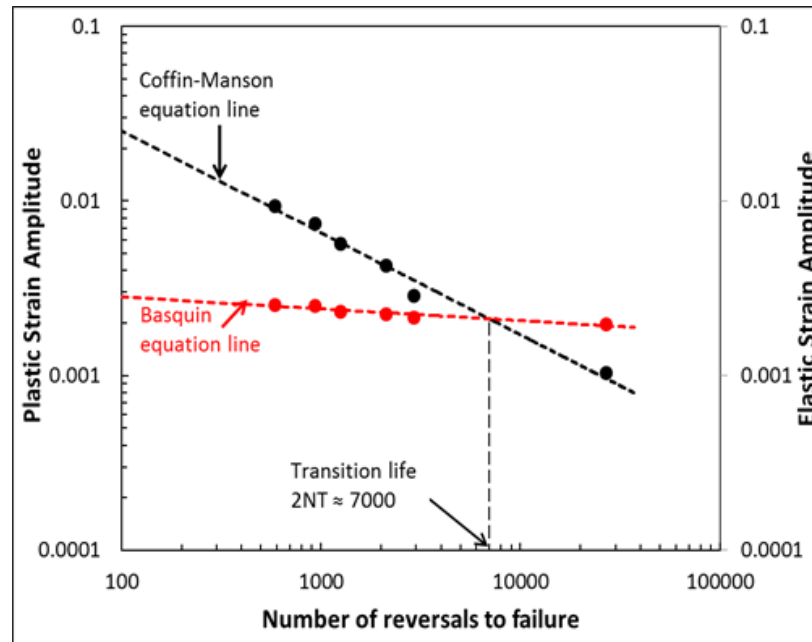


Figure 5.9 Fatigue strength life and fatigue ductility life curves for X65 linepipe steel.



**Table 5.3 Fatigue results for X65 linepipe steel under symmetric strain cycling.**

Strain amplitude (%)	0.30	0.50	0.65	0.80	1.00	1.20
Life (cycles)	13421	1466	1061	625	467	294
Stress amplitude (MPa)	416.4	453.2	475.8	491.1	531.3	536.3
Elastic strain amplitude (%)	0.197	0.215	0.226	0.233	0.252	0.254
Plastic strain amplitude (%)	0.103	0.287	0.428	0.568	0.745	0.938

## 5.4 Pit growth behaviour

### 5.4.1 Pit growth under no-flow conditions

Pit propagation kinetics (rate of anodic dissolution) was simulated by potentiostatic polarization of samples in 0.6 M NaCl for different durations of time in an unstressed condition. Triplicate tests were carried out. The maximum pit depth and pit width in a test is the average of measurements obtained from four different cross-sectional profiles of a pit. The results obtained after characterisation of the pits are summarised in Table 5.4. Theoretical values of pit depth were evaluated from the measured experimental volume using Faraday's relationship (Equation 3.4). Figure 5.10 presents plots of experimental and theoretical mean values of maximum pit depth versus time. Although the theoretical values show an overestimation of the experimental pit depths, the correlation between both is fairly good. Figure 5.10 shows that the rate of pit growth decreased with time but there is a net increase in depth. Because the tests are with a non-flowing solution, the decrease in pit growth rate is attributed to a diffusion-control mechanism whereby corrosion products are not able to diffuse away from within the pit, thus limiting the mass transport of electrochemical species across the metal-electrolyte interface [5, 140, 265]. In addition, this condition also means that the cathodic species (dissolved oxygen) is also not easily transported to the reaction site. The coupling of these processes effectively reduces the rate of anodic dissolution and consequently the pit growth rate. The aspect ratio (depth : diameter) is generally used to specify the geometry of a corrosion pit and is also indicative of the severity of a corrosion pit. This has implications for strain localisation and crack nucleation behaviour. The evolution of the aspect ratio of the pits, with time, appears to follow the same trend as pit depth because the experimental conditions confine the diameter of the pit to that of the width of the microcapillary.

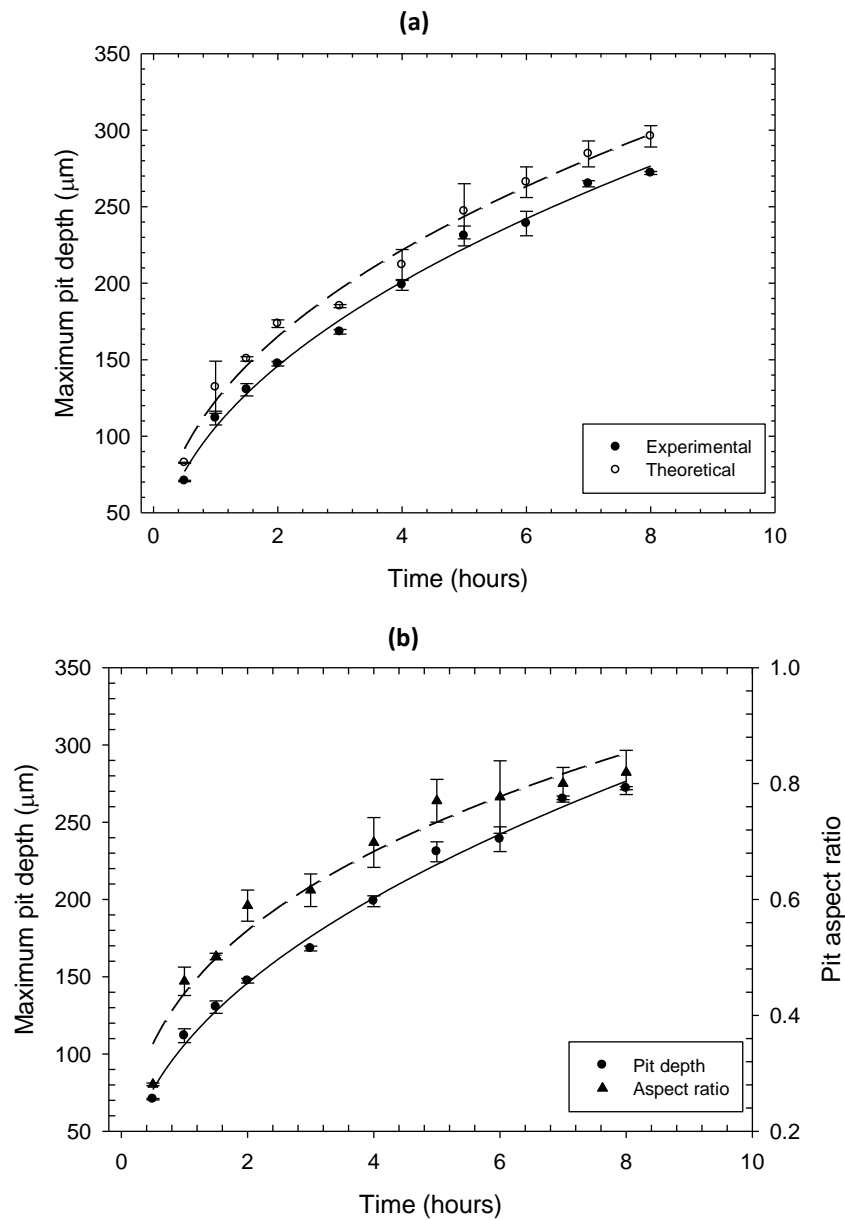


Figure 5.10 Maximum pit depth (a) and pit aspect ratio (b) versus time under static conditions.

Table 5.4 Mean value of pit characteristics obtained at different polarization times.

Time (s)	Pit depth ( $\mu\text{m}$ )	Aspect ratio	Pit volume ( $\mu\text{m}^3$ )
1800	71.5	0.281	11074275
3600	112.5	0.459	17753905
5400	133	0.501	21272460
7200	153.5	0.589	25204056
10800	169.5	0.616	33748293
14400	202.5	0.698	46848960
18000	232.5	0.770	51987840
21600	240	0.777	57473818
25200	264	0.800	70647164
28800	273	0.819	78252603

### 5.4.2 Pit growth behaviour under cyclic stress

The influence of cyclic stress on pit growth behaviour was investigated by carrying out tests with and without applied stress. Figure 5.11 shows the influence of applied cyclic stress on pit depth. For the same time interval, pit depths are larger under applied stress compared to when no stress was applied. This observation is consistent with results from previous studies [117, 124, 127, 250, 251] where relatively larger pit sizes were found with increasing applied stress. The effect of applied stress on pit growth is generally attributed to stress-assisted dissolution through increased local electrochemical activity [266, 267]. The strain localisation effect of the pit increases local activity of dislocations to which higher energy state atoms are associated. The less activation energy required to remove these atoms results in preferential electrochemical attack, thereby promoting dissolution of the steel matrix around the pit [268]. It was also observed from Figure 5.11 that the difference between the two sets of data tends to increase with time. This can also be associated with the mechanical-electrochemical effect of strain localisation on localised corrosion. Pit size becomes larger with time and the instantaneous magnitude of strain due to strain localisation also increases. This is expected to further increase dissolution rate and pit depth over time.

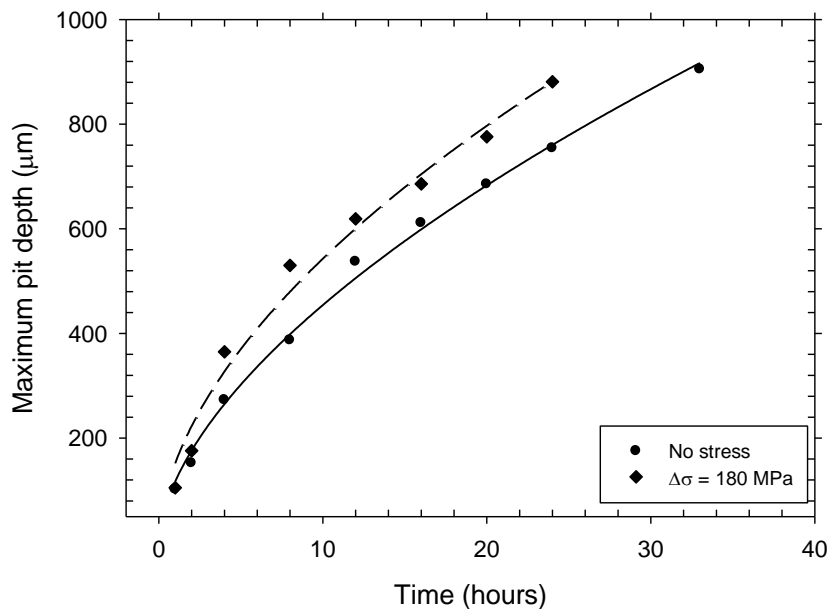
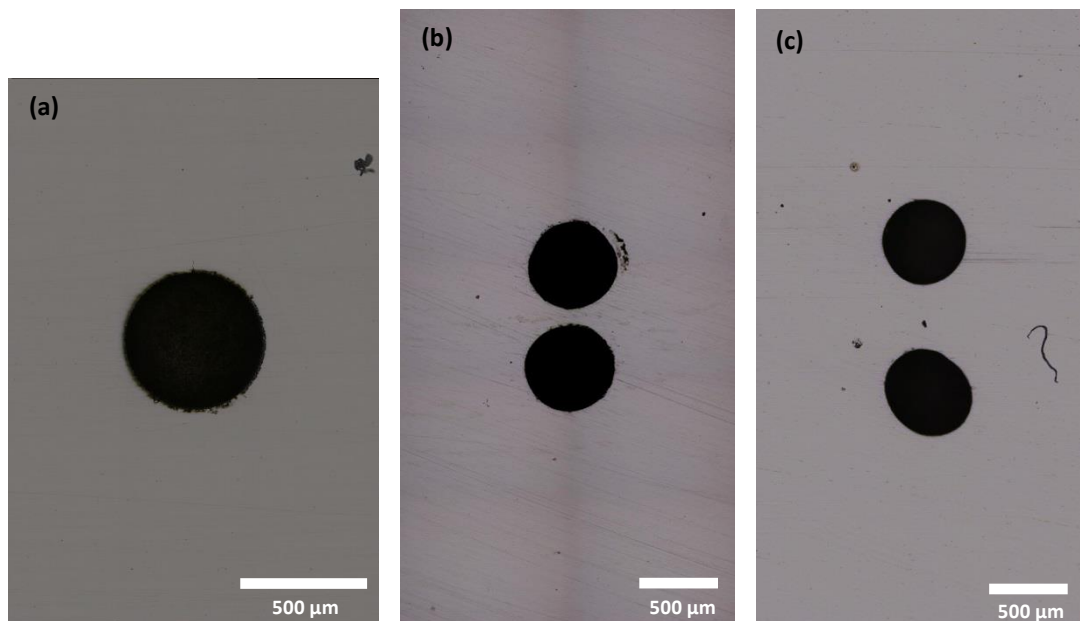


Figure 5.11 Dependence of pit growth rate on cyclic stress.

### 5.5 Fatigue and corrosion fatigue behaviour

In the present study, fatigue behaviour of plain and pre-pitted specimens was investigated in air and an aggressive environment. Specifically, tests were carried out to understand the influence of stress level, pit size (pit size subsequently refers to pit aspect ratio and pit depth) and operating environment on the behaviour of cracks emanating from corrosion pits. Plain (un-pitted) specimens were tested in air at stress ranges between 432 and 495 MPa to establish the baseline fatigue behaviour in air for evaluating the effects of pitting in air (mechanical) and corrosive environment (mechanical and corrosion) on fatigue behaviour. For single-pitted specimens tested in air and corrosion fatigue, three pit depths of 140  $\mu\text{m}$  ( $AR_p = 0.52$ ), 200  $\mu\text{m}$  ( $AR_p = 0.68$ ), and 270  $\mu\text{m}$  ( $AR_p = 0.82$ ) were chosen while stress range was varied between 350 and 450 MPa. In testing of double-pitted specimens, two stress ranges (427.5 and 405 MPa) and two pit depths: 200  $\mu\text{m}$  ( $AR_p = 0.68$ ), and 270  $\mu\text{m}$  ( $AR_p = 0.82$ ) were chosen while the centre-to-centre distance between the double pits (both having similar aspect ratios) varied between 0.68 and 1.94 mm. Figure 5.12 shows examples of single and double pits with different aspect ratios and separation distances. In some cases, when crack initiation was observed and/or during crack propagation, test specimens were unmounted so that optical and SEM images of the cracks could be obtained.



**Figure 5.12** Optical images showing single pit ( $d_p = 202 \mu\text{m}$ ,  $AR_p = 0.67$ ) in (a) and double pits in (b&c) with similar aspect ratios but different distances separating them: (b)  $d_{p,avg} = 197 \mu\text{m}$ ,  $AR_{p,avg} = 0.69$ ,  $s_{ee} = 105 \mu\text{m}$ ,  $s_{cc} = 693 \mu\text{m}$  (c)  $d_{p,avg} = 199 \mu\text{m}$ ,  $AR_{p,avg} = 0.68$ ,  $s_{ee} = 479 \mu\text{m}$ ,  $s_{cc} = 1066 \mu\text{m}$ .

### 5.5.1 Crack initiation behaviour

In order to study the initiation behaviour of cracks emanating from pits, crack initiation sites and crack initiation lives were analysed and evaluated as a function of pit size, stress level and test environment in single and double-pitted specimens. The crack initiation site is the region around the pit where a crack was found while the crack initiation life is the number of cycles at which a crack was first observed. Because cracking was monitored at intervals, it was impossible to determine the exact cycle number at which a crack initiated during the fatigue life. Hence, for all experiments, the crack initiation life and the corresponding crack length at initiation were defined as:

$$N_i = \frac{N_2 - N_1}{2} \quad 5.3$$

$$a_i = a_2 \quad 5.4$$

where  $N_i$  is the crack initiation life,  $N_2$  is number of cycles where a crack was first observed,  $N_1$  is the number of cycles at the last interval (before crack initiation),  $a_i$  is crack length at initiation and  $a_2$  is the crack length corresponding to  $N_2$ .

#### 5.5.1.1 Plain specimens

Where there was cracking on plain (un-pitted) specimens, cracks initiated at either and/or the corners or the edges of the fatigue specimen (within the dog bone gauge section). Figure 5.13 shows an example of a crack that initiated from the edge of a specimen. In samples that did not fail, no evidence of non-propagating cracks was found. Given that the edges of the specimens were longitudinally polished and rounded, to eliminate any premature crack nucleation as a result of artefact surface defects produced during machining, it is thought that some of the cracks might also have initiated from very small mechanical and microstructural imperfections. Further fractographic analyses will be required to confirm this (discussed later).

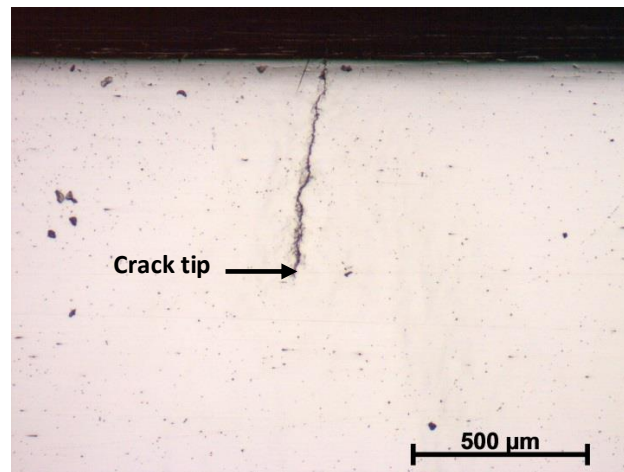


*Figure 5.13 Typical crack initiation from edge of a plain specimen in air ( $\Delta\sigma = 468$  MPa, crack length = 668  $\mu\text{m}$ ,  $N/N_f = 0.84$ ;  $N_f = 8.27 \times 10^5$ ).*

#### 5.5.1.2 Pre-pitted specimens

In all the specimens tested in air, fatigue cracks generally initiated predominantly from the pit mouth irrespective of stress level and pit size (single pits) and separation distance (in the case of double pits). The cracks observed on the majority of the double-pitted specimens emanated from the pit mouth in the region separating the two adjacent pits. Examples of crack initiation from the pit mouth in single pits in air are shown in Figures 5.14 and 5.15 while Figures 5.16 shows that of double-pits. Because of the size of the cracks relative to the pits, only the regions around the pit where cracks initiated are shown. The crack tips are indicated with arrows. Since the tests were conducted in air, these results suggest that the conditions for crack nucleation are more favourable at the pit mouth than at the pit bottom. Therefore, localisation of the crack initiation site to the pit mouth can only be attributed to the mechanical effects of pit shape and size. From previous studies [9, 105, 121, 202, 269], mechanics-based explanations have been given for this phenomenon. On the one hand, local yielding under loading conditions may result in redistribution of stresses around pits thereby leading to localisation of plastic strains at the pit mouth [121, 202]. On the other hand, if pits are considered to be equivalent to semi-elliptical cracks, the associated stress intensity factor, which varies along the periphery of the crack, is maximum at the pit mouth and minimum at the pit bottom [9, 269]. Both of these conditions, coupled with the minimum constraint existing at the surface of the specimen, where the stress field changes from plain strain in the interior to plane stress at the surface, facilitates crack nucleation near the pit mouth.

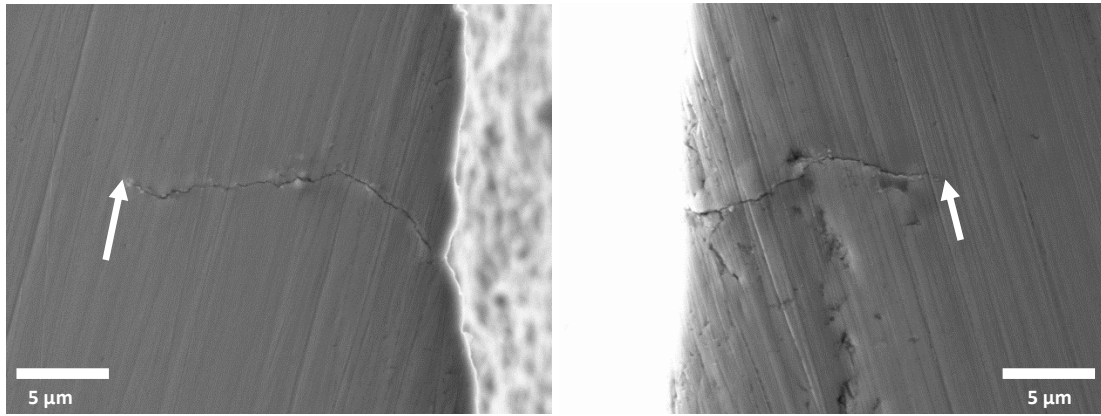


**Figure 5.14** SEM image showing initiation of short cracks at the mouth of a pit in air. ( $\Delta\sigma = 427.5$  MPa;  $d_p = 266$   $\mu\text{m}$ ;  $AR_p = 0.82$ ;  $N_i = 0.81N_f$ ;  $N_f = 1.03 \times 10^5$ ).

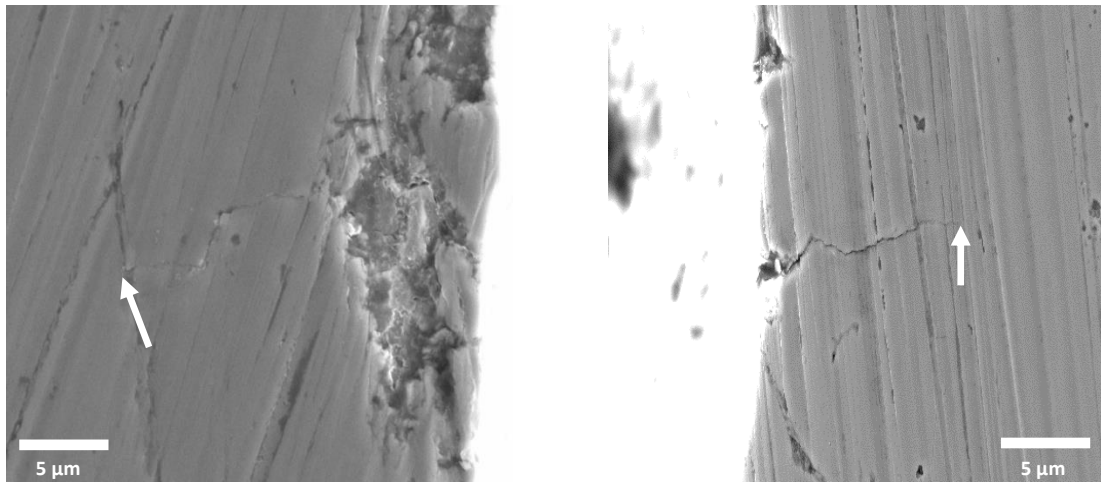


**Figure 5.15** SEM image showing initiation of short cracks at the mouth of a pit in air. ( $\Delta\sigma = 450$  MPa;  $d_p = 142$   $\mu\text{m}$ ;  $AR_p = 0.52$ ;  $N_i = 0.52N_f$ ;  $N_f = 7.51 \times 10^5$ ).

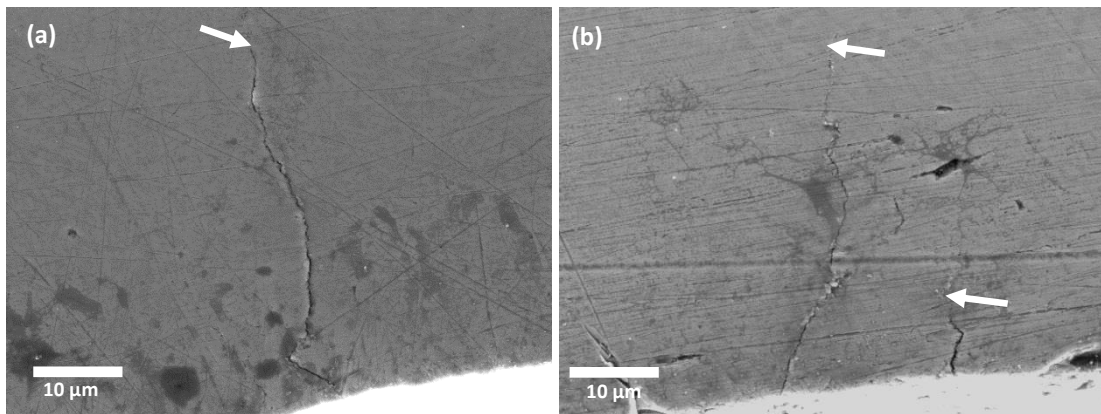


**Figure 5.16** SEM images showing initiation of short cracks from the mouth of double pits in air. (a)  $\Delta\sigma = 427.5$  MPa,  $d_p = 265$   $\mu\text{m}$ ,  $AR = 0.79$ ,  $s_{ee} = 398$   $\mu\text{m}$ ,  $s_{cc} = 1063$   $\mu\text{m}$ ,  $N_i = 0.76N_f$ ,  $N_f = 7.64 \times 10^5$  cycles (b)  $\Delta\sigma = 427.5$ ,  $d_p = 268$   $\mu\text{m}$ ,  $AR_p = 0.83$ ,  $s_{ee} = 207$   $\mu\text{m}$ ,  $s_{cc} = 857$   $\mu\text{m}$ ,  $N_i = 0.37N_f$ ,  $N_f = 5.06 \times 10^5$  cycles.

In all the double-pitted specimens tested in air, the pit mouth was also found to be the preferred site for crack initiation irrespective of stress level, pit size and separation

distance. Moreover, the cracks emanated in the region separating the two pits i.e. the region defined by the edge-to-edge distance,  $s_{ee}$  (see Figure 3.8 for definition of  $s_{ee}$ ). This suggests that the condition for crack initiation is more favourable at the pit mouth and in the region separating the two pits. It is thought that the proximity of any two pits will result in an interaction between their stress and/or strain fields. Consequently, strain levels may increase in this region and thereby result in a higher tendency for crack nucleation. Further FE analyses carried out to correlate these observations with interaction between strain distribution around the pits are reported in Chapter 6.

Due to the strain localisation around the pits, it is expected that cracks should initiate at both sides of a pit after a similar number of cycles. In general, this was not found to be true. In some of the single-pitted specimens, the crack initiation lives for both cracks emanating from adjacent sides of the pit differed in 60% of the tests, but not significantly. Because this difference could not be correlated with pit size and stress range, it is thought that this behaviour may be due to stochastic nature of crack initiation. Another possibility is the non-uniform localisation of strain that may have resulted from the real shape of the pit, which likely concentrated strain to one side of the pit more than the other. Similar observations were made on double-pitted specimens where the majority of the cracks initiated at only one of the two pits, except in few cases where cracks initiated at both pits together. Furthermore, in this case, no correlation was found with pit size, stress level and separation distance. In addition to the explanation given for the single pit samples, it is thought that the differences in strain distribution due to variation in the true pit sizes may be a contributing factor for double pits. It should be noted that only mean values of the sizes of the double pits are reported in the results whereas, in reality, the depths of the pits may vary by up to  $\pm 5\%$ . Hence, it is expected that the higher strain localization associated with relatively deeper pits might favour cracking. However, further analyses of the experimental data showed that majority of the crack-initiating pits were not always the pits with a relatively greater depth or aspect ratio.

Observations from previous studies have shown that cracks can initiate from the mouth [9, 121] as well as the pit bottom [189, 195]. The present results appear to show that cracks only initiate from the pit mouth. However, no conclusion can be made at this point because the replica method used in this study only permitted detection of surface cracks. Therefore it was important to ascertain whether cracks also initiated from other regions



other than the pit mouth. For corrosion fatigue tests, this was not a problem because the crack observation technique used was capable of detecting cracks everywhere around the pit. For the tests carried out in air, crack initiation from the pit bottom was assessed by fractography. The results from fracture surface analysis are reported in a Section 5.6.

In the tests carried out on single-pitted specimens in the Forties brine solution, cracks were found to initiate from both the mouth and bottom of pits. In previous work on HSLA steels with properties similar to the steel used in this work, cracks were found to initiate from the pit bottom [122, 270] while in other steel-environment systems, cracks initiated from the pit mouth [9, 105, 121, 269] as well as the pit bottom [169, 189, 269]. Figure 5.17 shows crack initiation from the different locations, notably; only the pit mouth (Figure 5.17a), the pit bottom (Figure 5.17b) or both mouth and pit bottom (Figure 5.17c). Table 5.5 summarises observations of crack nucleation sites with stress and pit size. Although no apparent correlation was found with pit size and stress level, the results generally suggest that crack initiation at the pit bottom tends to occur at relatively lower stresses and smaller pit size respectively. The only case where cracks initiated at the pit mouth occurred in the pit with depth of 270  $\mu\text{m}$  ( $AR_p = 0.82$ ) tested at the highest applied stress range (450 MPa). Comparison with the corresponding test carried out in air, suggests that crack initiation at the pit mouth in the brine solution might be attributed to the dominance of the mechanical effect of strain localisation at high stresses at the pit mouth.

*Table 5.5 Crack initiation characteristics from pits tested in brine solution.*

Stress range (MPa)	$AR_p = 0.52$	$AR_p = 0.68$	$AR_p = 0.82$
360	No data	No data	Pit bottom
405	Pit bottom	Pit bottom	Pit mouth and pit bottom
427.5	Pit bottom	Pit mouth and pit bottom	Pit mouth and pit bottom
450	Pit mouth and pit bottom	Pit mouth and pit bottom	Pit mouth

At the crack initiation stage, multiple cracks were often observed at the pit bottom and sometimes at the pit mouth (Figure 5.17b and 5.17c). As cycling continued, more cracks initiated at the pit bottom some of which coalesced with each other and also with the cracks that initiated at the pit mouth thus forming bigger cracks. It was interesting to see

that all the multiple cracks that initiated at the pit bottom are always aligned perpendicular to the loading direction (Figures 5.17b, 5.17c and 5.18a).

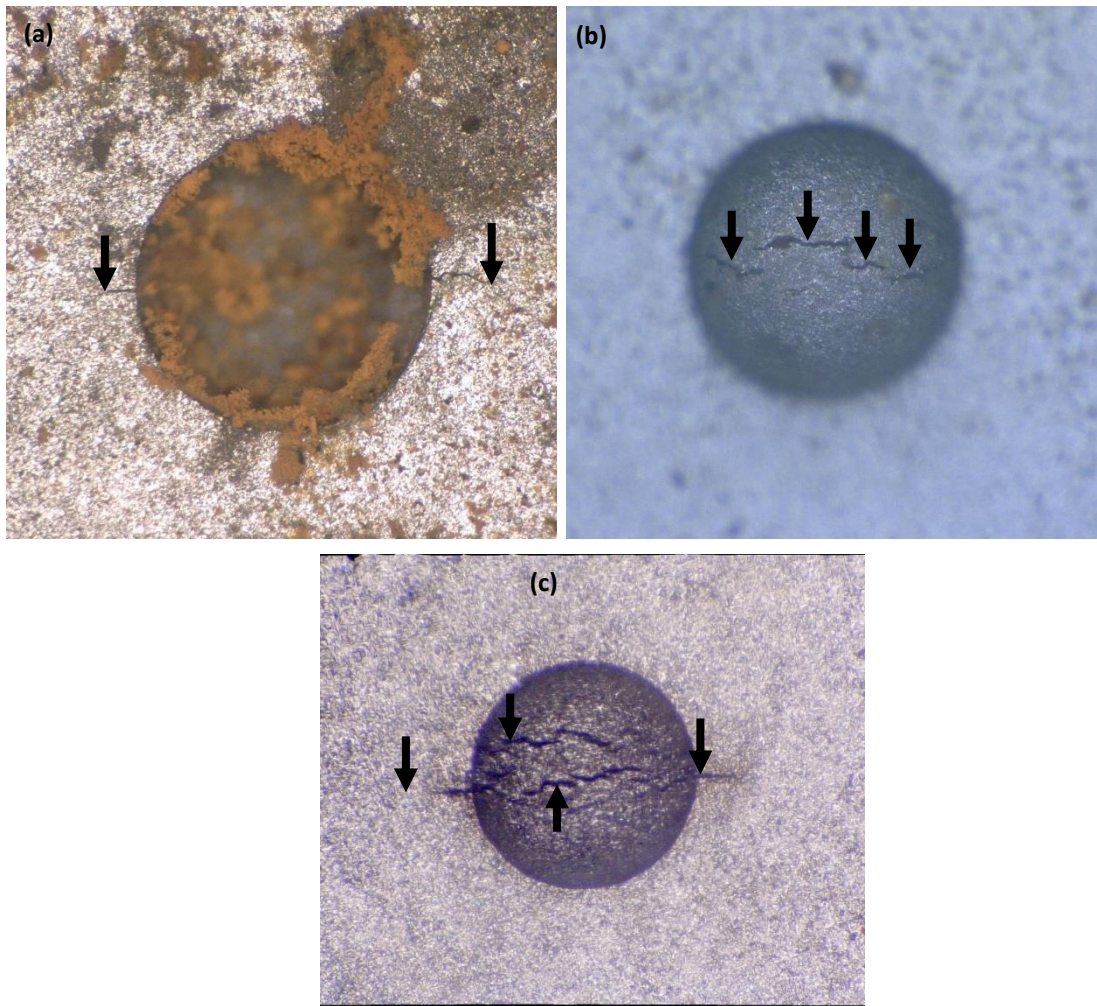


**Figure 5.17** Typical corrosion fatigue crack initiation behaviour from (a) pit mouth [ $\Delta\sigma = 450$  MPa;  $d_p = 271\ \mu\text{m}$ ;  $N_i = 0.66N_f$ ;  $N_f = 1.9036 \times 10^5$ ], (b) pit bottom [ $\Delta\sigma = 405$  MPa;  $d_p = 141\ \mu\text{m}$ ;  $N_i = 0.779N_f$ ;  $N_f = 4.17 \times 10^5$ ], and (c) pit mouth and pit bottom [ $\Delta\sigma = 427.5$  MPa;  $d_p = 202\ \mu\text{m}$ ;  $N_i = 0.813N_f$ ;  $N_f = 3.75 \times 10^5$ ]. Loading direction is from top to bottom.

To gain more insight, the test in Figure 5.18a was aborted and the specimen was cleaned, dried and examined on the SEM. Figure 5.18b shows an SEM image of the pit (with multiple crack initiation sites at the pit mouth and bottom). The main observation is that not all the cracks, which appear at the bottom of the pit, have extended into the specimen. For the cracks that have extended into the specimens, it appears that only those that are aligned with the cracks at the pit mouth, and perpendicular to the loading direction, became damaging i.e. coalesced with other cracks to form a larger crack. These results, which show crack initiation at the pit bottom at stress levels where no cracks were

observed at the pit bottom in air, suggest that the conditions for crack initiation were modified in the aggressive environment. One possible mechanism is that of strain-assisted dissolution of slip steps (combined with film rupture) resulting from the strain localization effect of the pit. Under cyclic loading, slip bands may be induced around the pit due to localised deformation [270]. The higher energy state of metal atoms associated with dislocations reduces the activation energy is required to remove the atoms from the material [268, 271]. Consequently, the aggressive environment will lead to preferential dissolution of the slip steps and promote crack initiation. In addition, electrochemical changes within the pit, such as changes in local solution composition, pH and electrochemical potential may also play an important role in the crack initiation behaviour. Further discussions on these factors in the context of the observations made in this study will be presented in Chapter 8.

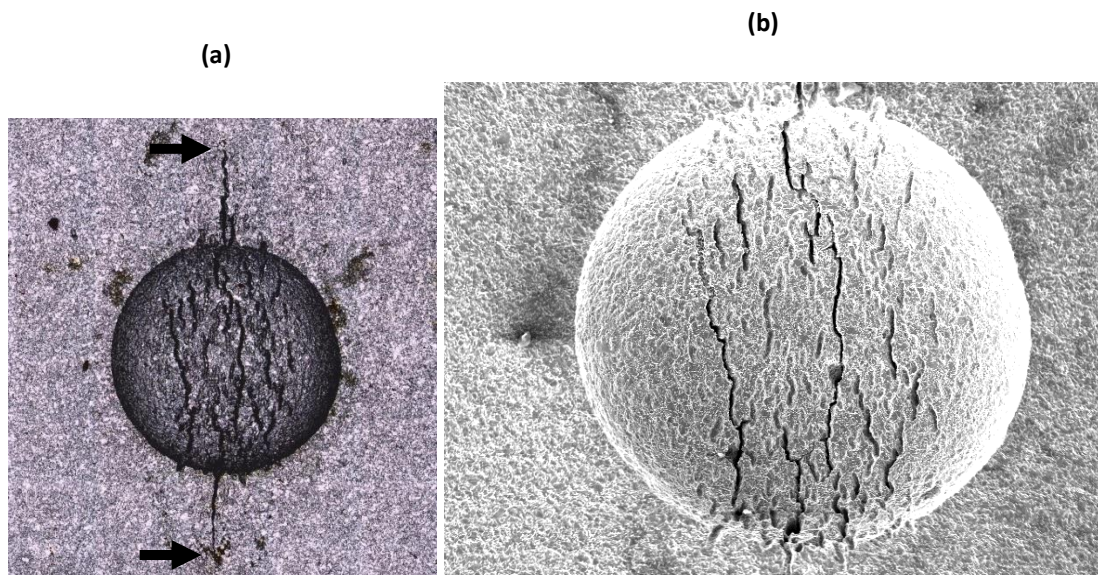


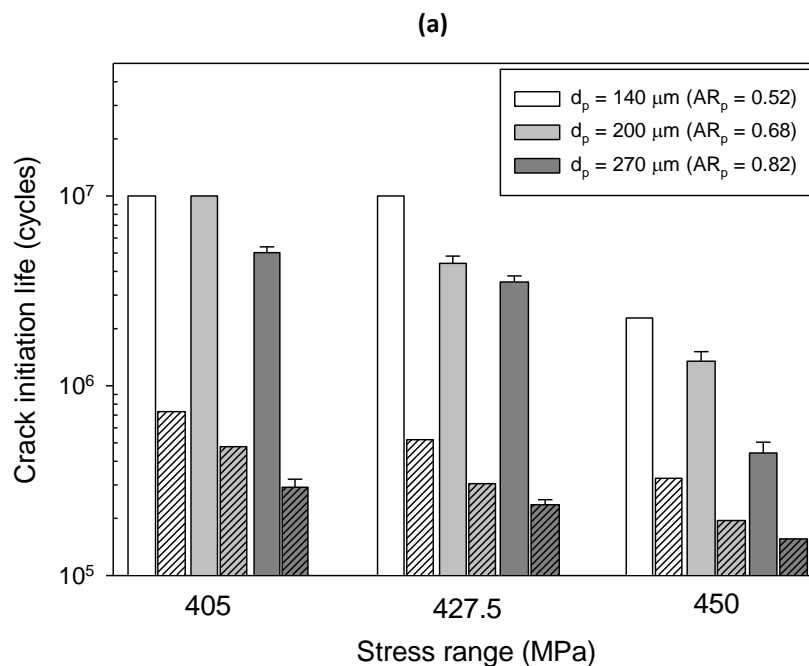
*Figure 5.18 Typical corrosion fatigue crack initiation behaviour from pits (a) optical and (b) SEM images. ( $\Delta\sigma = 427.5$  MPa;  $d_p = 266$   $\mu\text{m}$ ;  $AR_p = 0.82$ ;  $N_i = 0.754N_f$ ;  $N_f = 3.13 \times 10^5$ ). Loading direction is from left to right.*

### 5.5.1.3 Crack initiation lifetime

#### Single pits – fatigue tested in air and brine solution

Figure 5.19a shows the influence of pit size and stress level on crack initiation lifetimes in air and brine solution. For a given stress level and pit size, the crack initiation life ( $N_i$ ) decreased with increase in pit size and increase in stress level respectively. These trends were observed in both air and brine environment, thus showing that the overall influence

of pit size and stress level on crack initiation behaviour from pits in this material appears to be test environment independent (at these stress levels). This observation is consistent with reports from previous studies on steel-brine systems [16, 122] and can be attributed to the mechanical effects of pit size and applied stress on strain localisation at pit sites. An increase in the pit size and stress level increases the magnitude of the local strain around a pit and consequently result in greater susceptibility to early crack nucleation [1, 270]. Figure 5.19a also shows a significant reduction in the crack initiation life in the aggressive environment, compared to air, at all stress levels. The interaction between localised strain and the environment is expected to further increase susceptibility to cracking through strain-enhanced dissolution of slip steps [271-273]. Therefore, it easier for cracks to initiate in a shorter time in the presence of the environment. Comparison between the crack initiation life plotted as a fraction of fatigue life in air and brine solution is shown in Figure 5.19b. The notable observation here is that the fractions of lifetime taken for crack nucleation are generally higher than 60%. This indicates that the fatigue behaviour of the steel when pits are present depends more on initiation than propagation of cracks. However, the extent of this dependency is relatively greater in air (70-100%) than in corrosion fatigue (65-85%). Note that 100% fraction of lifetime represents a sample on which no crack was found or did not fail after  $10^7$  cycles.



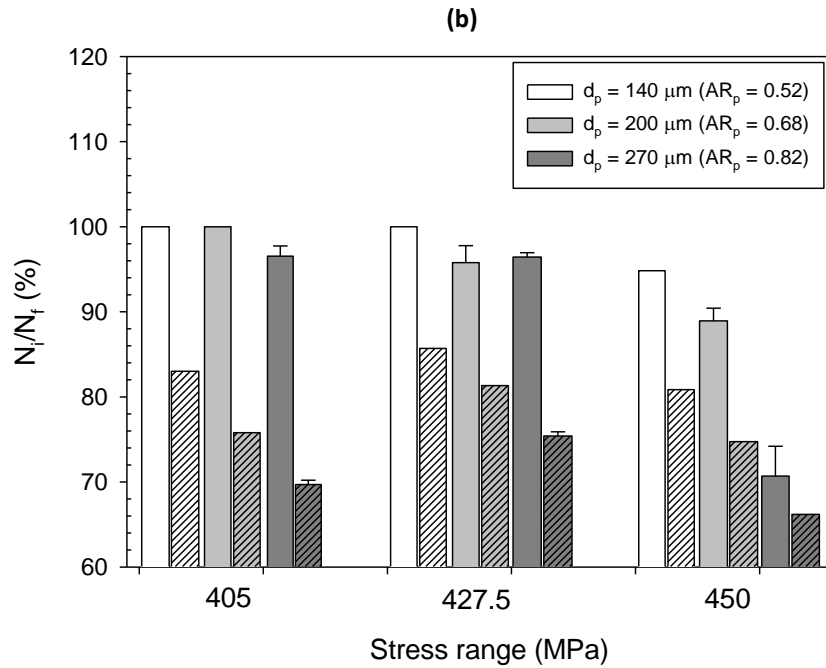


**Figure 5.19** Comparison between crack initiation lives in air and brine solution for different stress levels and pit sizes as function of (a) number of cycles and (b) fraction of total lifetime. [Plain bars = Air; Hatched pattern bars = Corrosion fatigue].

### Double pits – fatigue tested in air

The relationship between crack initiation life and centre-to-centre distance (subsequently referred to as separation distance) between double pits, for different pit sizes and stress levels, is shown in Figure 5.20a. As a reference, corresponding values obtained for single pits are also shown as horizontal lines on the figure. For all the pit sizes and stress levels studied, a dependency was found between crack initiation lifetime and separation distance between pits, up to a pit-to-pit separation distance of about 1400  $\mu\text{m}$ . Below this separation distance,  $N_i$  generally decreased with decrease in separation distance. This indicates that the closer the pits are to each other, the shorter the crack initiation life. Furthermore, at the same separation distance, stress and pit size influenced crack initiation life. At a given stress level,  $N_i$  was relatively lower for a deeper pit (or larger aspect ratio) and vice versa. Similarly, at a given pit aspect ratio,  $N_i$  decreased when the stress range increased from 405 to 427.5 MPa. Since these tests were carried out in air, these results only show the effect of the mechanical interaction between double pits on crack initiation life. This interaction can be related to the stress and strain fields around the pits, which depend on pit size and applied stress [1, 201, 204]. The smaller the

separation distance, the greater the mechanical interaction between pits and the higher the tendency for the pit to transition to a crack. The dependence of crack initiation life on pit size and applied stress is attributed to the strain localisation effect of the pits [201, 234]. At a given stress level, increase in pit size will result in greater strain localisation and for a given pit size, increasing the applied stress level will have similar effect. In all cases, the overall consequence is a higher tendency to initiate a crack and therefore decrease the crack initiation life. The present results show that the nucleation of cracks from pits depends on pit size, applied stress and proximity of pits to each other.

To quantify the effect of pit proximity on overall fatigue life, crack initiation lifetimes were plotted as a fraction of the total fatigue life (Figure 5.20b). A horizontal has been drawn on this figure to indicate the mean of the percentage crack initiation lifetimes obtained for 200 and 270  $\mu\text{m}$  deep single pits cycled at  $\Delta\sigma = 405$  and 427.5 MPa. A single horizontal line was used because the difference between the percentage crack initiation lifetimes for both pit depths at these two stress ranges was less than 6%. The main observation is that, depending on separation distance, the interaction between pits significantly reduced the fraction of the total fatigue required for crack initiation. Whereas crack initiation life was up to 95% of the fatigue life in the case of single pits, it can be reduced by as much as a factor of five to about 20% when there is interaction between the pits. The increase in percentage crack initiation life from about 20% at short separation distances to about 95% at relatively longer distance indicates that the fatigue behaviour changed from being dominated by crack propagation, to that of crack initiation, as the pits become further apart. These results suggest that the fatigue behaviour of the material can change from being initiation-dominant to propagation-dominant when multiple pits interact with each other.

It can also be observed in Figure 5.20a that the trends in increase in crack initiation life appear to be exponential and also tended towards maximum values that are similar to those obtained for single pits (indicated with horizontal lines). From these results, there appears to be a threshold, separation distance, beyond which there is little interaction between pits, in terms of the influence on crack initiation life. This threshold distance was found to be dependent on the applied stress level and pit aspect ratio. For instance, increasing the stress level from 405 to 427.5 MPa increased the threshold distance required



to mitigate the combined effect of the pits on crack initiation. The threshold distances evaluated from Figure 5.20a as the distance when the trend line intersects the horizontal lines representing the crack initiation lives for the single pits are given in Table 5.6. The results show that the threshold distance increased with increase in pit size and stress range.

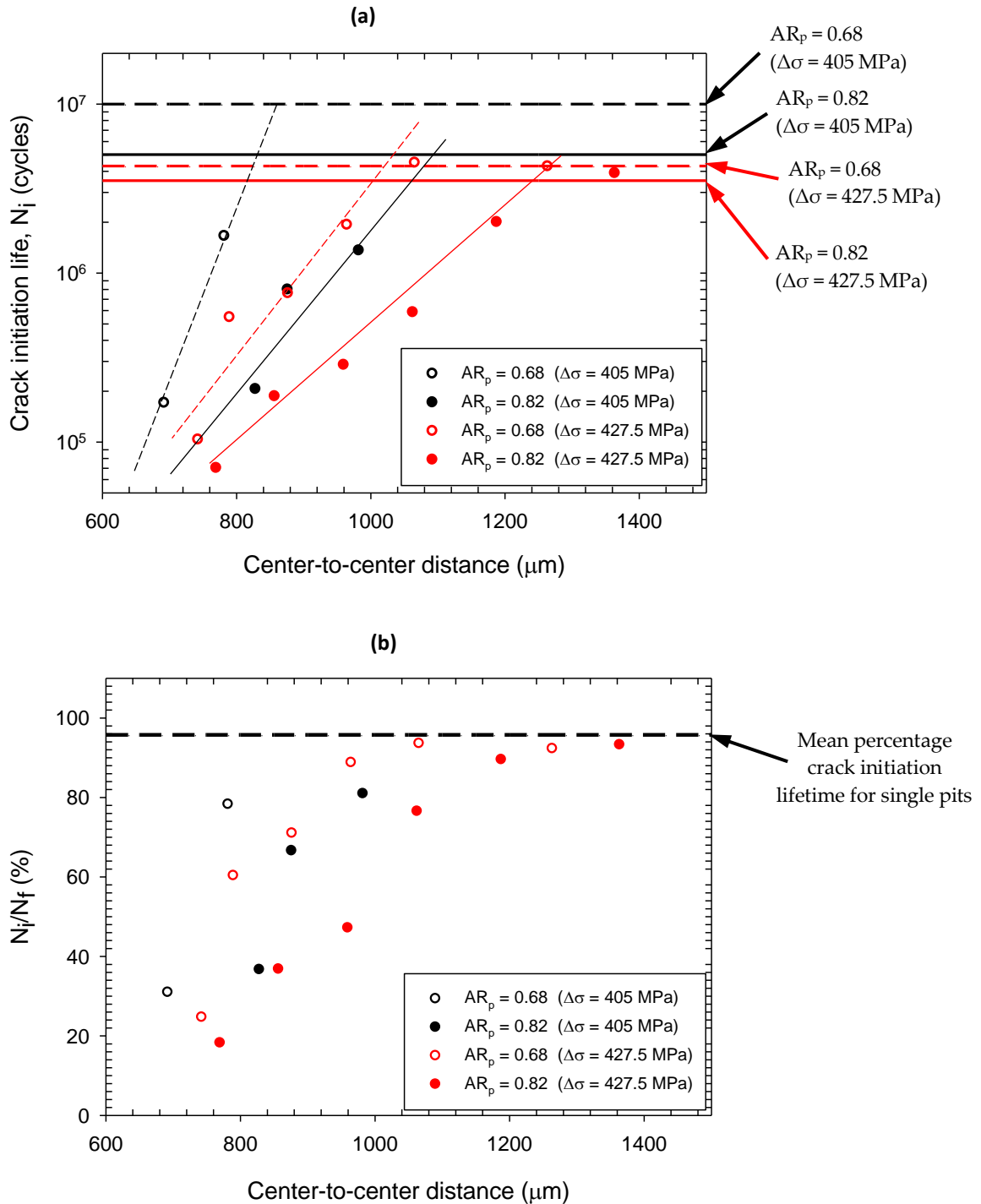


Figure 5.20 Crack initiation lives versus separation distance between two pits as a function of pit size and applied stress plotted in (a) number of cycles and (b) fraction fatigue life. Horizontal lines represent corresponding values for single pits.

**Table 5.6** Estimated threshold values for separation distances between double pits.

Stress range (MPa)	$d_p = 200 \mu\text{m}$ ( $AR_p = 0.68$ )	$d_p = 270 \mu\text{m}$ ( $AR_p = 0.82$ )
405	860	1040
427.5	980	1210

## 5.5.2 Crack propagation behaviour

### 5.5.2.1 Crack development from pits in air

Typical behaviour of the cracks that initiated from single and double pits in air are shown in Figure 5.21 and Figures 5.22—5.23 respectively. For single pits, cracks initiated from adjacent sides of the pit mouth and propagated in the direction perpendicular to the applied stress until failure of the specimen (Figure 5.21). No evidence of crack branching was found. In some cases, where a crack initiated from only one side of the pit mouth, a delay in cycles was observed before a second crack initiate from the adjacent side of the pit mouth. In the tests where this occurred, the delay in crack initiation times is thought to be random as no correlation was found between the loading conditions and pit sizes.

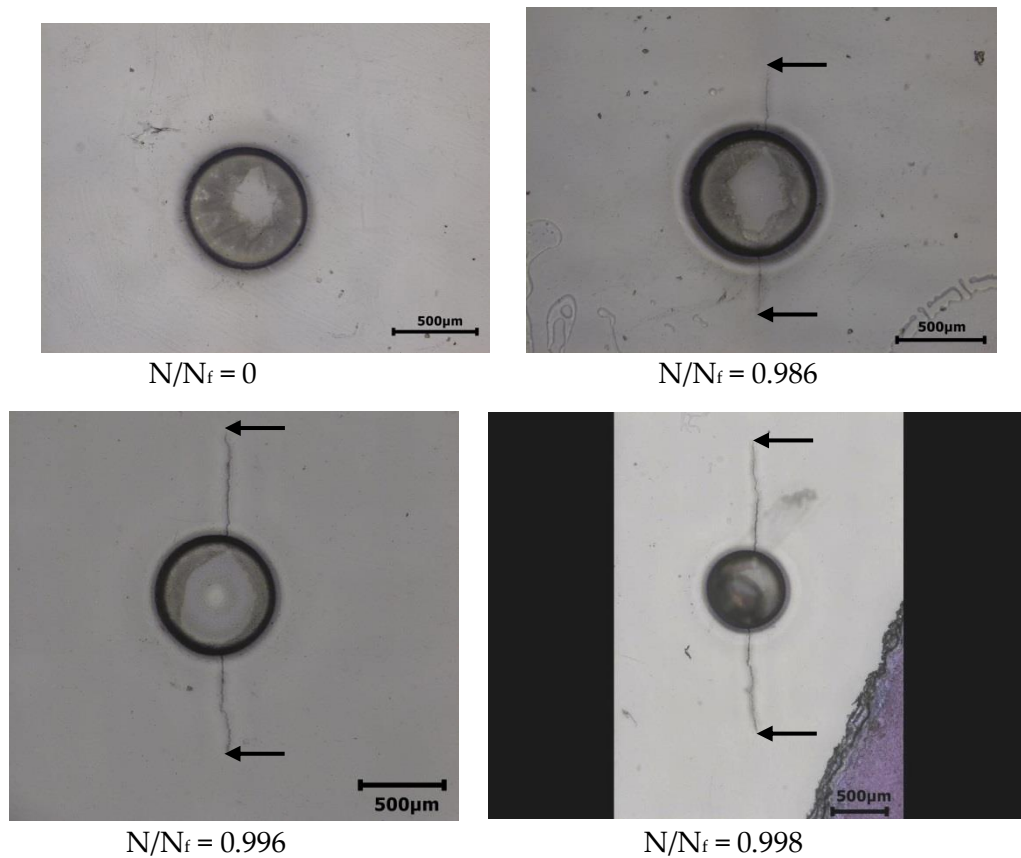


**Figure 5.21** Typical air fatigue crack development from single pits. Images obtained from replicas.  $\Delta\sigma = 405 \text{ MPa}$ ,  $d_p = 265 \mu\text{m}$ ,  $AR_p = 0.81$ ,  $N_i = 5.025 \times 10^5$  cycles,  $N_f = 5.205 \times 10^5$  cycles. Arrows indicate crack tips and loading direction is from left to right.



Crack initiation behaviour for double-pitted specimens exhibited different behaviour. When only a single crack initiated at the mouth of one of the pits, as was observed in the majority of the tests, it propagated perpendicularly to the loading direction into the adjacent pit (Figures 5.22 - 5.23). When two cracks initiated from each of the adjacent pits, each crack propagates until coalescence occurs (Figures 5.24 - 5.25). It has been suggested that when two cracks are close enough, the mechanical interaction of the plastic zones at each of the leading crack tips may cause both cracks to coalesce, causing an abrupt increase in crack size and acceleration of crack growth [274-277]. It is interesting to note that deviations in the adjacent crack tips take place just before coalescence occurs. The deviation is more notable in Figure 5.25 than in Figure 5.24, possibly being due to the slight offset in the mid-planes of the adjacent pits. Similar observations reported by other authors [275, 278-280] were attributed to the fact that it is energetically unfavourable for any two adjacent crack-tips to extend without such deviations. As noted by Forsyth [280], crack tip offset distance and stress intensity factor level effects determine the conditions for crack coalescence. It is apparent from Figures 5.24 and 5.25 that the closeness between the tips of the cracks appears to have facilitated the interaction of the plastic zones at each of the crack tips, causing both cracks to coalesce. This interaction will also reduce the tendency of the cracks following crystallographic paths. A schematic of this process is shown in Figure 5.26. Since, there is a greater offset distance in Figure 5.25, the plastic zone interaction will be more pronounced and the deviation will be greater than in Figure 5.24.

Another notable observation from Figures 5.24 and 5.25 is that the two cracks appear to have different growth rates prior to coalescence, with one crack propagating at a rate faster than the other. From observations made at intervals before coalescence, it appeared that the smaller crack stopped growing for some time (non-propagating) but re-propagated just before coalescence occurred. This behaviour may be attributed to the shielding effect of the larger crack (usually initiated first), which retards the growth rate of the smaller crack until the latter becomes non-propagating. This is due to the lower effective stress at the tip of the smaller crack, resulting from the deviation of the lines of force of the relatively larger crack [281].

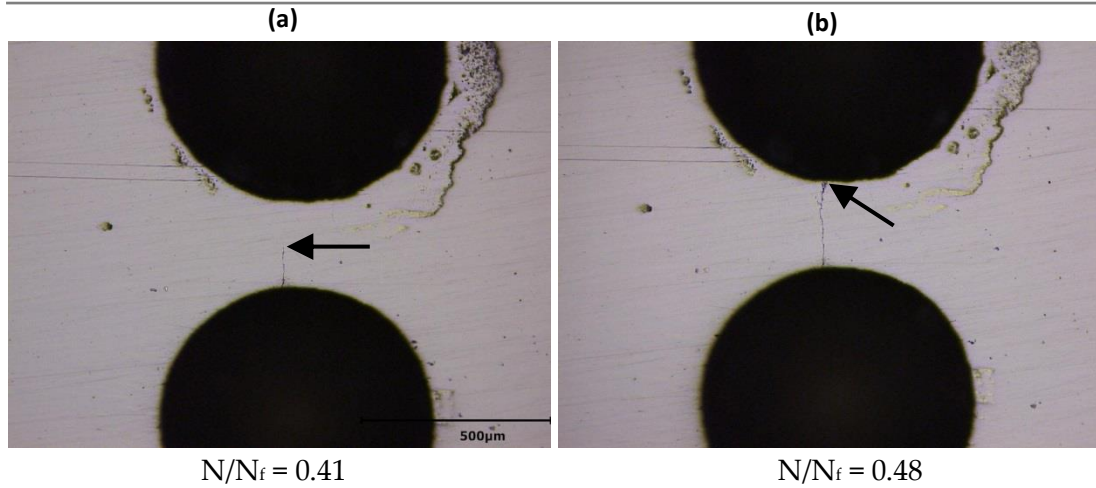


Figure 5.22 Typical fatigue crack development in double-pitted specimens in air.  $\Delta\sigma = 427.5 \text{ MPa}$ ,  $d_{p(1)} = 269 \text{ }\mu\text{m}$ ,  $d_{p(2)} = 265 \text{ }\mu\text{m}$ ,  $AR_{p(1)} = 0.83$ ,  $AR_{p(2)} = 0.80$ ,  $s_{ee} = 207 \text{ }\mu\text{m}$ ,  $s_{cc} = 857 \text{ }\mu\text{m}$ ,  $N_i = 1.86 \times 10^5$  cycles,  $N_f = 5.06 \times 10^5$  cycles. Arrows indicate crack tips and loading direction is from left to right.

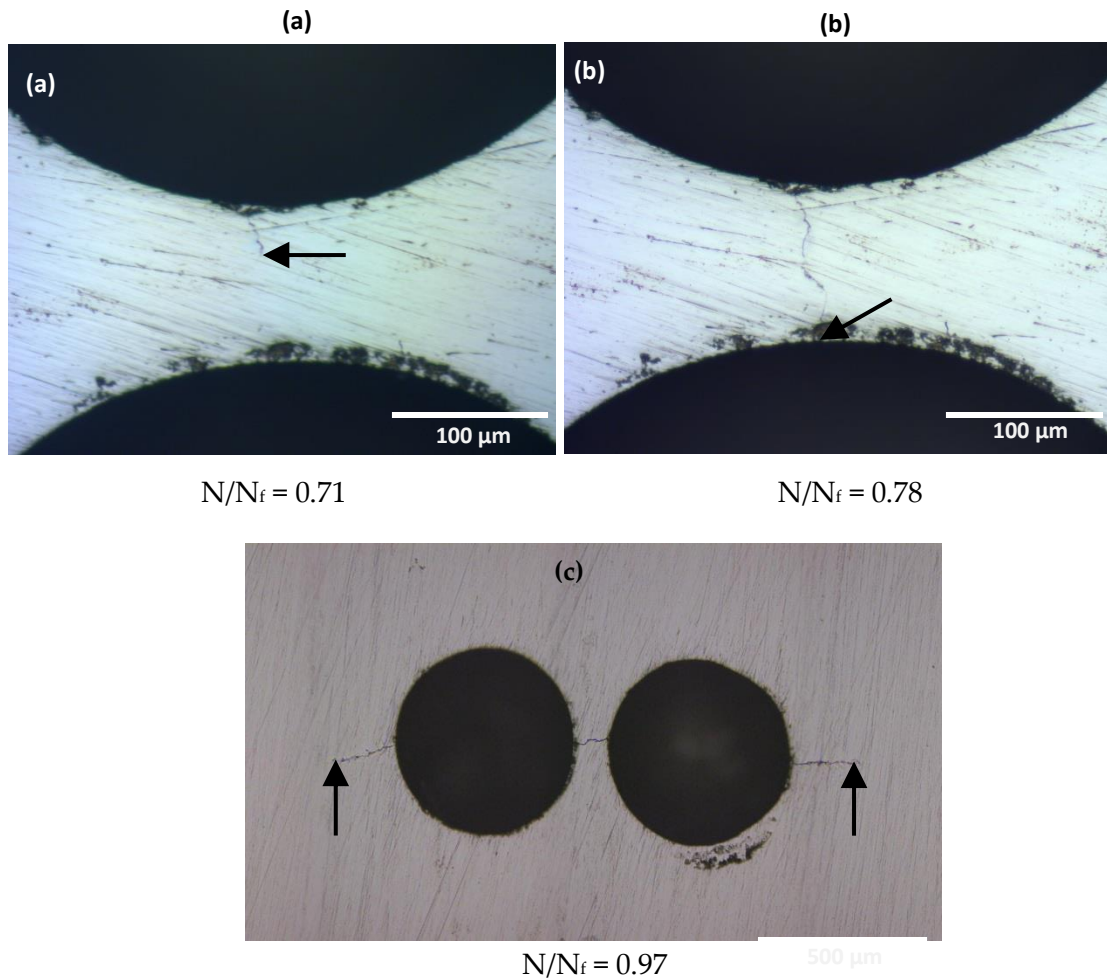
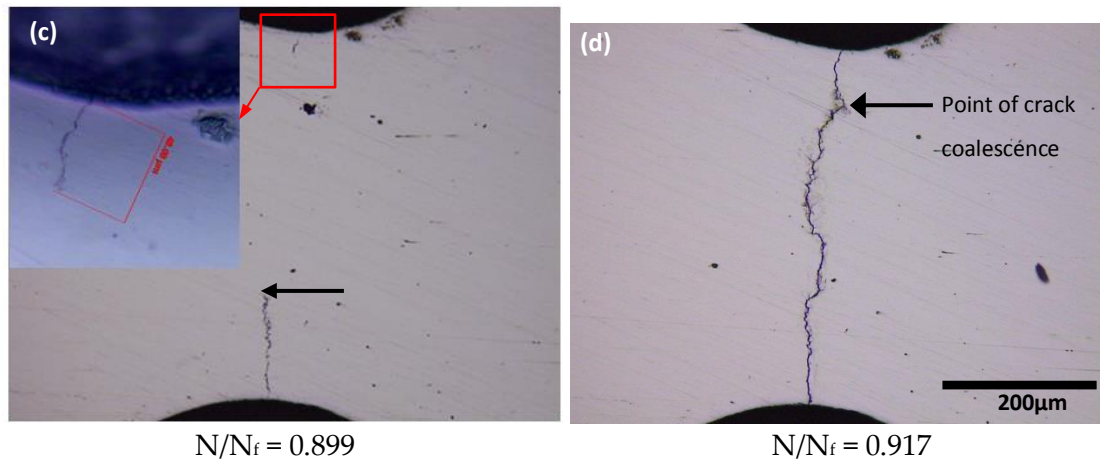
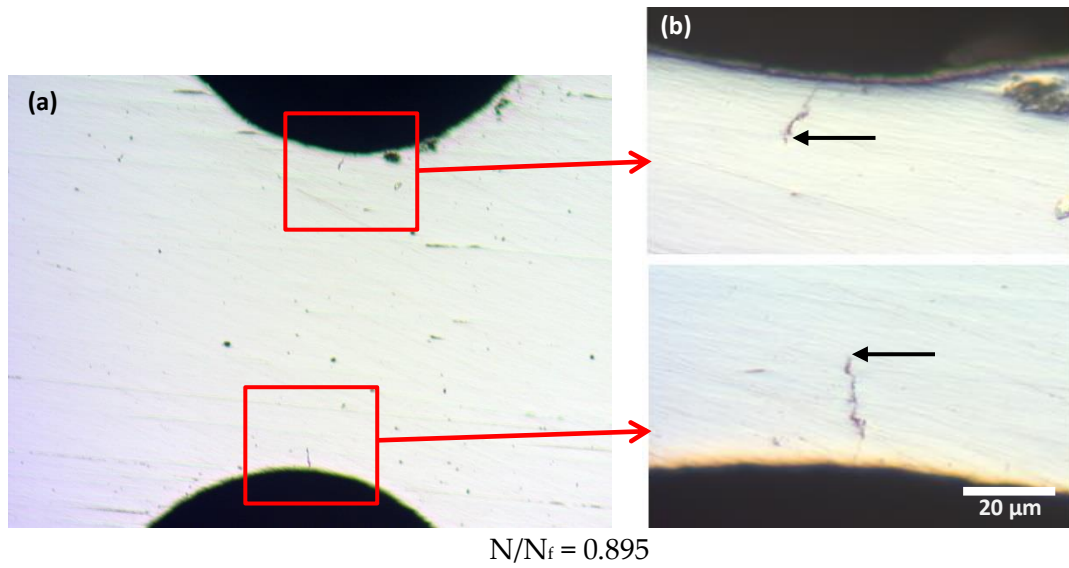
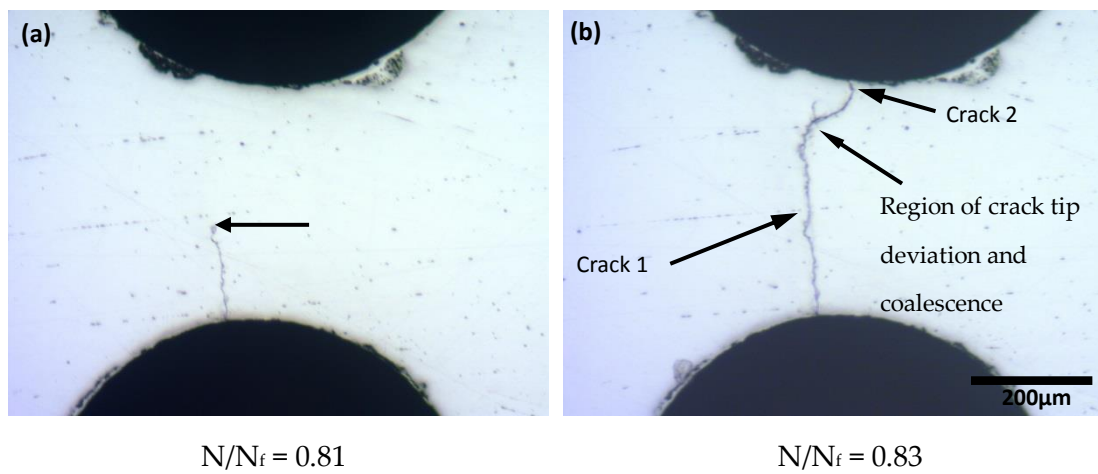


Figure 5.23 Typical fatigue crack development in double-pitted specimens in air.  $\Delta\sigma = 405 \text{ MPa}$ ,  $d_{p(1)} = 196 \text{ }\mu\text{m}$ ,  $d_{p(2)} = 198 \text{ }\mu\text{m}$ ,  $AR_{p(1)} = 0.68$ ,  $AR_{p(2)} = 0.69$ ,  $s_{ee} = 105 \text{ }\mu\text{m}$ ,  $s_{cc} = 693 \text{ }\mu\text{m}$ ,  $N_i = 3.8 \times 10^5$  cycles,  $N_f = 5.5 \times 10^5$  cycles. Arrows indicate crack tips and loading direction is from left to right.



**Figure 5.24** Typical crack coalescence during fatigue crack development in air.  $\Delta\sigma = 427.5$  MPa,  $d_{p(1)} = 264$   $\mu\text{m}$ ,  $d_{p(2)} = 272$   $\mu\text{m}$ ,  $AR_{p(1)} = 0.81$ ,  $AR_{p(2)} = 0.81$ ,  $s_{ee} = 525$   $\mu\text{m}$ ,  $s_{cc} = 1188$   $\mu\text{m}$ ,  $N_i = 19.96 \times 10^5$  cycles,  $N_f = 22.31 \times 10^5$  cycles. Loading direction is from left to right.



**Figure 5.25** Typical crack branching during fatigue crack development in air.  $\Delta\sigma = 427.5$  MPa,  $d_{p(1)} = 274$   $\mu\text{m}$ ,  $d_{p(2)} = 265$   $\mu\text{m}$ ,  $AR_{p(1)} = 0.83$ ,  $AR_{p(2)} = 0.79$ ,  $s_{ee} = 398$   $\mu\text{m}$ ,  $s_{cc} = 1063$   $\mu\text{m}$ ,  $N_i = 5.84 \times 10^5$  cycles,  $N_f = 7.64 \times 10^5$  cycles. Loading direction is from left to right.

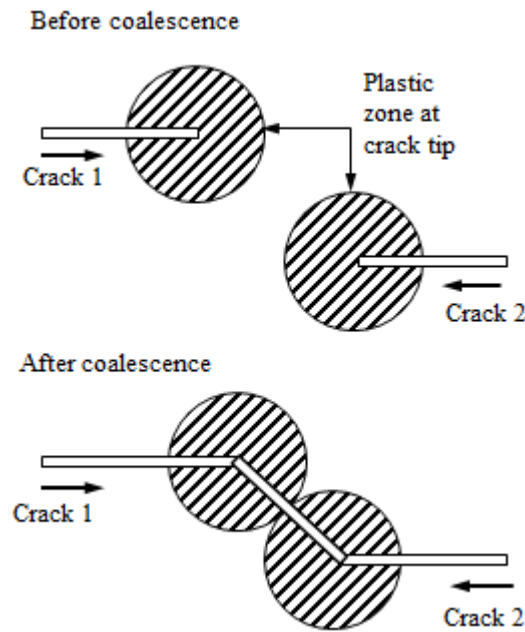
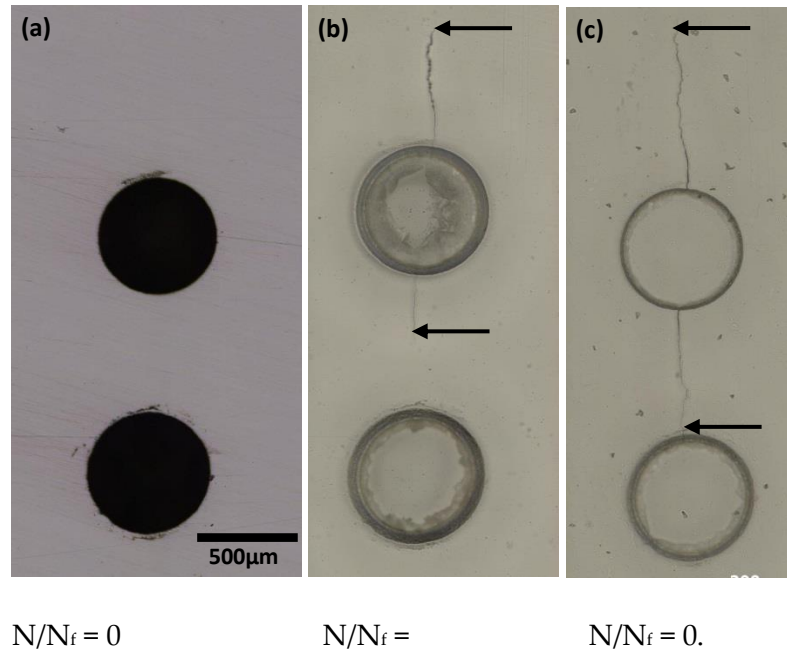


Figure 5.26 Schematic showing stages of crack deviation and coalescence involving interaction of plastic zones on approaching crack tips (after [280]).

It was previously mentioned that there appears to be a threshold separation distance between pits beyond which the cracking initiation behaviour is similar to that of a single pit (see Figure 5.20 and Table 5.6). An example where cracks can be seen to initiate and propagate from only one pit when the separation distance did not influence the crack initiation lifetime is shown in Figure 5.27. Although the  $N_i$  for the single and double pits may be similar, it was expected that cracks should initiate from both pits since both pits have similar depth and aspect ratio. However, this was not the case and may be due to scatter in crack initiation lifetime. For instance, the crack propagation lifetime for this specimen ( $3.1 \times 10^5$  cycles) may be similar to the scatter in crack initiation lifetime for a single pit of the same size cycled at the same stress range. In this case, the cracks that initiated from one pit would likely have propagated to a size that is large enough to dominate the damage process before cracks could initiate from the other pit.

Irrespective of the different crack propagation behaviour described above, the cracks propagate, in a direction perpendicular to that of loading, into the adjacent pit. The nature of propagation of the cracks on the double-pitted specimens made it impractical to measure crack extension, once a crack propagates to the edge of the adjacent pit or when two initiated cracks coalesce into a single crack. Therefore, crack propagation data was

only obtained between crack initiation and when a crack propagates to the edge of the adjacent pit or when two adjacent cracks coalesced.



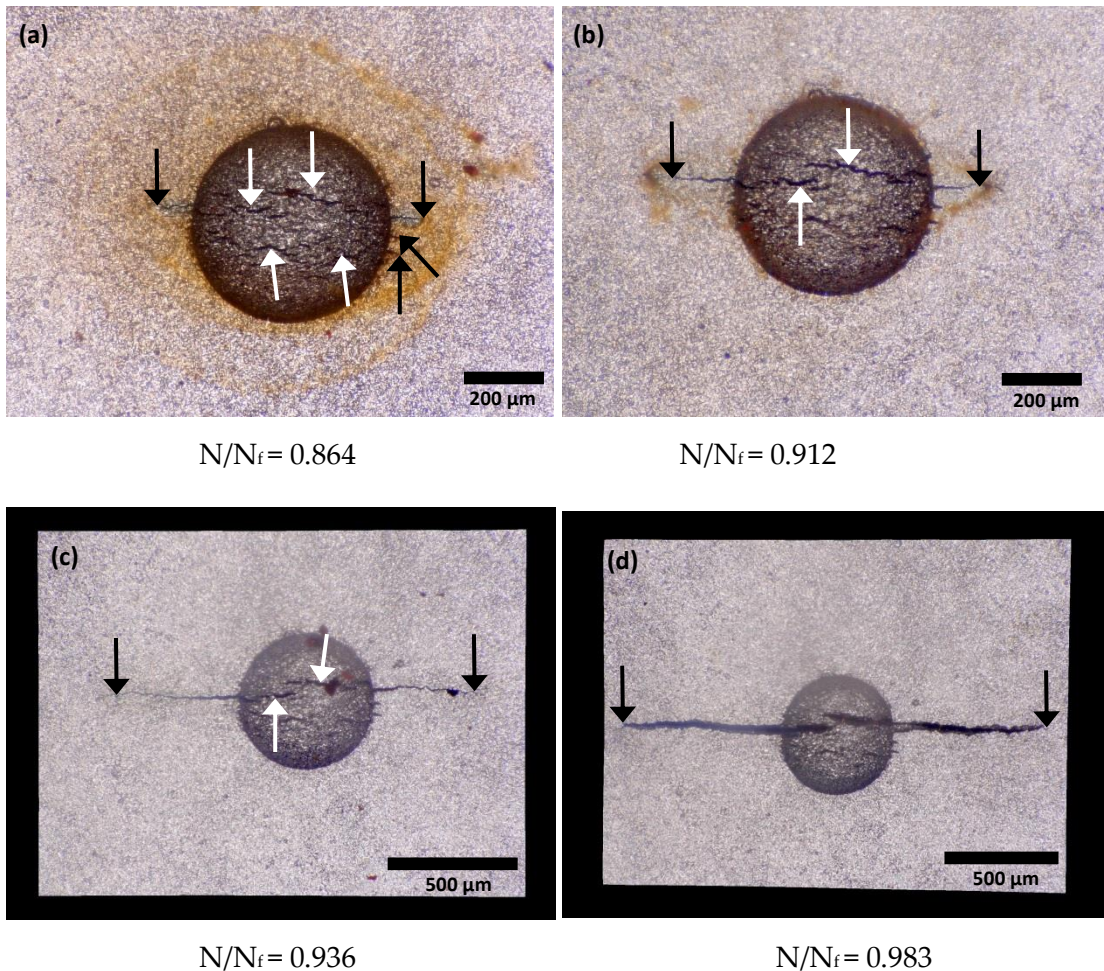
*Figure 5.27 Typical crack development behaviour in air when there is no interaction between the strain fields of pits.  $\Delta\sigma = 427.5$  MPa,  $d_{p(1)} = 272$   $\mu\text{m}$ ,  $d_{p(2)} = 268$   $\mu\text{m}$ ,  $AR_{p(1)} = 0.83$ ,  $AR_{p(2)} = 0.81$ ,  $s_{ee} = 703$   $\mu\text{m}$ ,  $s_{cc} = 1364$   $\mu\text{m}$ ,  $N_i = 3.90 \times 10^5$  cycles,  $N_f = 4.18 \times 10^5$  cycles. Arrows indicate crack tips and loading direction is from left to right.*

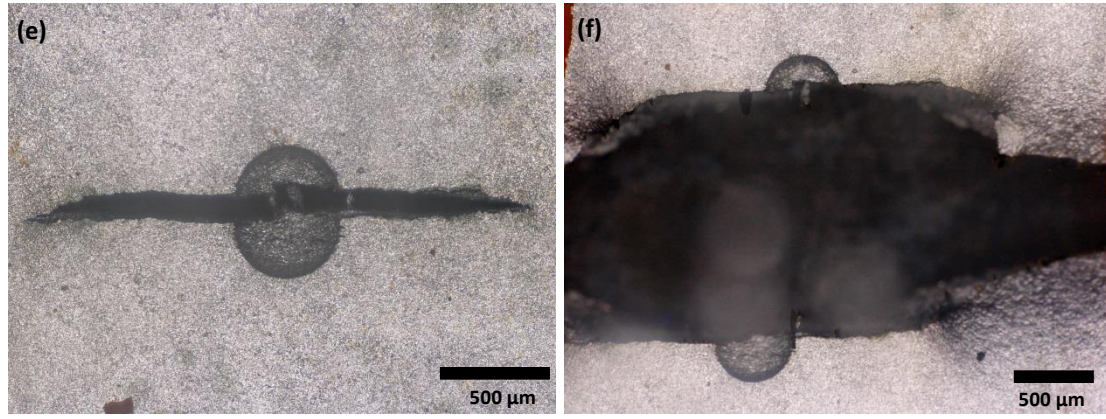
### 5.5.2.2 Crack development from pits in corrosion fatigue

For corrosion fatigue tests, surface crack extension was monitored in-situ using a digital microscope. Although the crack initiation behaviour in the aggressive environment showed that cracks can initiate from the pit bottom, these cracks extended into the specimen making it difficult to characterise them, in terms of crack extension using optical observation. An implication of this is that, if a crack initiated first from the pit bottom, the cycle number at crack initiation and that corresponding to the first crack extension measurement (at the pit mouth) will be different. This difference was observed to be significant especially at relatively lower stresses, hence, must be accounted for. Since crack growth rates are based on surface crack lengths, this difference was only added to the overall crack initiation life. Figure 5.28 shows typical development of cracks that initiated from a pit in the brine environment. The white arrows indicate cracks that initiated from the pit bottom, while the black arrows indicate the cracks that initiated



from the pit mouth. In Figure 5.28a, multiple cracks can be observed to have formed at the mouth and bottom of the pit. Out of the three cracks that initiated from the right side of the pit mouth, only one became dominant (Figure 5.28b). Similarly, of all the cracks that seemed to have initiated at the pit bottom, two appeared to have coalesced with other cracks and thus became dominant. In Figure 5.28c and 5.28d, the dominant cracks at the pit bottom coalesced with those growing from the mouth and joined at the latter stages of crack development (Figure 5.28e). In other tests, cracks from the pit mouth and bottom coalesced during the propagation stage earlier than shown in this example. The fractured specimen is shown in Figure 5.28f.





$N/N_f = 0.99$

$N/N_f = 1.00$

**Figure 5.28 Typical corrosion fatigue crack development.** White and black arrows indicate cracks that initiated from pit bottom and the crack tips of those from the pit mouth respectively.  $\Delta\sigma = 405$  MPa,  $d_p = 265 \mu\text{m}$ ,  $AR_p = 0.81$ ,  $N_i = 3.32 \times 10^5$  cycles,  $N_f = 4.19 \times 10^5$  cycles. Loading direction is from top to bottom.

### 5.5.2.3 Crack growth rates in air and corrosion fatigue

After crack initiation, fatigue crack propagation rates, in both air and brine solution, were determined by measuring the crack extension  $a_{ce}$ , which is the crack length extension beyond the pit mouth. This allows correlation of crack size with short crack behaviour and dimensions of the microstructure. A schematic of the two is shown in Figure 5.29. Fatigue crack growth rates,  $da/dN$ , were estimated by using the secant method below:

$$\left(\frac{da}{dN}\right)_{i+\frac{1}{2}} = \frac{a_{i+1} - a_i}{N_{i+1} - N_i} \quad 5.5$$

where  $a_i$  and  $a_{i+1}$  are two consecutive surface crack lengths at  $N_i$  and  $N_{i+1}$  number of cycles respectively. Since the fatigue crack growth rate represents the growth of a crack at the midpoint of two consecutive crack lengths, the corresponding average crack length at this point is  $0.5(a_i + a_{i+1})$ .

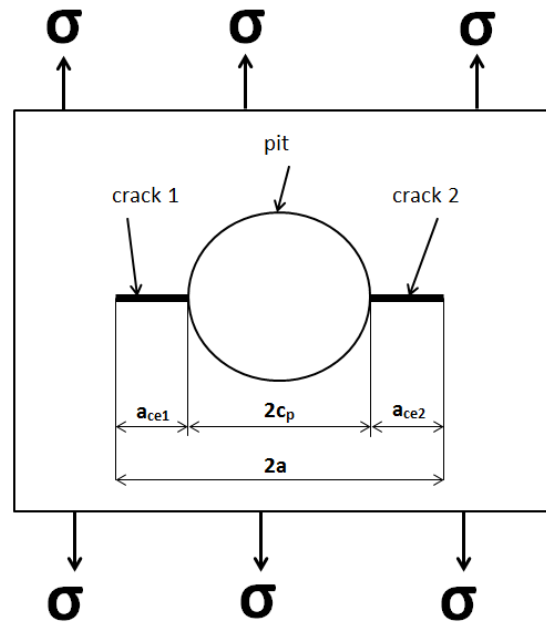


Figure 5.29 Schematic of surface length and crack extension of cracks that initiated from a pit.

#### Single pits – fatigue tested in air and corrosion fatigue

Plots of average crack extension from pit mouth versus fraction of fatigue life ( $(a_{ce})_{avg} - N/N_f$ ) and crack growth rates ( $da/dN - (a_{ce})_{avg}$ ) at different stress levels and for different single pit sizes are shown in Figures 5.30 – 5.36. Cracks that initiate but become non-propagating are also shown on these plots. The results generally exhibited some scatter, which was attributed to a number of factors including differences between crack initiation lives for the two cracks emanating from the two adjacent pit mouth regions, crack coalescence and the nature of the crack extension monitoring techniques e.g. replicas in air and digital microscope in brine solution. In addition, the corrosion fatigue data exhibits more scatter because of the inability to ascertain the exact tip of the fatigue crack due to surface corrosion, leading to a variation of about  $30\text{ }\mu\text{m}$ , giving a scatter of around  $3 \times 10^{-9}\text{ m/cycle}$  from the exact value. Nevertheless, all the results show apparent trends in the data. To assess the influence of the environment, applied stress and pit size on crack growth behaviour, the results were grouped in terms of pit sizes and stress levels respectively in both air and brine solution.

Figure 5.30 shows a comparison of plots of crack extension from the pit mouth versus number of cycles as a fraction of fatigue life for specimens containing  $200\text{ }\mu\text{m}$  deep pits (aspect ratio  $\approx 0.68$ ) cycled at different stress levels in air and brine solution. The plots for



a pit depth of 140  $\mu\text{m}$  (aspect ratio  $\approx 0.52$ ) cycled at  $\Delta\sigma = 450$  MPa are also shown. Figure 5.31 shows similar plots for a 270  $\mu\text{m}$  deep (aspect ratio  $\approx 0.82$ ) pit.

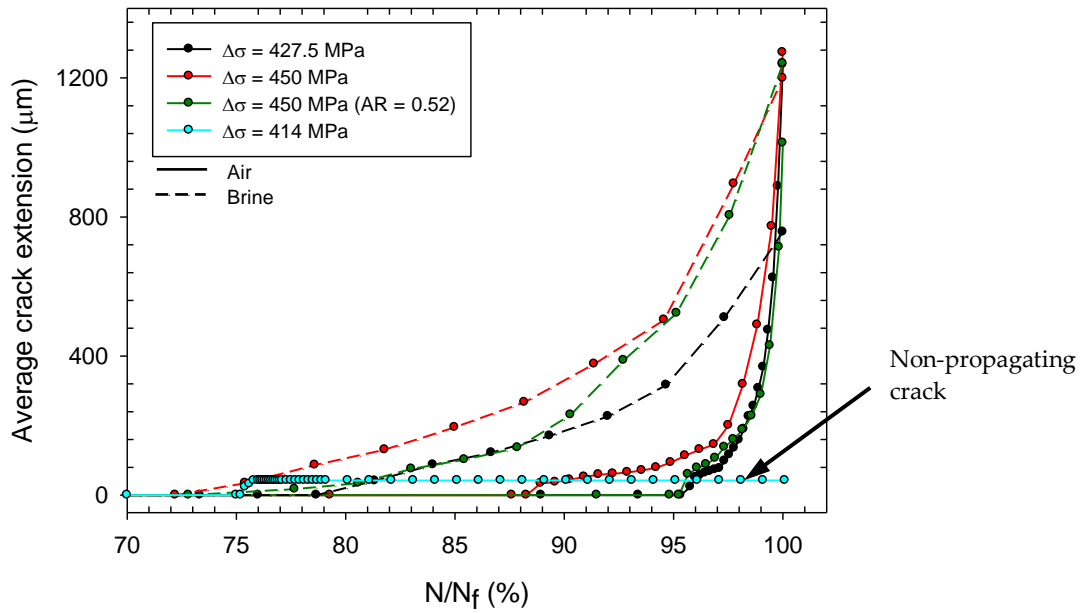


Figure 5.30 Average crack extension versus fraction of lifetime in air and brine solution at different stress levels. [ $d_p \approx 200$   $\mu\text{m}$ ,  $AR_p = 0.68$ ,  $R = 0.1$ ,  $f = \text{air} - 15$  Hz,  $\text{brine} - 2$  Hz]. Crack length data pit depth of 140  $\mu\text{m}$  ( $AR_p = 0.52$ ) cycled at  $\Delta\sigma = 450$  MPa is also shown.

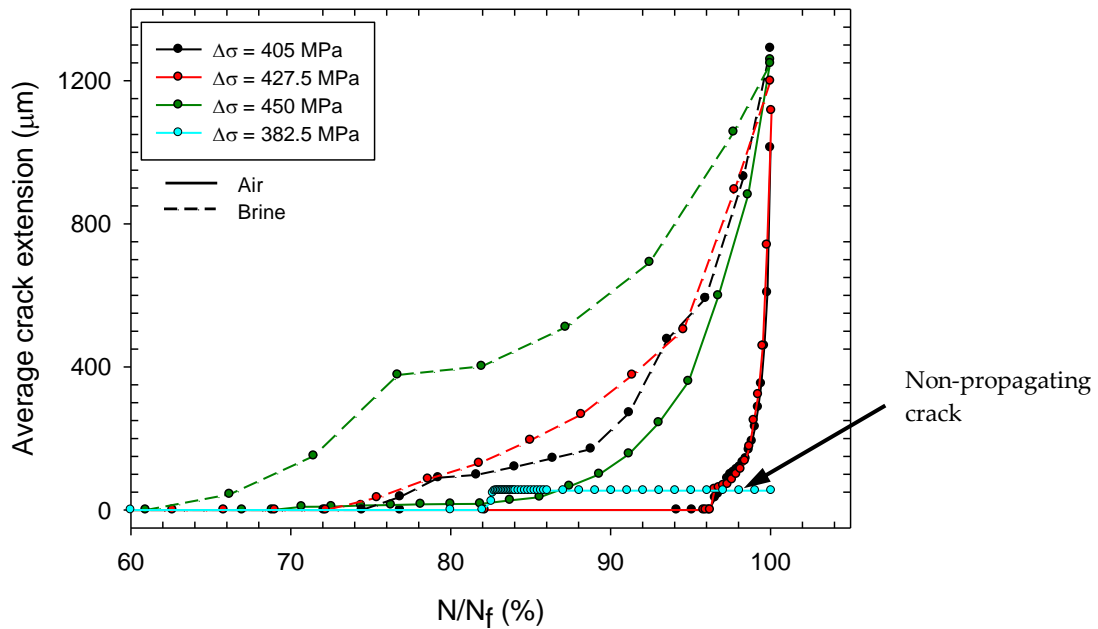


Figure 5.31 Average crack extension versus fraction of lifetime in air and brine solution at different stress levels. [ $d_p \approx 270$   $\mu\text{m}$ ,  $AR_p = 0.82$ ,  $R = 0.1$ ,  $f = \text{air} - 15$  Hz,  $\text{brine} - 2$  Hz].

For all the tests carried out in air, the results appear to show accelerations and decelerations in crack growth rate at relatively shorter crack lengths, typically below 150  $\mu\text{m}$ , (Figures 5.32 and 5.33). These results are consistent with other studies where cracks, which emanated from corrosion pits were found to exhibit oscillations in their growth rates and sometimes stopped propagating due to crack arrest [21, 55]. A distinctive characteristic of microstructurally short fatigue cracks is the oscillatory nature of their growth rates especially in the early stages of crack growth [33, 54, 70, 282]. For cracks emanating from smooth surfaces, this behaviour is attributed to sensitivity to local variations in microstructure with the crack growth rates alternately decelerating and accelerating until dominant microstructural barrier is reached [37, 53, 61, 70, 71]. Typical microstructural factors, which can retard crack growth, include grain boundaries, second-phase particles, twin boundaries, inclusions, precipitates, grain orientation, and etc. Crack arrest occurs at these barriers when cracks are not able to re-propagate into the neighbouring grain and thus stop propagating and becomes non-damaging. Examples of crack arrest in air are highlighted in Figures 5.32 and 5.33. For pit depths of 200 and 270  $\mu\text{m}$ , non-propagating cracks were observed at relatively lower stress ranges of 414 and 382.5 MPa respectively.

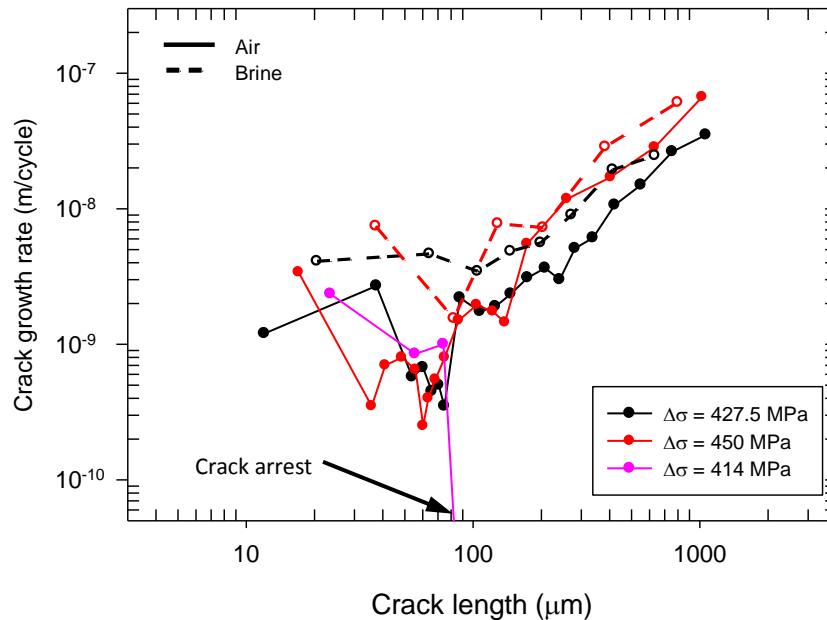


Figure 5.32 Comparison between fatigue crack growth rates in air and brine solution at different stress levels. [ $d_p \approx 200 \mu\text{m}$ ,  $AR_p = 0.68$ ,  $R = 0.1$ ,  $f = \text{air} - 15 \text{ Hz}$ ,  $\text{brine} - 2 \text{ Hz}$ ].

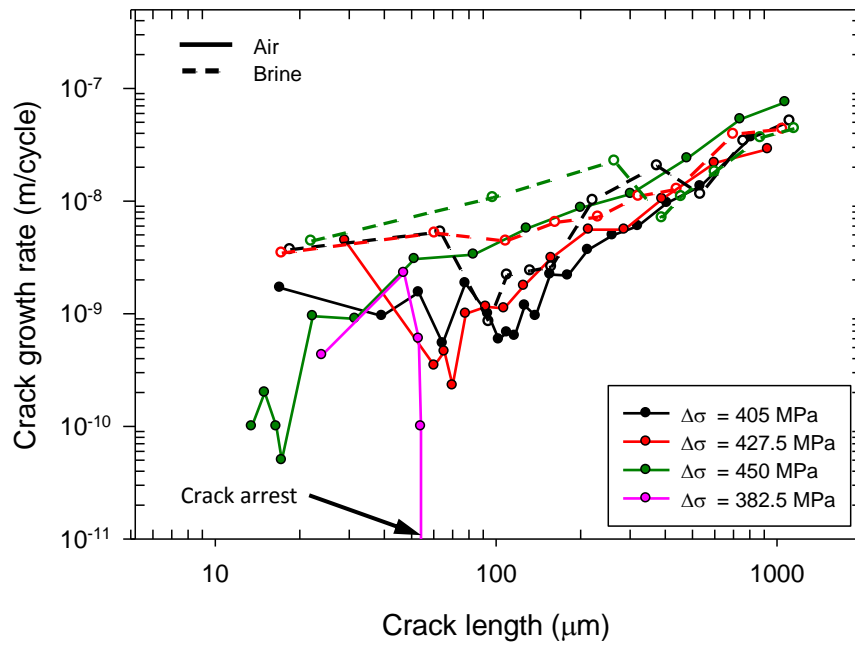


Figure 5.33 Comparison between fatigue crack growth rates in air and brine solution at different stress levels. [ $d_p \approx 270 \mu\text{m}$ ,  $AR_p = 0.82$ ,  $R = 0.1$ ,  $f = \text{air} - 15 \text{ Hz}$ ,  $\text{brine} - 2 \text{ Hz}$ ].

Under corrosion fatigue conditions and at relatively short crack lengths, the crack growth rates were found to be higher than in air at all stress levels and pit depths (Figure 5.34 and 5.35). These results suggest that the presence of the corrosive environment increased crack growth rates. Many authors have reported higher growth rates for short fatigue cracks in aggressive environments compared to air [89, 127, 128, 165, 167, 168]. This behaviour may be attributed to strain-assisted anodic dissolution mechanism which effectively results in relatively larger crack sizes per unit time compared to air [127, 165]. From Figures 5.34 and 5.35, it can also be observed that the oscillations in crack growth rates observed in air at relatively short crack lengths seem not to be present in the environment. One of the factors to which this behaviour can be attributed is the weakening effect of the brine solution on the resistance of the microstructural barriers [89, 166, 283]. The interaction between strain localization around the pit and the brine likely resulted in strain-assisted dissolution which accelerated the transfer of a Stage I shear crack to a Stage II tensile crack so that the microstructural resistance is eliminated. As concluded by Akid [88, 126, 127], strain-assisted dissolution can reduce the transition length or eliminate the microstructural barriers and allow re-propagation cracks.

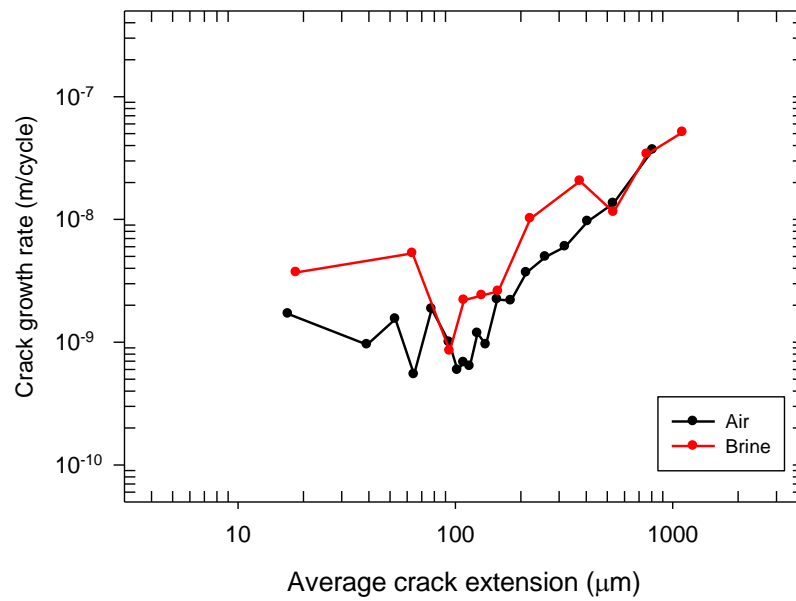


Figure 5.34 Comparison between fatigue crack growth rates in air and brine solution for pits with similar depths. [ $d_p \approx 140 \mu\text{m}$ ,  $\Delta\sigma = 450 \text{ MPa}$ ,  $R = 0.1$ ,  $f = \text{air} - 15 \text{ Hz}$ ,  $\text{brine} - 2 \text{ Hz}$ ].

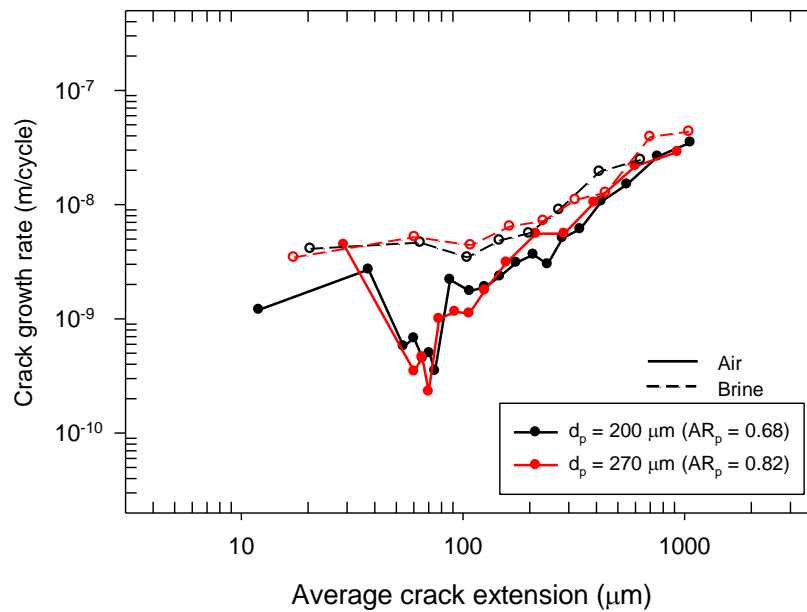


Figure 5.35 Comparison between fatigue crack growth rates in air and brine solution for pits with different depths. [ $\Delta\sigma = 427.5 \text{ MPa}$ ,  $R = 0.1$ ,  $f = \text{air} - 15 \text{ Hz}$ ,  $\text{brine} - 2 \text{ Hz}$ ].

At relatively longer crack lengths, above 200-300  $\mu\text{m}$ , the crack growth rates were generally found to increase with increase in crack lengths with little or no oscillations in air and brine solution. For a given crack length in this regime, cracks growth rates seem greater at relatively high stress ranges in air (Figures 5.32 and 5.33). Under corrosion fatigue conditions, the cracks growth rates may remain higher than in air (Figure 5.32,

5.34 and 5.35) or may decrease to the rates observed in air (Figures 5.33 and 5.36). The reduction in crack growth rates to those of air may be attributed to the wedging of the crack surfaces by corrosion products/oxide debris, which can be very significant at low stress ratios (e.g.  $R = 0.1$ ). This can lead to a reduction of the effective driving force available for crack propagation and thereby reduce growth rates [170, 284, 285].

A notable observation that is more apparent in Figures 5.32, is that the effect of the environment on crack propagation at relatively longer crack lengths seem to be more significant at a stress range of 427.5 MPa than at 450 MPa. This behaviour can be explained by considering that the effect of the mechanical driving force, which dominates crack growth at high stresses, will be reduced such that time-dependent electrochemical processes increasingly contribute to the crack tip failure process [126, 166]. Therefore, the crack growth rates will be higher in the environment at relatively lower stress.

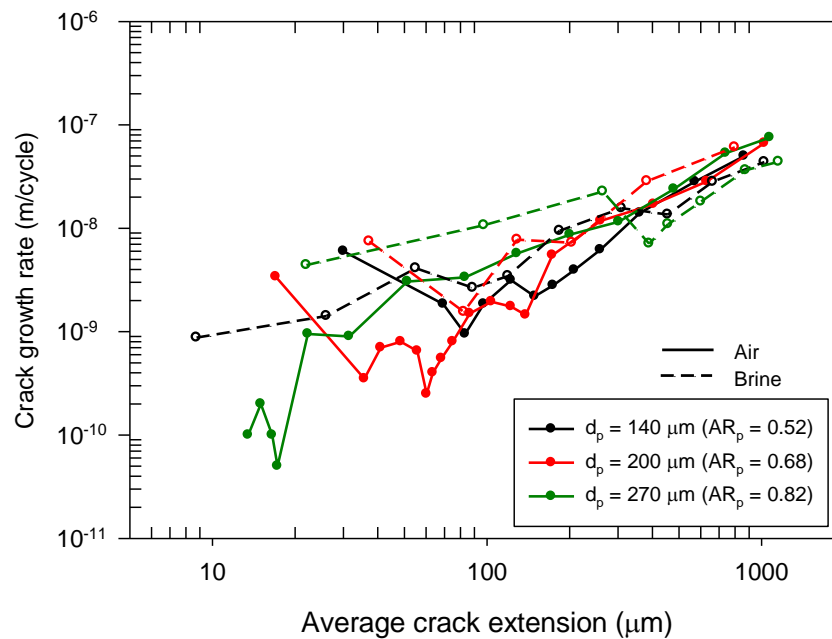


Figure 5.36 Comparison between fatigue crack growth rates in air and brine solution for pits with different depths. [ $\Delta\sigma = 450$  MPa,  $R = 0.1$ ,  $f =$  air - 15 Hz, brine - 2 Hz].

### 5.5.3 Behaviour of non-propagating cracks

It was reported in the previous section that non-propagating cracks were observed in air for pit depths of 200 and 270 μm at stress ranges of 414 and 382.5 MPa respectively. Previous studies have shown that cracks that emanated from pits can stop growing thereby become non-damaging [9, 195, 286]. Crack arrest leading to non-propagating

cracks together with the oscillations in crack growth rates suggest that the microstructure may have played a role in the behaviour of cracks that emanated from the pits. Cracks can become non-propagating due to crack arrest at stress levels below the fatigue limit because the mechanical driving force, which is a function of the crack tip plastic zone size, associated with the initiated crack is not sufficient to cause crack advance by activating slip planes in adjacent grains [57, 64]. To reveal any influence of the microstructure on crack arrest, the specimens containing non-propagating cracks were etched in 2% Nital. Figure 5.37 indicates that the tip of the non-propagating crack appears to be located at the boundary between two ferrite grains. This is consistent with previous studies, which reported crack arrest at ferrite-ferrite grain boundaries [283, 287]. Re-propagation of arrested cracks may be made possible in several ways. As far as the present study is concerned, two ways would be by increasing the applied stress range, which effectively increases the mechanical driving force and by removing the microstructural barrier to crack advance through anodic dissolution. Hence, the two specimens with non-propagating cracks were further tested by loading one at a higher stress level for a short period and the other in an aggressive environment.

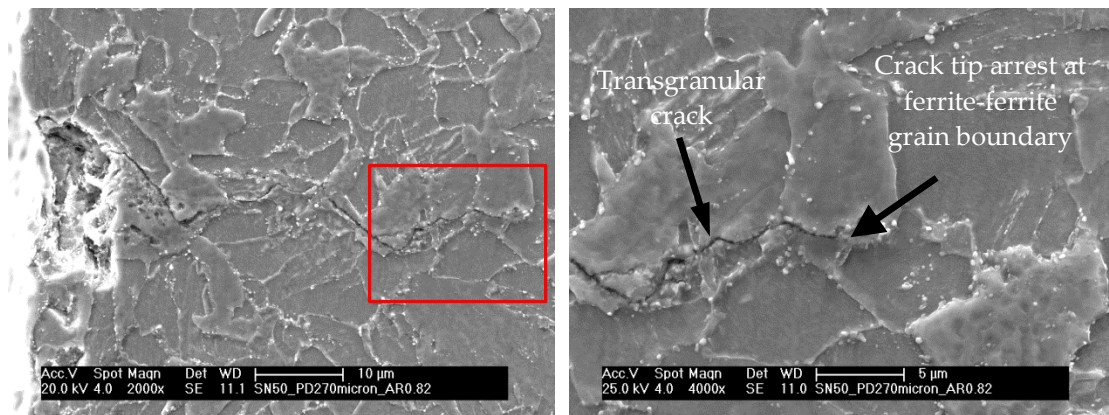


Figure 5.37 Micrograph showing arrest of a crack at a ferrite grain boundary [ $\Delta\sigma = 382.5$  MPa,  $d_p = 274$   $\mu\text{m}$ ,  $AR_p = 0.82$ ,  $N_i = 82.56 \times 10^5$  cycles]. Loading direction is from top to bottom.

#### 5.5.3.1 Effect of increase in stress range on non-propagating crack

In this test, the specimen previously tested in air at  $\Delta\sigma = 414$  MPa and on which a non-propagating crack was observed was tested further by increasing the stress range from 414 to 425 MPa (increase of 2.7%) for 20,000 cycles to increase the crack length. The stress range was then reduced to and fatigue cycled at 414 MPa. As shown in Figure 5.38, by increasing the stress range from 414 to 425 MPa, the previously arrested crack was able to

re-propagate, when returned to the original stress level of 414 MPa. This suggests that the stress intensity factor, associated with the crack length (212  $\mu\text{m}$ ) at the point when the stress was reduced, was above the threshold needed to sustain continuous crack propagation at this stress level.

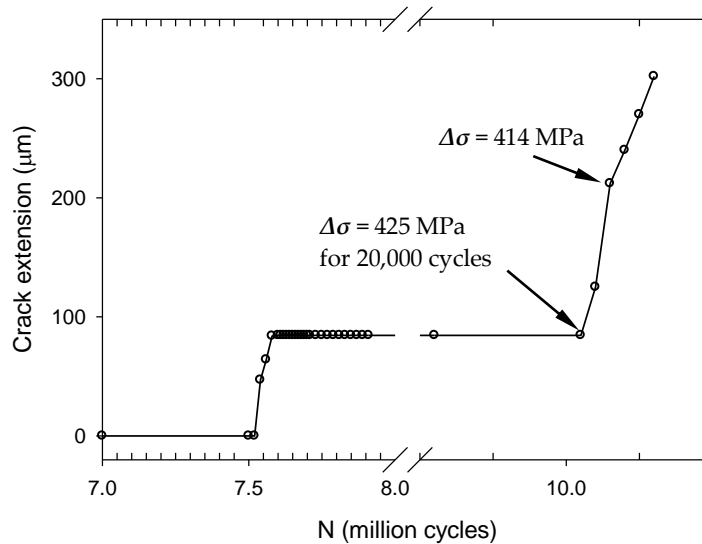


Figure 5.38 Average crack extension versus number of cycles for a non-propagating crack in air [ $d_p = 198 \mu\text{m}$ ,  $R = 0.1$ ,  $f = 15 \text{ Hz}$ ].

### 5.5.3.2 Effect of environment on non-propagating crack

In this test, the specimen previously tested in air and on which a non-propagating crack was observed was tested further in brine solution for 10,000 cycles. The sample was then removed from the corrosion cell dried and subsequently tested in air. The loading conditions throughout these tests were the same. Figure 5.39a shows plots of crack extension versus number of cycles while Figure 5.39b shows the crack growth rates versus crack length plot for this test compared to the test conducted at  $\Delta\sigma = 405 \text{ MPa}$ . It can be observed from Figure 5.39a that an introduction of the environment for a short period resulted in re-propagation of the previously arrested crack. The re-propagation of the crack was attributed to strain-assisted dissolution effect of the environment through reduction or elimination of the resistance of the microstructural barriers to crack advance and/or crack broadening. The effect of the environment can also be seen in Figure 5.39b, where the crack growth rate increased significantly (approximately 2 orders of magnitude) when the environment was introduced. The re-propagated crack did not stop propagating when the environment was removed, but continued to propagate until the

specimen failed. However, the crack growth rates decreased to values marginally lower than those observed from tests carried out at a higher stress level ( $\Delta\sigma = 405$  MPa). It has been suggested that continued crack propagation in air is only possible when the length of a crack is the same as or greater than a threshold crack length [89]. These results suggest that the environment was instrumental in promoting growth of the crack from pits beyond barriers inherent within the microstructure. The continued crack propagation after removal of the environment suggests that the role of the environment in crack growth is important in the early stages when the cracks are short.

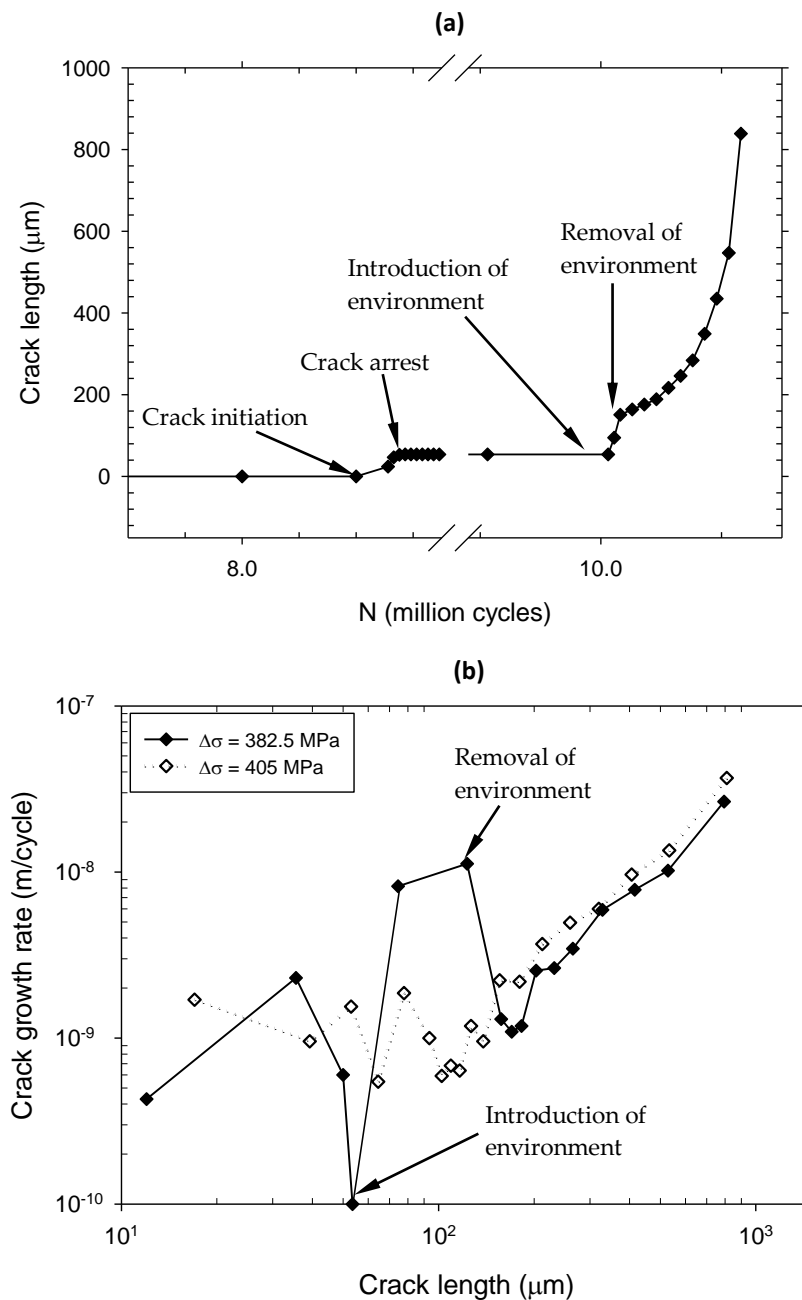


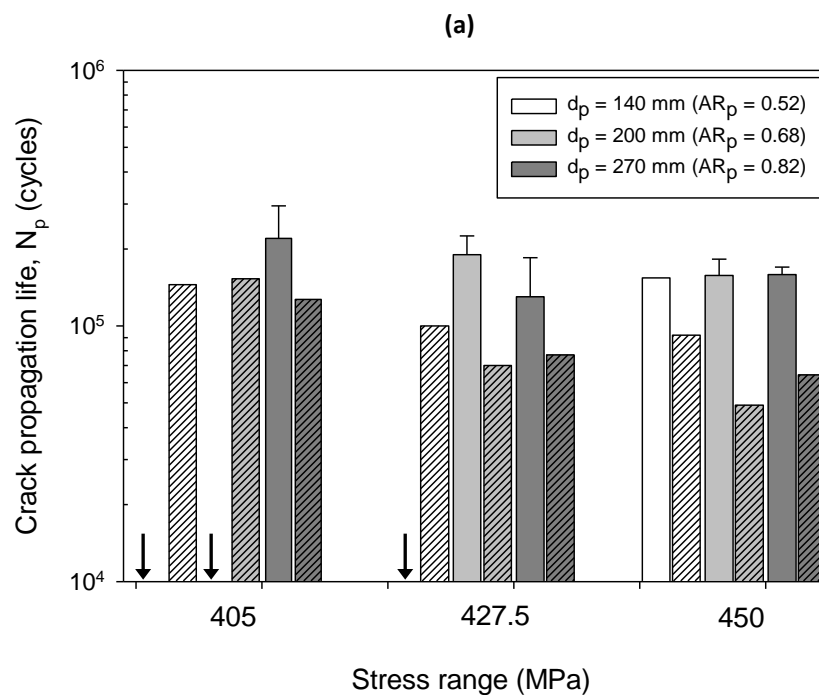
Figure 5.39 (a) Crack extension versus number of cycles for a non-propagating crack in air subjected temporarily to an aggressive environment, (b) crack growth rates versus crack length for data in (a) [ $d_p = 274 \mu\text{m}$ ,  $AR_p = 0.82$ ].



### 5.5.4 Crack propagation lifetimes

#### 5.5.4.1 Single pits – fatigue tested in air and corrosion fatigue

Figures 5.40a shows that the overall propagation lifetime of the cracks emanating from pits is mainly influenced by the test environment and stress level, whereas the pit size appears to have no significant effect. Where cracks did not initiate, notably in air,  $N_p$  is zero hence, no plots were shown for this cases. Generally,  $N_p$  in brine solution are lower than in air for all stress levels, and increase with decrease in stress levels for both environments. For a given stress level, there seems to be no apparent differences between the propagation lifetime observed for different pit sizes. The propagation lifetimes were plotted as a fraction of fatigue life as shown in Figure 5.40b. The notable observation here is that, the propagation life ratios are generally less than 40% of the fatigue lives, which indicates the fatigue behaviour is still dominated by the crack initiation stage in both air and corrosion fatigue conditions. However, the percentage crack propagation lives appears to be greater in corrosion fatigue than in air and they generally decrease with reduction in pit size at a given stress level. This is expected since the fatigue behaviour is dominated by crack initiation lives, which were earlier shown to increase with decrease in pit size and are lower (as a fraction of the total fatigue lives) in the brine solution than in air.



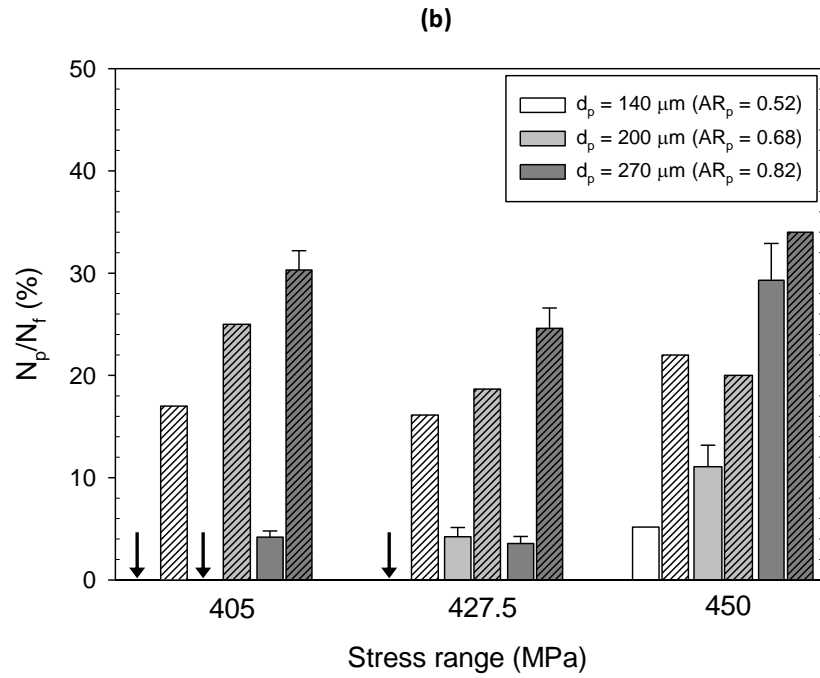


Figure 5.40 Comparison between crack propagation lives in air and brine solution for different stress levels and pit sizes as function of (a) number of cycles and (b) fraction of total lifetime. [Plain bars = Air; Hatched pattern bars = Corrosion fatigue]. Arrows indicate that  $N_p$  &  $N_p/N_f \approx 0$ .

#### 5.5.4.2 Double pits – fatigue tested in air

Changes in fatigue behaviour from initiation-dominant to propagation-dominant behaviour was investigated by plotting propagation lifetimes ( $N_p$ ) and fatigue lifetimes ( $N_f$ ) as a function of separation distance between the pits (Figures 5.41 – 5.42).  $N_p$  is given by  $N_p = N_f - N_i$ . Unlike crack initiation lifetime results, a large scatter in  $N_p$  was observed, with only a marginal trend, notably that  $N_p$  decreased with increase in separation distance (see trend lines in Figure 5.41a). Furthermore, for a constant separation distance, whereas  $N_p$  were generally higher at lower stresses, no dependency on pit size was observed. The scatter in the data is thought to be due to factors which include crack coalescence and crack initiation from only one or both pits. For instance, at a given stress level and separation distance, crack coalescence can shorten crack propagation life compared to when there is no coalescence.

To explain the decrease in  $N_p$  with increasing separation distance, the crack size as a function of separation distance was considered. At a given stress level, consider two specimens A and B containing double pits with the same depth but different edge-to-edge distances  $s_{ee,A}$  and  $s_{ee,B}$  respectively where  $s_{ee,A} < s_{ee,B}$ . Due to the greater separation

distance, the effective size and the SIF associated with a crack propagating in the region separating both pits in specimen B will be greater than in specimen A.

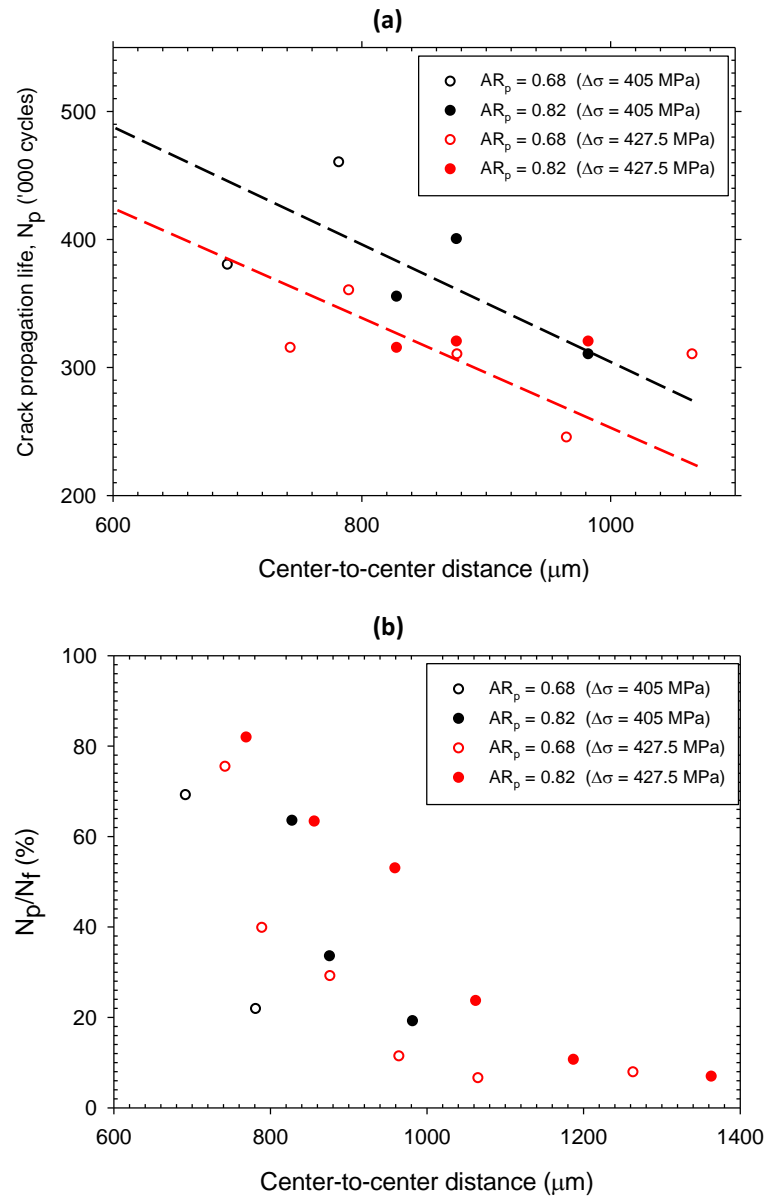


*Figure 5.41 Crack propagation lives versus centre-to-centre distance between two pits as a function of pit size and applied stress, plotted in terms of (a) number of cycles and (b) fraction fatigue life.*

Consequently, the growth rate will be faster in specimen B and hence, generating a shorter  $N_p$ . The SIF is also a function of applied stress for a given crack size, which implies that increasing the applied stress range will result in faster propagation rate and shorter  $N_p$ . This explains why, for the same separation distance, propagation lives tend to be shorter for tests carried out at  $\Delta\sigma = 427.5$  MPa compared to those at 405 MPa. The

independency observed between pit size and  $N_p$  also suggests that the role of the former in the fatigue behaviour in the presence of multiple pits may be limited mainly to the crack initiation stage.

Re-plotting the data in terms of percentage propagation lifetimes ( $N_p/N_f$ ) (Figure 5.41b), as expected, shows a reverse of the trend observed in the percentage crack initiation ( $N_i/N_f$ ). For all the stress levels and pit sizes,  $N_p/N_f$  generally decreased with increasing separation distance. Comparison of Figures 5.20b and 5.41b shows that for the pits closest together, where the mechanical interaction of the pits is expected to be greatest, the ( $N_i/N_f$ ) is lowest while the ( $N_p/N_f$ ) is highest, indicating that fatigue behaviour is propagation-dominant. As the separation distance increases, the interaction between the pits reduces and thus, initiation of cracks becomes less likely. Consequently, ( $N_i/N_f$ ) increases and the fatigue life increasingly becomes initiation-dominant.

The relationship between the overall fatigue lives and separation distance is shown in Figure 5.42 where fatigue lives can be seen to decrease with decrease in separation distance at all stress levels and pit sizes. This is consistent with previous observation that fatigue behaviour of double pitted samples, in air, is controlled by the crack initiation stage when there is mechanical interaction between the pits.

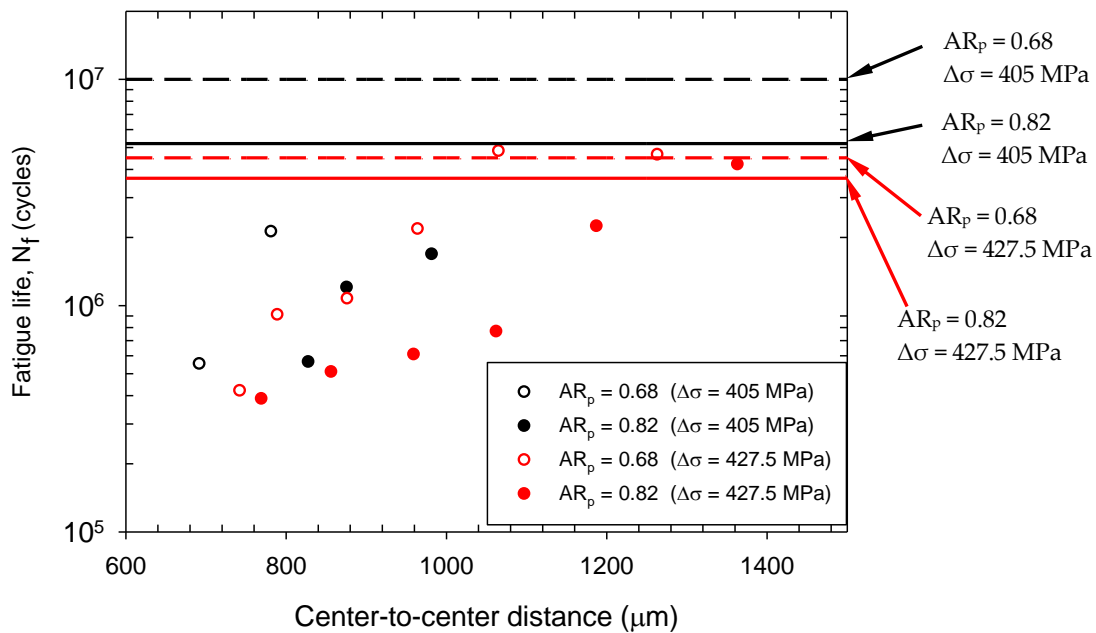


Figure 5.42 Fatigue lives versus separation distance between two pits as a function of pit size and applied stress. Horizontal lines represent corresponding values for single pits.

## 5.6 Fracture surface analysis

Fracture surface of specimens tested in air and corrosion fatigue were analysed using the SEM to understand the nature and mechanisms of crack initiation and propagation, including the profiles of the cracks.

### 5.6.1 Observations from air fatigue tests

For plain specimens, fatigue damage process consisted of crack initiation (CI), crack propagation (CPZ) and fast fracture (FFZ) (see Figure 5.43). Analyses of the fracture surfaces showed initiation sites, mainly at small surface defects on the edge of the specimen (crack initiation sites indicated with arrows). These cracks then propagated perpendicular to the loading axis into the interior of the specimen until the crack size became critical. A general trend in the final lengths of the edge cracks before fracture was that they decreased with increasing applied stress. For instance, the final lengths measured before fracture was 694 and 1890  $\mu\text{m}$  for tests carried out at 486 and 468 MPa respectively (Figure 5.43a and 5.43b). This behaviour can be explained by the fracture toughness of the material, which is equivalent to the stress intensity factor required for unstable crack growth. For this specific crack shape and specimen geometry, the crack size required to achieve this critical stress intensity factor will decrease when the applied stress is increased [31].

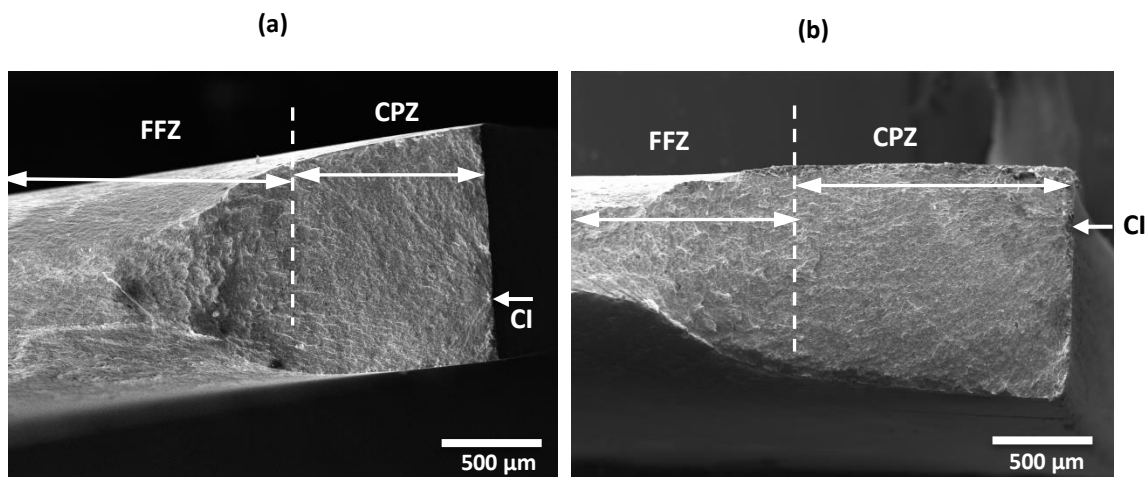
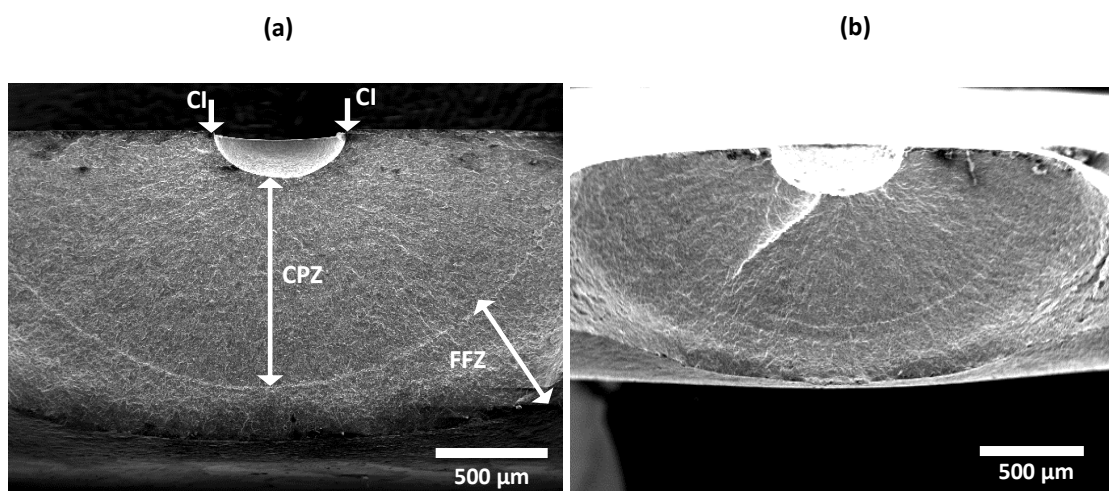


Figure 5.43 Crack initiation in plain specimens tested in air (a)  $\Delta\sigma = 486 \text{ MPa}$ ;  $N_f = 1.16 \times 10^5$  cycles (b)  $\Delta\sigma = 468 \text{ MPa}$ ;  $N_f = 8.27 \times 10^5$  cycles.

Figures 5.44 and 5.45 respectively show representative fracture surfaces of specimens containing single and double pits of different sizes tested in air and at different stress

levels. Fractographic analyses showed that the fatigue damage process proceeded through the following stages: crack initiation (CI), crack propagation (CPZ) and fast fracture (FFZ). These stages, shown in Figure 5.44a, were observed on all fractured specimens. Some of the samples were fractured in liquid nitrogen to reveal the shape of the cracks, which was found to be approximately hemispherical. High magnification analyses suggest that cracks initiated predominantly from the pit mouth. On the single-pitted specimens, the cracks that initiated at the pit mouth propagated radially outwards and likely coalesced at some point during the propagation stage. A notable observation at the bottom of the single pits was the differences in the propagation plane of the two cracks (Figures 5.44b and 5.44d). Differences in crack planes indicate that there were two different cracks. This was not observed in any of the double-pitted specimens since either only a single initiated crack or two cracks coalesced into a dominant crack and then propagated to failure during the fatigue life of the double-pitted specimens. Figure 5.45d shows a typical fracture surface of specimen on which the separation distance between the double pits was above the threshold distance for a particular pit size and stress level. The fracture surface and crack profile were similar to those of the single-pitted specimens except the presence of the second pit, which seems not to have any effect on the crack front. This corroborates the observations made during crack propagation monitoring, which showed that the double pits seemed to behave as single pits when their separation distance is above a threshold value.



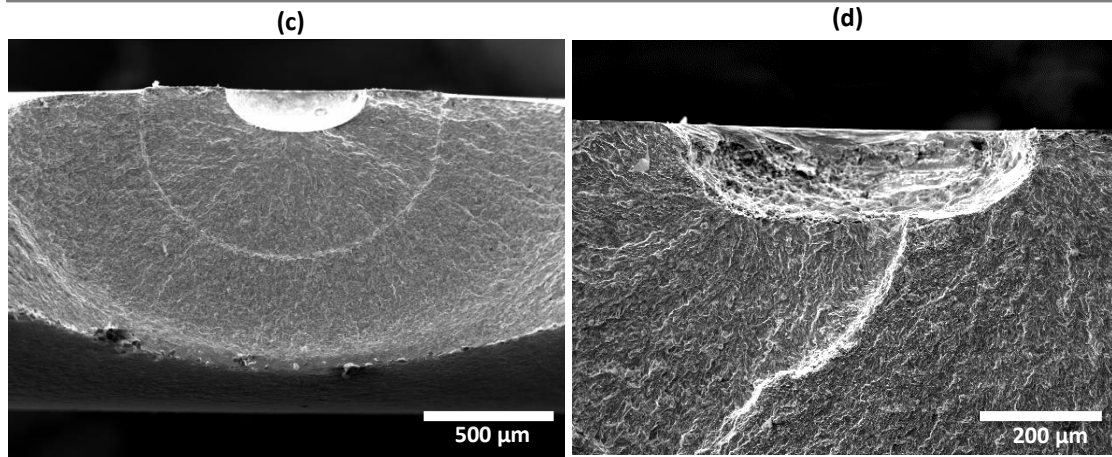


Figure 5.44 SEM images of fracture surface of single-pitted specimens in air. (a)  $\Delta\sigma = 427.5$  MPa,  $d_p = 202$   $\mu\text{m}$ ,  $N_i = 0.958 N_f$ ,  $N_f = 44.97 \times 10^5$  cycles; (b)  $\Delta\sigma = 405$  MPa,  $d_p = 265$   $\mu\text{m}$ ,  $N_i = 0.965 N_f$ ,  $N_f = 52.05 \times 10^5$  cycles; (c)  $\Delta\sigma = 450$  MPa,  $d_p = 267$   $\mu\text{m}$ ,  $N_i = 0.707 N_f = 5.35 \times 10^5$  cycles; (d)  $\Delta\sigma = 450$  MPa,  $d_p = 204$   $\mu\text{m}$ ,  $N_i = 0.889 N_f$ ,  $N_f = 15.13 \times 10^5$  cycles.

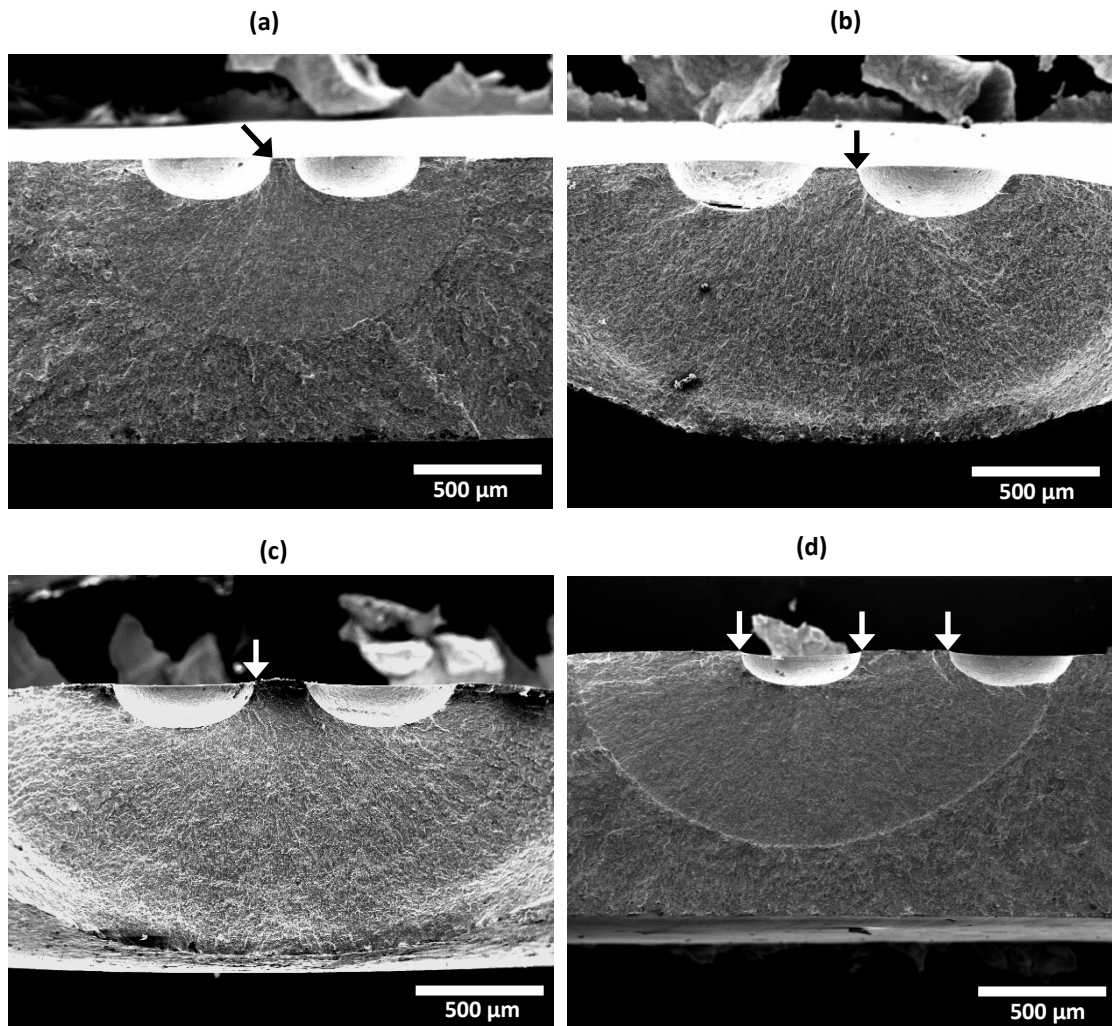


Figure 5.45 SEM images of fracture surface of double-pitted specimens in air (a)  $\Delta\sigma = 427.5$  MPa,  $d_{p(1)} = 268$   $\mu\text{m}$ ,  $d_{p(2)} = 274$   $\mu\text{m}$ ,  $s_{cc} = 776$   $\mu\text{m}$ ,  $N_i = 0.7 \times 10^5$  cycles,  $N_f = 3.85 \times 10^5$  cycles; (b)  $\Delta\sigma = 405$  MPa,  $d_{p(1)} = 265$   $\mu\text{m}$ ,  $d_{p(2)} = 273$   $\mu\text{m}$ ,  $s_{cc} = 877$   $\mu\text{m}$ ,  $N_i = 7.96 \times 10^5$  cycles,  $N_f = 1.196 \times 10^6$  cycles; (c)  $\Delta\sigma = 405$  MPa,  $d_{p(1)} = 197$   $\mu\text{m}$ ,  $d_{p(2)} = 206$   $\mu\text{m}$ ,  $s_{cc} = 782$   $\mu\text{m}$ ,  $N_i = 1.652 \times 10^6$  cycles,  $N_f = 2.112 \times 10^6$  cycles; (d)  $\Delta\sigma = 427.5$  MPa,  $d_{p(1)} = 203$   $\mu\text{m}$ ,  $d_{p(2)} = 195$   $\mu\text{m}$ ,  $s_{cc} = 1066$   $\mu\text{m}$ ,  $N_i = 4.485 \times 10^6$  cycles,  $N_f = 4.795 \times 10^6$  cycles. Crack initiation sites are indicated with arrows.

### 5.6.2 Observations from corrosion fatigue tests

Figure 5.46 shows representative fracture surfaces of single-pitted specimens tested in brine at different stress levels. Fractographic analyses showed that the corrosion fatigue damage process also proceeded through crack initiation (CI), crack propagation (CPZ) and fast fracture (FFZ) (Figure 5.46a and 5.46b). Several white lines emanating from the pit and the different crack planes observed on the entire test specimens especially at the pit bottom suggests multiple crack initiation sites (Figure 5.46c and 5.46d). This supports the observations made during crack growth monitoring where multiple cracks initiated from the pit bottom. The crack shapes in the aggressive environment were also found to be approximately hemispherical (see crack depth and width measurement on Figure 5.46a).

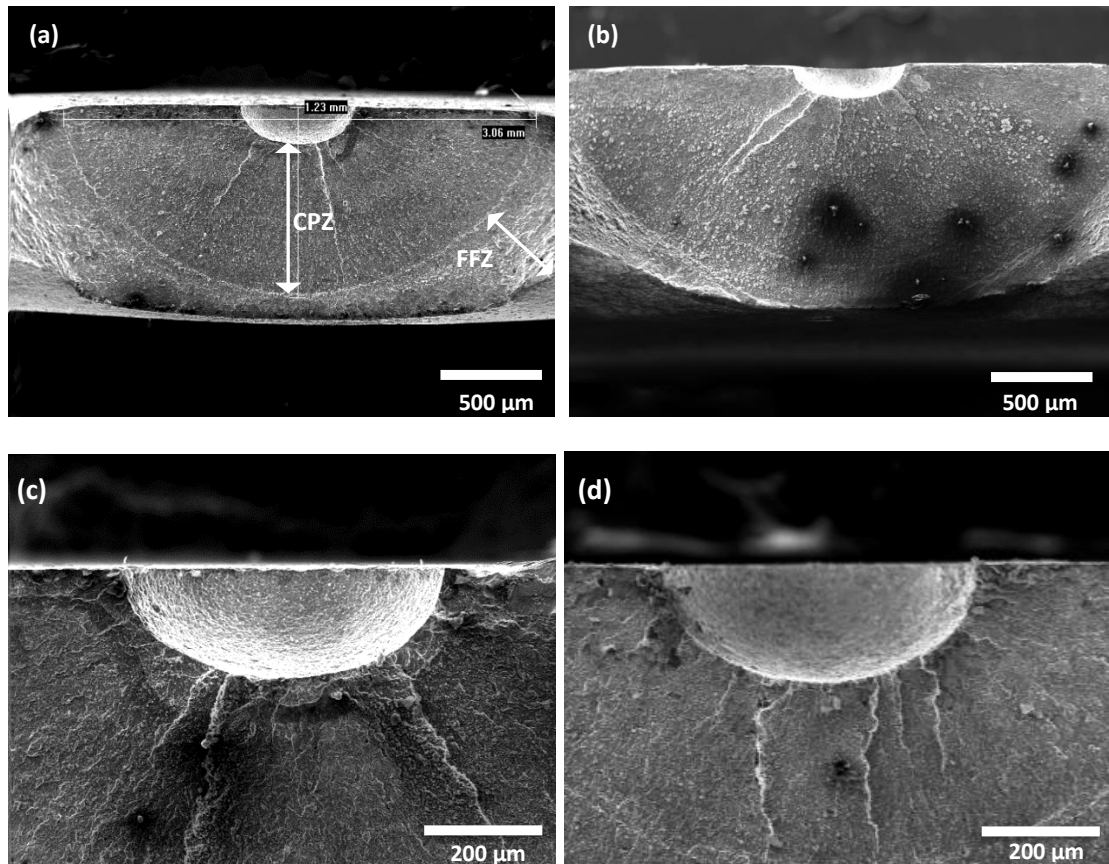


Figure 5.46 SEM images of fracture surface of single-pitted specimens in brine. (a&c)  $\Delta\sigma = 427.5$  MPa,  $d_p = 266 \mu\text{m}$ ,  $AR_p = 0.82$ ,  $N_i = 2.36 \times 10^5$  cycles,  $N_f = 3.13 \times 10^5$  cycles; (b)  $\Delta\sigma = 450$  MPa,  $d_p = 197 \mu\text{m}$ ,  $AR_p = 0.68$ ,  $N_i = 1.95 \times 10^5$  cycles,  $N_f = 2.44 \times 10^5$  cycles; (d)  $\Delta\sigma = 405$  MPa,  $d_p = 265 \mu\text{m}$ ,  $AR_p = 0.81$ ,  $N_i = 2.92 \times 10^5$  cycles,  $N_f = 4.19 \times 10^5$  cycles.



### 5.6.3 Aspect ratio of cracks emanating from pits

The replica method for crack monitoring only allows for measurement of the surface length of cracks; hence, it was impossible to measure the depth of the cracks. However, if the aspect ratio of a crack is known, it will be possible to make a realistic prediction of its depth from a known surface length. The aspect ratio,  $AR_c$ , of a surface crack was evaluated as the ratio of crack depth,  $d_c$ , to the crack surface length (including the pit width),  $a_c$ . The crack shapes of specimens tested in air and brine solution were analysed by measuring the depth and width of the crack front from the fracture surface of non-failed specimens, broken in liquid nitrogen. Figures 5.44a, 5.45a and 5.46a show representative fractographs of the crack shapes in air (single and double pits) and corrosion fatigue. Irrespective of the test environment, stress level, pit size and number of pits on the surface of the specimen, the surface cracks appear to have semi-elliptical shapes. Table 5.7 shows the dimensions and aspect ratios of cracks. It is noted that these images were taken at  $N > 0.7N_f$ , which only represents the crack shapes in the latter stages of cracking. The different crack planes together with results from in-air crack initiation behaviour from pit mouth suggest that the cracks in the early stages of cracking were corner cracks. These corner cracks grew separately on both sides of the pit until they were at or beyond the root of the pit where they merge into a single semi-elliptical crack.

*Table 5.7 Typical aspect ratios of surface cracks emanating from pits in air and corrosion fatigue.*

Specimen No	Stress range (MPa)	Pit depth ( $\mu\text{m}$ )	Pit aspect ratio	Crack depth ( $\mu\text{m}$ )	Crack width ( $\mu\text{m}$ )	Crack aspect ratio
SNAF64	427.5	198	0.68	1020	2528	0.81
SNAF51	450	141	0.52	793	1650	0.96
SN3PAF	427.5	268	0.82	1022	2460	0.83
SNAF39	405	272	0.82	1325	3117	0.85
SNCF59	405	265	0.81	1230	3060	0.80
SNCF61	450	197	0.68	1150	2860	0.80
SNCF84	450	141	0.52	752	1714	0.88
SNCF85	450	271	0.82	1239	2951	0.84

### 5.6.4 Mechanisms of fatigue damage

For all test types of carried out, the prevalent mechanisms of damage during the fatigue damage process were identified. Figure 5.47 shows representative low and high magnifications of morphology of fracture surfaces for tests carried out in air and the brine

solution. In the crack propagation zone, ductile fatigue striations, which are characteristic of sub-critical transgranular crack growth, were observed in air (Figures 5.47a – 5.47b).

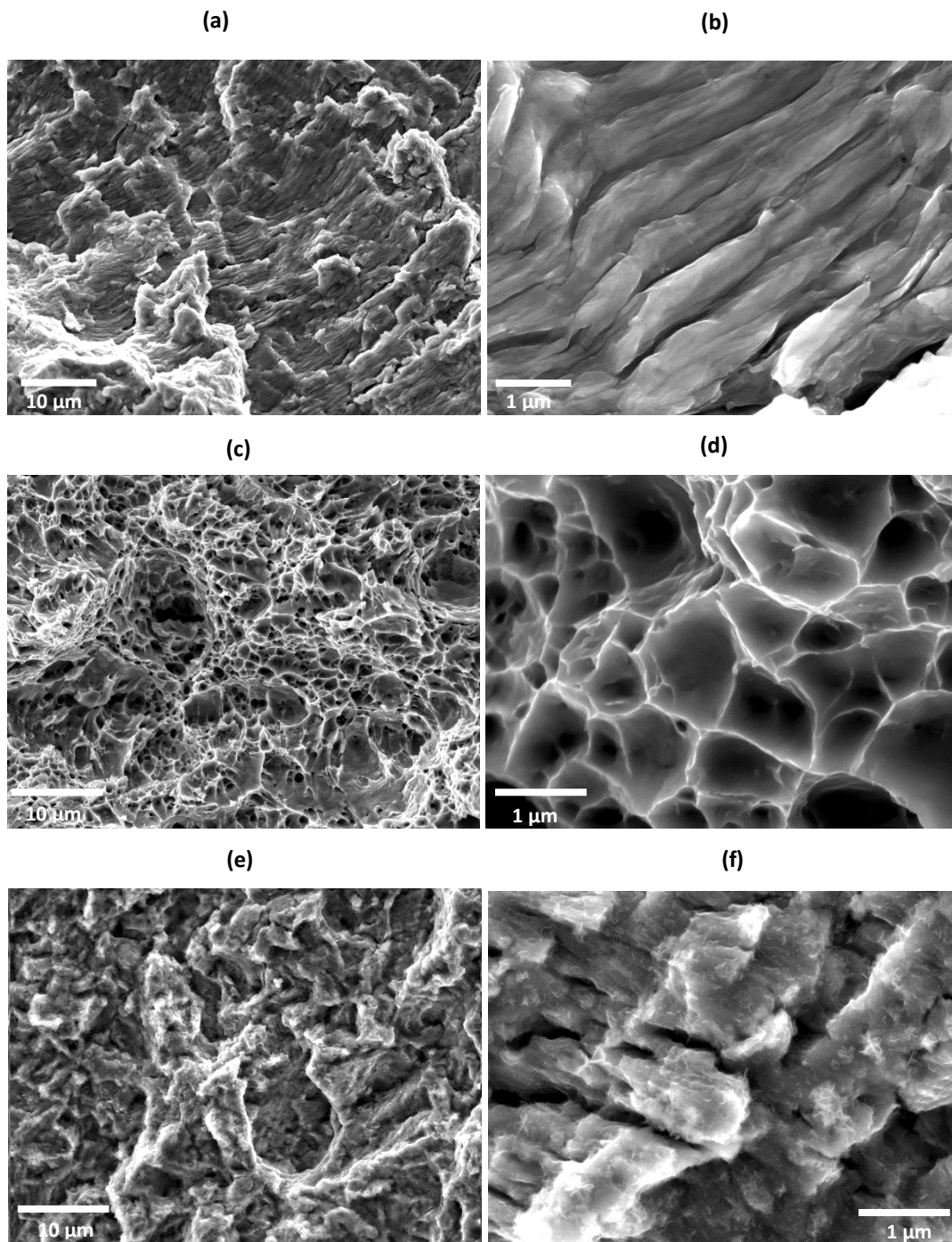


*Figure 5.47 Representative morphology of fracture surfaces for tests carried out (a & b) in air showing fatigue striations, (c & d) in air showing dimple rupture and micro-void coalescence and (e & f) in brine showing oxide products.*

A generally accepted model for rationalizing striation formation in ductile materials is the repetitive plastic blunting and re-sharpening occurring at the crack tip [288]. Figures 5.47c

– 5.47d show the fast fracture region where damage was by ductile tearing through dimple rupture and coalescence of microvoids in air and the test environment. In the aggressive environment, transgranular fracture mode and pronounced oxide products were found on the fracture surface, which typically indicates anodic dissolution during crack propagation (Figures 5.47e – 5.47f). On one hand, anodic dissolution process can lead to enhanced crack growth rates and shorter fatigue lives [16, 122, 289]. On the other hand, the wedge effect of oxide products can result in oxide-induced crack closure thereby reducing the crack growth rates [170, 290, 291]

### 5.7 Stress-life (S-N) curves

The fatigue endurance lifetime ( $N_f$ ) of pre-pitted specimens in air and brine solution were obtained from the summation of the crack initiation ( $N_i$ ) and crack propagation ( $N_p$ ) stages. The relationship between stress range and cycles to failure for the plain specimens in air for this material is given in Figure 5.48. It shows that a plain fatigue limit stress range (450 MPa) exists below which specimens did not fail under these loading conditions. Testing of single and double-pitted specimens in air and corrosion fatigue was carried out at stress ranges below the plain fatigue limit. Figure 5.48 shows that fatigue lives generally increased with decrease in stress range in air irrespective of pit size. The S-N curves for the pitted specimens relative to that of the plain specimen show that fatigue limit decreased with increasing pit size. Since the applied stresses are below the plain specimen fatigue limit, these results suggest that the pit acted as a strain localisation site where cracks initiated, which otherwise, would not initiate in the absence of the pit. The curves also show that limiting stresses are associated with each pit size at which specimens did not fail irrespective of whether cracks initiated from the pit or not. The estimated limiting stress range corresponding to each pit size is given in Table 5.8. The differences between the minimum stress range at which the specimen did not fail (including those with non-propagating cracks) and the maximum stress range at which failure occurred was taken to be the uncertainty in fatigue limit values. The table shows that a greater pit size generally leads to a lower fatigue limit.

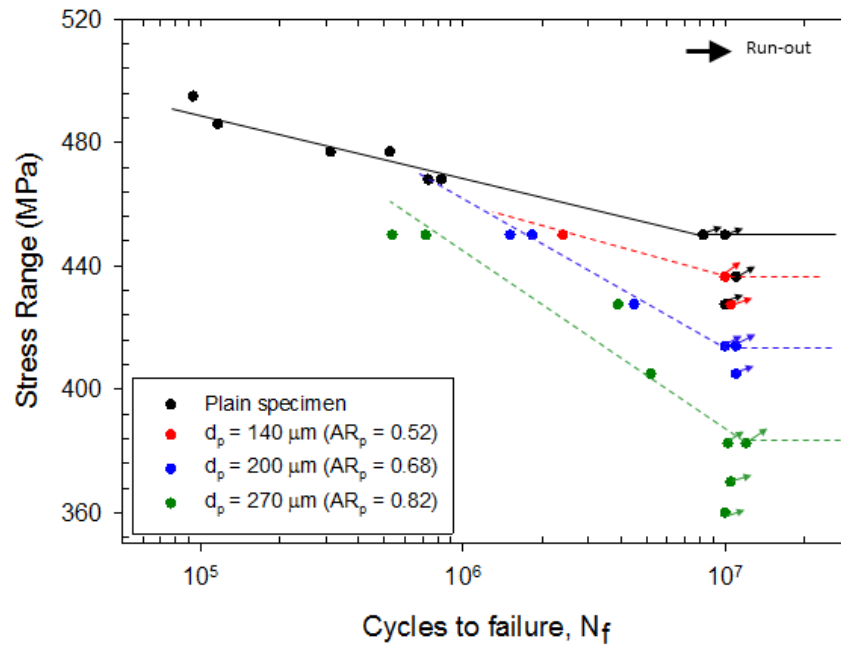


Figure 5.48 S-N endurance curves for plain and single-pitted specimens in air.

Table 5.8 Fatigue limit of X65 steel with and without pits ( $R = 0.1$ ,  $f = 15$  Hz)

Pit depth ( $\mu\text{m}$ )	Aspect ratio	Fatigue limit (MPa)
Plain	-	450
140	0.52	$436.5 \pm 13.5$
200	0.68	$414 \pm 13.5$
270	0.82	$382.5 \pm 22.5$

The endurance curves for double-pitted specimens were also compared with those of plain and single-pitted specimens. Ideally, double pits, which have different sizes but identical separation distances can only be compared at the same stress level on the S-N curve. As discussed previously, the limitation of the experiment procedure employed for generating the double pits meant that the separation distance between pits of the different sizes varied, although not significantly (7% maximum). The effect of double pits on fatigue lives is depicted in Figure 5.49. A shift of the S-N curves to the left, compared to the single pits, indicates a further reduction in fatigue life when double pits are present; even for the same stress level and pit sizes. However, the extent of the reduction depends on the separation distances between the pits. Irrespective of pit size, fatigue lives generally become shorter with decreasing separation distance between pits and with increasing stress level. Furthermore, for a given stress level, fatigue lives are shorter when the pit size increases. It is interesting to note that the slopes of the S-N curves for double

pits with similar separation distances appear to be similar irrespective of pit size and that the slopes of the curves when  $s_{ee}$  is 200  $\mu\text{m}$  is similar to the slopes of corresponding single pit sizes. The latter observation suggests that there may be endurance limits that will correspond to a fatigue life of  $10^7$  cycles but will be lower than that associated with that of single pit.

Figure 5.50 shows the results for the tests conducted in brine solution, plotted with reference to air tests. It can be observed that fatigue lives are shorter in the brine solution compared to air. Fatigue lives were also found to increase with decreasing stress range and decreasing pit size. A progressive decrease in the S-N curve compared to corresponding in-air plots show the effect of the aggressive environment in the form of a significant degradation in fatigue performance. Three additional tests (also plotted on the corrosion fatigue S-N curve) were carried out for each pit size at a lower stress range (350 MPa) to evaluate the possibility of an endurance limit in corrosion fatigue. This chosen stress was the lowest possible given the available testing time. The trend in the curves for each pit size suggests a reduction/elimination of the fatigue limit under corrosion fatigue conditions for all pit sizes.

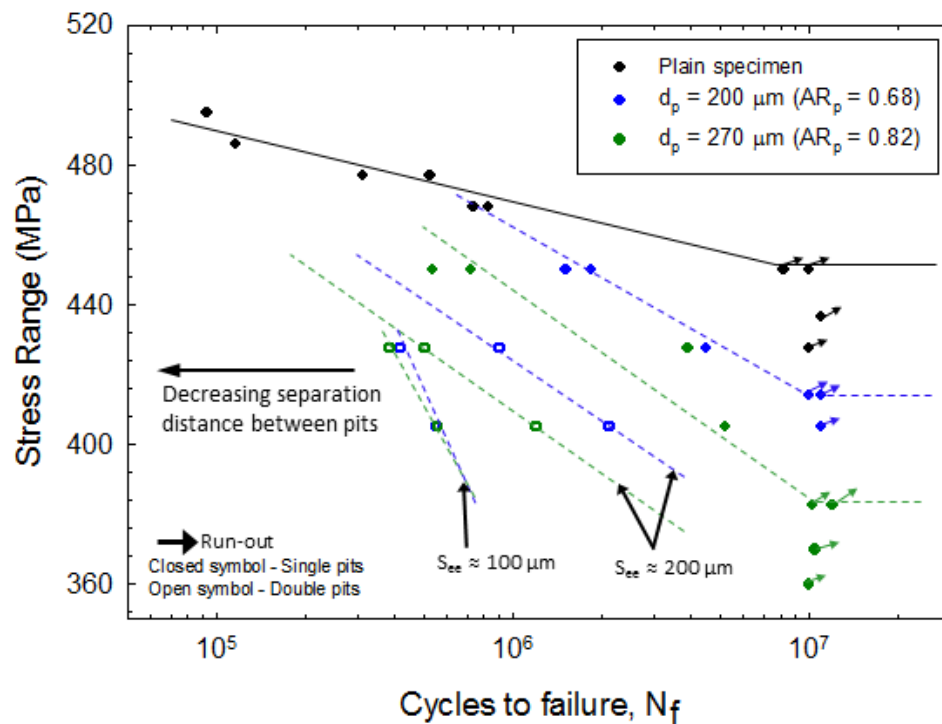


Figure 5.49 S-N endurance curves for plain, single-pitted and double-pitted specimens in air.

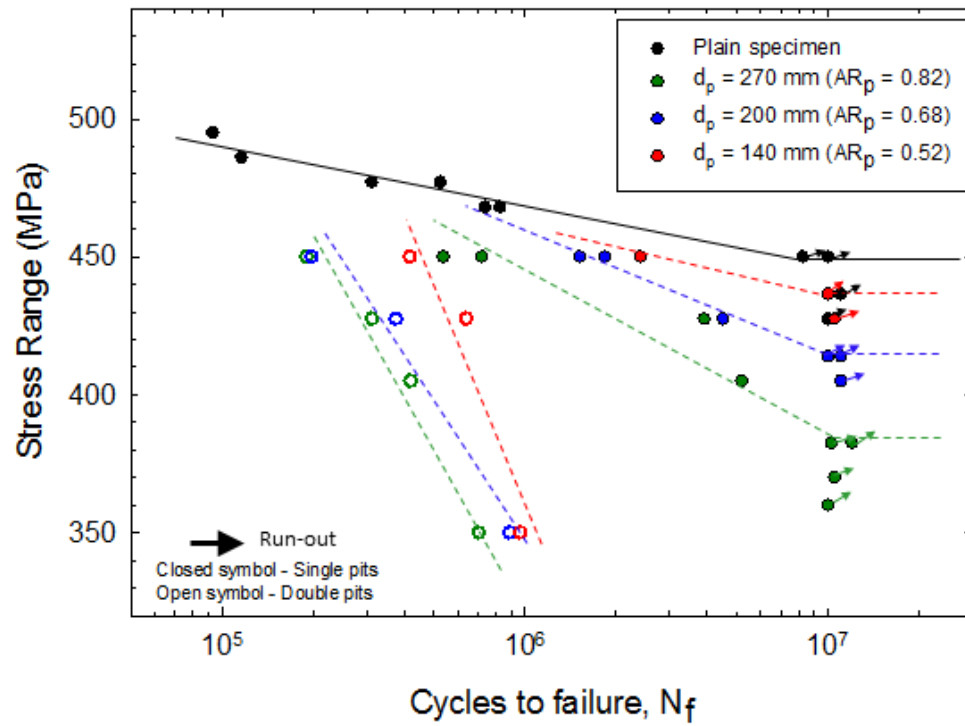


Figure 5.50 S-N endurance curves for single-pitted specimens in air and brine solution.

---

# **Chapter 6**

## **Finite Element Analysis Results and Discussion**

---

## 6.1 Introduction

In many metal-environment systems where corrosion pits are precursors to fatigue cracks, understanding the conditions that facilitate cracking from corrosion pits is important in order to predict pit-to-crack transition. As discussed in **Chapter 5**, the present research study showed that corrosion pits are the preferred sites for crack nucleation and that the preferred sites around pits where crack initiate and pit-to-crack transition lifetimes depend on pit characteristics (pit depth, pit aspect ratio and proximity between pits), stress level, operating environment and interactions between them. These results demonstrate that the conditions required for transition depend not only on electrochemical, but also on mechanical factors. Although the latter, through strain-assisted dissolution, can influence corrosion kinetics to a large extent, its primary influence is through stress and strain localization effect, which can induce plasticity in the vicinity of the pit and thereby result in cracking. Therefore, the relationship between these mechanical factors, the size, shape and proximity of pits and applied stress must be appropriately understood for accurate pit-to-crack transition modelling. Although stress and strain localization effectively increases the maximum stress and strain on a component, the mechanical response cannot be determined solely by the maximum stress (elastic stress concentration factor) or strain (elastic strain concentration factor) around the pit. Other factors such as stress/strain distribution profile (elastic-plastic behaviour), cyclic loads and material properties must be considered. In the present study, these phenomena were investigated in detail with a view to gaining greater insight into the mechanics-based conditions that facilitate emergence of cracks from pits. Based on the results derived during this study, plausible explanations are postulated to support experimental observations relating to crack initiation sites and pit-to-crack transition lifetimes.

A detailed FEA was carried out to evaluate the distribution of stress and strain around 'artificial' and 'ideal' pits of varying sizes, shapes and separation distances, subject to a remote tensile loads. The artificial pits are those pits obtained experimentally using the micro-capillary cell, while the ideal pits are idealizations of the experimental pits as elliptically shaped 3-D models having a smooth surface (see Section 4.4 for description of procedure). The models of the artificial pits were obtained from 3-D scans by employing a



3-D confocal microscope. In general, each or both types of 3-D models were analysed depending on computational time limitations. The results from the present investigation have been divided into the following categories:

1. Evaluation of changes in pattern of distribution of stress and strain as a result of changes in pit sizes due to pit growth.
2. Assessment of the correlations between localisation of crack initiation sites, pit size, proximity between pits, applied stress and general pit-to-crack transition behaviour.

## 6.2 Mesh convergence study

The results presented in Figure 6.1 show that the stress concentration factor converged after a finer mesh element size of 10 and 5  $\mu\text{m}$  for the ideal and artificial pits respectively. Therefore, in the finer and coarse regions respectively, element sizes of 10 and 100  $\mu\text{m}$  were employed for ideal pits and 5 and 100  $\mu\text{m}$  for artificial pits. Depending on pit characteristics, mesh density around the pits will change to ensure consistency in the size of elements created around a pit but the levels of accuracy should be similar.

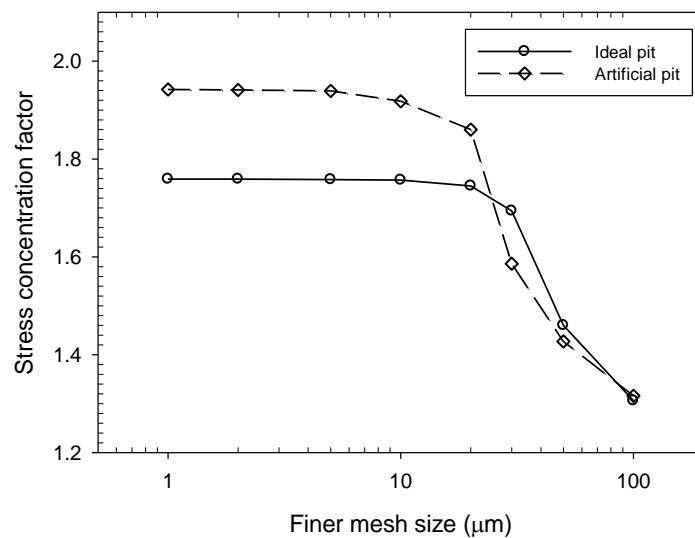


Figure 6.1 Variations of stress concentration factor with finer mesh size.

## 6.3 Model validation

Figure 6.2 shows that predictions from the FE model are in good agreement with those obtained empirically. A satisfactory agreement can also be observed in Figure 6.3, which

compares the surface strain predictions from the FEA of an artificial pit with those obtained from DIC experiment. In general, it can be concluded that the FE models of the ideal and artificial pits are reasonably valid for conducting further investigations on stress and strain distributions around corrosion pits.

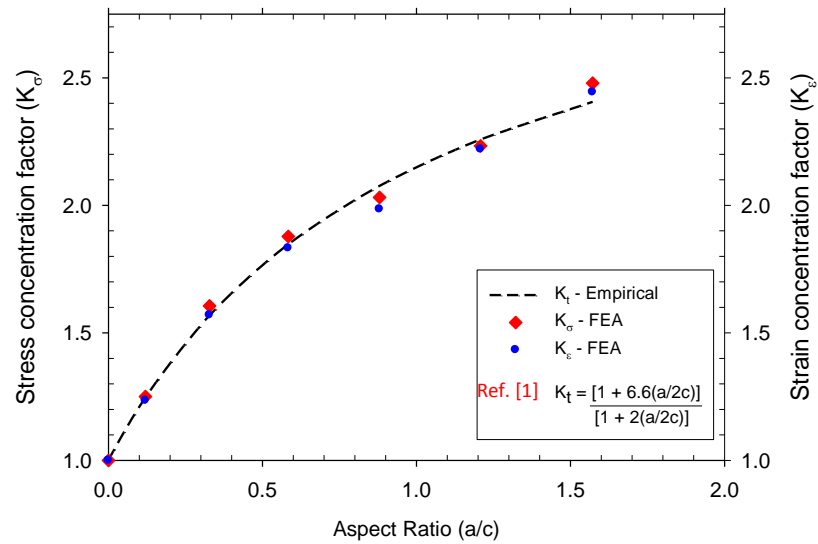
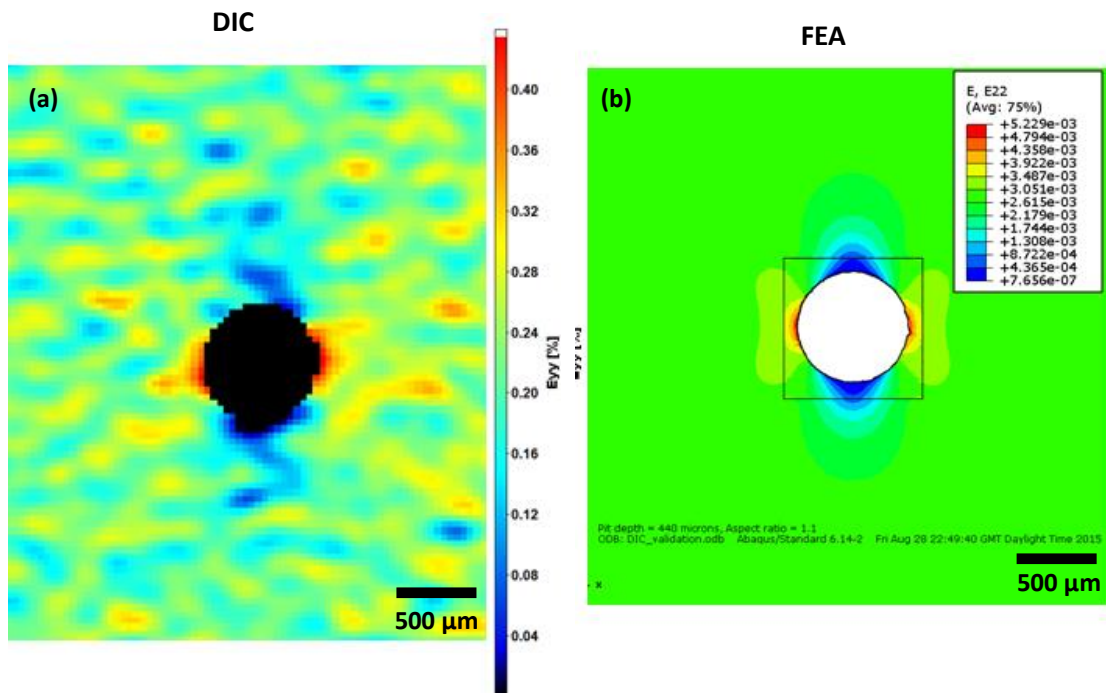


Figure 6.2 Comparison between empirical and FEA model predictions of stress and strain concentration factors for various pit aspect ratios.



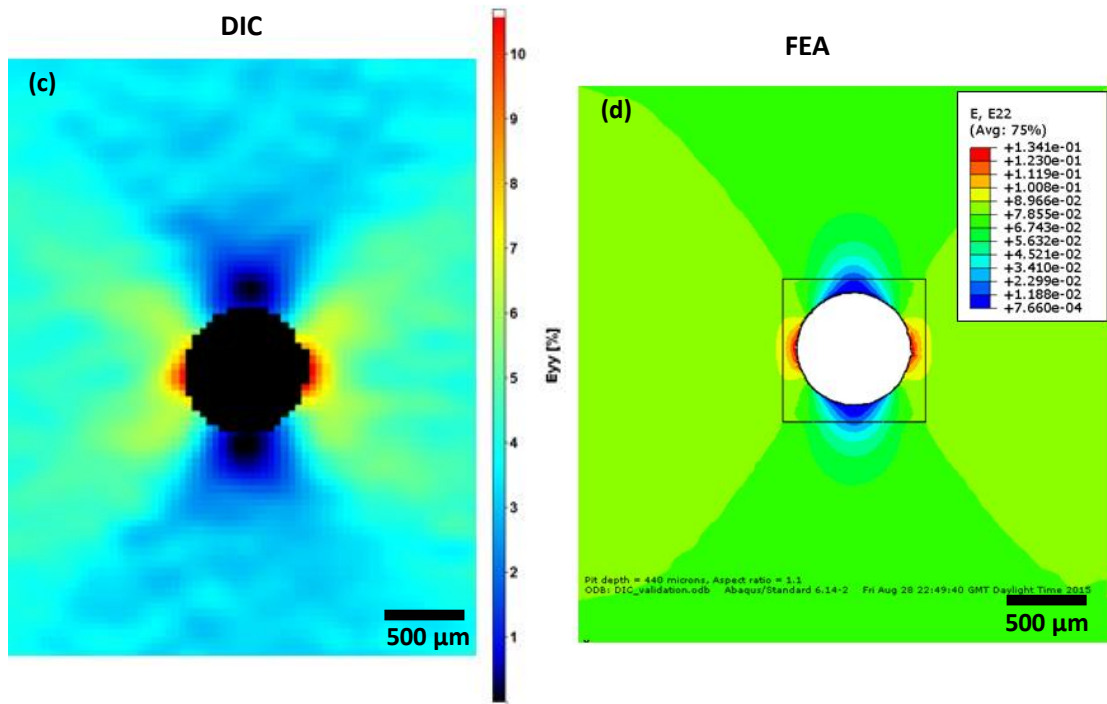


Figure 6.3 Validation of FEA model predictions and surface strain maps obtained from DIC measurements for an artificial pit that is 440  $\mu\text{m}$  deep pit and with aspect ratio of 1.1 loaded to 470 MPa in (a & b) and 596 MPa in (c & d). Loading direction is from top to bottom.

#### 6.4 Changes in stress and strain distribution due to pit growth

Since modelling of pit growth in a continuous mode is very challenging, a discretized approach was adopted in which pit sizes at discrete time intervals were modelled to simulate pit growth. Thus the influence of time-dependent increasing pit size (pit growth) on localization of stress and strain was investigated by evaluating the distribution of stress and strain around pits of different depths and aspect ratios. The modelled pit sizes, which were obtained from pit growth experiments, were chosen to simulate the instantaneous pit size at different time periods ranging from 3600 to 28800 seconds. The 3-D models of fatigue specimens containing the pits were loaded to stresses between 425 and 500 MPa (similar to those applied during experiments). Table 6.1 summarises the experimental average values of the characteristics of the pits that were modelled.

Table 6.1 Summary of characteristics of pits obtained experimentally.

Time (s)	Pit depth ( $\mu\text{m}$ )	Pit aspect ratio
3600	112	0.44
7200	140	0.52
14400	200	0.68
21600	240	0.78
28800	270	0.82

Figure 6.4 shows representative 3-D distribution of stress and total strain in a modelled pre-pitted flat fatigue specimen containing a 270  $\mu\text{m}$  pit and loaded to 500 MPa. It can be observed that the critical region where stress and strain are localized is generally in the vicinity of the pit in the direction perpendicular to the loading axis. This agrees with experimental observations where cracks were found to initiate from the pits in pre-pitted specimens due to strain localisation.

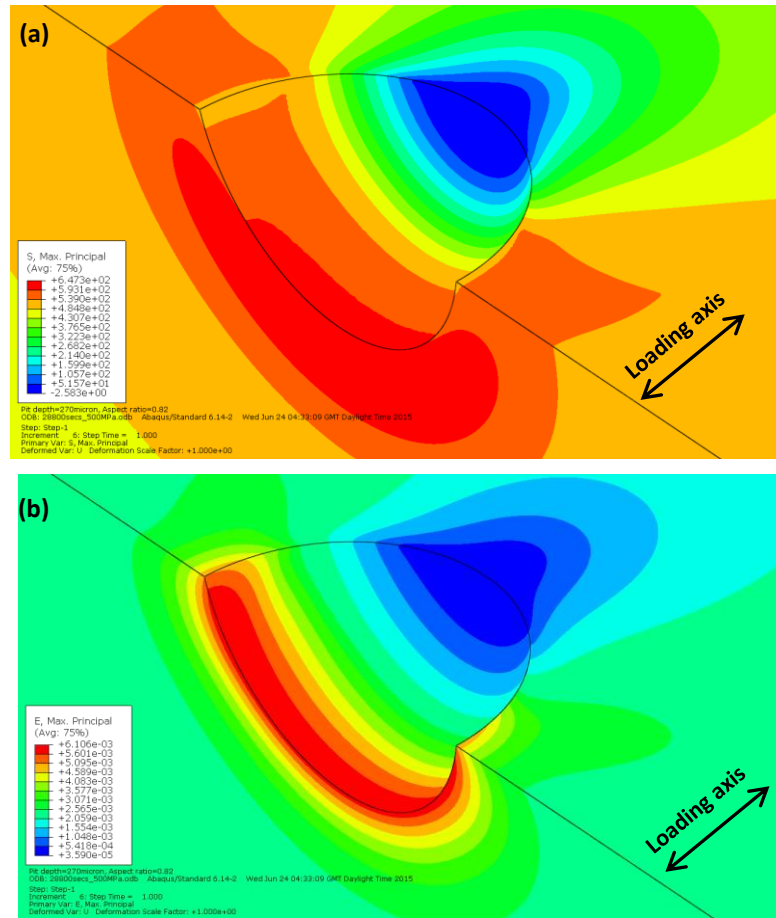


**Figure 6.4** Representative contour plots showing maximum principal stress distribution (a) and maximum principal strain distribution (b) around a 270  $\mu\text{m}$  pit in a flat fatigue specimen loaded to 500 MPa.

The localised stresses and strains evaluated as maximum values of the principal stress, principal strain and plastic strain for each pit size at different stress levels are compared graphically in Figure 6.5. The corresponding relations of the localised stresses with yield stress of the material and of localised strains with yield strain (equivalent total strain at yield point) and nominal strain (elastic strain equivalent to the elastic nominal stress) are shown in Figures 6.5a, 6.5b and 6.5c respectively. In general, local stresses and strains are higher than the yield stress and yield strain of the material indicating localised plasticity.

The localised stress and strain increased with increasing pit depth, pit aspect ratio and applied stress. Similar findings have been reported in previous studies on the mechanical effect of pits in structural components [201, 230, 234]. By way of extension, since the investigated pit characteristics are time-dependent, the results also suggest that the localised resulting from pits increase with time. This will further intensify these effects as time increases. An interpretation of this is that a growing pit with increasing size may be inducing corresponding increasing levels of stress and strain with time, a behaviour which can be perceived as the pit inducing local dynamic strain. However, it is conceivable that this intensification would not normally continue endlessly since the conditions for crack nucleation will be determined by a combination of a critical pit size and mechanical and electrochemical factors. As dynamic strain, notably dynamic plastic strain is recognized to result in the nucleation of cracks, it is thought that the plastic strain rate resulting from the growing pit would increase.

From the perspective of cracking, it has been recognised that localised plastic flow is the main driving force for fatigue crack nucleation [31, 292, 293]. Based on this premise, the results shown in Figures 6.5b and 6.5c would suggest that the conditions required for crack nucleation will be more favoured at relatively larger pit sizes and higher applied nominal stresses for which local total and plastic strains are relatively higher. In other words, cracks will tend to initiate more readily i.e. shorter period for crack nucleation, at relatively larger pit sizes and higher stress levels. This agrees well with experimental observations in air and aggressive environment reported in Chapter 5 where it was shown that pit-to-crack transition lifetimes decreased with increase in pit depth, pit aspect ratio and stress level (see Section 5.5.1.3).

To explain the nucleation of cracks from the pit mouth, the distribution of principal stress, principal strain and plastic strain in the pit region is examined further by comparing the cross section in the pit region viewed perpendicular to loading for 112 and 270  $\mu\text{m}$  pits representing shallow (early stages of pitting) and deep pits (latter stages of pitting). Representative results for 425 MPa and 500 MPa are presented in Figures 6.6 and 6.7 respectively. It can be observed that stress distributions appear to be uniform around the pits although the stress tends to be more concentrated at the pit base at relatively higher stresses and larger pit size (Figure 6.6a&b and 6.7a&b).

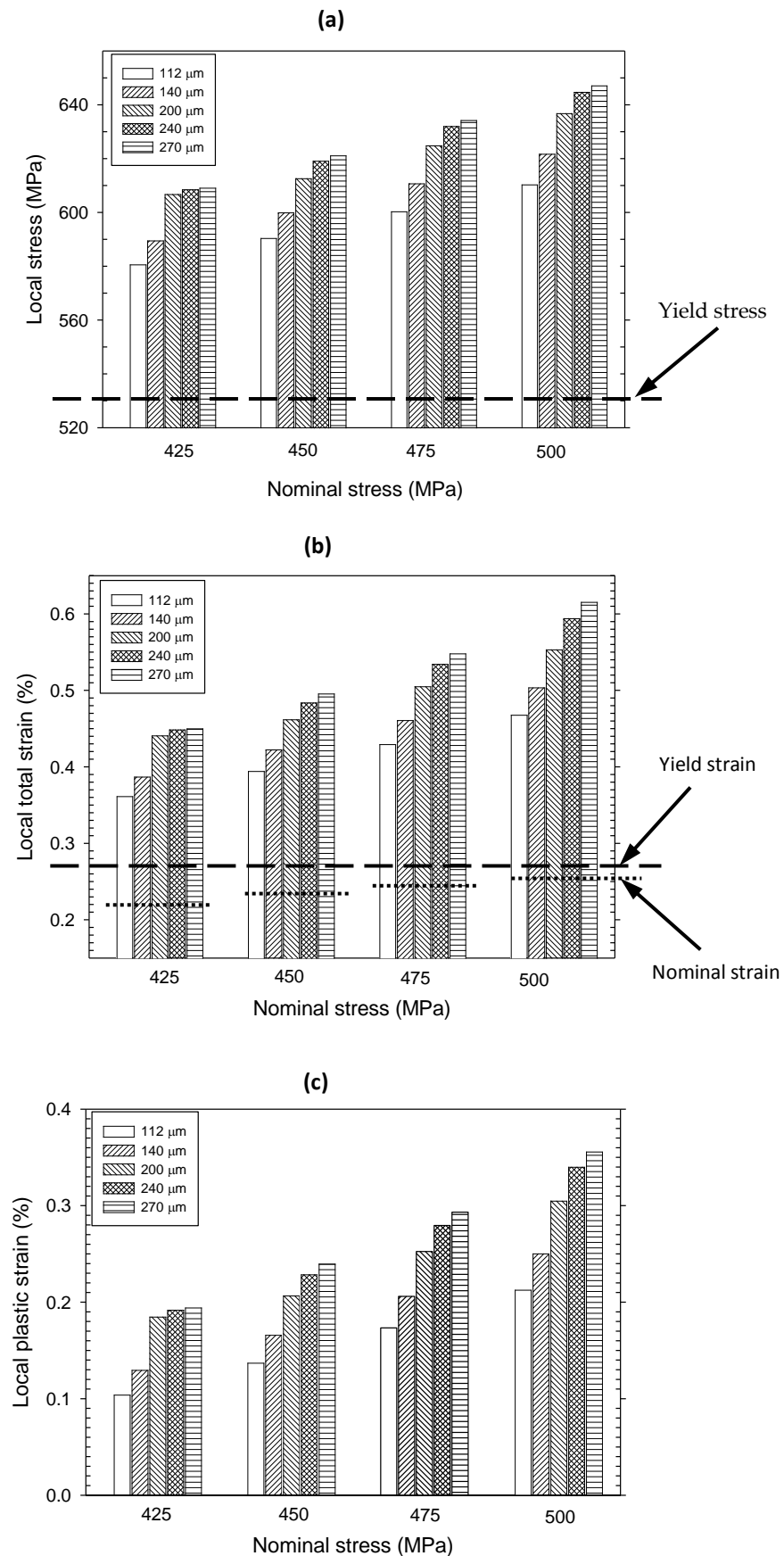
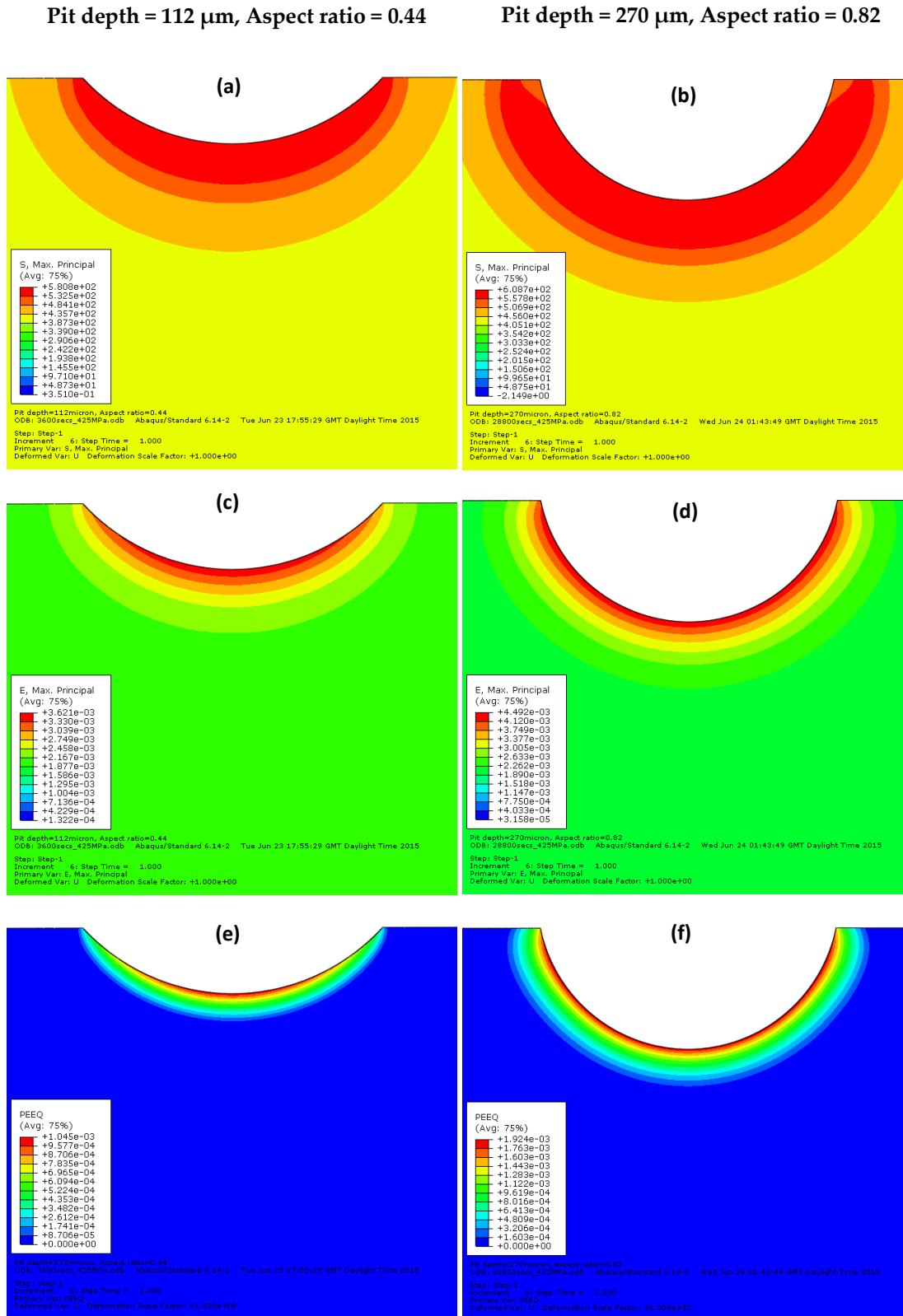
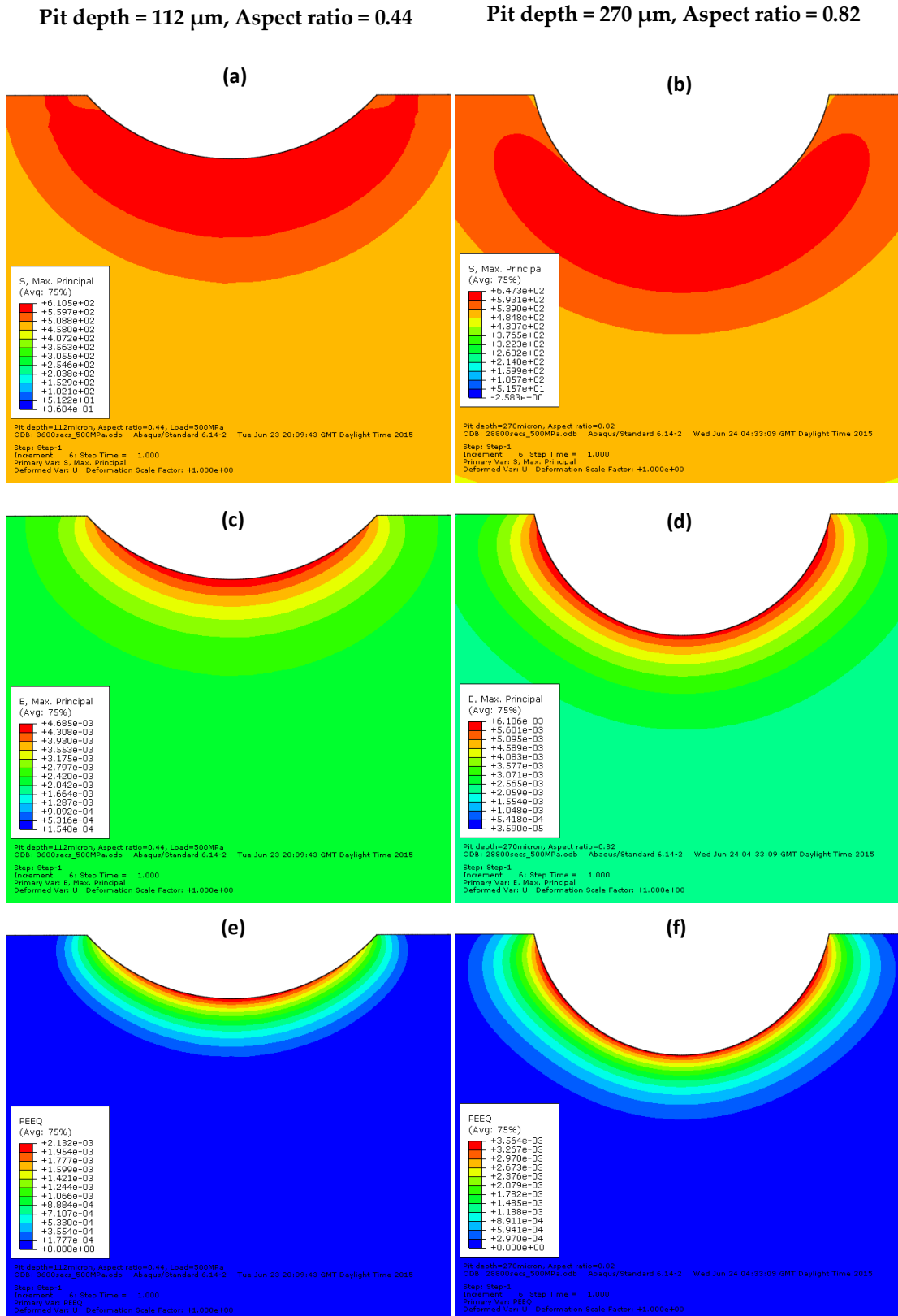


Figure 6.5 Summary of maximum values of (a) local maximum stress (b) local maximum total strain and (c) local maximum plastic strain for pits of increasing.



**Figure 6.6** Comparison between stress distribution (a,b), total strain distribution (c,d), and plastic strain distribution (e,f) between a 112  $\mu\text{m}$  (a,c,e) and 270  $\mu\text{m}$  (b,d,f) pit loaded at 425 MPa and viewed perpendicular to the loading axis.



**Figure 6.7 Comparison between stress distribution (a,b), total strain distribution (c,d), and plastic strain distribution (e,f) between a 112  $\mu\text{m}$  (a,c,e) and 270  $\mu\text{m}$  (b,d,f) pit loaded at 500 MPa and viewed perpendicular to the loading axis.**



Qualitative results of inspection of the area around the pit surface (Figure 6.8) at different load levels shows that the maximum stresses occurred at the pit bottom (see principal stress section of Table 6.2). Figure 6.6c&e and 6.7c&e show that the distributions of total strains and plastic strains appear to be concentrated at the base for the shallow pit but tend to shift away from the base to the region between the pit mouth and pit base. The maximum strains occurred at different regions depending on pit size (see principal strain and plastic strain sections of Table 6.2). Whereas the maximum strains are predominantly located at the base at pit depths up to 200  $\mu\text{m}$  at all stress levels, they are shifted away from the base to region closer to the pit mouth (point 'B' in Figure 6.8) at relatively larger pit depths. However, further analysis of these deeper pits shows that the differences between the values at regions B and E (pit base) is generally less than 1%. Therefore, it is concluded that the strain distribution within the pit are largely uniform from the mouth to the base of the pit and not concentrated at the pit mouth.

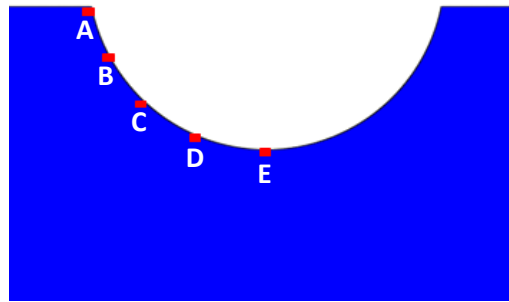


Figure 6.8 Schematic of critical areas of stress and strain concentration around a pit.

Table 6.2 Summary of locations of maximum stresses and strains around pits of various sizes loaded to different stress levels. (Refer to Figure 6.8—for location of letters A to E).

**Principal stress**

Pit depth ( $\mu\text{m}$ )	425 MPa	450 MPa	475 MPa	500 MPa
112	E	E	E	E
140	E	E	E	E
200	E	E	E	E
240	E	E	E	E
270	E	E	E	E

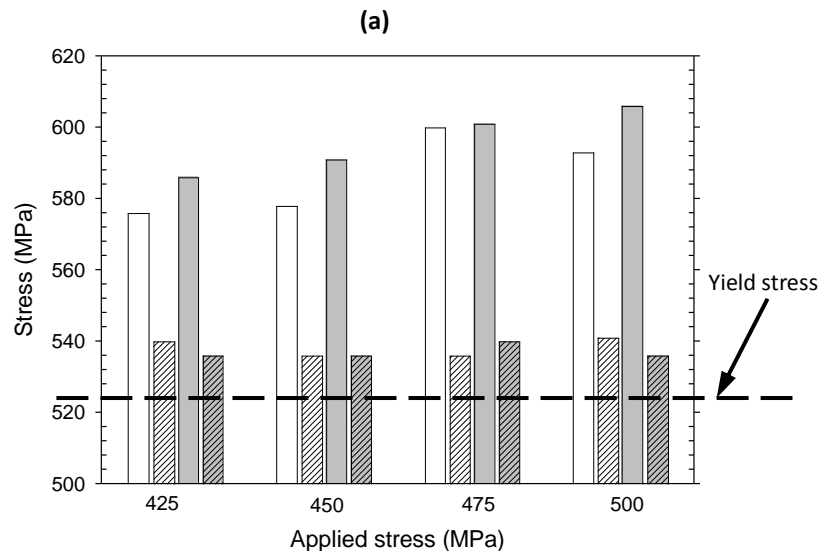
**Principal (total) strain**

Pit depth ( $\mu\text{m}$ )	425 MPa	450 MPa	475 MPa	500 MPa
112	E	E	E	E
140	E	E	E	E
200	E	E	E	E
240	E	B	B	B
270	B	B	B	B

Plastic strain

Pit depth ( $\mu\text{m}$ )	425 MPa	450 MPa	475 MPa	500 MPa
112	E	E	E	E
140	E	E	E	E
200	E	E	E	E
240	E	D	B	B
270	B	B	B	B

Figure 6.9 shows comparisons between the maximum values of principal stresses and strains obtained at the pit mouth (point 'A' in Figure 6.8) and pit bottom (point 'E' in Figure 6.8). The main observation is that stresses and strains are generally higher at the pit bottom than at the pit mouth. This observations is consistent with findings reported in [234, 269]. In an investigation on the role of mechanics in determining the location if crack initiation, it was concluded that cracks initiated from the region around a pit where the maximum principal stress acted [294]. These results would suggest that the mechanical conditions for crack nucleation are more favourable at the pit bottom hence, cracks should preferentially initiate at the pit bottom rather than at the pit mouth. However, this is not in agreement with experimental observations where cracks were found to initiate predominantly from the pit mouth in air tests and at high stresses in corrosion fatigue tests.



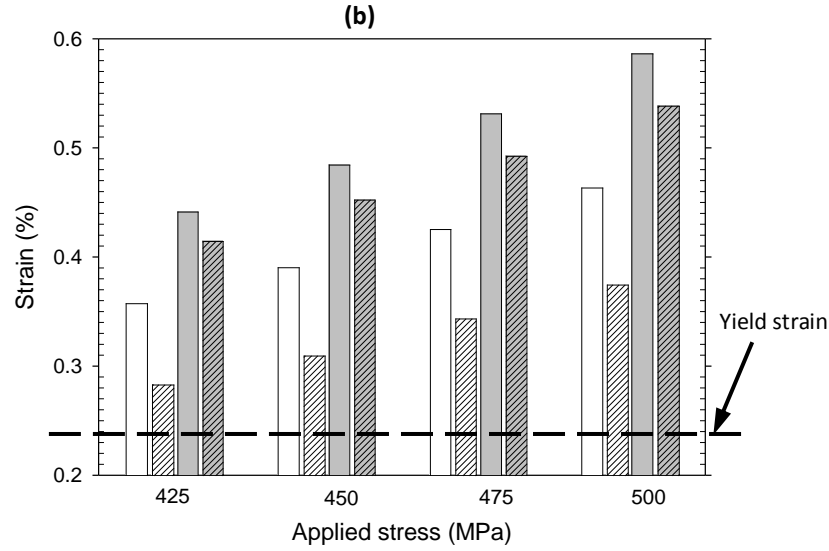


Figure 6.9 Comparison between (a) stress distribution, and (b) strain distribution at the pit base and pit mouth for pits with depths of 112 and 270  $\mu\text{m}$  loaded to different stress levels. White and grey colour fills are for 112 and 270  $\mu\text{m}$  pits respectively. Plain and hatched patterns are for pit base and pit mouth respectively.

Further investigation was carried out by considering that a corrosion pit can be modelled as a two-dimensional semi-elliptical crack hence, the stress intensity associated with a pit can be estimated. Employing stress intensity factor solutions for a semi-elliptical surface crack in a semi-infinite plate, Equation 6.4 [295, 296], the values of stress intensity factor were evaluated at the pit mouth (where  $\Phi = 0$ ) and pit bottom (where  $\Phi = 90^\circ$ ) using the experimental aspect ratios for the 140, 200 and 270  $\mu\text{m}$  pits and  $\Delta\sigma = 450$  MPa. These three pit aspect ratios ( $a/c < 1$ ) were chosen so as to correlate with those employed for fatigue testing while the stress was chosen because it was the stress range at which cracks were able to initiate from the three chosen pits.

$$\Delta K_I = \frac{\sigma\sqrt{\pi a}}{E(k)} \left[ \left[ M_1 + M_2 \left( \frac{a}{t} \right)^2 + M_3 \left( \frac{a}{t} \right)^4 \right] g f_\Phi f_w \right] \quad 6.4$$

where  $\Delta K_I$  is the stress intensity factor at a point on the crack surface lying at an angle,  $\Phi$ , to the major axis,  $\sigma$  is the applied stress range,  $E(k)$  is the shape factor for an ellipse which is given by the square of the complete elliptical integral of the second kind and  $M_1$ ,  $M_2$ ,  $M_3$ ,  $f_\Phi$ ,  $f_w$  and  $g$  are boundary correction factors, the expressions for which can be found in [295].  $a$ ,  $c$ ,  $t$  and  $\Phi$  are defined in Figure 6.10.

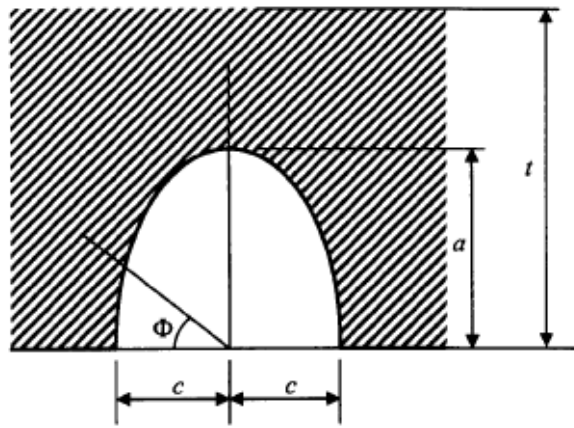


Figure 6.10 Schematic representation of stress intensity factor in a corrosion pit.

The results, summarised in Table 6.3, show that the stress intensity values corresponding to a given pit size are not significantly different at the pit bottom and pit mouth. These results, which are also in agreement with results from stress and strain distributions discussed, suggest that conditions for crack nucleation are more favourable at the pit bottom than at the pit mouth. This is also inconsistent with experimental observations where cracks initiated predominantly from the pit mouth. In a bid to gain more insight into the reason for this cracking behaviour, it was conceived that crack nucleation from the mouth of the pits may be due to stress and strain distribution associated with the real shape and actual morphology of a pit rather than the ideally uniform and smooth surface hemispherical shapes assumed for the pits (notably for modelling convenience). Such a difference may account for the inconsistencies between experimentally observed crack initiation sites and strain localisation around a pit. Details of this investigation are presented in the following section.

Table 6.3 Summary of stress intensity factor at the pit mouth and pit bottom at point of pit-to-crack transition assuming a pit is a 2-D semi-elliptical crack.

Pit depth ( $\mu\text{m}$ )	Pit mouth $K_I$ ( $\text{MPa}\sqrt{\text{m}}$ )	Pit bottom $K_I$ ( $\text{MPa}\sqrt{\text{m}}$ )
140	3.85	3.97
200	3.26	3.29
270	2.94	3.23

## 6.5 Analyses of stress and strain distribution in artificial pits

### 6.5.1 Single pits

In this investigation, the distribution of stresses and strains were evaluated in artificial pits in order to gain insight into pit-to-crack transition behaviour that was observed experimentally i.e. cracks initiating predominantly from the pit mouth. As discussed in Section 6.5, results from stress and strain analyses, employing uniform and smooth 3-D models of pits and LEFM, could not explain this behaviour. Hence, analyses were carried out on artificial pits instead of ideal pits. The procedure employed for the 3-D modelling of the artificial pits has been previously described in Section 4.3. It was impractical to analyse all the pre-pitted specimens mainly because of the excessively large size of the 3-D pit scans which required significant computing. The alternative was to down-sample the *.step* files (i.e. reduction of resolution of scan data) but this resulted in inaccurate pit profiles. Therefore, only representative pit sizes from which cracks initiated during in-air and corrosion fatigue tests were selected for this study. A sample containing double pits was also modelled to evaluate the influence of proximity between pits on crack initiation lifetimes.

Representative contour plots showing distribution of principal stresses and strains associated with the simulated pits viewed in the direction perpendicular to the loading axis are presented in Figures 6.11 - 6.12. These pits are from samples tested in air. The most notable observation is the localisation of strain towards the pit mouth close to the specimen surface whereas the stress is concentrated at the pit bottom. Note that the applied nominal stresses are elastic but the localised stresses and strains are higher than the material's yield stress (529 MPa) and yield strain (0.2524 %) thus indicating local plastic deformation around the pits. The localisation of strain towards the pit mouth can be ascribed to a reduced constraint to plastic flow at this location [202, 269]. This results in a preference for the material to yield towards the pit mouth rather than at other regions where constraint is relatively greater, notably, at the pit bottom.

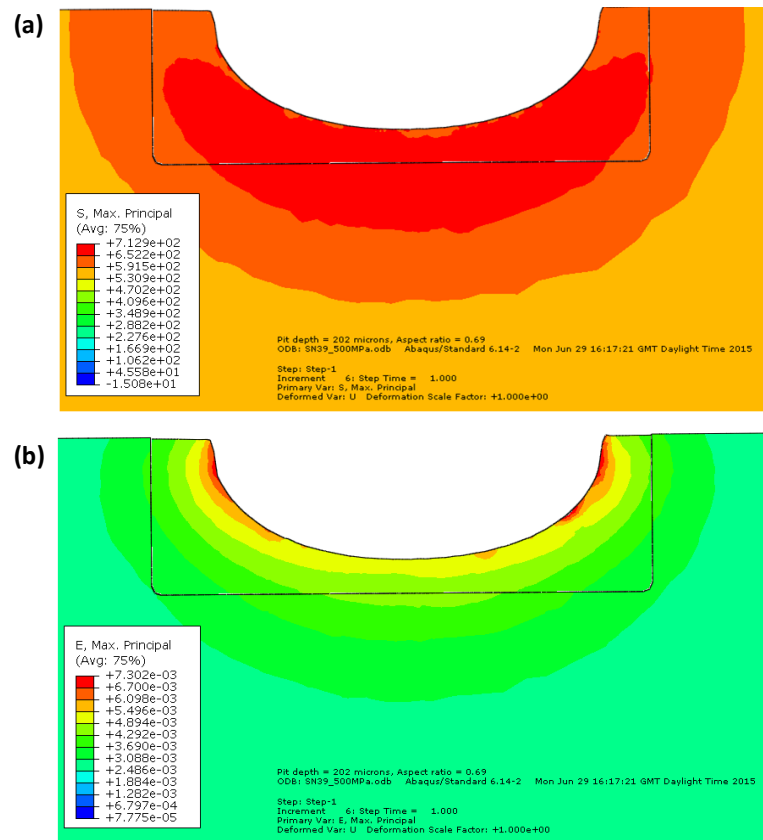


Figure 6.11 Contour plots showing the distribution of (a) principal stress, and (b) principal strain for a 202  $\mu\text{m}$  deep pit loaded to 500 MPa.

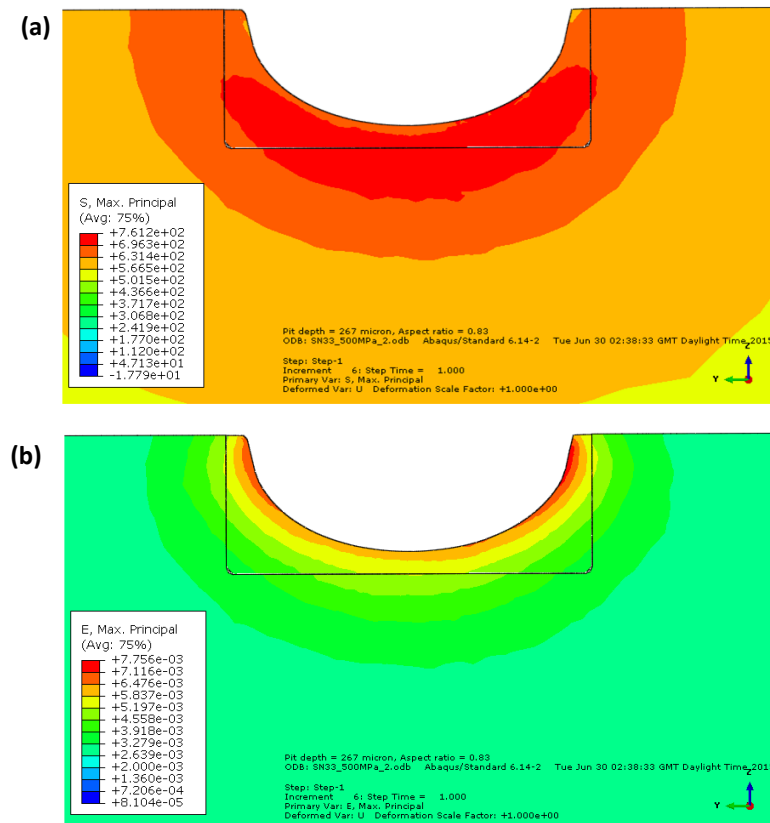


Figure 6.12 Contour plots showing the distribution of (a) principal stress, and (b) principal strain for a 202  $\mu\text{m}$  deep pit loaded to 500 MPa.

Analyses of the localised strains shows that strains appears to be more localised in the artificial pits than for ideal smooth pits. For instance, the maximum stress and strain observed in the artificial pit shown in Figure 6.11 are 713 MPa and 0.73 % respectively while the corresponding values in an ideal pit of the same size are 637 MPa and 0.55 %. Similarly for the artificial pit in Figure 6.12, the maximum stress and strain are 761 MPa and 0.78% while the corresponding values for an ideal pit are 647 MPa and 0.62%. It is thought that this observed increase may be an artefact associated with the procedure, therefore further analysis was carried out. This analysis involved comparisons of the elastic stress concentration factors for the artificial and ideal pits. The differences were generally less than 4%. Hence, it was concluded that the increased strain localisation observed for the artificial pits are significant. Since localised plasticity is the main driving requirement for fatigue crack nucleation [292], it is suggested that cracking will be promoted at the pit mouth. The present FEA results obtained in this study agree with those observed for in-air tests where surface cracks were observed to nucleate predominantly from the pit mouth. The correlation observed with experimental data appears to highlight the inaccuracies that can be associated with modelling corrosion pits as ideally smooth and uniform geometric defects. The plots shown in Figure 6.13 represent a pit, in a pre-pitted sample, that was tested in an aggressive environment (corrosion fatigue). Again, the results are similar to those above i.e. localisation of stress at the pit bottom and of strains towards the pit mouth. However, analysis of the fracture surface of the corresponding actual sample (see Figure 5.45c) showed that cracks initiated from the bottom rather than at the pit mouth. Since the localisation of strains reflects only the influence of mechanics, comparison with experimental results suggests that the conditions that facilitate crack nucleation from pits may depend not only on local stress/strain but also on electrochemical conditions.

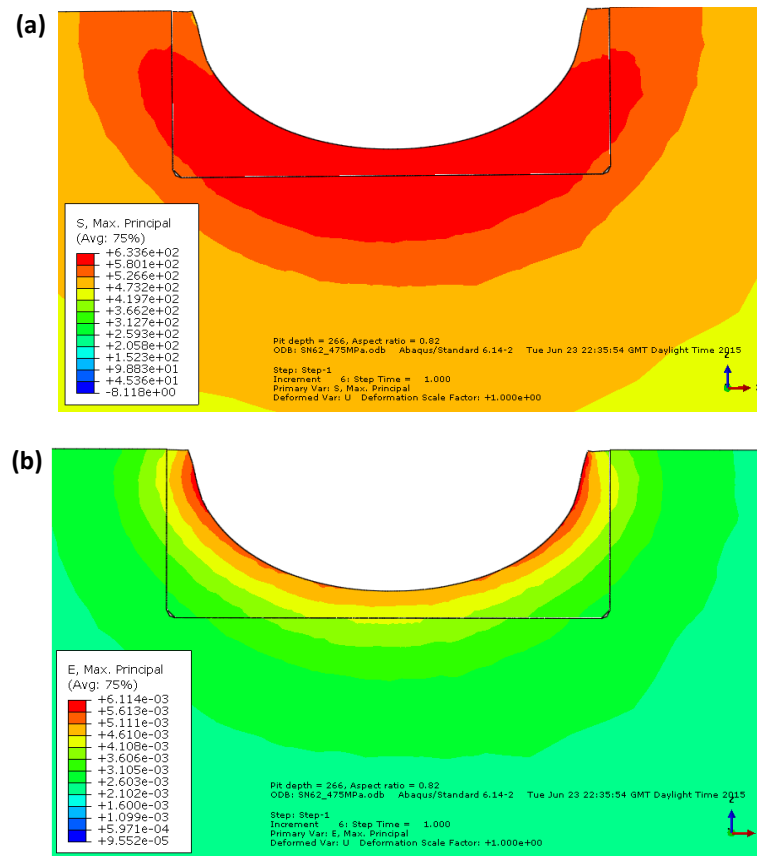


Figure 6.13 Contour plots showing the distribution of (a) principal stress, and (b) principal strain for a 266  $\mu\text{m}$  deep pit loaded to 475 MPa.

### 6.5.2 Double pits

The results of distribution of stress and strain for artificial double pits (pit depth  $\approx 200 \mu\text{m}$ , aspect ratio  $\approx 0.68$ ) are shown in Figure 6.14. The main observation is that the local stress is concentrated at the pit base (Figure 6.14a), whereas the strain is localised towards the pit mouth in the region separating the two pits (see black box in Figure 6.14b). From a purely mechanics perspective, this suggests that the conditions for crack nucleation will be more favoured in these locations. This would explain the experimental observations wherein cracks initiated only at the pit mouth and in the region separating two pits. The non-symmetric distribution of strains in the region of separation between the pits (see black rectangle in Figure 6.14b) may also explain why cracks sometimes initiated from the mouth of only one of the pits and not simultaneously, as observed from experiments (see Figures 5.22 – 5.23). These results also highlight the effect proximity between pits on level of localised strains i.e. an increase in the level of strains when compared with single pits. The interpretation is that, an increase in level of localised strain will result in a higher



tendency for crack and hence, early crack nucleation compared to single pits. Further investigation on the effect of proximity between pits on distribution of stresses and strains are presented in the next section.

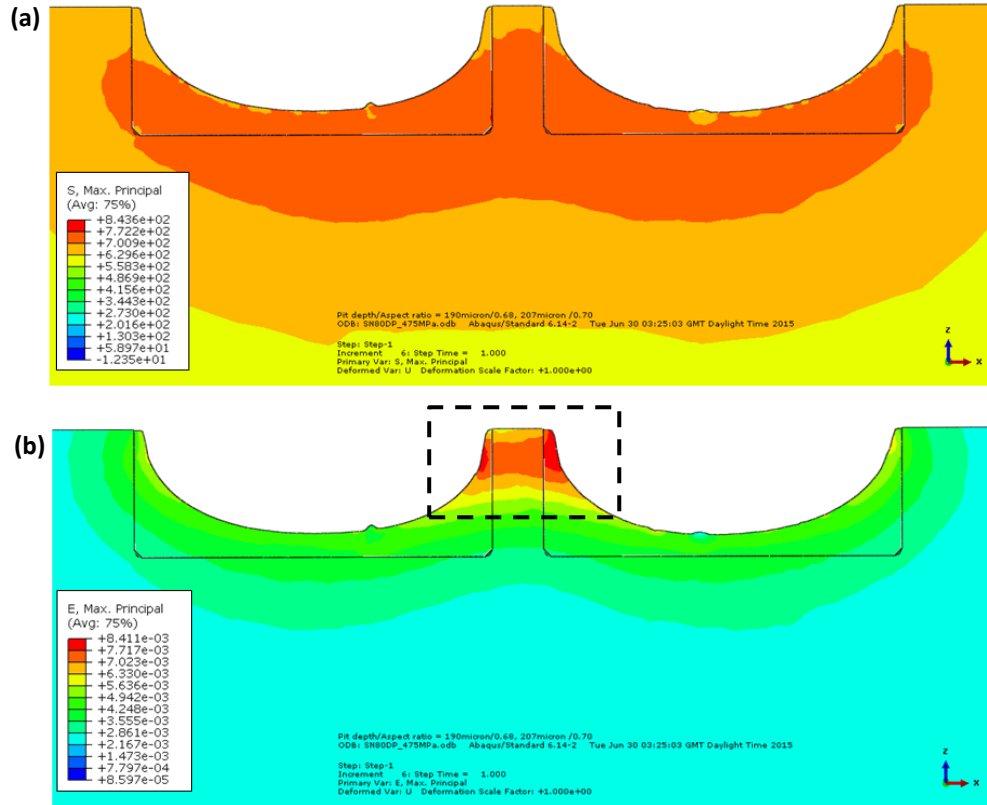


**Figure 6.14** Contour plots showing distribution of (a) principal stress, and (b) principal strain for double pits loaded to 475 MPa.

## 6.6 Effect of pit-to-pit proximity on stress and strain distribution

Experimental observations from fatigue tests carried out in air revealed that the proximity between corrosion pits, pit size and applied stress level play an important role in determining crack initiation behaviour. In this study, the effect of proximity (separation distance) between pits on the local mechanical conditions around pits was investigated further to understand crack nucleation in more details. This was achieved by analysing the distribution of stress and strains around double ideal pits with varying separation distances. 3-D models of fatigue specimens with double ideal pits were developed to simulate experimental conditions. Thus two identical (equal size) coaxial pits were modelled on flat fatigue samples by following the procedure described in Section 4.4. To ensure consistency with experiments, pit depths of 200 (aspect ratio = 0.68) and 270  $\mu\text{m}$  (aspect ratio = 0.82) were investigated at 450 and 475 MPa (these maximum stress values

correspond to the stress ranges at  $R = 0.1$  employed for testing) while the separation distance varied between 640 and 1660  $\mu\text{m}$ . An example of 3-D contour plots of equivalent stress and principal strain around double pits, each with depth of 270  $\mu\text{m}$  and separation distance of 760  $\mu\text{m}$  loaded to 475 MPa is shown in Figure 6.15. The main observation is that the numerical values of stress and strain are similar to those of artificial pits.

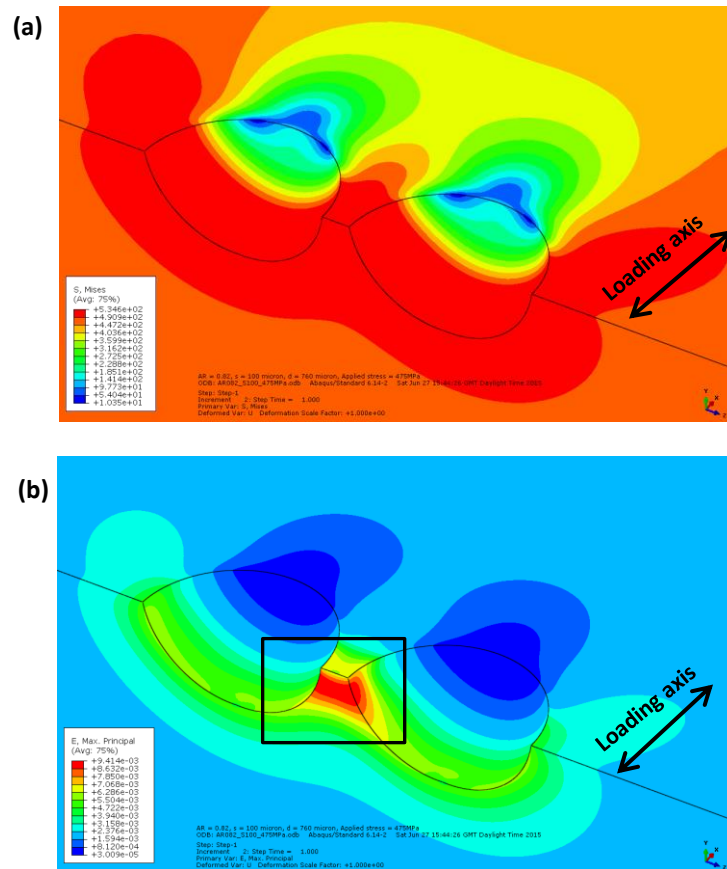


**Figure 6.15** Contour plots showing the distribution of equivalent stress (a) and principal strain (b) around two 270  $\mu\text{m}$  deep pits with separation distance of 760  $\mu\text{m}$ , loaded to 475 MPa.

The influence of proximity between pits on the distribution of stresses and strain is illustrated in Figures 6.16 and 6.17. The figures generally reveal interactions between stress and strain fields around pits depending on the separation distances. The closer the pits, the higher the tendency for their stress and plastic strain fields to interact. For instance, whereas there was no interaction between the stress and plastic strain fields of the pits at a separation distance of 1360  $\mu\text{m}$  (Figures 6.16c and 6.17c), an interaction was observed at separation distances of 710 and 960  $\mu\text{m}$  (Figure 6.18a&b, 6.17a&b). Further comparisons also show that whereas the maximum values of equivalent stress are similar, the principal

and plastic strains increased significantly with decreasing separation distance (Figure 6.18). The maximum values of strain occurred in the region of separation between the pits. These observations indicates that an interaction between the stress and strain field around pits further intensifies the strain localisation effects of pits, by increasing the prevailing strain level compared to when there is no interaction. A consequence of this will be a higher tendency for crack nucleation with decreasing separation distance. Therefore, cracks will likely initiate earlier thereby resulting in shorter pit-to-crack transition lives, compared to the case where there is no interaction.

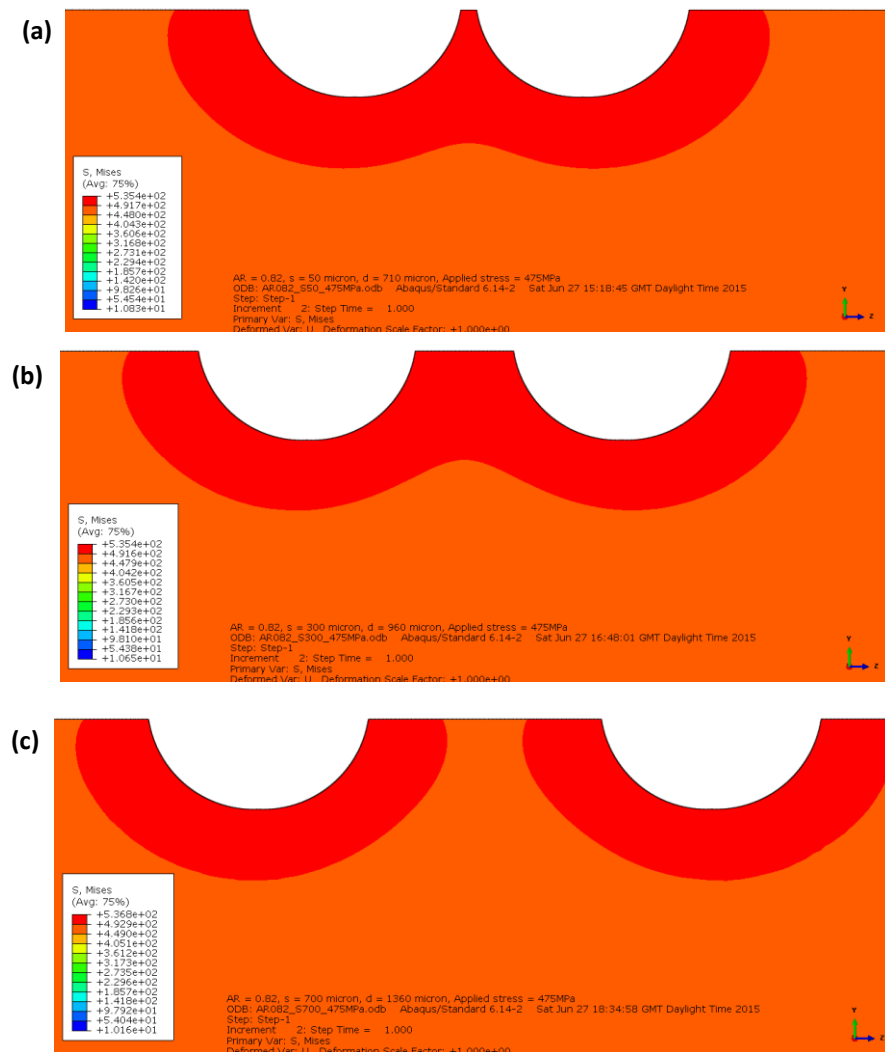


**Figure 6.16** Distribution of equivalent stresses around two 270  $\mu\text{m}$  deep pits with separation distances of (a) 710  $\mu\text{m}$ , (b) 960  $\mu\text{m}$ , and (c) 1360  $\mu\text{m}$ , loaded to 475 MPa.

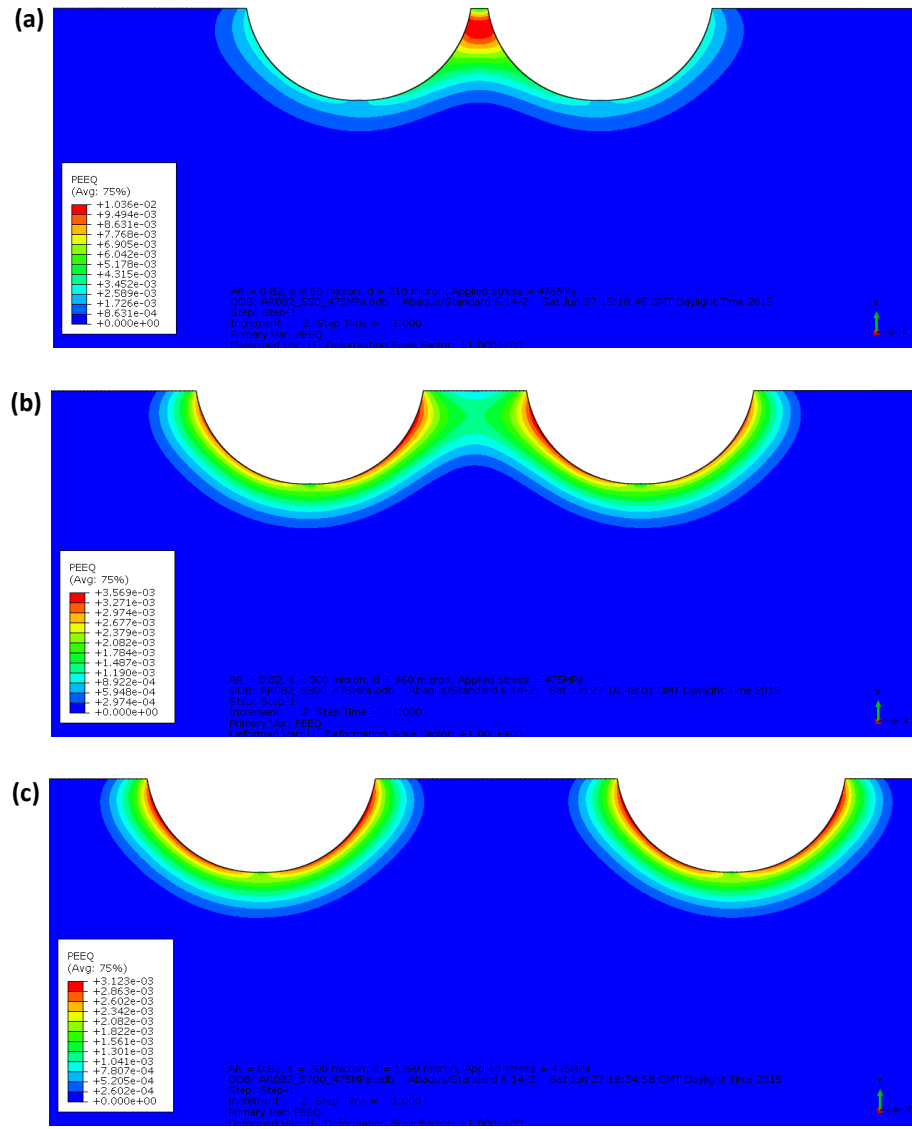


Figure 6.17 Distribution of plastic strain around two 270  $\mu\text{m}$  deep pits with separation distances of (a) 710  $\mu\text{m}$ , (b) 960  $\mu\text{m}$ , and (c) 1360  $\mu\text{m}$ , loaded to 475 MPa.

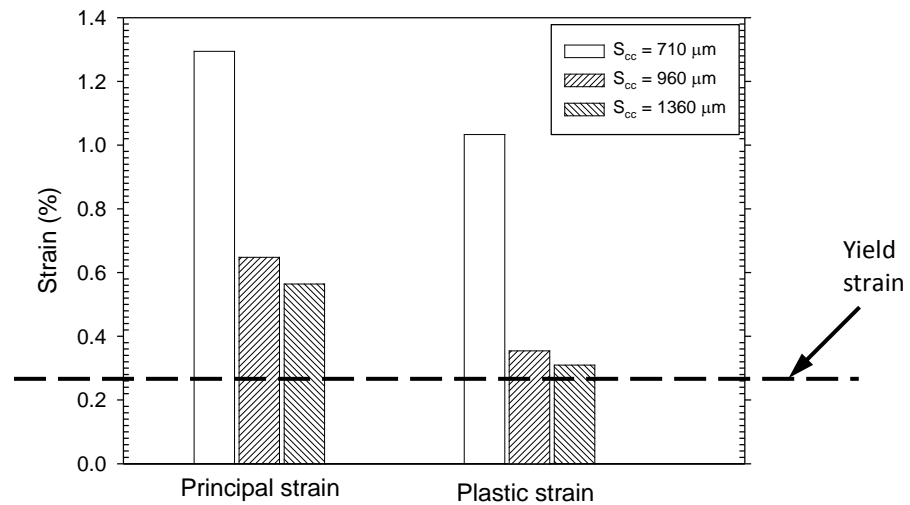


Figure 6.18 Plot of maximum values of strain as a function of separation distance ( $s_{cc}$ ) in the double pitted specimens loaded to 475 MPa.

The influence of proximity between pits on stress and strain localisation was further quantified as a function of pit size and applied stress level. The results generally show higher local strains for deeper pits (larger aspect ratios) (Figure 6.19) and at higher stresses (Figure 6.20) at any given separation distance. The results also show that while equivalent stress remained constant, principal strains and plastic strains increased with decrease in separation distance between pits. However, the observed increase in strain was significant only within a range of separations distances, which depend on the pit size and stress level, as was observed in experiments. At relatively greater separation distances, the levels of localised strains were just the same as those of individual pits. This appears to suggest that although proximity between pits could facilitate crack initiation, this is also dependent on applied stress and pit size. The dependency of the effect of separation distance on pit size and applied stress can be summarised as follows: the separation distance below which interaction between strain fields of pits becomes significant, thereby intensifying localised plasticity and consequently increasing the tendency for crack nucleation, increases with pit size and applied stress. The present results are consistent with the experimental results discussed in Section 5.5.1.3.

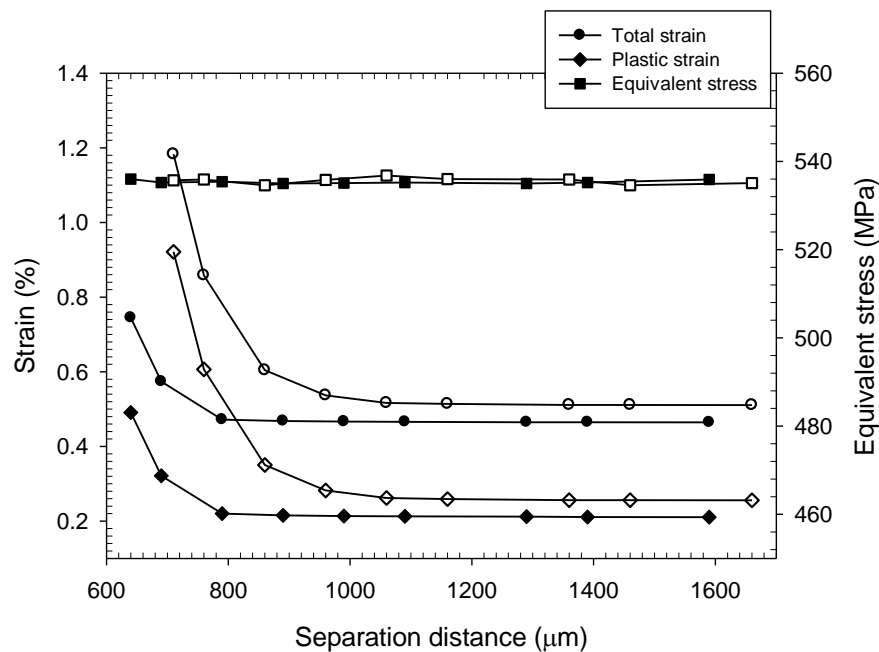


Figure 6.19 Plots of equivalent stress, principal strain and plastic strain versus separation distance between double pits loaded to (a) 450 MPa and. (Pit depth = 200  $\mu\text{m}$  - closed symbols, Pit depth = 270 - open symbols).

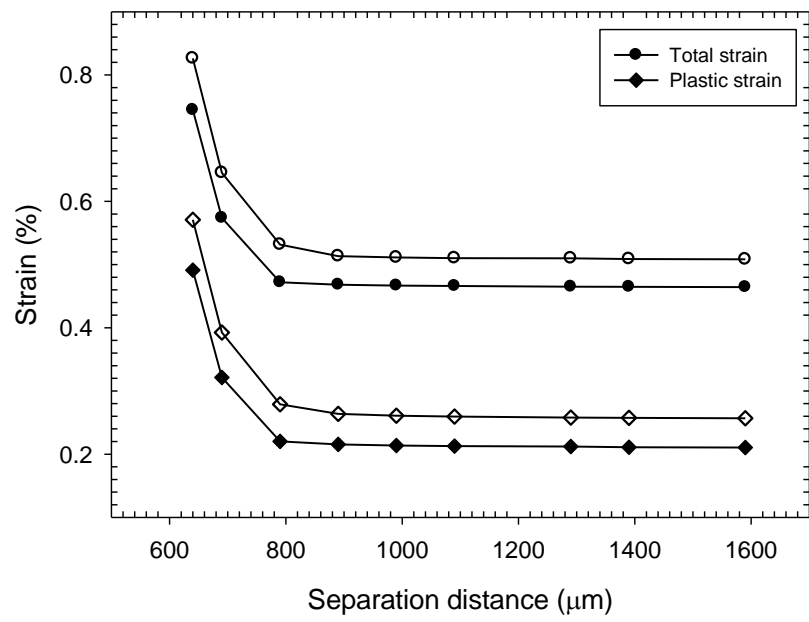


Figure 6.20 Plots of total strain and plastic strain versus separation distance for 200  $\mu\text{m}$  deep double pits at different stress levels (450 MPa – closed symbols, 475 MPa – open symbols).

---

# **Chapter 7**

## **CAFE Modelling**

### **Results and Discussion**

---

## 7.1 Introduction

One of the objectives of the present work is to develop a computational model that offers a more accurate prediction of the damage processes, based upon an understanding of the mechanisms that facilitate the development of a pit and its transition to a crack during corrosion fatigue damage. This model should be able to simulate the time-dependent interaction between corrosion and mechanical loading during the pre-crack stages of corrosion fatigue such that the evolution of localised damage (pitting), under the influence of applied stress and the evolution of dynamic strain distribution around the localised defect, can be quantified. Pit size evolution with accompanying stress and strain distribution, together with information about the threshold strain required for the pit-to-crack transition, can, then, be used to establish crack nucleation conditions from pits. To achieve this objective, the model development and validation process was divided into two stages: (i) Stage I: development of architecture, verification and validation of a 2-dimensional (2-D) cellular automata finite element (CAFE) model and (ii) Stage II – development of a 3-D CAFE model from the 2-D model produced in (i). The objective of this chapter is to present the progress of work on the development of a 3-D semi-probabilistic CAFE model that allows the simulation of the complex interactions between chemical reactions taking place in the electrolyte domain and at the metal-electrolyte interface and mechanical factors such as stress and strain distribution during pit development. The ultimate goal is to apply the model to simulate the evolution of pitting under the influence of applied stress and consequently predict crack initiation based on known mechanics-based transition criterion for cracking<sup>4</sup>.

A 2-D CAFE model, which couples cellular automata (CA) and finite element method (FEM) models, has been developed for simulating the interaction between localised corrosion and mechanical loading at a mesoscopic scale. In the first stage, CA is used to simulate the electrochemical component of the damage, i.e. changes in the dissolution kinetics of cells subject to local physical processes and local strains. In the second stage, the deformation of the cellular structure containing the defect (pit) is analysed by FEM. Consecutive execution of the CA and FE components, via a feedback loop between them,

---

<sup>4</sup> A PhD project is currently being undertaken by Mr. C. Evans to establish a strain-based transition criterion (threshold strain) for pit-to-crack transition using digital image correlation of surface strains around pits.



provides a good approximation of the interaction between the electrochemical (localised corrosion) and mechanical (fatigue) damage processes.

Simulations were carried out with and without applied stress to understand the influence of various input parameters on the evolution of pit characteristics and the distribution of dynamic strains around the pits. Specifically, the role of different model input parameters on the local corrosion kinetics and evolution of pit characteristics was investigated. The results obtained from the model together with those obtained from experiments are presented. In Section 7.8, preliminary results from the 3-D CAFE model are also presented. In the present work, maximum pit depth, pit aspect ratio and pit volume were chosen to correlate simulation model outputs with experimental data.

## 7.2 Simulation of the micro-capillary cell

The source code for the model and simulation of pit development was written in Matlab® [249] and carried out on a 128 GB RAM Dell Precision T7910 PC with Intel Xenon 48-core processor. The simulation time for the CA and FEM parts is dependent on the size of the CA matrix and the size of the pit in the FEA. In the latter, the simulation time increases with size of the pit especially when there is plasticity. Typical simulation time ranges from 20 to 40 minutes for CA and 100 to 220 minutes for FEA in each CAFE time step. It is necessary to establish the initial conditions in order to relate the experimental data with model outputs, therefore, the real time scale for each simulation is defined as the time step where the pit volume from the model and experiment at 1800 seconds are equal for any set of input probabilities.

Because the experimental data were obtained using the microcell, the 2-D CAFE modelling space was constructed in such a way that the microcell-solution-metal configuration can be simulated. The micro-capillary cell has already been described in Section 3.5.2. The region of interest here is the interface between the metal substrate, electrolyte and the walls of the capillary. A schematic of this configuration is shown in Figure 7.1a while the corresponding simulated CAFE modelling space is shown in Figure 7.1b. The carbon steel used for the experiment has no passive film on its surface; hence, the electrolyte is in contact with the substrate at the start of simulation.

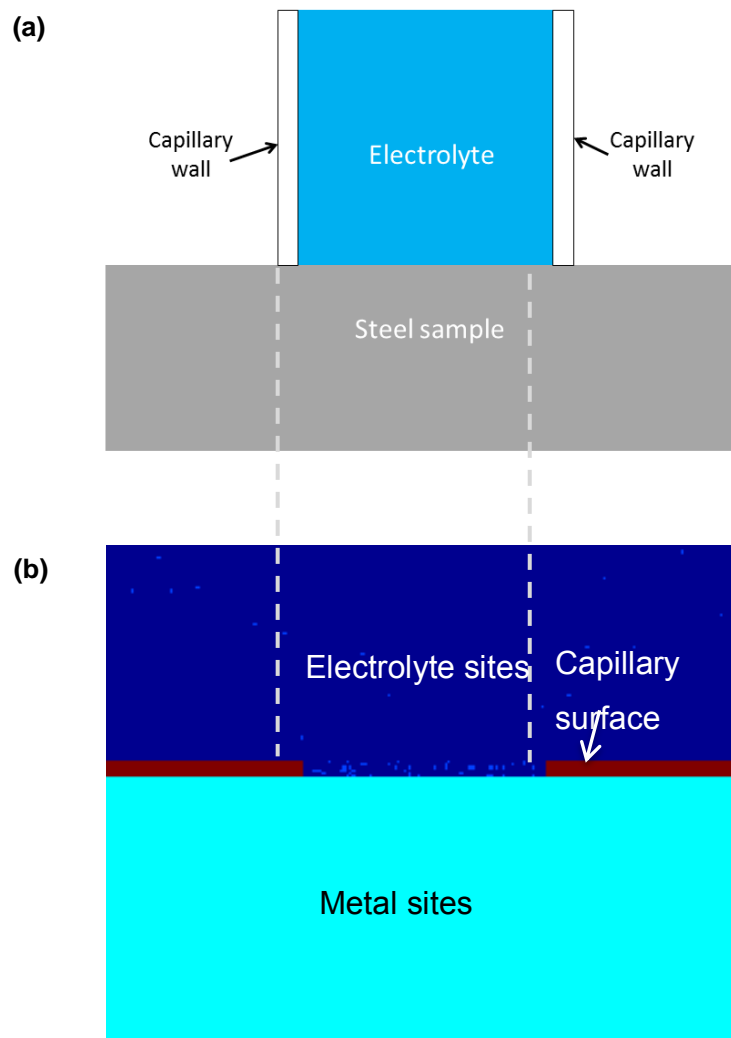


*Figure 7.1 Metal-electrolyte-capillary configuration showing (a) schematic of micro-capillary cell and (b) CAFE modelling sites of the system in (a).*

### 7.3 Model parameter sensitivity analysis

Sensitivity analysis is an important aspect of computational model development. In sensitivity analysis, the objective is to identify the relative importance of each input parameter in determining model outputs. Computational models can be classified into deterministic and stochastic models. In the former, the predictions for a specific set of identical initial conditions are the same. The latter, like the one developed in this work, have varying outputs between simulations even if initial conditions and parameter values are the same [297]. In the sensitivity analysis (SA) of stochastic models, the mean values of different distributions of output variables are normally compared rather than comparing two single outputs, as is the case with deterministic models. SA in the present work was carried out using a screening method, because simulations with CA-based models are

generally time-consuming. Moreover, the method has a relatively low computational cost when compared with other approaches such as differential analysis, Monte Carlo analysis and response surface methods [298]. In the screening method (SM), the goal is to identify the input parameters that contribute significantly to uncertainty in the outputs [299].

The SM has been used extensively in the literature [298, 300] and more recently in pitting corrosion CA-models [299]. It is a variance-based method involving one-factor-at-a-time experiments where one factor is varied at a time whilst observing changes that are attributed to variations in the individual input parameters in the model predictions. The main objective is to determine which input parameters have effects which are negligible, linear and additive, non-linear or involve interactions with other input parameters. The sensitivity  $F_i$  of the model output  $K$  to a single input parameter  $q_i$  is repeated  $r$  times and the mean  $\mu_i$  and standard deviation  $S$  of these  $r$  computations plotted graphically and used to assess the relative importance of the parameter  $q_i$ .

In the present model, maximum pit depth and pit volume were the output variables selected for sensitivity analysis. Table 7.1 summarises the range of values of the input parameters employed for the SA analysis. Due to the assumption of isotropy of diffusion,  $P_{diffH}$ ,  $P_{diffFeII}$  and  $P_{diffFeIII}$  all have identical values in a given simulation (see Section 4.4.1.2). Hence, only  $P_{diffH}$  was specified in Table 7.1.

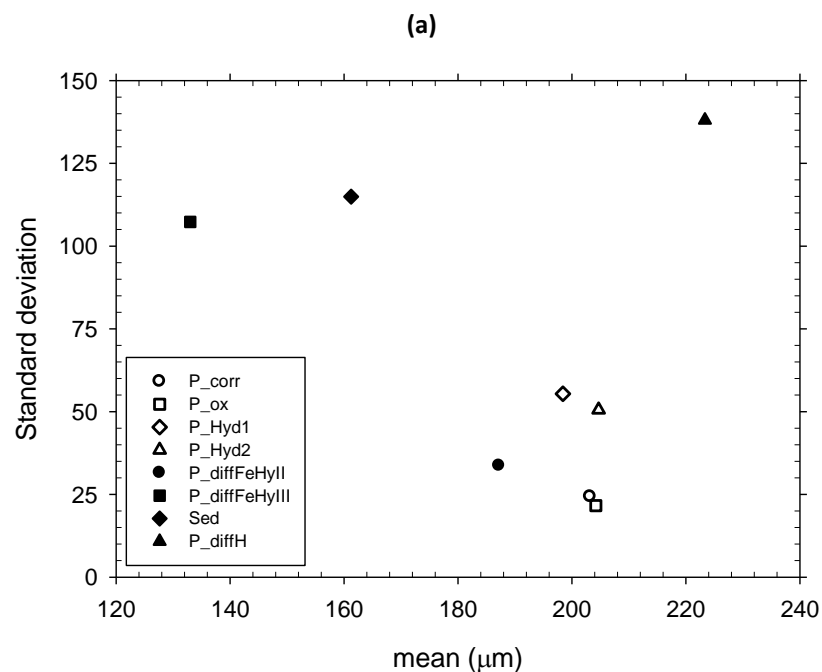
**Table 7.1 Summary of range of values of input parameters employed for sensitivity analysis.**

Probability	Initial value	Varied values
$P_{corr}$	0.5	0.02, 0.3, 0.5, 0.7, 0.9
$P_{ox}$	0.5	0.02, 0.3, 0.5, 0.7, 0.9
$P_{Hyd1}$	0.05	0.005, 0.01, 0.05, 0.1, 0.3, 0.5
$P_{Hyd2}^*$	1.5	0.005, 0.01, 0.05, 0.1, 0.3, 0.5
$P_{diffH}$	0.1	0.05, 0.1, 0.2, 0.3, 0.4
$P_{diffFeHyII}$	0.05	0.005, 0.01, 0.05, 0.1, 0.3, 0.5
$P_{diffFeHyIII}$	0.05	0.005, 0.01, 0.05, 0.1, 0.3, 0.5
$Sed$	2	1, 2, 3, 4, 5

\*Actual value of  $P_{Hyd2}$  is taken to be its given value multiplied by  $P_{Hyd1}$ .

**Figure 7.2** presents the mean versus standard deviation plots for each input parameter in the model. According to the SM, a large value of mean (away from the origin – mean, standard deviation = 0,0) indicates an input that has a significant overall influence on the output while a high value of standard deviation indicates an input which has a non-linear

influence on the output or an input whose effect on the output depends on its interaction with other input parameters [298, 300]. The relative importance of each of the input parameters can also be measured by defining a sensitivity measure: the Euclidean distance from the origin in the  $(\mu, S)$  space, denoted by  $\delta$ . The plots for maximum pit depth and pit volume, which are presented in Figures 7.2a and 7.2b, generally show the same trend due to the direct relationship between both outputs. The values of mean for all the parameters are substantially different from zero, indicating that the pit depth and pit volume are sensitive to all the input parameters of the model. Similarly, the standard deviation for each of the input parameters are large, indicating that they have non-linear effects which depend on their interaction with other input parameters (relatively large  $S$  values). The order of importance  $\delta$  determined for all the input factors is summarised in Table 7.2 and Table 7.3 for maximum pit depth and pit volume respectively. Comparison of the values shows that all the input parameters are equally important for determining localised corrosion behaviour. The exceptions are the probabilities of diffusion of acidic sites ( $P_{diffH}$ ) and iron II ions ( $P_{diffFeHyII}$ ) and iron III ions ( $P_{diffFeHyIII}$ ), which are the most important.



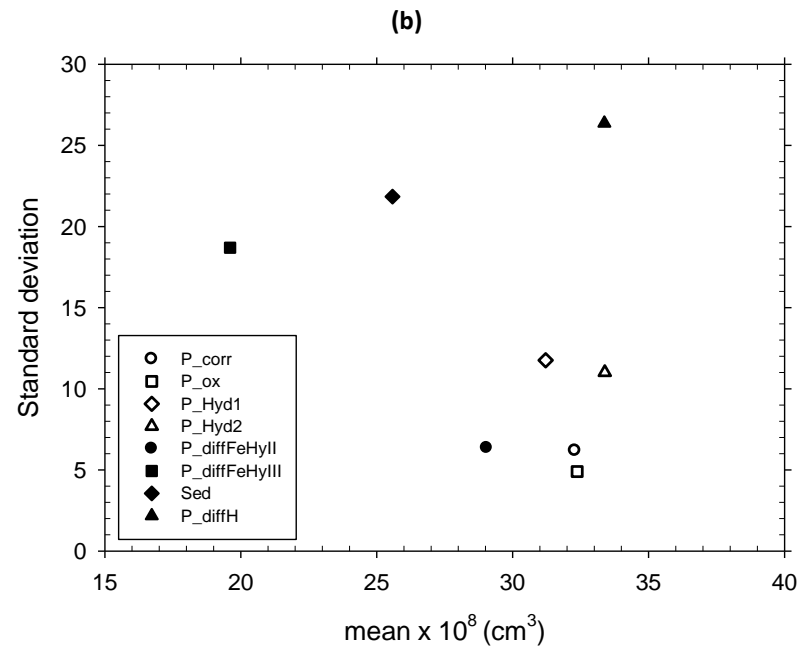


Figure 7.2  $\mu$ -S plots for each of the input parameters associated with (a) maximum pit depth and (b) pit volume.

Table 7.2 Summary of values of the three sensitivity measures  $\mu$ ,  $S$  and  $\delta$  associated with the maximum pit depth for each of the input parameters.

Probability	$\mu$ ( $\mu\text{m}$ )	$S$ ( $\mu\text{m}$ )	$\delta$
$P_{corr}$	203	24	204
$P_{ox}$	204	22	205
$P_{Hyd1}$	198	55	206
$P_{Hyd2}$	205	51	211
$P_{diffH}$	223	138	263
$P_{diffFeHyII}$	187	34	190
$P_{diffFeHyIII}$	133	107	171
$Sed$	161	114	198

Table 7.3 The values of the three sensitivity measures  $\mu$ ,  $S$  and  $\delta$  associated with the pit volume for each of the input parameters.

Probability	$\mu \times 10^7$ (cm <sup>3</sup> )	$S \times 10^7$ (cm <sup>3</sup> )	$\delta \times 10^7$
$P_{corr}$	3.23	0.62	3.36
$P_{ox}$	3.24	0.90	3.24
$P_{Hyd1}$	3.12	1.18	3.34
$P_{Hyd2}$	3.34	1.10	3.52
$P_{diffH}$	3.34	2.64	4.25
$P_{diffFeHyII}$	2.90	6.36	2.97
$P_{diffFeHyIII}$	1.96	1.87	2.71
$Sed$	2.56	2.18	3.36

These SA results underscore the complex interactions occurring between several competing and complex processes taking place during localized corrosion. For instance, increasing the probability of oxidation of Fe to  $\text{Fe}^{2+}$  ( $P_{corr}$ ) and probability of oxidation of  $\text{Fe}^{2+}$  to  $\text{Fe}^{3+}$  ( $P_{ox}$ ) will potentially increase the initial rate of metal dissolution. However, this effect depends on the availability of acidic sites, which depends on the probability of its diffusion ( $P_{diffH}$ ) and rate of accumulation of corrosion products that are formed as corrosion progresses. Hydrolysis is a process that can increase or decrease the rate of corrosion but these effects depend on the availability of water sites and species that are formed as a result of the oxidation process. Accumulation of corrosion products can decrease corrosion rate by creating a diffusion barrier for corrosion species but this also depends on the rate of precipitation of corrosion products ( $Sed$ ), which in turn is related to the probability for hydrolysis ( $P_{Hyd1}/P_{Hyd2}$ ).

#### 7.4 Influence of model parameters

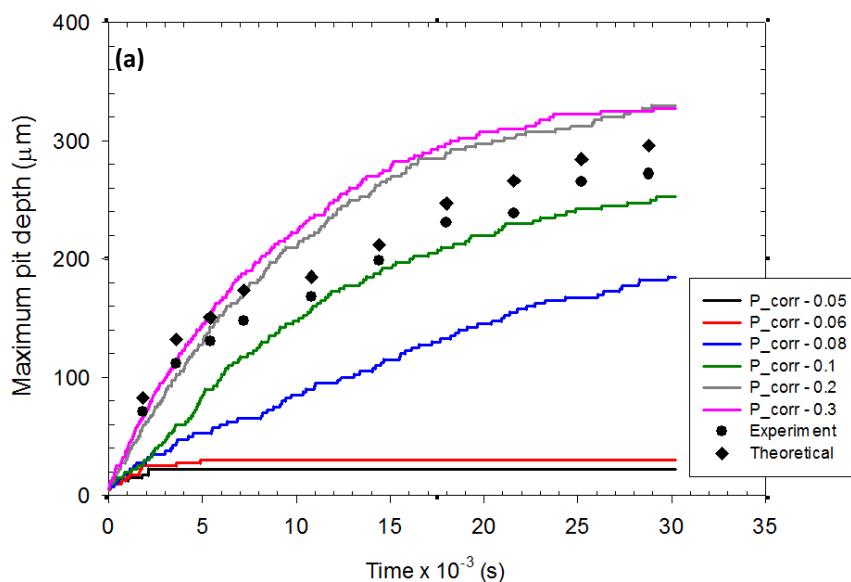
Localised corrosion is a complex stochastic process whose kinetics can be affected by several mechanisms including metal dissolution, diffusion, precipitation, and hydrolysis, all of which have non-linear behaviour. In the present system, different parameters were defined that account for these processes and their stochastic nature. From the sensitivity analysis carried in the previous section, all the input parameters were found to influence the model outputs. Moreover, they also show interactions with each other. The behaviour of the CA model was investigated further by evaluating the roles of selected input parameters on the time-dependent localised corrosion kinetics and evolution of pit depth and pit volume. Due to computational time limitations, the parameters selected for further investigation include; oxidation of metal to  $\text{Fe}^{2+}$  denoted by  $P_{corr}$ , oxidation of  $\text{Fe}^{2+}$  to  $\text{Fe}^{3+}$  denoted by  $P_{ox}$ , hydrolysis of  $\text{Fe}^{2+}$  to  $\text{Fe}(\text{OH})_2$  denoted by  $P_{Hyd1}$  and precipitation of  $\text{Fe}(\text{OH})_2$  and  $\text{Fe}(\text{OH})_3$  denoted by  $Sed$ .

Simulations were carried out by varying the values of each of these probabilities and fixing other input parameters. The resulting pit depth and pit volume versus time profiles were determined from the simulations, which were undertaken using a  $1000 \times 500$  lattice. The width of each cell in the lattice was set to  $2.5 \mu\text{m}$ . Theoretical and experimental data are also shown on the profiles for the purpose of comparison. Theoretical pit depths were obtained from Faraday's law (see Section 3.8.2). The following probabilities were

employed for the input parameters for the simulations:  $P_{corr} = 0.2$ ,  $P_{ox} = 0.2$ ,  $Phyd1 = 0.09$ ,  $P_{Hyd2} = 1.5 P_{Hyd1}$ ,  $P_{DiffH} = 0.5$ ,  $P_{DiffFeII} = 0.5$ ,  $P_{DiffFeIII} = 0.5$ ,  $P_{DifFeHydII} = 0.06$ ,  $P_{DifFeHydIII} = 0.06$ ,  $Sed = 3.4$ .

#### 7.4.1 Effect of oxidation of Fe to $Fe^{2+}$

The probability of corrosion,  $P_{corr}$ , was introduced in the model to simulate the rate at which Fe is oxidized to  $Fe^{2+}$ . Higher probability for corrosion increases the tendency for oxidation, increases the concentration of the corrosion specie,  $Fe^{2+}$ , and consequently the rate of metal dissolution. Figure 7.3 shows the variation of maximum pit depth and pit volume with time at various  $P_{corr}$  values. The same trend is generally observed for both pit volume and maximum pit depth i.e. power law relationship with time. This is expected because of the correlation between metal loss (pit volume) and pit depth as described by Faraday's law [301]. It has been observed that a power-law relationship generally exists between both maximum pit depth and pit volume and time [124, 302]. These results illustrate the time-dependent nature of localised corrosion damage and the characteristic role of diffusion in this process. These results illustrate the time-dependent nature of localised corrosion damage and the characteristic role of diffusion in this process.



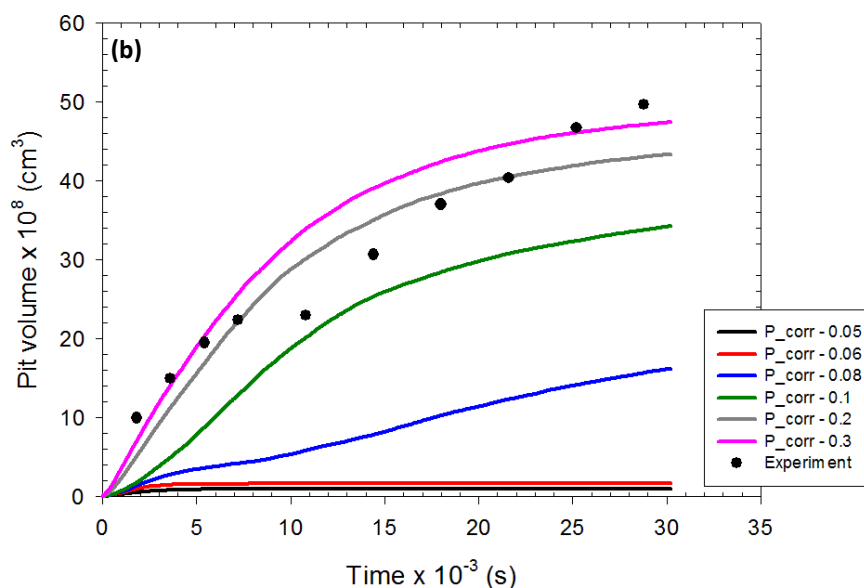


Figure 7.3. The role of different corrosion probabilities on time-dependent localised corrosion behaviour. (a) maximum pit depth and (b) pit volume.

The amount of damage generally increases with increase in probability but was not significantly different at  $P_{corr}$  values of 0.2 and 0.3. This is thought to be a consequence of diffusion processes whereby there will be a limit to which increasing the rate of oxidation (increasing  $P_{corr}$ ) will have a substantial effect on dissolution rate. The rate of localised damage will be controlled by the diffusion processes simulated with diffusion probabilities in the model rather than oxidation rate of Fe to Fe<sup>2+</sup>.

#### 7.4.2 Effect of accumulation of corrosion products

As mentioned earlier, a sedimentation factor,  $Sed$ , was introduced into the model to account for accumulation of corrosion products (Fe(OH)<sub>2</sub> and Fe(OH)<sub>3</sub>) during localised dissolution. This simulates a stagnant system where the corrosion products are not able to be conveyed away from the pit through mass transport, which would otherwise be possible in a flowing system. The variation of maximum pit depth and pit volume with time at various  $Sed$  values is shown in Figure 7.4. It can be observed that higher values of  $Sed$  result in lower values of maximum pit depth and pit volume at a given time interval. In addition, for a given  $Sed$  value, the rate of damage decreases with time. This generally indicates that an increase in the rate of accumulation of corrosion products (increase in  $Sed$ ) reduces the rate of damage by reducing pit growth and metal loss rate. This accumulation can determine the rate of metal dissolution through a diffusion control



mechanism by presenting a diffusion barrier for the species involved in the corrosion process [303, 304], in this case,  $\text{Fe}^{2+}$  and acidic sites.

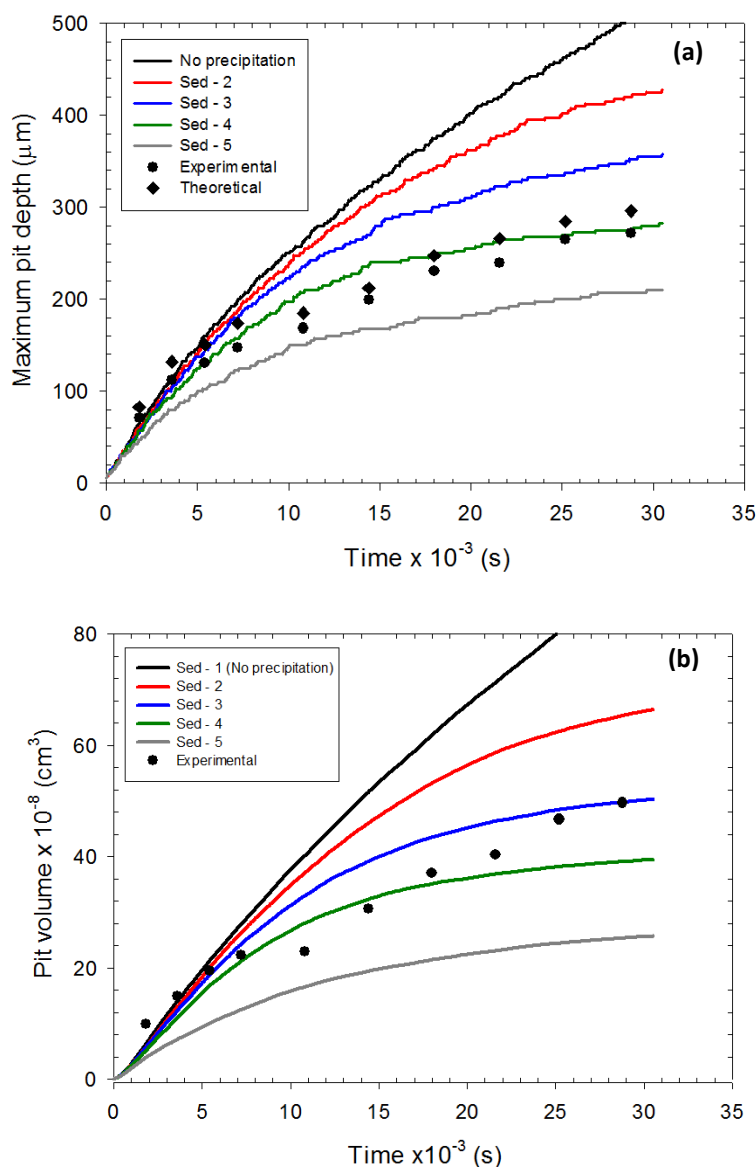


Figure 7.4. The role of different sedimentation factors on time-dependent localised corrosion behaviour. (a) maximum pit depth and (b) pit volume.

#### 7.4.3 Effect of hydrolysis of $\text{Fe}^{2+}$ to $\text{Fe}(\text{OH})_2$

Figure 7.5 shows that the overall damage (maximum pit depth and metal loss) is lowest when the probability for hydrolysis is highest. On one hand, the primary effect of hydrolysis is to increase the rate of dissolution by an acidification process through the production of acidic sites. On the other hand, increasing the tendency for hydrolysis will increase the rate of formation of corrosion product ( $\text{Fe}(\text{OH})_2$ ). When the sedimentation

factor is large enough, more corrosion products accumulate and consequently result in less damage as discussed above (Section 7.4.2).

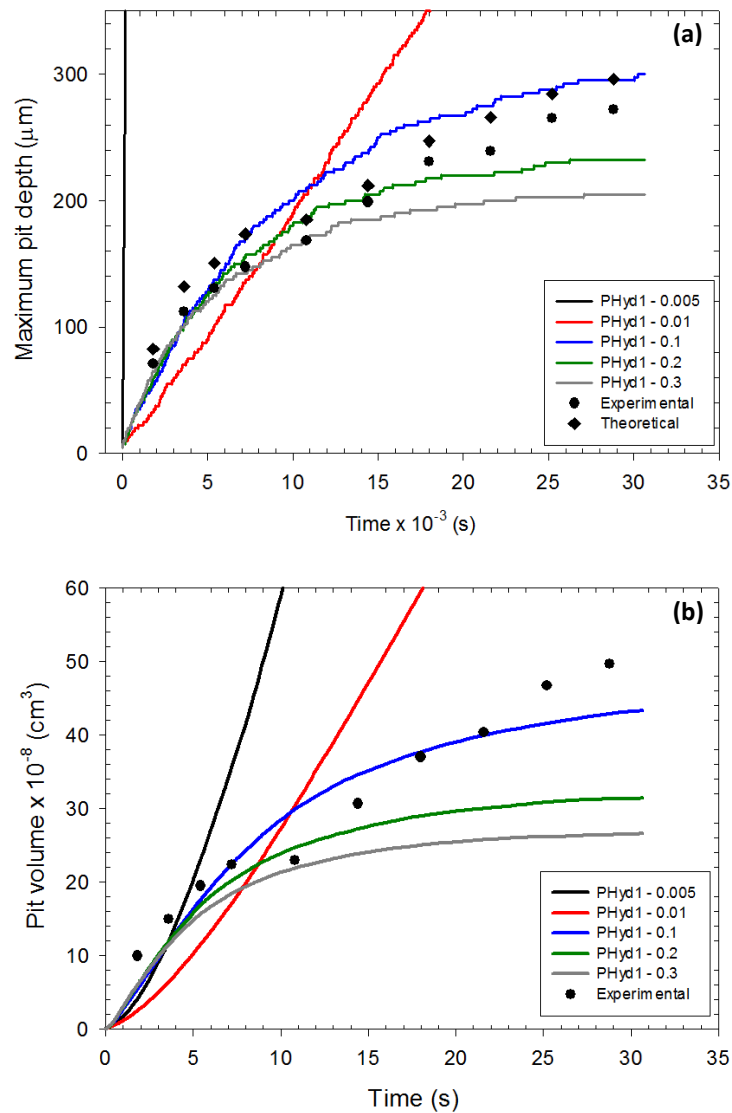


Figure 7.6. The influence of different hydrolysis probabilities on time-dependent localised corrosion behaviour. (a) maximum pit depth and (b) pit volume.

## 7.5 Model validation

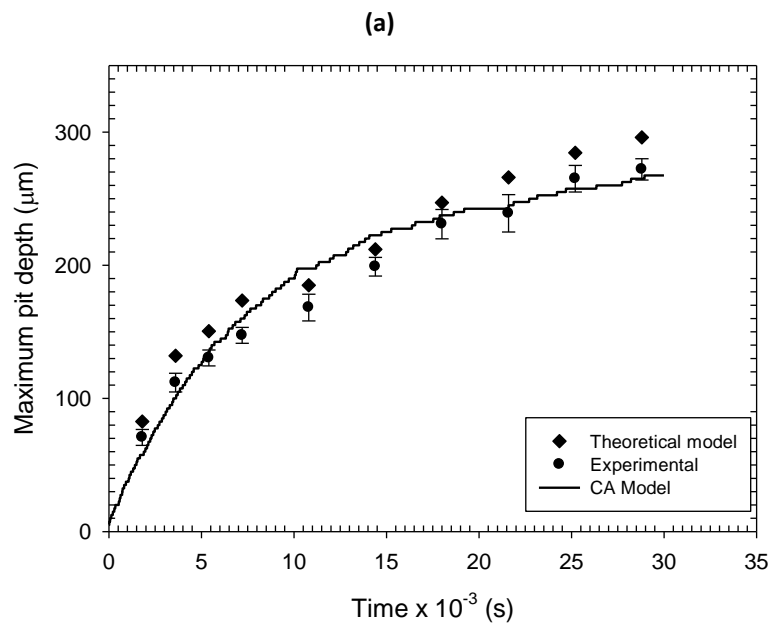
The usefulness of the CAFE model lies in its ability to predict the time-dependent evolution of depth and geometry of pits and their associated strain distribution. To ensure that the model can simulate this time-dependent behaviour, its outputs can be compared with available experimental data through a validation process. As discussed in Sections 7.3 and 7.4, the values of the input parameters determined the time-dependent evolution of pit depth and pit geometry. Therefore, the validity of the model will depend on a combination of specific values for each of the defined input probabilities. Since the model

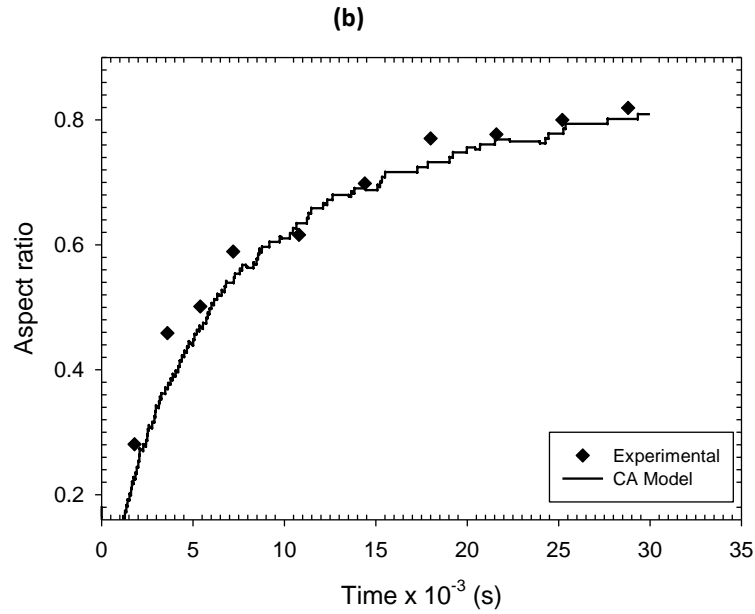
possesses several input parameters, optimization was necessary to obtain a combination of a specific set of values for each of the input parameters. The optimized model was obtained by evaluating different combinations of values of input parameters that minimises the disparity between model predictions and experimental data. The model was optimized to simulate the two sets of experiments that were carried out in the present work i.e. with and without (stagnant) flow. The values of probabilities obtained for the optimized models in each case are given in Table 7.4.

**Table 7.4 Summary of probabilities obtained for optimized models for stagnant (without flow) and flow conditions.**

Probability	Stagnant	With flow
$P_{corr}$	0.19	0.20
$P_{ox}$	0.30	0.30
$P_{Hyd1}$	0.15	0.15
$P_{Hyd2}$	0.30	0.30
$P_{diffH}$	0.50	0.50
$P_{diffFeHyII}$	0.06	0.06
$P_{diffFeHyIII}$	0.06	0.06
$Sed$	3.30	1.10

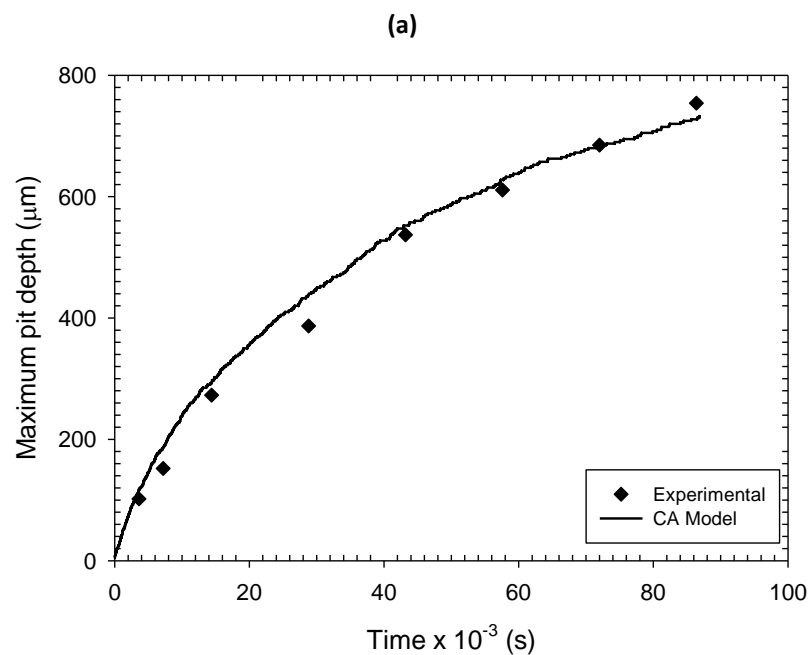
Representative results obtained from the optimized models together with the experimental data for stagnant and flowing conditions are shown in Figure 7.6 and Figure 7.7 respectively.





*Figure 7.6 Plots of (a) maximum pit depth and (b) pit aspect ratio as a function of time simulating pit growth under stagnant (without flow) conditions.*

Figures 7.6a and 7.7a show that the model predictions for maximum pit depth show good agreement with experimental data. In terms of pit aspect ratio, correlation with experimental data was better under stagnant conditions than under flow conditions. Although these results are satisfactory, further model refinement is still needed to minimize the variance between the model predictions and experiment results. The results from three simulations for each model are summarised in Appendix C.



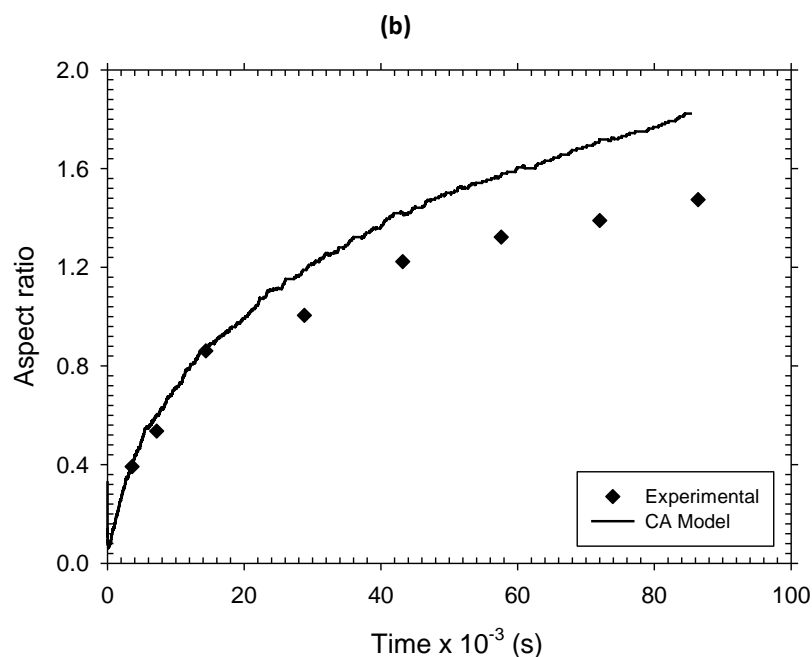
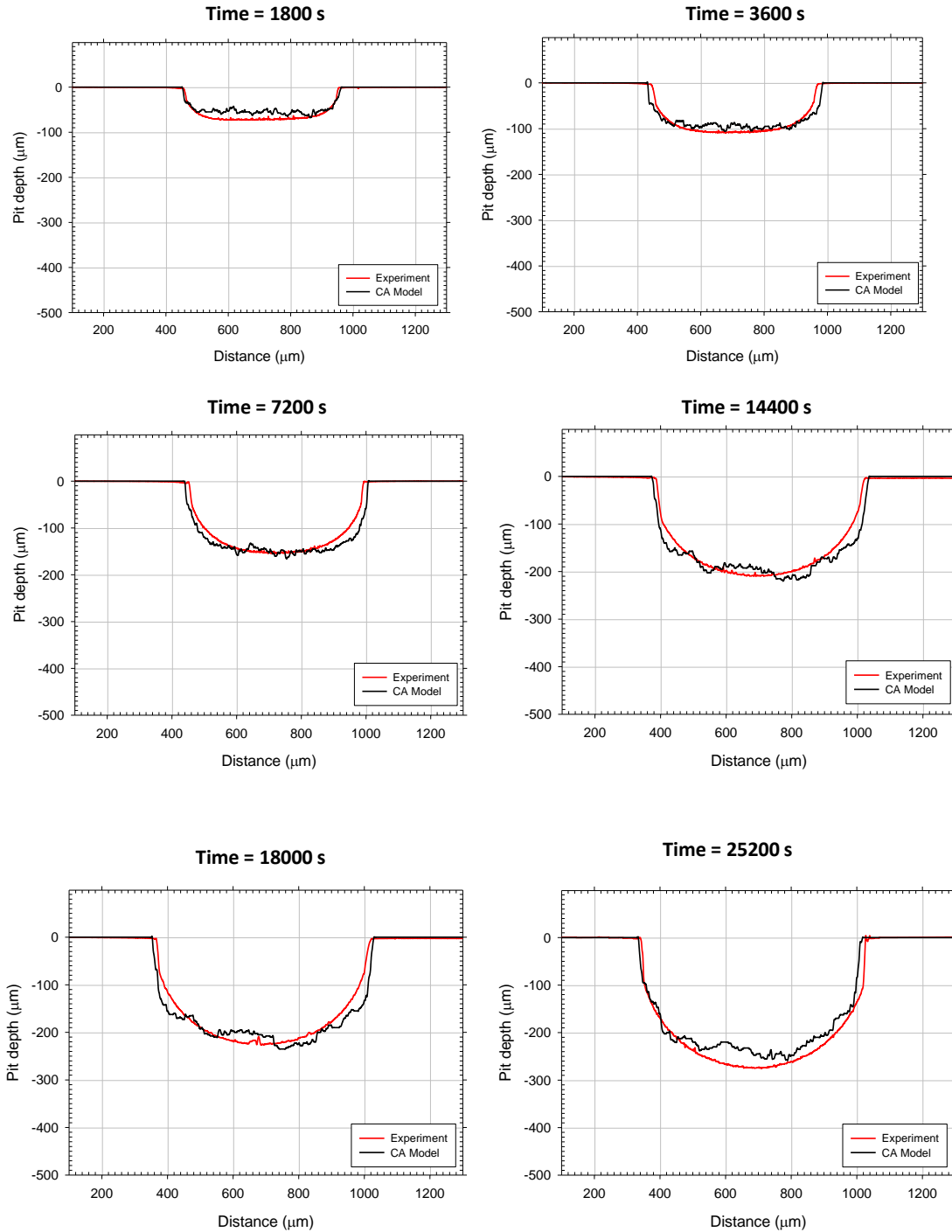


Figure 7.7 Plot of (a) maximum pit depth and (b) pit aspect ratio as a function of time simulating pit growth under flow conditions.

Comparison between the input parameters for the two models (see Table 7.4) shows that the only difference is the sedimentation factor, which accounts for the accumulation of corrosion products ( $\text{Fe}(\text{OH})_2$  and  $\text{Fe}(\text{OH})_3$ ). Compared to a *Sed* value of 3.3 for static conditions, a lower value of 1.1 under flowing conditions indicates a relatively lower tendency for corrosion products to accumulate due the mass transport effect of flow [304]. Consequently, the resulting diffusion barrier to corrosion species will be minimized, the rate of metal loss will increase [304] and rate of pit growth will be higher compared to when there is no flow [265].

Figure 7.8 shows the cross-sectional profiles of the pits obtained from the CA model at different times under stagnant conditions compared to the corresponding cross-sectional profiles of those obtained experimentally. It can be seen that both sets of data show good correlation, in terms of pit depth and pit width. The disparity between both sets of data in Figure 7.6 is not apparent in the cross-sectional profiles. This is because the plots shown in Figure 7.6a are for maximum pit depth, which is defined in the model as the numerical difference between the minimum and maximum points in the metal space rather than average pit depth (plotted for experimental data). The same is applicable to the plots for the pit width (Figure 7.6b). It can also be observed from Figure 7.8 that the profiles obtained from the model are not as smooth as those from the experiments. This is due to

the size of the lattice employed for the study ( $1000 \times 500$ ) for which the cell size is  $2.5 \mu\text{m}$ . Increasing the size of the lattice will smoothen the pit profile but will increase computation time exponentially.



**Figure 7.8** Comparison between cross-sectional profiles of pits obtained from experiment and CA model at different times.

The results show good agreement between experimental data and the outputs of the model (maximum depth, width and cross-sectional profiles of the pits). This gives

evidence that the 2-D CA model appears appropriately validated and sufficiently accurate for making predictions of the depth and geometry of a growing pit. Hence, the model was employed for studying pit development behaviour as will be presented in the next section.

## 7.6 Evolution of pit depth with and without stress

The optimized CA model was modified into a CAFE model by developing a 2-D FEA script, also with Matlab® scripting language, which was then integrated into the CA script. Due to computational time limitations, the frequency of the FE analysis was set at 5 i.e. one FE loop for every five CA time steps. Simulations were then carried out to investigate the influence of applied stress on local corrosion kinetics. It was necessary to perform this simulation using a larger lattice size (2000 x 1000) lattice in order to eliminate the edge effect of thinning of both sides of the pit, which was found to artificially increase the prevailing strain to unrealistic values especially at relatively larger pit depths. This ensured that the modelled pit is surrounded by sufficient solid material so that the resulting stress and strain are due to the pit only. Maximum pit depth was compared at  $\sigma_{max} = 0$  and 200 MPa for both stagnant and flowing conditions. The stress level was chosen to allow comparison with experimental data, which was obtained for tests carried out at  $\Delta\sigma = 180$  MPa ( $\approx \sigma_{max} = 200$  MPa at  $R = 0.1$ ).

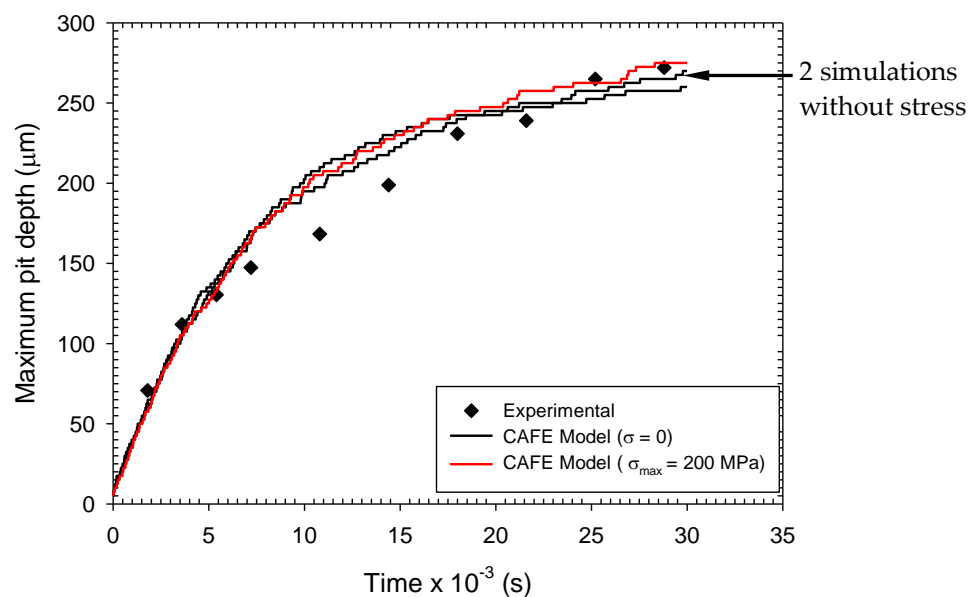
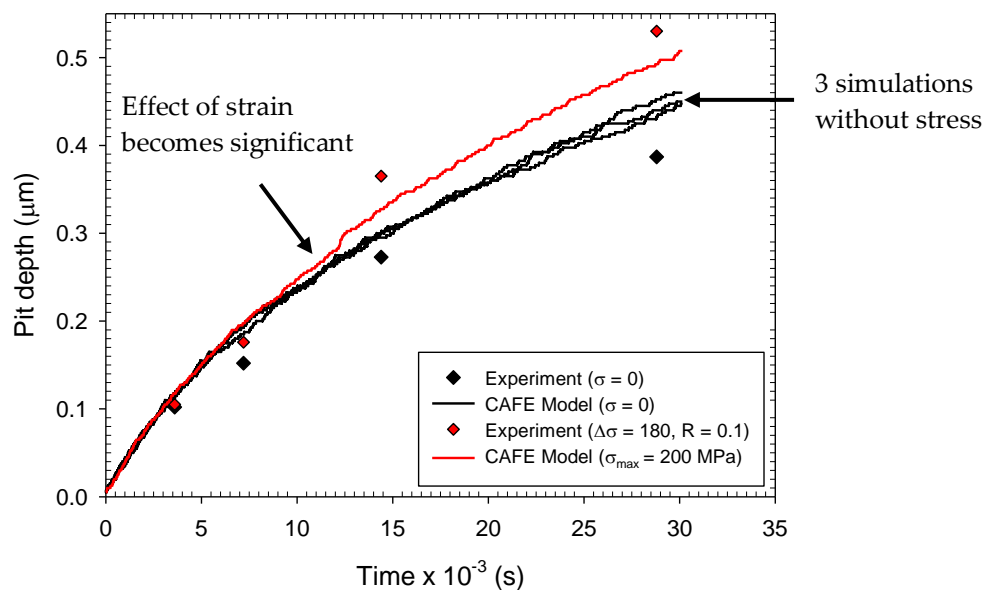


Figure 7.9 Evolution of maximum pit depth with time with and without stress for no flow conditions.



**Figure 7.10** Evolution of maximum pit depth with time with and without stress for flowing conditions.

Since the model accounted for the effect of deformation on corrosion kinetics, it was expected that the applied stress would result in an increase in the rate of metal dissolution, especially when localised plasticity is associated with the pit and consequently, increase in pit depth. Under stagnant conditions, no significant difference was observed in the evolution of pit depth with time with and without stress (Figure 7.9). The variance between the data with stress is within the standard deviation of the results of the simulations without stress (see Appendix C).

In contrast, the results from the model optimized for flow conditions (Figure 7.11) show that the evolution of pit depth is affected by stress. Generally, the model appears to show good correlation with experimental data, although maximum pit depth seems to be underestimated at relatively greater pit depths. Interestingly, the plot seems to show that the effect of stress on pit growth only becomes significant at some stage during pit growth (after about 12,000 seconds - highlighted in Figure 7.10). Before this stage, the evolution of pit depth with and without stress was not significantly different. This was attributed to the quantitative effects of elastic and plastic strains on the mechano-electrochemical influence factor i.e. plastic strains have a greater effect on the influence factor than elastic strains. To verify this claim, Equation 4.54 (influence factor for elastic deformation) and Equation 4.55 (influence factor for plastic deformation) were evaluated at room



temperature (298 °K) using elastic and plastic strains obtained from finite element analysis of an idealised 3-D pit model. Numerical values of the elastic strain at a point just before onset of plasticity and plastic strain after yielding (equivalent plastic strain - PEEQ of 0.1%) were applied as inputs to the equations. The influence factor obtained was 1.03 for elastic strain compared to 1.33 for the plastic strain. Conceptually, this means that a given  $P_{corr}$  value will increase by a factor of 1.03 and 1.33 for elastic and plastic deformation respectively. Hence, a higher probability for oxidation of Fe to  $Fe^{2+}$  when there is localised plasticity compared to when there is none. Also in Figure 7.10, similar to the experimental results, the difference between the maximum pit depth-time plots with and without stress seems to be increasing progressively with time as the pit become deeper. This agrees with earlier discussion of the effect of stress on corrosion rate. The onset of plasticity increases the probability for oxidation of metal, which may result in development of deeper pits. At a given applied stress level, the plasticity associated with a growing pit (increasing size) will likely increase progressively with pit size, thereby increasing the pit growth rate.

Comparison between the results presented in Figures 7.9 and 7.10 shows that, whereas the local corrosion kinetics was not affected significantly by applied stress under stagnant conditions, the influence was apparent under flow conditions. This suggests that the influence of mechanical stress depends on other processes taking place in the pit, in this case, accumulation of corrosion products. Although, deformation (through the mechano-electrochemical effect) may increase the tendency for dissolution [252, 305] i.e. oxidation of the Fe (metal sites) to  $Fe^{2+}$ , the accumulated corrosion products presented a diffusion barrier to the reaction species (in this case the acidic sites) required for oxidation to proceed. Consequently, the rate of metal loss remains unchanged as when no stress is applied. In the model simulating flow, the reduction in the rate of accumulation of corrosion products (i.e. relatively lower  $Sed$  value of 1.1) results in a lower diffusion barrier. This coupled with the increased tendency for oxidation as a result of deformation, will effectively increase the rates of anodic dissolution and pit growth.

### 7.7 Evolution of stress and strain with time

Understanding the evolution and distribution of stress and strain associated with time-dependent changes in geometry of a growing pit, in a stressed component, is important in order predict the conditions necessary for the transition of a pit to crack. Apart from the

mechano-electrochemical effect on corrosion kinetics, applied stress also induces local dynamic strain, which is recognized to result in nucleation of cracks around a pit [202]. When plasticity is significant, accumulation of plastic strains and changes in plastic strain rates increases the dynamic strains and consequently the susceptibility to cracking. Given that the simulation of continuous growth of a corrosion pit in 3-D is difficult, previous attempts to evaluate the distribution of stress and strain around pits have been based on a discretized approach whereby pit sizes at different stages during pit development are idealized as elliptical/hemispherical models on which FEA is conducted [1, 201, 230, 248, 306, 307]. More recently, the discretized approach has been improved to account for accumulated plasticity by simulating increment in pit size (pit growth) in a step-wise manner with retention of the history of the previous step [202]. Although this approach showed more accurate results, the number of pit size increments that can be simulated is limited. Furthermore, some assumptions regarding pit shape and actual pit depth have to be made. From a mechanics-based point of view, the CAFE model can help to overcome these challenges because:

1. No assumptions are required concerning changes depth, aspect ratio, morphology and shape symmetry of a growing pit (with time). Strains associated with actual pits simulated by the model are evaluated.
2. The influence of elastic and plastic deformation on corrosion kinetics and strain localization is accounted for.
3. Strain distribution corresponding to each pit size at every time step and its evolution during pit growth can all be evaluated automatically.

Typical Von Mises stress and total strain (maximum principal strain) distributions around the 2-D pits obtained at different time intervals in a direction parallel to loading are shown in Figure 7.11 and Figure 7.12 respectively. The results generally show that the distribution and evolution of stress and strain around a growing pit can be monitored and evaluated at every stage during pit development irrespective of depth, aspect ratio and morphology of the pit using the CAFE model. Whereas the extent of strain localization (evaluated as maximum principal strain) generally increased with time, pit depth and pit aspect ratio, the maximum effective stress did not change significantly for the range of pit depths shown. The latter indicates localised yielding given the yield strength of 530 MPa for this material.

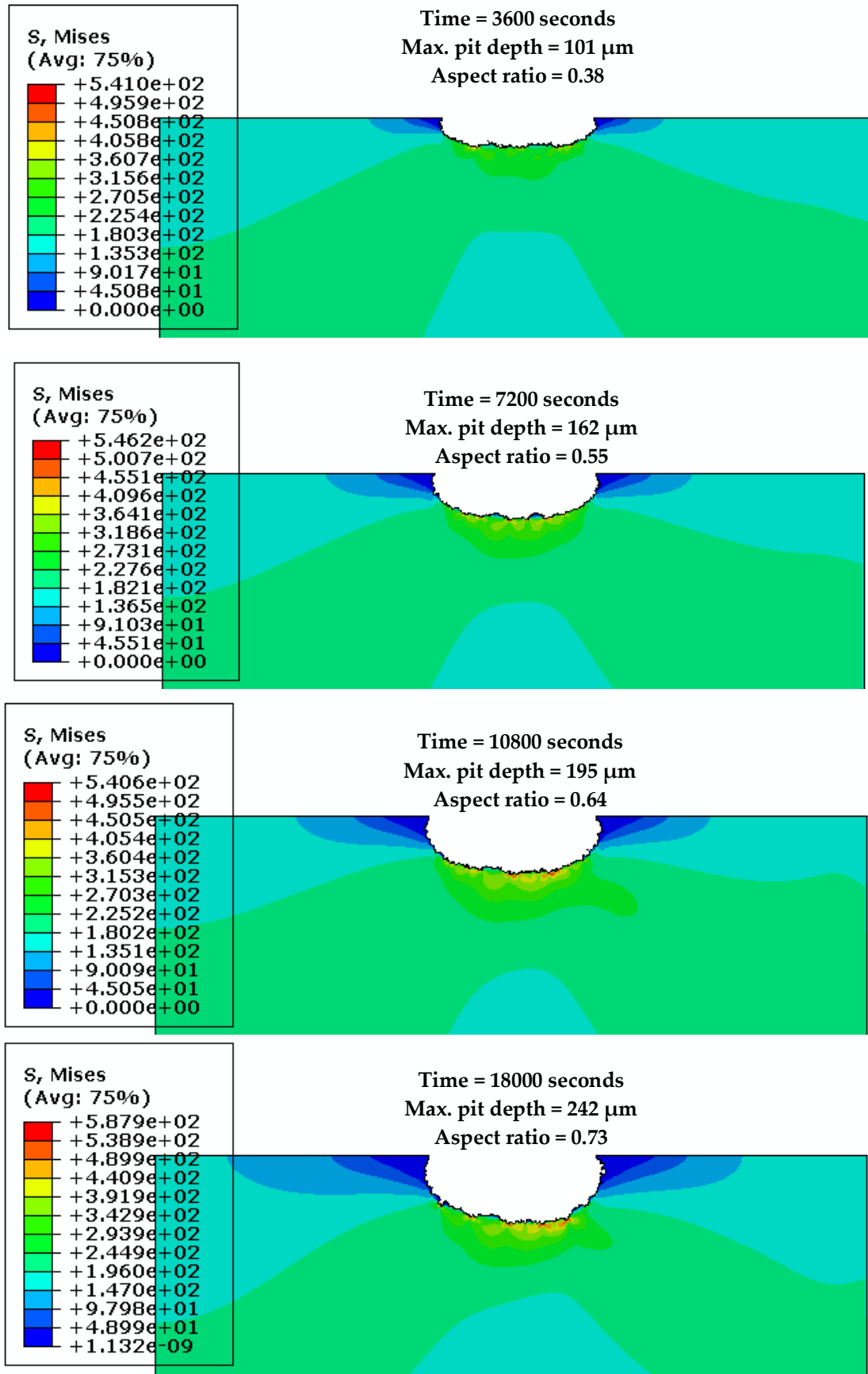


Figure 7.11 Evolution and distribution of equivalent stress around a growing pit in a static stress field simulated with the 2-D CAFE model. ( $\sigma_{\max} = 200 \text{ MPa}$ ).

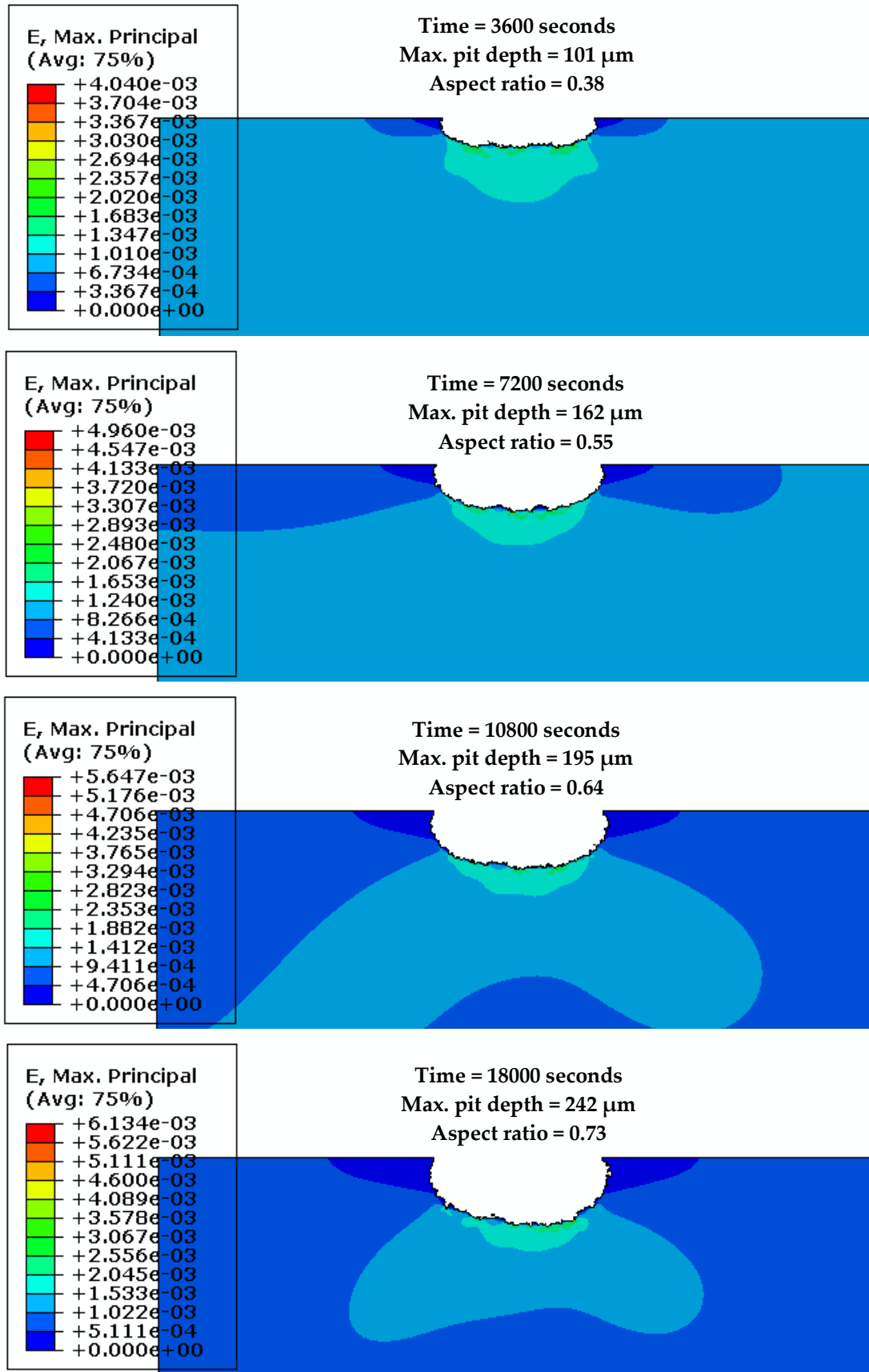
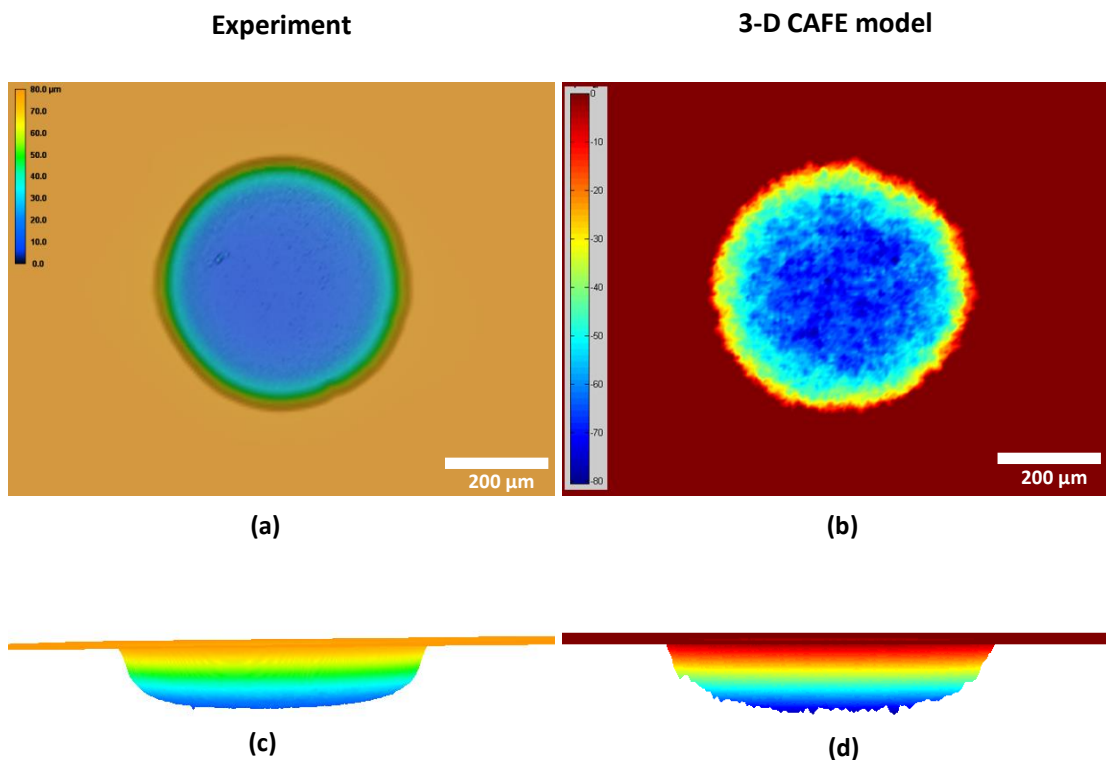


Figure 7.12 Evolution and distribution of total strain around a growing pit in a static stress field simulated with the 2-D CAFE model. ( $\sigma_{\text{max}} = 200 \text{ MPa}$ ).

## 7.8 Preliminary results from 3-D cellular automata model

As stated previously, the overall objective of this work is to develop a 3-D CAFE model for simulating time-dependent pit growth. Preliminary results from simulations employing a 3-D CA model are presented in this section. The validated 2-D model described in preceding sections has been modified into 3-D and employed to simulate pit development with no applied stress. Stress has not been applied at this stage because the script for carrying out the FEA part is still being developed. A Von Neumann neighbourhood (see Figure 4.9) was employed to minimize computational time compared to the Moore employed for the 2-D model. Figure 7.13 shows comparisons between model outputs and experimental data after an equivalent time of 1800 seconds. It is noticeable that both results show good correlation in the depth, width and morphology of the pits. The behaviour of the 3-D CAFE model was investigated further by simulating pit growth for longer periods. Figure 7.14 shows the evolution of the morphology and profile of a growing pit at different time periods. It can be observed that the trends in the results are in good agreement with those obtained from the 2-D model and from experiments. In general, these results show that the 3-D CAFE model is capable of simulating the changes in depth, aspect ratio and morphology of a growing pit.



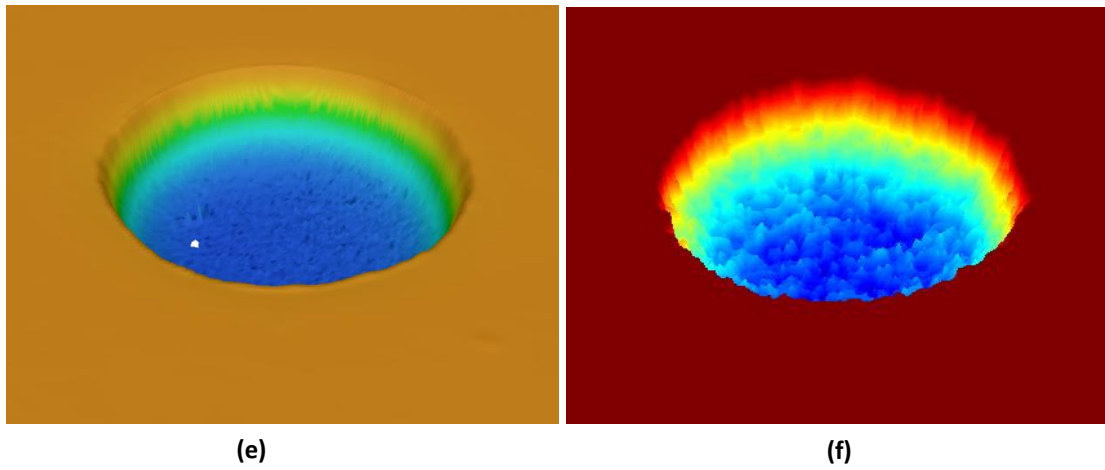
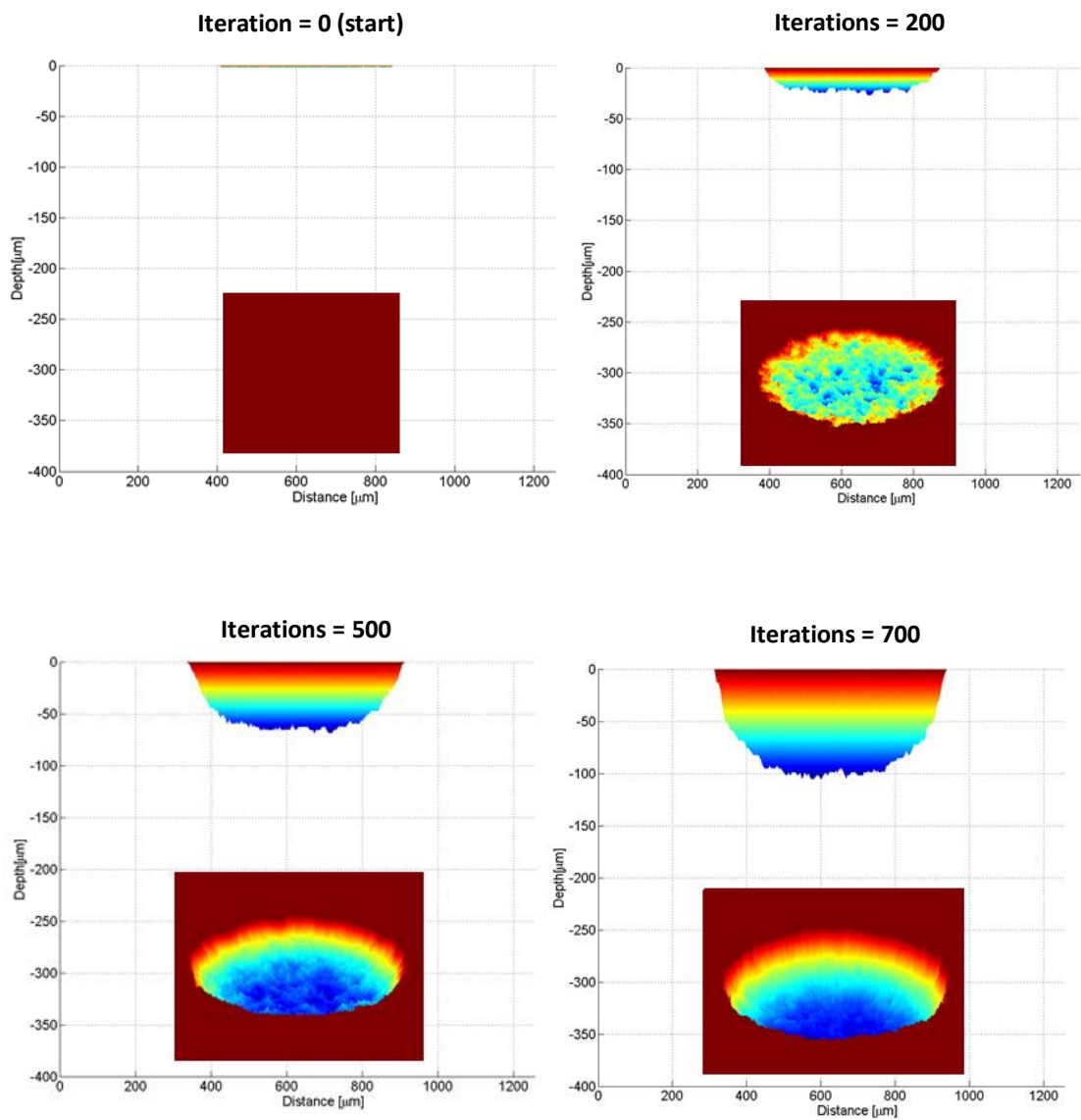
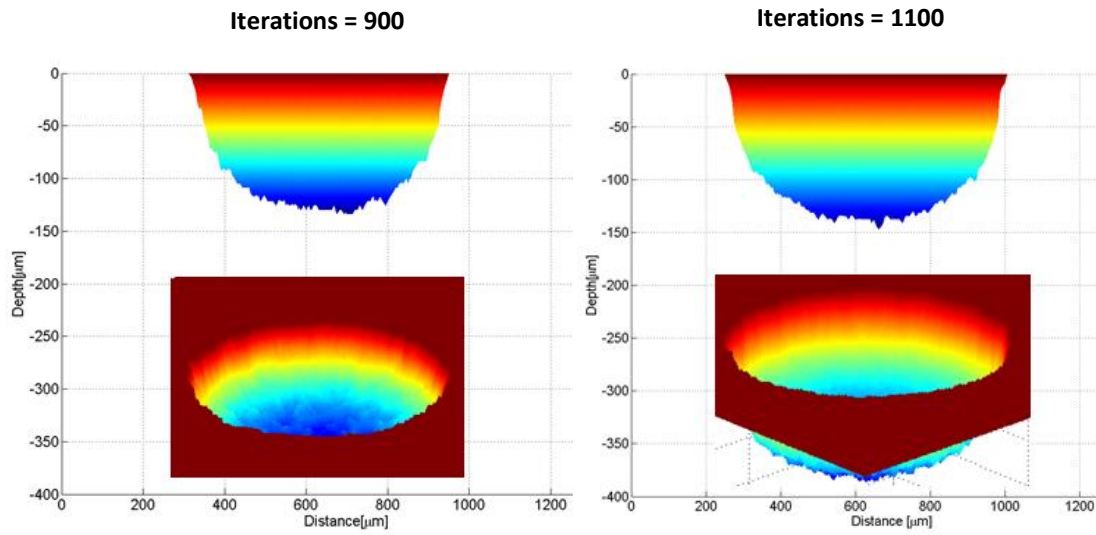


Figure 7.13 Comparison between 3-D profiles of pits obtained experimentally using the confocal microscope (a,c,e) and from 3-D CA model (b,d,f) at  $t = 1800$  seconds.





*Figure 7.14 Morphology and profile of a growing pit obtained from 3-D CA model at different iteration steps.*

---

# **Chapter 8**

## **Fatigue Lifetime**

### **Modelling**

---



## 8.1 Introduction

Corrosion fatigue is a damage process occurring due to synergistic interaction of electrochemical, metallurgical and mechanical loading. A predictive approach to lifetime management based on quantifying the evolution of damage from the earliest stage, including crack precursor development, is a major undertaking that requires developments in mechanistic understanding of the controlling processes and modelling capability. In this chapter, an attempt has been made to develop suitable multi-stage lifetime models for the air and corrosion fatigue tests carried out in the present study.

## 8.2 Multi-stage damage accumulation model

The core feature of the present predictive scheme is the quantification of the rate of damage development during the corrosion fatigue process; a damage process divided into the following four stages:

1. Pit development
2. Pit-to-crack transition
3. Short crack growth and
4. Long crack growth

Individual empirical model(s) have been developed for predicting the lifetimes (number of cycles) spent in each these regimes as a function of pit size, microstructure, environment and stress. The total fatigue lifetime is the accumulated lifetimes expressed as

$$N_{Total} = N_{pg} + N_{ptc} + N_{sc} + N_{lc} \quad 8.1$$

where  $N_{Total}$  is total fatigue life,  $N_{pg}$  is lifetime taken to generate a pit to specified depth,  $N_{ptc}$  is lifetime to nucleate a crack from a pit,  $N_{sc}$  is lifetime to propagate a crack up to the dominant microstructural barrier, and  $N_{lc}$  is lifetime taken to propagate the crack beyond this barrier until failure of the specimen. It is worth emphasizing the entire model development effort is based on corrosion fatigue systems where corrosion pits are precursors to fatigue cracks. Hence, material-environment systems where cracks emanate from defects other than corrosion pits are not considered. It was assumed that scale/film breakdown has already taken place so that active anodic dissolution of the underlying

metal through pit development is the first stage. In subsequent sections, the models developed for each of the different stages are presented.

### 8.2.1 Modelling pit growth

The time-dependent pit growth stage involves the evolution of damage (pit depth) with time. The relationship between pit depth and time may be expressed in the form

$$d_p = A_{pg} \cdot t^{n_{pg}} \quad 8.2$$

where  $d_p$  is maximum pit depth ( $\mu\text{m}$ ),  $t$  is time (hours), and  $A_{pg}$  and  $n_{pg}$  are the pit growth coefficient and exponent respectively both of which depend on the metal-environment system. These constants were determined by fitting Equation 8.1 to the maximum pit depth-time experimental data obtained for tests conducted with and without stress. The values obtained for  $A_{pg}$  and  $n_{pg}$  are 104.2 and 0.654 for the unstressed test ( $\Delta\sigma = 0$ ) and 118.5 and 0.640 at  $\Delta\sigma = 180$  MPa respectively. The coefficient,  $A_{pg}$ , show a dependency on stress hence, it was expressed as a function of stress range (Equation 8.2) in order to capture the effect of stress on pit growth.

$$A_{pg} = 104.242 (1.008)^{\Delta\sigma} \quad 8.3$$

where  $\Delta\sigma$  is the applied stress range (MPa).

Therefore, the general equation for predicting pit development as a function of time was expressed as

$$d_p = 104.2 (1.008)^{\Delta\sigma} \cdot t^{0.645} \quad 8.4$$

The pit depths predicted from this model at a given stress range (Figure 8.1) show good correlation with experimental data.

From Equation 8.3, the pit growth lifetime,  $N_{pg}$ , i.e. number of cycles required to generate a pit of given depth can be predicted by expressing  $t$  as a function of cyclic frequency,  $f$ , (i.e.  $N = t \cdot f$ ) as given below.

$$N_{pg} = 3600 \cdot f \left[ \frac{d_p}{104.242 (1.0076)^{\Delta\sigma}} \right]^{\frac{1}{0.645}} \quad 8.5$$

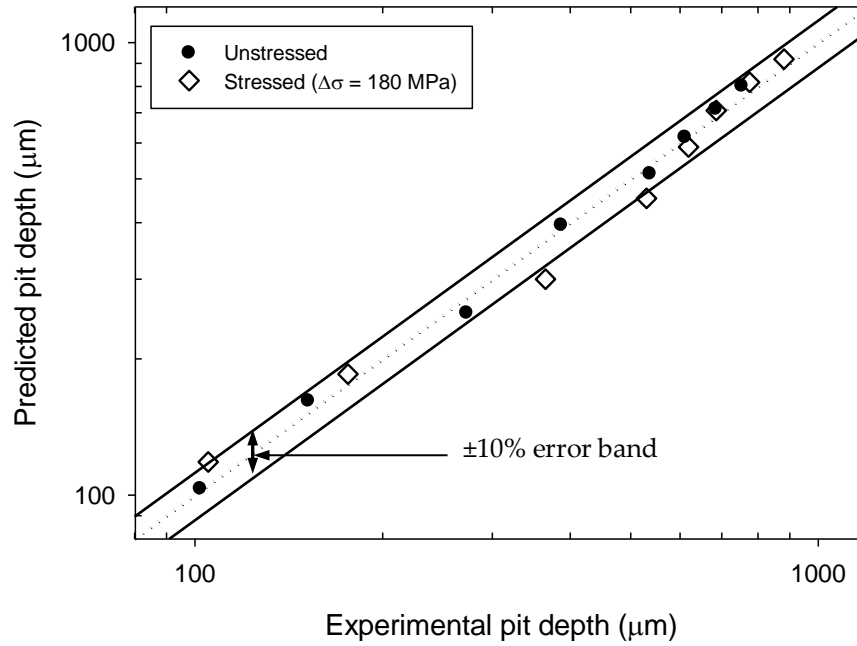


Figure 8.1 Comparison between experimental and predicted pit depths from pit growth model.

It is recognized that the constants in Equation 8.4 are based on experimental data from only two stress levels. For the model to be applicable at other stress levels, new values of constants should be evaluated from the experimental data for stress ranges of interest. Nevertheless, for analysis purposes, the constants were assumed to be valid at all stress ranges. Based on Equation 8.4, pit growth lifetime calculations were made for a given pit depth, stress range and test frequency (2 Hz for the present study).

### 8.2.2 Modelling pit-to-crack transition lifetimes

The number of cycles to crack initiation in air and corrosion fatigue were experimentally observed to depend on applied stress and pit size. It is therefore important to predict pit-to-crack transition lifetimes as a function of these two variables. The relationship between crack initiation lifetime for single pits,  $N_{ptc}$ , and pit aspect ratio,  $AR_p$ , can be expressed as

$$N_{ptc} = G \cdot (AR_p)^g \quad 8.6$$

where  $G$  and  $g$  are material-environment constants. The values of  $G$  and  $g$  in air and corrosion fatigue, given in Table 8.1, were determined by regression analysis of  $N_{ptc} - AR_p$  experimental data obtained at different stress ranges. Both constants depend on stress hence, both were expressed as a function of stress range,  $\Delta\sigma$ , as given in Equations 8.7 and 8.8.

$$G = K \cdot (\Delta\sigma)^p \quad 8.7$$

$$g = L \cdot (\Delta\sigma)^q \quad 8.8$$

The values obtained for the constants by regression analysis of data in **Table 8.1** are:

$$K = 1.6 \times 10^{43}, L = -1.2 \times 10^{13}, p = -14.088, \text{ and } q = -4.811 \quad (\text{air})$$

$$K = 8.0 \times 10^{20}, L = -1.3 \times 10^5, p = -5.974, \text{ and } q = -1.845 \quad (\text{corrosion fatigue})$$

**Table 8.1 Summary of material constants for pit-to-crack transition lifetime equation.**

$\Delta\sigma$ (MPa)	Air fatigue		Corrosion fatigue	
	$G$	$g$	$G$	$g$
405	$2.423 \times 10^6$	-3.676	$2.056 \times 10^5$	-1.983
427.5	$2.046 \times 10^6$	-2.342	$1.623 \times 10^5$	-1.752
450	$5.434 \times 10^5$	-2.222	$1.094 \times 10^5$	-1.634

Substituting Equations 8.7 and 8.8 into Equation 8.6 yields Equation 8.9, which predicts pit-to-crack transition lifetimes for known stress range and pit aspect ratio. This model is based on the assumption that the stress range-pit depth combination has satisfied the pit-to-crack transition conditions in air and corrosion fatigue i.e. either the stress range is above the fatigue limit associated with a particular pit size or the pit depth is above the critical size that will initiate a crack.

$$N_{ptc} = K \cdot (\Delta\sigma)^p \cdot (AR_p)^{L \cdot (\Delta\sigma)^q} \quad 8.9$$

Based on Equation 8.9, pit-to-crack transition lifetimes were calculated for air and corrosion fatigue environments. The predicted lifetimes together with experimental data are shown in Figure 8.2.

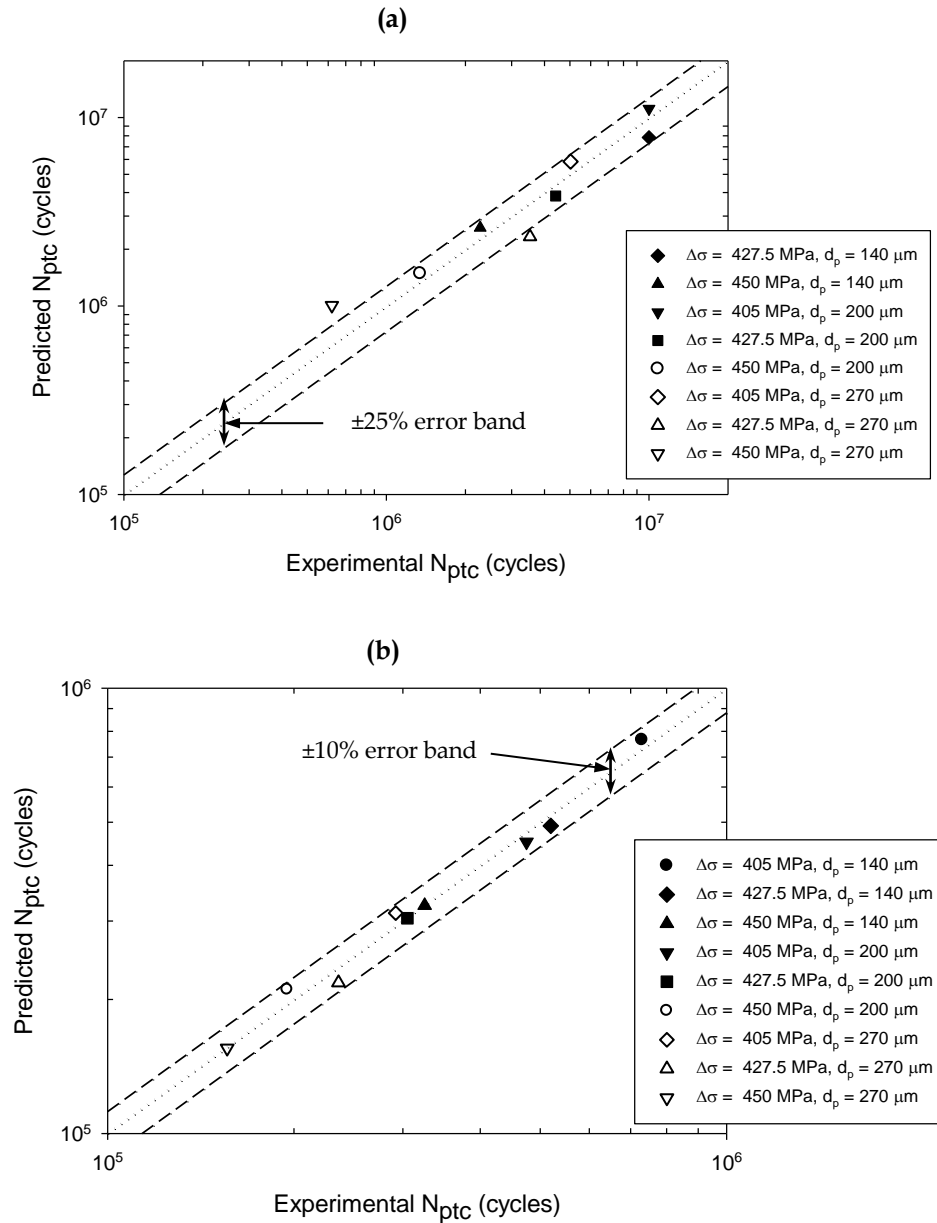


Figure 8.2 Comparisons between experimental and predicted pit-to-crack transition lifetimes in (a) air and (b) corrosion fatigue.

### 8.2.3 Modelling effect of proximity between pits

The decrease in crack initiation lifetimes, when pit-to-pit separation distance decreases, as observed in air in the present work, reflect the dependency of crack initiation behaviour on proximity between pits. It is therefore important to account for the influence of separation distances between pits on the crack initiation lifetimes. Experimental results showed that this influence is subject to a threshold separation distance,  $d_{th}$ , schematically shown in Figure 8.3. In region A, separation distance between pits,  $d$ , influences crack initiation lifetime, but does not, in region B. The transition between both regions has been

defined by  $d_{th}$ . For  $d < d_{th}$ ,  $N_i$  is given by line (1) with  $d$  ranging from a minimum value up to  $d_{th}$ . For  $d \geq d_{th}$ ,  $N_i$  is given by line (2) and it tends towards the crack initiation lifetimes for single pits with similar geometry loaded to the same stress level. Therefore, it is necessary to model this relationship over the entire possible range of separation distances. This has been done in the present work by developing equations for  $d_{th}$  and lines (1) and (2), highlighted on Figure 8.3. In the present model,  $d$  is assumed to always have a positive value and is greater than a minimum value (obtained by observation) in order to be able to influence crack initiation behaviour. This means that events such as pit coalescence are excluded. The model also assumes that the depths and aspect ratios of two different pits developing close to each other are equivalent.

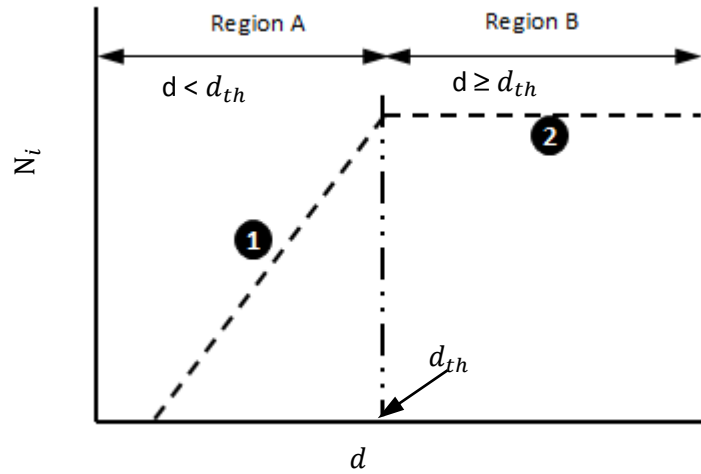


Figure 8.3 Schematic showing different regions on a crack initiation lifetime-separation distance plots for double pits in air.

The threshold separation distance is a function of pit aspect ratio and can be expressed in the form

$$d_{th} = A_{th} (AR_p)^{\beta_{th}} \quad 8.10$$

where  $d_{th}$  is threshold separation distance,  $AR_p$  is pit aspect ratio, and  $A_{th}$  and  $\beta_{th}$  are constants whose values depend on material-environment. The values were determined by non-linear regression analysis of the  $d_{th}-\Delta\sigma$  data in Table 5.6. The values obtained for  $A_{th}$  and  $\beta_{th}$  are given in Table 8.2, which shows that both constants are stress dependent. Since all the tests were conducted in air, these constants are expressed as a function of applied stress range only, as given below.

$$A_{th} = A_{th}' (\Delta\sigma)^{a_{th}'} \quad 8.11$$

$$\beta_{th} = \beta_{th}' (\Delta\sigma)^{b_{th}'} \quad 8.12$$

The values obtained for  $A_{th}'$ ,  $\beta_{th}'$ ,  $a_{th}'$  and  $b_{th}'$  are  $6.63 \times 10^{-9}$ ,  $5.29 \times 10^{-8}$ , 4.31 and 2.73 respectively. They were determined by fitting Equations 8.11 and 8.12 with the corresponding data in Table 8.2. Substituting Equations 8.12 and 8.13 into Equation 8.10, a general model obtained for predicting  $d_{th}$  for a given combination of pit aspect ratio and applied stress range is presented in Equation 8.13. Comparison between the experimental and predicted values enumerated in Table 8.3 show good agreement.

$$d_{th} = 6.63 \times 10^{-9} (\Delta\sigma)^{4.31} (AR_p)^{5.29 \times 10^{-8} (\Delta\sigma)^{2.73}} \quad 8.13$$

**Table 8.2 Summary of the constants for threshold separation distance equation.**

$\Delta\sigma$ (MPa)	$A_{th}$	$\beta_{th}$
405.0	1125.536	0.698
427.5	1420.643	0.809

**Table 8.3 Comparison between experimental and predicted threshold separation distances.**

$\Delta\sigma$ (MPa)	Pit depth ( $\mu\text{m}$ )	Pit aspect ratio	Experiment ( $\mu\text{m}$ )	Equation 8.13 ( $\mu\text{m}$ )
405.0	200	0.68	860	856
427.5	200	0.68	1040	1035
405.0	270	0.82	980	975
427.5	270	0.82	1210	1204

**Table 8.4 Summary of the constants for crack initiation lifetime equation for double pits.**

Pit depth ( $\mu\text{m}$ )	Aspect ratio	$A_{double}$		$\beta_{double}$	
		405 MPa	427.5 MPa	405 MPa	427.5 MPa
200	0.68	6.702	80.995	0.0152	0.0104
270	0.82	29.763	450.100	0.0111	0.0068

Line (1) in Figure 8.3, defines the relationship between crack initiation lifetime and separation distance between double pits at  $d < d_{th}$ . The experimental data (see Figure 5.20) show exponential rise in crack initiation lifetimes with increase in separation distance, therefore line (1) is expressed in the exponential form given below

$$N_{i,double} = A_{double} \exp^{\beta_{double}(d)} \quad 8.14$$

where  $d$  is the centre-to-centre distance in  $\mu\text{m}$ ,  $N_{i,double}$  is crack initiation lifetime for two pits located close to another.  $A_{double}$  and  $\beta_{double}$  are material constants. Their values (see Table 8.4) were determined from crack initiation lifetime-centre-to-centre distance experimental data (see Appendix D) by regression analysis. Note that the subscripts 'double' indicate a variable or constant associated with two pits in proximity to each other. Both constants can be observed to depend on pit size and stress. The constants were first expressed as a function of pit aspect ratio as

$$A_{double} = A'_{double} (AR_p)^{a'_{double}} \quad 8.15$$

$$\beta_{double} = \beta'_{double} (AR_p)^{b'_{double}} \quad 8.16$$

where  $A'_{double}$ ,  $\beta'_{double}$ ,  $a'_{double}$ , and  $b'_{double}$  are constants, which were then expressed in terms of stress range in **Equations 8.17 - 8.20**.

$$A'_{double} = A''_{double} (\Delta\sigma) + C' \quad 8.17$$

$$\beta'_{double} = \beta''_{double} (\Delta\sigma) + C'' \quad 8.18$$

$$a'_{double} = a''_{double} (\Delta\sigma)^{a''} \quad 8.19$$

$$b'_{double} = b''_{double} (\Delta\sigma)^{b''} \quad 8.20$$

where  $A''_{double}$ ,  $\beta''_{double}$ ,  $a''_{double}$ ,  $b''_{double}$ ,  $a''$ ,  $b''$ ,  $C'$ , and  $C''$  are all constants. Their values, listed below, were obtained from non-linear regression analysis of the constants obtained from Equations 8.15 and 8.16.

$$A''_{double} = 116.80, a''_{double} = 1.39 \times 10^{-6}, a'' = 2.591, C' = -47159$$

$$\beta''_{double} = -1.62 \times 10^{-4}, b''_{double} = -2.39 \times 10^{-15}, b'' = 5.693, C'' = 7.35 \times 10^{-2}$$

Line (2) in Figure 8.3, defines the relationship between crack initiation lifetime and separation distance between double pits at  $d \geq d_{th}$ . Since this is a horizontal line with zero slope,  $N_{i,double}$  will equate to the statistical distribution of crack initiation lifetime for a single isolated pit,  $N_{i,single}$ . Thus,  $N_{i,double}$  in this region will be similar to the crack initiation lifetime at  $d = d_{th}$ . This can be expressed as

$$N_{i,double} = A_{double} \exp^{\beta_{double}(d_{th})} \quad 8.21$$

For a given combination of separation distance, pit aspect ratio and applied stress range,  $d_{th}$  was first calculated from Equation 8.13. The crack initiation lifetimes were then predicted based upon Equations 8.14 when the given separation distance is less than the



predicted  $d_{th}$  and based upon Equation 8.21 when separation distance less than  $d_{th}$ . Figures 8.4 and 8.5 show the predicted crack initiation lifetimes and the corresponding experimental values. The numerical values are presented in Appendix D.

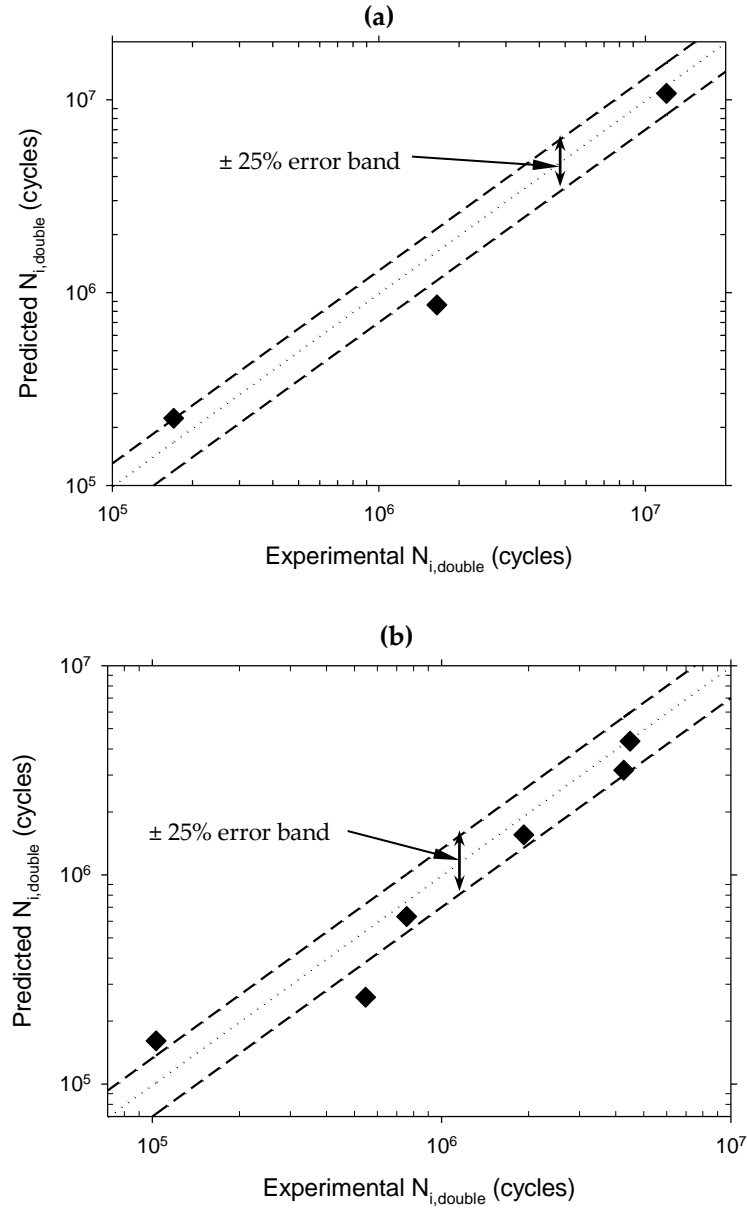


Figure 8.4 Comparison between experimental and predicted crack initiation lifetimes in air for 200  $\mu\text{m}$  deep pits (aspect ratio = 0.68) loaded at (a)  $\Delta\sigma = 405 \text{ MPa}$  and (b)  $\Delta\sigma = 427.5$ .

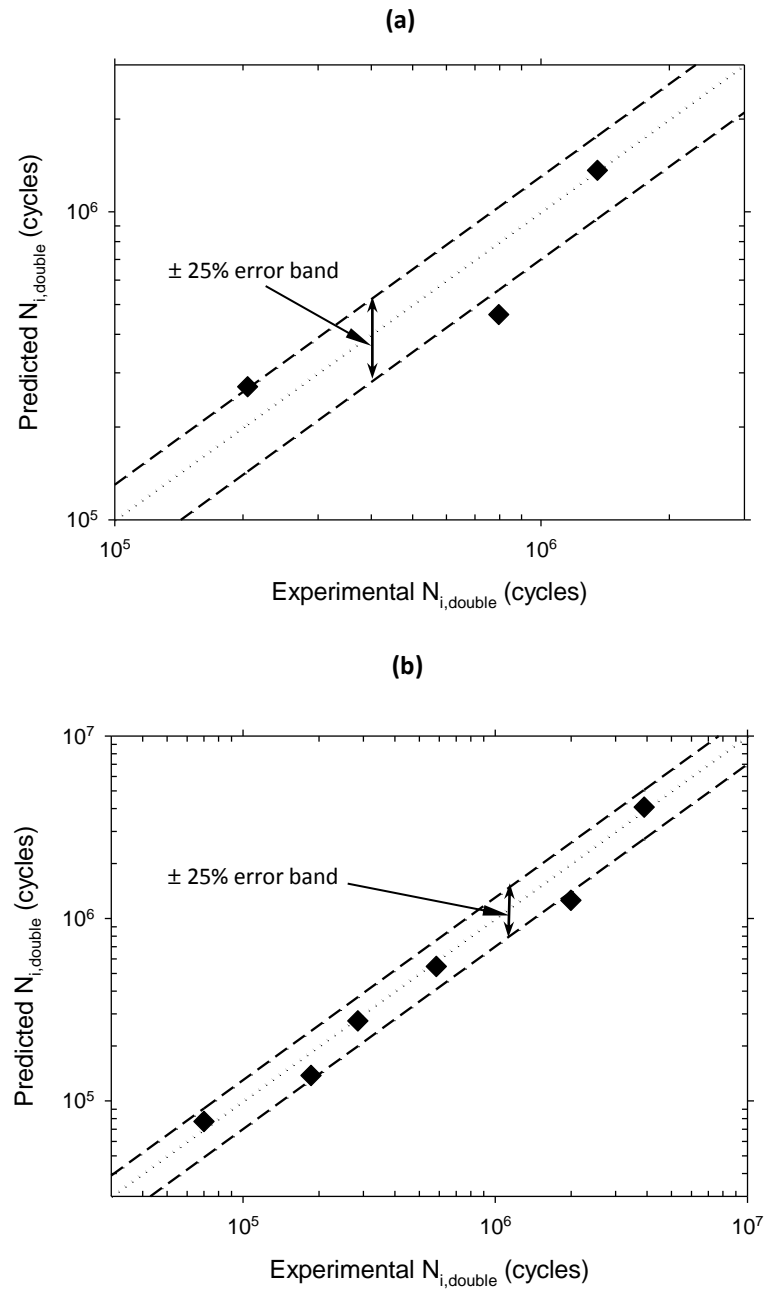


Figure 8.5 Comparison between experimental and predicted crack initiation lifetimes in air for 270  $\mu\text{m}$  deep pits (aspect ratio = 0.82) loaded at (a)  $\Delta\sigma = 405 \text{ MPa}$  and (b)  $\Delta\sigma = 427.5 \text{ MPa}$ .

### 8.2.4 Modelling crack growth

The perturbations in crack growth rates and crack arrest when cracks were shorter (notably Stage I crack growth regime) as observed in the present work reflect the dependency of propagation behaviour of cracks on microstructure. It is therefore important to model the influence of microstructure on growth rates of the cracks which emanated from the pits. At relatively longer, physically small crack lengths, the cracks had encompassed several grains and the influence of the microstructure is seen to

diminish (see Figure 5.31 – 5.35) because the crack has overcome the dominant barrier to crack growth. In this regime (Stage II crack growth regime), the crack growth rate is an increasing function of crack length. It is generally accepted that LEFM models cannot provide accurate predictions of growth rates of cracks exhibiting these types of behaviour due to the large plastic zone compared to the crack size [33, 82]. Hence, the microstructural fracture mechanics and elastic-plastic fracture mechanics approaches, based on the model developed by Hobson *et al.* [54] for in-air fatigue and later modified by Akid *et al.* [36, 89, 183] for corrosion fatigue were adopted in the present work. These models have been employed to successfully describe the discontinuous growth of short cracks subject to perturbations arising from resistance of microstructural variables to crack advance [36, 90, 183].

#### 8.2.4.1 Short fatigue crack growth

According to these models, the propagation behaviour of microstructurally short (Stage I) cracks can be expressed as

$$\frac{da_s}{dN} = C_s \cdot (d_i - a_s) \quad 8.22$$

where  $\frac{da_s}{dN}$  is microstructurally short crack growth rate,  $d$  is the distance between adjacent microstructural barriers to crack propagation,  $a_s$  is the surface length of a short crack.  $C_s$  is a material constant which depends on applied stress and environment and can be expressed as

$$C_s = A_i \cdot \Delta\sigma^{\alpha_i} \quad 8.23$$

where  $\Delta\sigma$  is the applied stress range and  $A$  and  $\alpha$  are also material constants. Combination of Equations 8.22 and 8.23 yields the general Equation 8.24.

$$\frac{da_s}{dN} = A_i \cdot \Delta\sigma^{\alpha_i} \cdot (d_i - a_s) \quad \text{for } i=1,2,\dots,n \quad 8.24$$

where  $i$  is the grain number and  $n$ th grain is the average number of grains which equates the length of the dominant barrier. The constants were determined from experimental data obtained in air and brine environments.

It is clear that the applicability of Equation 8.24 depends on the establishment of a microstructural parameter,  $d$ , which describes the distance between successive barriers

and a dominant microstructural barrier, the dimensions of which represents the transition crack length from a short crack growth to long crack growth regimes. Both are determined by the material's microstructure and may vary within the same material depending on the texture. The in-air crack growth rate-crack length data in the regions with decelerations in crack growth rates were analysed using linear regression analysis to determine the value of  $d$ . The results showed a large variation that reflects the variation in the material's grain size suggesting that the values of the transition crack length and the distances between successive barriers may vary between a range of values. This will relate to the grain size distribution and actual grain sizes throughout the microstructure. The transition length in air was estimated by considering the lengths of the observed non-propagating cracks and the lengths obtained from experimental data. Since the experimental data represents both short and long crack regimes, the point of inflexion of a best fit third order polynomial fitted to the data was taken as a close approximation of the transition length (see Figure 8.6). Table 8.5 shows that the estimated values of the transition length range between 54 and 146  $\mu\text{m}$  and its mean value is 105  $\mu\text{m}$ .

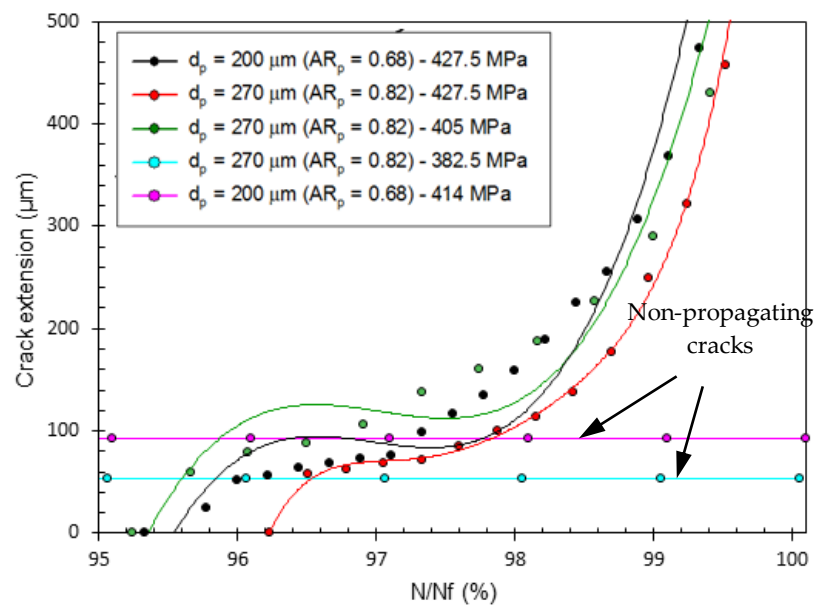


Figure 8.6 Measured surface crack extension histories and fitted polynomials for different fatigue tests conducted in air together with non-propagating cracks.

Table 8.5 Estimated values of Stage I to Stage transition length in air.

$\Delta\sigma$ (MPa)	Pit depth ( $\mu\text{m}$ )	$d$ ( $\mu\text{m}$ )
450	140	132

414*	200	92
427.5	200	93
450	200	125
382.5*	270	54
405	270	128
427.5	270	71
450	270	146

\* Non-propagating crack

The distances between successive barriers will likely tend toward the size of the largest grains therefore, a representative value of 25  $\mu\text{m}$  was adopted for the material and subsequently used in crack growth data analysis. The mean value of the average transition length (105  $\mu\text{m}$ ) was divided by this representative size of the largest grains (25  $\mu\text{m}$ ), to obtain  $n = 4$  in Equation 8.24. The coefficient,  $C_s$ , in Equation 8.22 was determined as the slope of plots of  $\frac{da_s}{dN}$  versus  $d_i - a_s$  for each successive grain barrier and for each crack that initiated from a pit. The obtained values are given in Table 8.6.

Table 8.6 Coefficients for short and long crack growth equations in air.

$\Delta\sigma$ (MPa)	Short crack growth ( $C_{sa}$ in Equation 8.22)				Long crack growth ( $C_{la}$ in Equation 8.25)
	0 – 25 $\mu\text{m}$	25 – 50 $\mu\text{m}$	50 – 75 $\mu\text{m}$	75 – 100 $\mu\text{m}$	100 – 1300 $\mu\text{m}$
405	$5.063 \times 10^{-4}$	$5.063 \times 10^{-4}$	$1.454 \times 10^{-4}$	$1.090 \times 10^{-4}$	$3.077 \times 10^{-5}$
427.5	$6.531 \times 10^{-4}$	$6.531 \times 10^{-4}$	$2.279 \times 10^{-4}$	$1.133 \times 10^{-4}$	$3.564 \times 10^{-5}$
450	$7.170 \times 10^{-4}$	$7.170 \times 10^{-4}$	$3.410 \times 10^{-4}$	$1.166 \times 10^{-4}$	$4.021 \times 10^{-5}$

Due to limited experimental data points for crack lengths less than 25  $\mu\text{m}$ , sensible values could not be obtained for the coefficients for the first grain barrier,  $d_1$ . Hence, for analysis purposes, the coefficients obtained for the second barrier i.e.  $d_2$  were also assumed to be applicable for  $d_1$ . The variations that can be seen in the values of  $C_s$  at the same stress level indicate that the crack growth rates in different grains are not necessarily the same at a given stress level. This expected because the growth rate of an individual crack will depend on the size of the grain in which it is growing and the orientation of the grain's slip plane and slip direction with respect to the loading axis.  $C_s$  was expressed as a function of applied stress range by non-linear regression analysis of the  $C_s$ - $\Delta\sigma$  data in Table 8.6 to obtain the constants in Equation 8.24. The values of the constants are:

$$A_i = 1.18 \times 10^{-12}, 1.16 \times 10^{-25} \text{ and } 2.33 \times 10^{-6} \quad (\text{for grains 2 – 4 respectively})$$

and  $\alpha_i = 3.315, 8.092 \text{ and } 0.640 \quad (\text{for grains 2 – 4 respectively})$

with  $d_i = 25, 50, 75$  and  $100 \mu\text{m}$ .

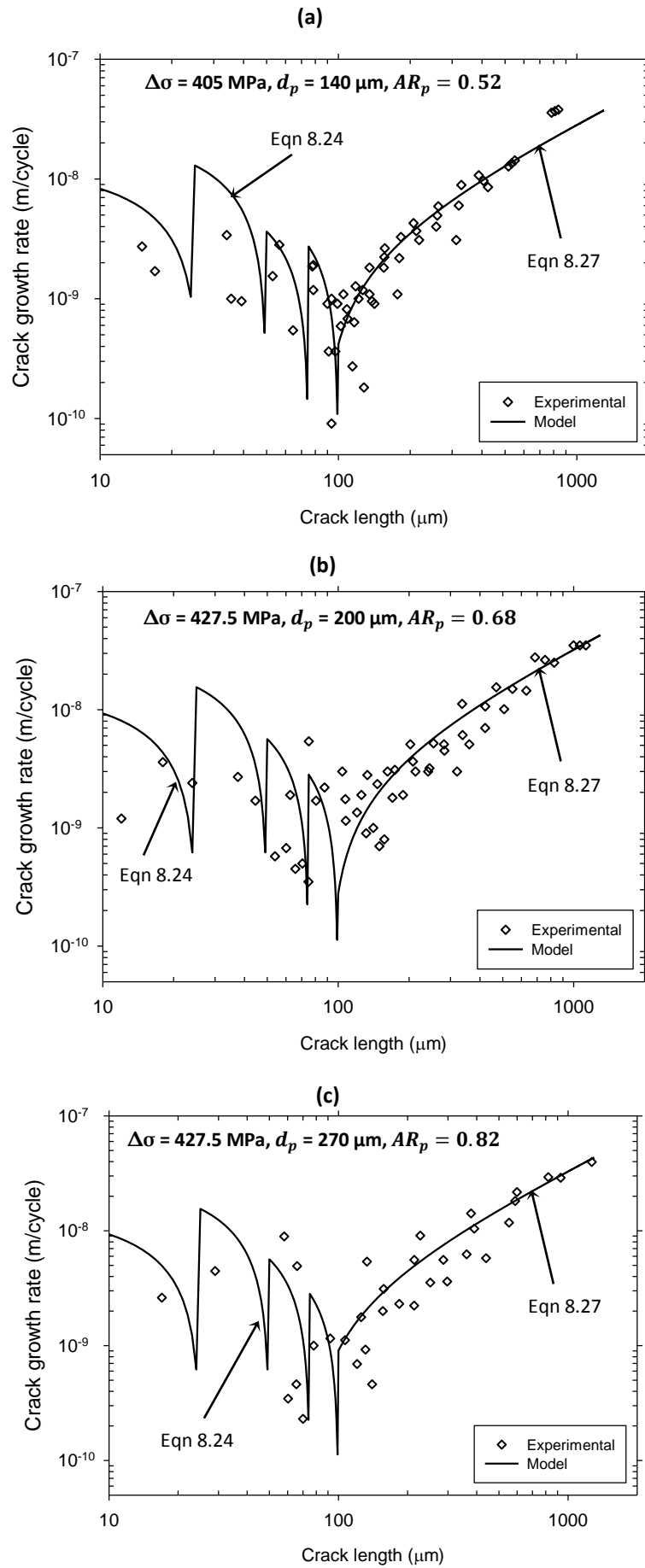
The crack growth rates in this regime were calculated for air fatigue by substituting the values of these constants in to Equation 8.24. The results, plotted together with experimental data, are shown in Figure 8.7.

For corrosion fatigue conditions, there appears to also be perturbations in observed crack growth rates although not as marked as in air. In order to be able to model the growth behaviour of corrosion fatigue short cracks, it was assumed that once a crack initiates from a pit, the microstructure also influences propagation behaviour. Unfortunately there were insufficient experimental data points for determining  $C_s$  at different stress levels hence,  $A_i$  and  $\alpha_i$  could also not be determined experimentally. Since the growth rates of the short cracks were higher in the aggressive environment than in air, a conservative approach that adopted for modelling crack growth in this regime, was to increase the values of  $C_s$  obtained in air by a specific factor. This factor should correlate with the difference in the number cycles taken to propagate a short crack beyond the dominant microstructural barrier in corrosion fatigue compared to air. From comparative inspection of experimental crack length-number of cycles data obtained in air and corrosion fatigue, an average value of 2 seemed appropriate. Therefore, the values obtained for the constants are:

$$A_i = 2.95 \times 10^{-12}, 2.89 \times 10^{-25} \text{ and } 5.84 \times 10^{-6} \quad (\text{for grains 2 - 4 respectively})$$

and  $\alpha_i = 3.315, 8.092 \text{ and } 0.640 \quad (\text{for grains 2 - 4 respectively})$

The crack growth rates in corrosion fatigue were calculated using these values for the constants in Equation 8.24. The results are plotted together with experimental results as shown in Figure 8.8.



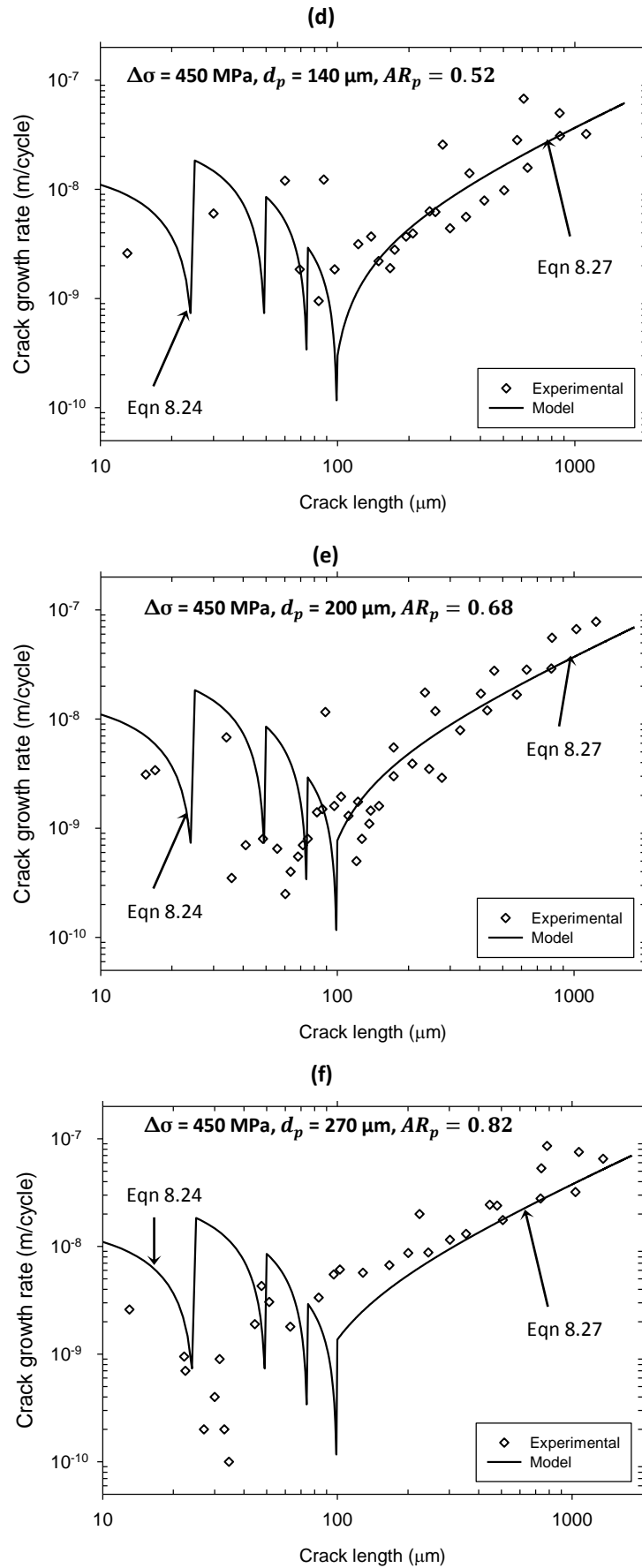
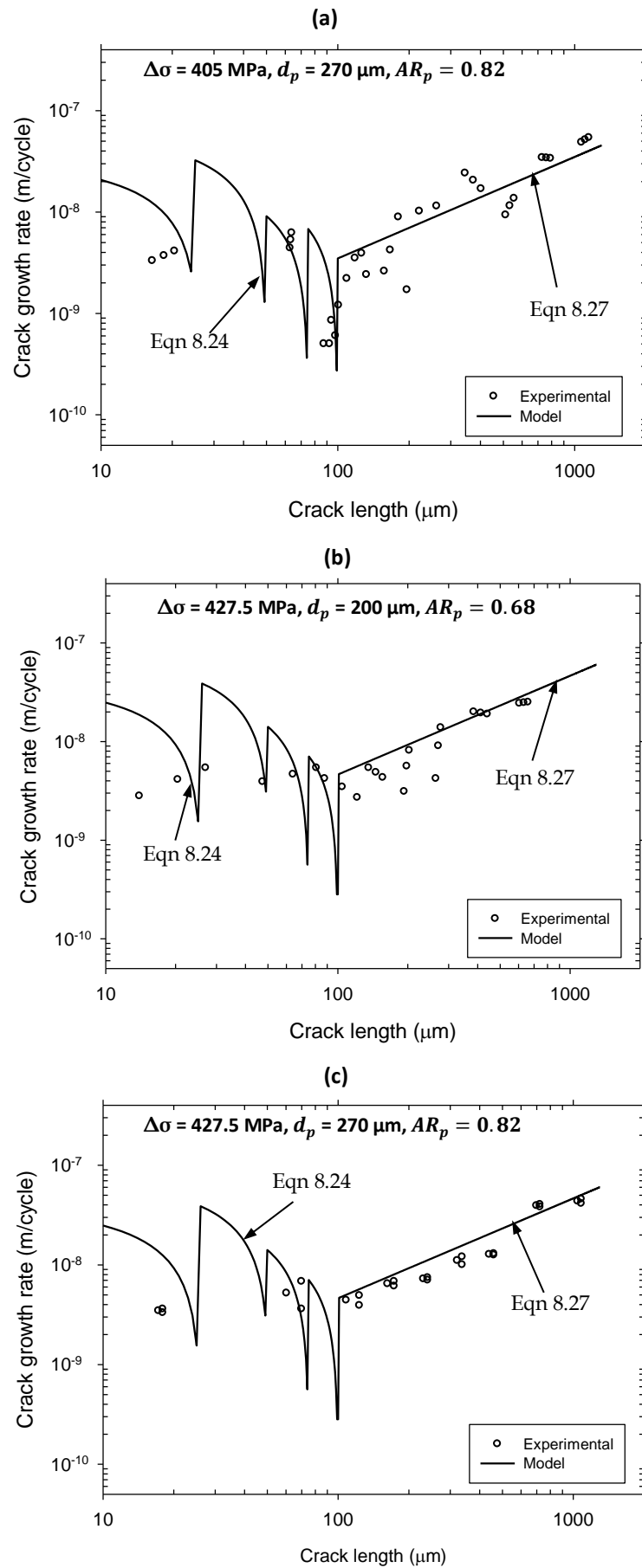


Figure 8.7 Comparison of predicted and experimental fatigue crack growth rates in air.





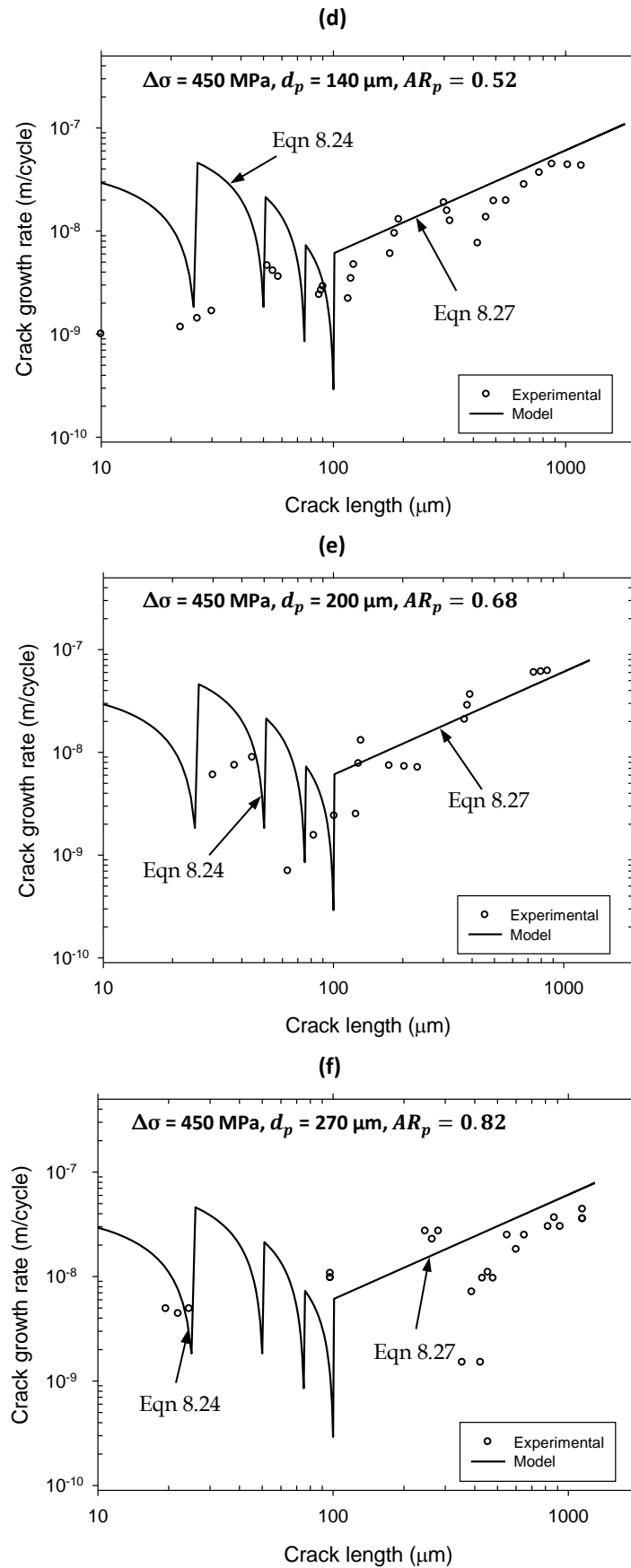


Figure 8.8 Comparison of predicted and experimental crack growth rates in corrosion fatigue.

### 8.2.4.2 Long fatigue crack growth

In the long crack growth regime, there is little or no influence of microstructure on crack growth hence, the crack growth rates increase continuously with crack length. The propagation rate of the cracks in this regime can be expressed as

$$\frac{da_l}{dN} = C_{la} \cdot a_l - D_l \quad 8.25$$

where  $\frac{da_l}{dN}$  is long crack growth rate and  $D_l$  is a stress dependent crack growth rate threshold.  $C_{la}$  is stress and environment dependent material constant that may be expressed as

$$C_{la} = B \cdot \Delta\sigma^\beta \quad 8.26$$

where  $\Delta\sigma$  is the applied stress range and  $B$  and  $\beta$  are material constants.

Substituting Equation 8.26 into Equation 8.25 yields the general Equation 8.27.

$$\frac{da_l}{dN} = B \cdot \Delta\sigma^\beta \cdot a_s - D_l \quad 8.27$$

The values of the coefficient,  $C_{la}$ , at different stress levels were first determined as the slopes of crack growth rates-crack length data for crack lengths greater than  $d_{tr}$  in air and corrosion fatigue i.e. 100  $\mu\text{m}$  (see Table 8.6 for the values of  $C_{la}$ ). Non-linear regression analysis was then conducted on the  $\Delta\sigma$ - $C_{la}$  data to obtain the constants in Equation 8.27. In air and corrosion fatigue, the values obtained for  $B$  and  $\beta$  are  $7.301 \times 10^{-12}$  and 2.542 and  $7.604 \times 10^{-19}$  and 5.240 respectively.

The constant,  $D_l$ , represents a minimum threshold crack growth rate that is dependent on the stress range at which the crack growth rate approaches zero.  $D_l$  was therefore calculated from the fatigue limit by employing the following equation

$$D_l = B \cdot (\Delta\sigma_0)^\beta d_{tr} \quad 8.28$$

where  $\Delta\sigma_0$  is the fatigue limit.

Since the experimental results showed that the fatigue limit in air is a function of pit size, different  $D_l$  values were obtained for different pit sizes. The values obtained in air are given in Table 8.7. To determine the fatigue limit in corrosion fatigue, a trendline was applied to the corrosion fatigue S-N data. The fatigue limit for each pit size was then

evaluated as the point of intersection at  $10^7$  cycles. These were 200, 160 and 140 MPa for pit aspect ratios of 0.52, 0.68 and 0.82 respectively. Although there appears to be dependence between both, it is expected that this limiting stress range will be independent of pit size at these lower stress ranges due to the dominance of corrosion over that of mechanical damage. Moreover, the difference between predicted number of cycles at highest – 200 MPa and lowest – 140 MPa stress ranges predicted from the model is generally less than 3%. Hence, a single value of 140 MPa was adopted as a conservative fatigue limit of this material in the aggressive environment. This was used to determine the value of  $D_I$  for corrosion fatigue crack growth (see Table 8.7).

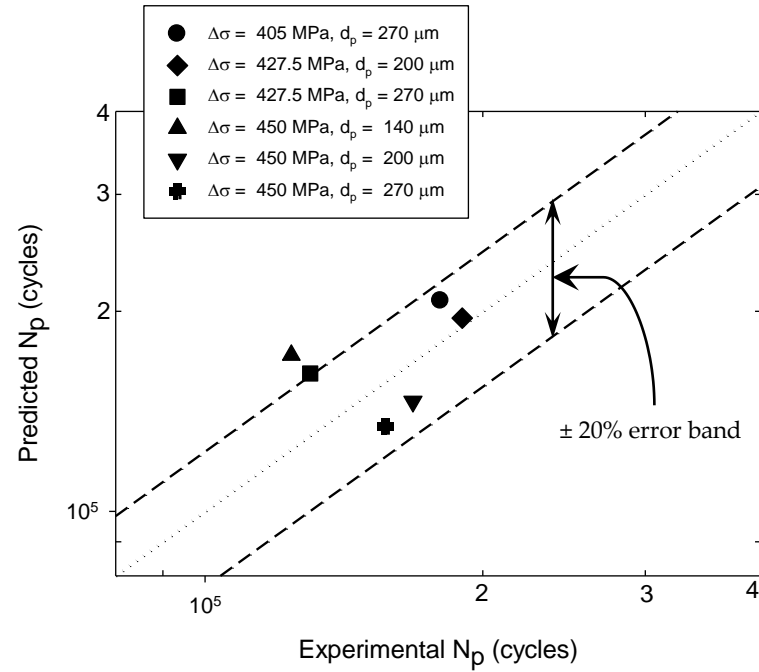
*Table 8.7 Calculated values of  $D_I$  for different pit sizes in air and corrosion fatigue.*

Pit depth ( $\mu\text{m}$ )	Aspect ratio	$\Delta\sigma_0$ (MPa)	$D_I$ ( $\mu\text{m}/\text{cycle}$ ) Air	$D_I$ ( $\mu\text{m}/\text{cycle}$ ) Corrosion fatigue
140	0.52	436.5	$3.733 \times 10^{-3}$	$1.339 \times 10^{-5}$
200	0.68	414.0	$3.264 \times 10^{-3}$	$1.339 \times 10^{-5}$
270	0.82	382.5	$2.667 \times 10^{-3}$	$1.339 \times 10^{-5}$

The crack growth rates in this regime, which were calculated using Equation 8.27, are also shown in Figure 8.7 for air and in Figure 8.8 for corrosion fatigue.

#### 8.2.4.3 Crack propagation lifetimes calculations

The individual lifetimes spent in the short and long crack regimes in air and corrosion fatigue were calculated by integrating Equation 8.23 in the range 0 to 100  $\mu\text{m}$ . Likewise, the number of cycles spent in the long crack regime were calculated by integrating Equation 8.27 in the range 100  $\mu\text{m}$  to the final crack length,  $a_f$ . Experimentally,  $a_f$  was observed for the majority of the tests to be approximately 1300  $\mu\text{m}$ . The crack propagation lifetimes were then obtained by adding these individual lifetimes. A comparison between experimental and predicted crack propagation lifetimes is presented in Figure 8.9a for air and Figure 8.9b for corrosion fatigue. It can be observed that the model predictions show good agreement with experimental data.



(b)

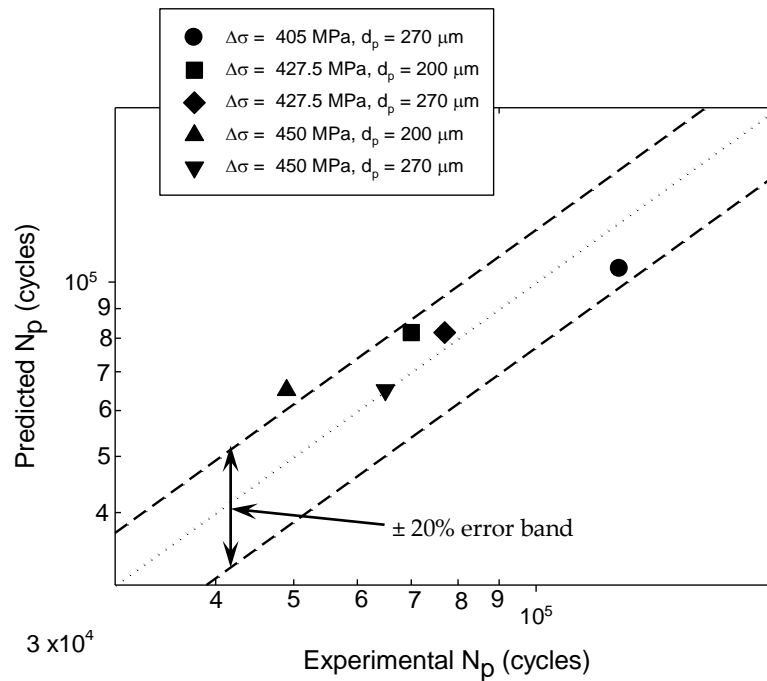


Figure 8.9 Comparison between experimental and predicted crack propagation lifetimes in (a) air and (b) corrosion fatigue.

### 8.2.5 Fatigue lifetime predictions

The total lifetime was obtained as the sum of the lifetimes spent propagating damage in each of the individual regimes applicable to air (Equation 8.29) and corrosion fatigue (Equation 8.30).

$$N_{af} = N_{ptc} + N_{sc} + N_{lc} \quad 8.29$$

$$N_{cf} = N_{pg} + N_{ptc} + N_{sc} + N_{lc} \quad 8.30$$

The predicted lifetimes in each regime and their summation i.e. fatigue lifetimes are summarised in Table 8.8 for air and in Table 8.9 for corrosion fatigue.

*Table 8.8 Comparison between experimental and predicted air fatigue lifetimes.*

$\Delta\sigma$ (MPa)	$d_p$ ( $\mu\text{m}$ )	$AR_p$	$N_{ptc}$ (cycles) Eqn. 8.9	$N_{sc}$ (cycles) Eqn. 8.24	$N_{lc}$ (cycles) Eqn. 8.27	Predicted lifetime	Experimental lifetime
405	140	0.52	28134266	-	-	28134266	> 10000000
427.5	140	0.52	7831872	-	-	7831872	> 10000000
450	140	0.52	2598558	42314	126117	2766989	2400000
405	200	0.68	11142619	-	-	11142619	> 10000000
427.5	200	0.68	3834830	49069	142217	4026116	4603000
450	200	0.68	1487404	42314	100569	1630287	1514000
405	270	0.82	5838120	59143	143398	6040661	5205000
427.5	270	0.82	2329835	49069	108126	2487030	3655000

*Table 8.9 Comparison between experimental and predicted corrosion fatigue lifetimes.*

$\Delta\sigma$ (MPa)	$d_p$ ( $\mu\text{m}$ )	$AR_p$	$N_{pg}$ (cycles) Eqn. 8.5	$N_{ptc}$ (cycles) Eqn. 8.9	$N_{sc}$ (cycles) Eqn. 8.24	$N_{lc}$ (cycles) Eqn. 8.27	Predicted lifetime	Experimental lifetime
405	140	0.52	7165	765572	29497	73357	875591	889000
427.5	140	0.52	6977	490558	24890	55240	577665	669000
450	140	0.52	6795	325066	21709	42210	395780	431300
405	200	0.68	12455	451625	29497	73357	566934	651000
427.5	200	0.68	12130	304255	24890	55240	396514	396000
450	200	0.68	11812	210497	21709	42210	286229	265000
405	270	0.82	19835	312479	29497	73357	435168	447000
427.5	270	0.82	19316	218003	24890	55240	317449	341000
405	140	0.52	18811	155432	21709	42210	238162	249000

### 8.3 Discussion

Empirical models for predicting fatigue lifetimes of pre-pitted specimens in air and corrosion fatigue were developed in this work. The lifetime models attempt to quantify damage at different stages of the fatigue process viz pit growth, pit-to-crack transition, short crack growth and long crack growth in air and in an aggressive environment. By accumulating the lifetimes spent in each of these regimes, the overall lifetimes have been calculated. Experimental results showed that lifetime to crack initiation depend on applied stress, pit size and environment. The model accounts for these factors thus, the

crack pit-to-crack transition lifetimes can be predicted for a given combination of applied stress range and pit size in air or in corrosion fatigue. The predicted lifetimes presented in Figure 8.2 show good agreement with experimental data. A special case of crack initiation behaviour was also modelled where the crack initiation lifetime, for samples containing double pits in close proximity, can also be predicted for a known combination of pit size, and stress range and separation distance between two pits. It can be observed from Figures 8.4 and 8.5 that the model predictions show good agreement with experimental data. The disparities between both sets of data may be attributed to inaccuracies in determining the  $d_{th}$  values, which were only estimated from experimental data. With sufficient experimental data points and for a wider range of stress range and pit aspect ratio, the model can be improved to provide more accurate predictions.

After initiation, the cracks propagate through in the so-called 'short crack regime' where the growth rates of the cracks show perturbations due to the effect of the microstructure. The model accounts for this effect by modelling deceleration of crack growth rate. After progressing beyond the dominant microstructural barrier, the effect of the microstructure diminishes and cracks were assumed to behave as long cracks. The model also predicts the growth rates of the cracks in this long crack regime based on the fatigue limit for a given pit size. In the aggressive environment, the crack growth rates are faster than in air, thereby resulting in shorter lifetimes in both short and long crack regimes. The crack growth curves generated using the short and long crack growth models, Figures 8.7 and 8.8 respectively, as well as the predicted crack propagation lives, Figure 8.9 all show good correlation with experimental data.

By accumulating the individual lifetimes spent to initiate a crack and propagate the crack through the short and long crack regimes to failure, total fatigue lifetime in air was predicted (see Figure 8.10a). In corrosion fatigue, the overall fatigue lifetime was predicted by summation of the individual lifetimes spent in the individual regimes described above, see Figure 8.10b. The predicted lifetimes showed good agreement with experimental data.

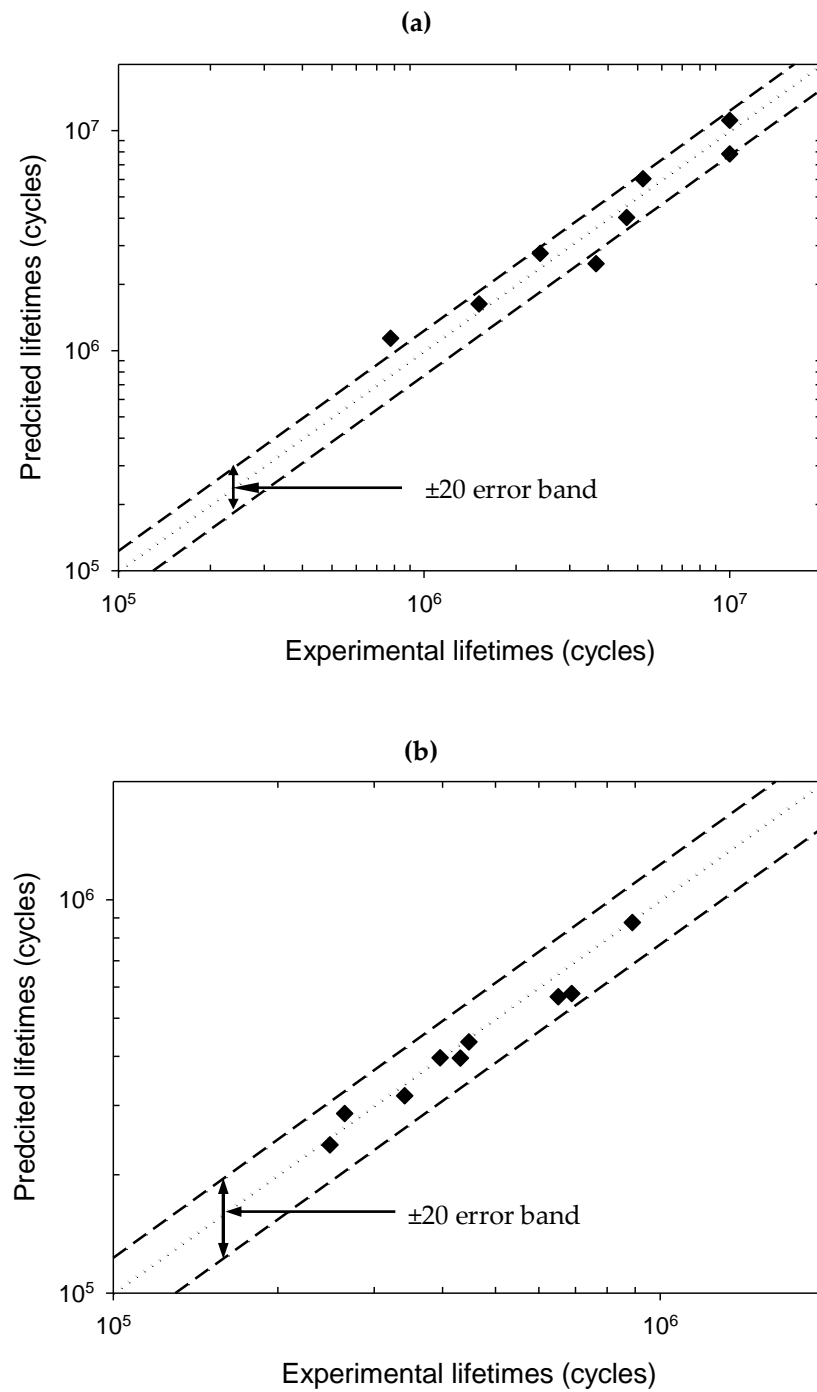


Figure 8.10 Comparison of experimental and predicted fatigue lifetimes in (a) air and (b) corrosion fatigue.



---

# **Chapter 9**

## **General Discussion**

---

## 9.1 Introduction

The fatigue and corrosion fatigue behaviour of API 5L X-65 HSLA linepipe steel has been investigated by both experimental and modelling techniques. Results and discussions for the experimental studies were presented in Chapter 5 while those relating to finite element analysis and cellular automata finite element model development were reported in Chapter 6 and Chapter 7 respectively. The objective of this chapter is to present a general discussion of the overall objectives of this research, while taking into account evidence from each of the experimental (Chapter 5) and modelling (Chapter 6 and Chapter 7) studies.

## 9.2 The fatigue limit

From in-air tests conducted on plain specimens, a limiting stress range was observed below which cracks did not initiate, therefore the specimens did not fail. This plain specimen fatigue limit was evaluated to be  $\Delta\sigma = 450$  MPa. However, at stress levels below this stress range, it was found that cracks were still able to initiate and propagate when pits were present on the specimens, thus suggesting a reduction in the plain specimen fatigue limit. Observations showed that a limiting stress also exists below which cracks either did not initiate from a pit, or if initiated, became non-propagating. The fatigue limit was previously related to a safe stress range below which cracks do not initiate, hence there will be no failure. However, based on the knowledge of the fatigue limit is not a consequence of non-initiation of cracks but related with the materials ability to arrest an initiated crack at this stress range [36, 58, 86, 90]. Therefore, the fatigue limit of metals has been described as the stress range below which cracks may initiate but do not propagate. This limiting stress range was found to decrease with increasing pit size (based on uniaxial loading conditions employed in the tests).

Cracks can become non-propagating when the mechanical driving force at the crack tip is not sufficient for continued crack propagation. Further investigations suggest that the arrest of cracks was most likely due to the resistance of the microstructure, the stress intensity factor range associated with the crack being below the threshold level required for continued crack propagation or a combination of both. In the inert environment, crack

tips were arrested at ferrite-ferrite grain boundaries whereas no crack arrests were observed for tests carried out in aggressive environment despite testing at stress levels well below that at which cracks arrested in air. The ability of the non-propagating cracks to re-propagate to failure at the previous in-air fatigue limit after (i) increasing the crack size by cycling at a higher stress level for a very short period and/or (ii) introducing an aggressive environment, all be it temporarily, showed an elimination of the pitted specimen fatigue limit. In practice, a momentary transient of the stress range above the in-air fatigue limit (overload) can increase the length of cracks that previously initiated from a pit but had arrested, and thereby increase the associated stress intensity factor. Introduction of the environment may also effectively increase the crack size and/or or reduce the resistance of the microstructural barrier. In both the above cases, arrested cracks are able to re-propagate. Therefore, it can be argued that the adoption of the in-air fatigue limit as a safe operating stress range may only be valid if the operating conditions exclude any possibility of overloads or aggressive environments.

In contrast to in-air tests, non-propagating cracks were not observed in corrosion fatigue tests and there appeared to be no apparent fatigue limit at stress ranges as low as 300 MPa. In other words, once cracks initiated, they were able to propagate until failure of the samples. This highlights the influence an aggressive operating environment can have on the fatigue properties of materials, notably a reduction of a safe operating stress range. Although the present study showed that the non-propagating crack re-propagated when the aggressive environment was introduced, it does not mean that cracks emanating from pits cannot stop propagating in the presence of an aggressive environment as found in some material-environment systems [9, 195, 209].

### **9.3 Influence of pit size on fatigue strength**

Stress-life curves, particularly for tests carried out in air (see Figure 5.47), show that fatigue strength is dependent on pit size. Figure 9.1 reveals that, for the present loading conditions, the fatigue strength (plotted as a factor of the plain fatigue limit) reduces with increase in pit size, but only for pit sizes greater than a critical value. This value is estimated from the plot to be 110  $\mu\text{m}$ , suggesting that the fatigue strength should be independent of a pit with depth less than 110  $\mu\text{m}$ . To verify this assertion, an additional

test was carried out on a pre-pitted specimen with a pit depth of 90  $\mu\text{m}$ , loaded at  $\Delta\sigma = 450$  MPa (i.e. the plain specimen fatigue limit). The aspect ratio of the pit was 0.43. As indicated on Figure 9.1 ('Additional test'), no cracks initiated from this pit size hence, it had no effect on the plain fatigue strength.

From a practical viewpoint and from the above, prediction of the effect of small defects such as pits on the fatigue strength of structural components is important for design and lifetime assessment [31, 308]. Two existing models are the fatigue notch factor and fracture mechanics approaches discussed below.

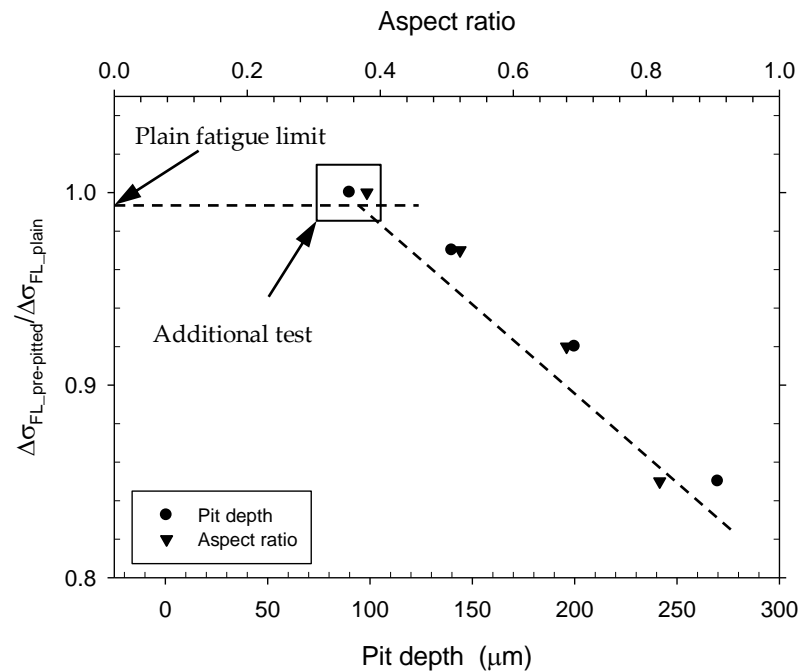


Figure 9.1 Fatigue strength reduction factor as a function of depth and pit aspect ratio.

### Assessment of pits as notches

This approach assumes that corrosion pits are equivalent to notches due to their geometric discontinuity effect on stress distribution i.e. stress gradient so that the notch factor,  $K_f$ , defined as the ratio of the fatigue strength of plain specimen to that of a notched (pre-pitted) specimen at  $10^7$  cycles, can be determined. The question in debate is: are pits equivalent to notches in terms of their effects on fatigue strength?. In order to answer this, a comparison was made between experimental,  $K_f$ , and those calculated using fracture mechanics models,  $K'_f$ . Here the pits were assumed to be blunt notches since their elastic stress concentration factors are less than 3 [309, 310].

$K'_f$  was calculated using empirical models developed by Peterson [311, 312] (Equation 9.1) and Smith and Miller [313] (Equation 9.2).

$$K'_f = 1 + \frac{K_T - 1}{1 + \Psi/r} \quad (9.1)$$

$$K'_f = \left[ 1 + 4.67 \sqrt{\frac{a}{r}} \right]^{\frac{1}{2}} \quad (9.2)$$

where  $a$  is the notch depth and  $r$  is the notch root radius.  $\Psi$  is a material constant calculated to be 226  $\mu\text{m}$  using Equation 9.3 [310] and  $K_T$  is the stress concentration factor obtained from finite element analysis.

$$\Psi = 0.0254 \left( \frac{2067}{S_{UTS}} \right)^{1.8} \quad (9.3)$$

where  $S_{UTS}$  is ultimate tensile stress (620 MPa for X65 steel).

The calculated fatigue notch factors plotted as a function of pit depth in Figure 9.2 generally show the same trend as the experimental data i.e. increase with pit depth, indicating that the pit depth governs the fatigue behaviour. However, the models did not correlate well with the experimental data; the former being generally greater than the latter by as much as a factor of approximately 1.9. This suggests that assessing these pits as blunt notches will overestimate their effect on fatigue strength. This overestimation agrees with previous studies [123]. Moreover, the observation of non-propagating cracks from pits does not agree with a characteristic of blunt notches, which is that, the initiation and propagation threshold stresses are the similar so that initiated cracks are able to propagate at the same stress level [314]. If the pits are equivalent to blunt notches, then the stress level for initiation should also be sufficient to propagate the initiated crack until failure. Hence, there should be no non-propagating cracks.

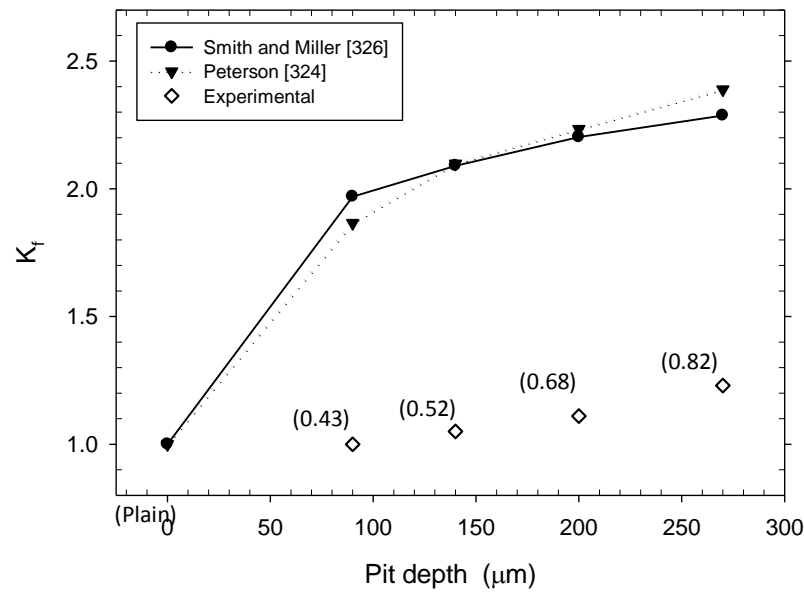


Figure 9.2 Fatigue notch factors obtained empirically and experimentally for different pit depths, assuming pits are equivalent to notches. The numbers in bracket are the values of pit aspect ratios for the particular pit depth.

### Assessment of pits as long cracks

This approach assumes that corrosion pits are equivalent to long cracks in order to obtain a stress intensity factor range. This is then compared with the threshold stress intensity factor range ( $\Delta K_{th}$ ) to establish whether or not a crack will initiate from a pit. This approach has been applied in a range of systems to predict crack initiation from pits, particularly in existing corrosion fatigue lifetime models [124, 169, 214-216, 315]. For instance, employing conventional LEFM (Equation 9.4) and models by Lindley [214] (Equation 9.5) and Kondo [169] (Equation 9.7) to evaluate  $\Delta K_{th}$  yields the values given in Table 8.5.

$$\Delta K_{th} = Y \Delta \sigma_{th} \sqrt{\pi a} \quad 9.4$$

where  $\Delta K_{th}$  is threshold stress intensity factor range (for long cracks),  $\Delta \sigma_{th}$  is threshold fatigue strength (fatigue limit),  $a$  is pit depth and  $Y$  is taken as 0.67 for a semi-circular surface crack.

$$\Delta K_p = 2.24 \sigma_a \sqrt{\pi c \frac{\alpha}{Q}} \quad 9.5$$

where  $\Delta K_p$  is critical pit condition (equivalent to  $\Delta K_{th}$ ),  $\sigma_a$  is half threshold stress range,  $c$  is half pit diameter,  $\alpha$  is pit aspect ratio and  $Q$  is given by

$$Q = 1 + 1.464 \alpha^{1.65} \quad 9.6$$

$$K_{th} = \frac{\Delta \sigma_{th} \sqrt{(\pi a) [1.13 - 0.07 \alpha^{0.5}]}}{[1 + 1.47 \alpha^{1.64}]^{0.5}} \quad 9.7$$

The changes in  $\Delta K_{th}$  values as a result of changes in pit depth indicate a clear breakdown of the application of LEFM conditions to the pits. This is because, under small scale yielding conditions and with no influence of microstructure,  $\Delta K_{th}$  should be nominally independent of crack length [94, 316] (pit size in this case), which is clearly not the case in the present work. This highlights the difficulty and inaccuracy in applying this approach for assessing whether or not cracks will initiate from pits. It is therefore expected that predictions based on this approach will lead to over-conservative lifetime models.

**Table 9.1** Calculated threshold stress intensity factor range as a function of pit depth and pit aspect ratio.

Pit depth ( $\mu\text{m}$ )	Aspect ratio	Fatigue limit (MPa)	Eq. (9.4)	Eq. (9.5)	Eq. (9.7)
90	0.38	450	5.07	6.92	7.44
140	0.52	436.5	6.13	7.76	6.72
200	0.68	414	6.95	8.05	5.85
270	0.82	382.5	7.46	8.61	5.03

### Assessment of pits as short cracks

Considering the dependence of the fatigue limit on pit size (see Figure 9.1), the influence of microstructure leading to crack arrest, and the plastic fields around the pit sizes employed in the present study, it is sensible to consider pits to be equivalent to short cracks. The Kitagawa-Takahashi model describes the variation of the limiting threshold stress that will cause crack initiation, crack arrest or fatigue failure with known pre-existing crack size, in this case pit size. Based on the empirical relationship proposed by El-Hadad and co-workers (Equation 9.8) [92] by defining an intrinsic defect size (in the present case pit size),  $a_0$ , for estimating the threshold stress intensity factor range for small defects, the limiting condition for pit size effect on the fatigue strength can be captured. Although the physical meaning of the intrinsic defect size is not well understood, its applicability to pits has been demonstrated [9, 123, 215, 317]. With a  $\Delta K_{th}$

value of  $8 \text{ MPa}\sqrt{\text{m}}$ ,  $a_0$  was evaluated from Equation 9.9 as  $220 \text{ }\mu\text{m}$ . This intrinsic pit size is appreciably larger than any microstructural characteristics; hence cannot be related to the material's microstructure.

$$\Delta K_{th} = Y \Delta \sigma_{th} \sqrt{\pi(a + a_0)} \quad (9.8)$$

$$a_0 = \frac{1}{\pi} \left( \frac{\Delta K_{th}}{Y \Delta \sigma_{FL}} \right)^2 \quad (9.9)$$

The applicability of the assessment of pits as short cracks is illustrated in a Kitagawa type diagram (Figure 9.3). The curve calculated from Equation 9.8 predicts the transition between the two limiting conditions i.e.  $\Delta \sigma_{FL}$  and  $\Delta K_{th}$ . As the pit depth increases, the fatigue strength decreases progressively from the plain fatigue limit towards that predicted from Equation 9.4, i.e. deeper pits greater than 1mm can be treated as long cracks. Although the curve underestimates the effect of pit size on fatigue strength, it provided a better approximation than when the pits are considered as blunt notches and long cracks.

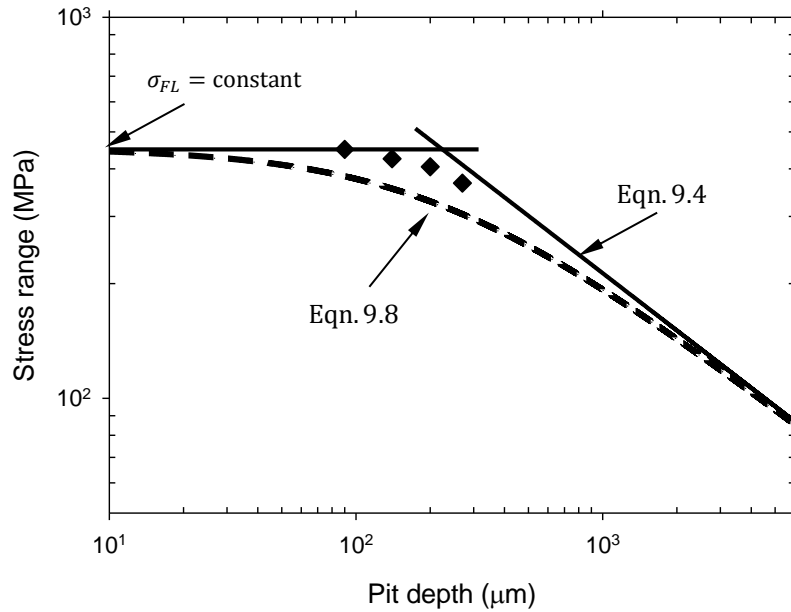


Figure 9.3 Kitagawa type diagram illustrating the effect of pit depth on the fatigue limit.

#### 9.4 Effect of stress on pit development

The pit growth regime constitutes an important time-dependent stage in corrosion fatigue systems, where pits are precursors to cracking. The rate of pit growth may be considered to be influenced mainly by material properties, local solution chemistry and stress state.



Some previous studies have shown that pit growth rate can be influenced by the magnitude of applied stress [117, 124, 250], while other studies suggested that this effect may depend on the degree of plasticity around the pit [127, 250, 318]. Experimental results from the present work revealed that cyclic stress promotes local kinetics of dissolution occurring in the pit by increasing the rate of metal loss, thus increasing the rate of pit growth. The influence of applied stress on localised dissolution rate is attributed to strain-assisted dissolution [89, 90]. To offer more insight into this mechanism, the interaction between local kinetics in the pit and applied stress was investigated by employing a 2-D CAFE model. The results of this model, which employs an empirical model to account for the effect of stress on localised corrosion, are consistent with experimental results (see Figure 7.11) and give more credence to the role of stress in pit development i.e. increased dissolution rate which in turn results in faster pit growth rate.

A notable observation in the present study is the disparity between the plots of pit depth versus time with and without stress, which increased as the pits become deeper (greater aspect ratio) with time (see Figure 5.11). This behaviour was attributed to the strain localisation effect of a pit, in that the level of localised strain associated with a growing pit should also increase with time. Firstly, it was confirmed from 3-D FE analysis and from the 2-D CAFE model that the extent of strain localization increases with pit depth and with time. This implies that deeper pits would have a relatively greater level of local and possibly plastic strain if the yield strain is exceeded. It is noted here that the changing parameter is not applied stress but the size of the pit. Considering that in the mechanism of strain-assisted dissolution, the extent of the effect of strain on dissolution kinetics would be proportional to the level of localised strain, it is proposed that a growing pit (increasing size) will further promote dissolution of the pit's surrounding matrix due to its associated localised strain. Therefore, the resultant effect of this process would be an increase in metal loss under applied stress compared to the unstressed case. Moreover, the region of the pit where the plastic strain is highest will likely be the most susceptible to slip dissolution [305], which may have implications for crack nucleation.

The present results show that the strain localization effect of a pit is, not only mechanistically important for crack initiation, but also influences the rate of pit growth significantly. An increase in the pit growth rate as a result of increased stress will lead to a decrease in the fraction of lifetime spent in the pitting regime, prior to the pit-to-crack

transition, thereby shortening corrosion fatigue lifetime. Similarly, lowering the applied stress will increase this period because it will require a longer time to develop a pit that is sufficiently deep to promote crack initiation. In the present system where pits are taken to be the precursors to cracks, consideration of the relationship between pit growth rate and applied stress is of great importance for the development of realistic corrosion fatigue models. Therefore, the effect of applied stress was accounted for in the empirical pit growth model proposed in Equation 8.5. Previous studies have shown that the relationship between stress and pit growth can be linear or non-linear [124, 250]. For the present study, it cannot be concluded whether the contribution of stress to pit growth for the present material-environment system is linear or not since test was conducted at only one stress level. A more accurate relationship can be obtained if additional tests are carried out over a wider range of stresses.

### **9.5 Pit-to-crack transition behaviour**

Corrosion pits are generally accepted to be potential sites for crack nucleation. When pits are precursors to fatigue cracks, the point when pitting transitions to cracking constitutes a fundamental stage in the overall corrosion fatigue damage process [117, 123, 124, 167, 169, 319]. As discussed by Akid [139, 200], this stage is an important lifetime-controlling stage because it represents the point when damage transitions from a pitting (time-dependent) dominated regime to that of a mechanical (cycles-dependent) regime. Despite the implications that the pit-to-crack transition stage can have on the final lifetime of a structure, the actual conditions that facilitate the development of cracks from pits are still not well understood. Current schemes proposed for predicting transition of pits to cracks are based on the phenomenological model originally proposed in [214, 216] and developed further by Kondo [169]. The important point to note is that this approach does not have any mechanistic content relating to the complex interactions occurring between the metallurgical variables, local solution chemistry and mechanical loading. Moreover, the assumptions that pits are equivalent to cracks at transition, that cracks will initiate at the pit base, and that LEFM principles are applicable at the transitions stage, cast doubt on the validity of these approaches. In the present study, the early stages of fatigue crack development from pits have been investigated in air and brine environment. The results

are discussed further in this section with the purpose of elucidating the damage mechanisms that facilitate pit-to-crack transition.

### 9.5.1 Crack nucleation sites

Previous studies showed that region around pits where cracks nucleate can either be the pit side/mouth [9, 121, 209] or pit base [169, 189, 195]. In the present work, cracks were found to initiate predominantly from the pit mouth for tests carried out in air irrespective of stress level. In corrosion fatigue, cracks initiated from both the mouth and bottom of pits depending on stress level. These results, which suggest that the conditions for crack nucleation are more favourable at the pit mouth in air and at both pit mouth and pit base in the chloride environment, reflect the important roles of local mechanics (strain) and environment in determining the location of the crack nucleation site. These results also suggest that, recognising that pits having similar sizes were tested under similar loading conditions, the presence of an aggressive environment modifies the conditions required for crack nucleation from pits. These conditions, which are promoted at the pit mouth in air, appear to be more favoured at both the pit mouth and pit bottom in the brine environment.

#### 9.5.1.1 Role of local mechanics

For tests carried out in air, the absence of the aggressive environment implies that electrochemical factors do not play any role. It is also considered that the metallurgy (e.g. inclusion density, size and distribution, etc.) of the material in the immediate vicinity of the pit may likely not be exactly the same for all the pits, hence may influence the crack initiation behaviour. However, this factor is believed not to have any significant effect because all the pits were generated on the parent plate region hence, the metallurgy can, notionally, be assumed to be similar. Therefore, for the air tests, crack initiation is thought to depend mainly on local mechanical conditions around a pit. The crack initiation site was correlated with local mechanical conditions by evaluating the distribution of stress and strain around pits. FEA results are those obtained for the artificial pits, generally show that whereas, stress distribution is localised at the pit bottom, strain localization occurs on the pit sides towards the mouth (see Figures 6.13 – 6.14). It is proposed that this strain localization at the pit sides, coupled with the relatively lower constraints and change in the stress field from that of plane strain at the pit base and sample's interior to

that of plane stress near the surface will create a condition that favours crack nucleation at this region of the pit, as observed experimentally, rather than at the pit bottom where the stress is localised.

#### 9.5.1.2 Role of local environment

Similar stress levels and pit sizes were employed for in-air and corrosion fatigue tests, and therefore the local mechanical conditions around the pits in both environments, notably strain localization at the pit mouth, should be similar (see Figure 6.14). Furthermore, evaluation of the strains associated with the pits showed that the level of local strain increased with increase in pit size and applied stress (see Figure 6.7). Considering that the level of localised strain associated with the largest pit (aspect ratio  $\approx 0.82$ ) cycled at the highest stress level of  $\Delta\sigma = 450$  MPa is relatively high ( $\approx 0.65\%$ ) compared to lower stress levels and pit sizes, it is suggested that the cases where cracks nucleated at the pit mouth in the aggressive environment are likely due to the dominance of local mechanical conditions at the mouth over electrochemical factors during the corrosion fatigue process. For relatively smaller pit sizes, at relatively low stress levels, the level of local strains are reduced thereby undermining the dominance of local mechanics. Consequently, electrochemical and possibly metallurgical factors are able to influence the local conditions for crack initiation. Figures 6.13 – 6.14 show the strain distribution around pits tested in brine environment. Localization of strain occurred towards the pit mouth and not at the pit base, offering an explanation for the nucleation of cracks at the pit mouth but not explaining the simultaneous initiation of cracks observed at the pit base (see Table 5.5). At the lowest stress levels ( $\Delta\sigma = 360 - 405$  MPa), cracks initiated only at the pit bottom (also see Table 5.5) suggesting that this behaviour cannot be explained purely from a mechanics-based viewpoint.

Previous studies have shown that HSLA steels can be susceptible to hydrogen embrittlement when exposed to fatigue in aqueous environments [320-322]. Other studies suggested that the electrochemical conditions consisting of pit acidification coupled with a potential drop in the pit, can occur in such a way that hydrogen ion reduction, which was not thermodynamically possible (on the iron-water Pourbaix diagram) under conditions established on the metal surface, is facilitated inside the pit by shifting the potential in the pit to values below the reversible hydrogen potential [323-326]. Seys *et al.*

[323] and Fukuzumi *et al.* [326] showed that some portion of the evolved hydrogen embrittled the material around the pit and thus facilitated crack nucleation. On this basis, the slightly acidic ( $\text{pH} \approx 6$ ) brine solution that was employed for testing and the hydrolysis that may occur inside the pit suggest that it is possible that a hydrogen-induced mechanism may play some role in the crack initiation behaviour. Under free corrosion conditions, one possible cathodic reaction will be proton reduction to release hydrogen atoms that can adsorb and diffuse into the material at the cathodic sites [137, 138]. This can be aggravated due to the localised strain around the pit [135, 320]. The consequence, which is a reduction in the local bond energies in the pit region, may facilitate nucleation of the cracks. However, several reasons are thought to undermine this mechanism in the present work.

Since the brine solution is also naturally aerated, it is expected that the reduction of oxygen will be the dominant of the two possible cathodic reactions under open circuit conditions. Secondly, the occlusion due to the pit and the presence of corrosion products may deplete availability oxygen in the pit. This will shift most of the cathodic reaction to the region outside the pit, notably pit mouth, where oxygen is readily available. Although, some proton reduction may take place in the pit, the dominance of the oxygen reduction reaction is expected to limit it thereby minimizing or eliminating any adsorbed hydrogen effect on cracking. Moreover, the generated hydrogen might evolve from the pit as bubbles [323, 324] instead of adsorbing into the material. Thirdly, the low pH and the potential drop between the mouth and base of the pit can facilitate hydrogen reduction in the pit. In terms of the former, it is thought that there may be pH reduction in the pit but this may not be as low as values that will be obtained if the pits were generated in-situ. Moreover, potential drop has only been predominantly observed for pits growing on passive metal-chloride systems where the drop is ascribed to the ohmic drop between the passive film on the material surface and the active pit surface [327-329] which increases with pit aspect ratio [330]. Due to the active nature of the carbon steel surface in a brine environment, the low pit aspect ratios and the expected relatively low acidification compared to an in-situ-generated pit, the potential difference is not expected to be significant, although there may be some drop. Hence, it is unlikely that hydrogen reduction will take place in the pit. Finally, SEM fractography (Figures 5.46 – 5.47) did not show any evidence of hydrogen embrittlement, notably intergranular fracture mode. This

agrees with previous studies on pre-pitted steel with mechanical properties similar to the material used in this work [122]. Based on the discussion above, it is reasonable to conclude that, although a hydrogen-induced mechanism may possibly play some role in the crack initiation behaviour, this is not expected to be significant under the test conditions employed in the present study.

Another factor that may have facilitated crack initiation from the pit base is the more aggressive chemistry that is expected to be at the pit base compared to the pit sides. Possible changes in the local chemistry in the pit include; low oxygen concentration, acidification as a result of metal ion hydrolysis [323, 331] and high concentration of chloride ions by electromigration in response to the increase in metal ions concentration resulting from hydrolysis [327, 331] and potential drop [327, 330]. However, the aggressiveness of the pit solution is expected to be small since the pits were not generated in-situ. This is reflected in the pit depths measured after fracture, which were only slightly more (maximum of 9% at relatively lower stress ranges compared to no change at the highest stress range) than those obtained at the beginning of the corrosion fatigue experiments. Nevertheless, the change in pit depth compared to little change in pit width (increase in pit aspect ratio) suggests the possibility of an aggressive chemistry at the base of the pit. Akid and Miller [126, 283] studied low alloy steel in 0.6 M NaCl (pH = 2.0 – 6.0) at stress levels below air fatigue limit and showed that, at relatively lower solution pH, the favoured crack initiation mechanism is dissolution of slip band sites and the number of initiated cracks increased. Therefore, assuming dissolution controlled crack nucleation, it is possible that a low pH solution at the pit base could unblock dislocation pile-ups and allow further slip and easier crack initiation.

Based on the above discussion, the main mechanism of crack initiation is considered to be strain-assisted preferential dissolution of emerging slip steps as a result of the interaction between localised strain and the aggressive environment [122, 250, 270, 305, 332]. Results from finite element analysis showed that plasticity is localised around the pits despite applying loads that are in the elastic regime (see Figures 6.9 and 6.11). During cyclic loading, slip bands, which are known to be regions of high dislocation density, will emerge readily in the regions of plasticity [333]. Due to the high energy state of the metal atoms associated with the induced dislocations and the less activation energy required to remove these atoms, preferential dissolution is favoured at the emerging slip steps. In

addition, the to-and-fro motion of the slip bands will provide a continuous source of fresh metal surface for further dissolution, which can, in turn, result in removal of barriers thereby accelerating the cyclic slip process. A consequence of these interactions is that the crack nucleation process is facilitated compared to when the aqueous environment is absent.

Based on the above discussions, it is considered that crack initiation behaviour in the present work is due to strain-assisted dissolution (SAD) supported by an aggressive chemistry at the pit base and strain localization at the pit sides. With reference to Table 5.5, the following explanations are proposed:

1. For the deepest pits loaded at the highest stress ranges, strain is localised towards the pit mouth. As a result of SAD, crack initiation is facilitated thereby resulting in shorter pit-to-crack transition lifetimes compared to air. Cracks preferentially nucleated from the pit mouth due to the dominance of local mechanical conditions over local electrochemical conditions at this site.
2. For shallow pits loaded at the lowest stress ranges, the levels of localised strains are relatively low and strain localization occurs at the pit bottom. Because the pits are shallow, the local environment in the pit will be less aggressive compared to deeper pits hence, SAD is facilitated at the pit bottom where the local strain is concentrated. Hence, crack will initiate from the pit base.
3. For pit sizes and stress ranges between (1) and (2) above, the strain is localised towards the pit mouth and the level of local strains is high, but not as high as in (1) and the local pit chemistry is also more aggressive than in (2). As a result of SAD, cracks are able to initiate earlier compared to air.

### 9.5.2 Crack initiation lifetimes

The results of crack initiation lifetimes obtained in this study reflect the dependency of fatigue lifetimes on local mechanics and local environment in pits. Increasing pit size and stress range resulted in shorter crack initiation lifetimes in both air and brine environments (Figure 5.19). Also, shorter crack initiation lifetimes were found in the latter compared to the former (also see Figure 5.19). The initiation-dominant fatigue behaviour observed for the present material-environment system suggests that the limiting event

determining fatigue lifetimes is that of crack initiation. Once cracks are initiated, the propagation lifetimes account for a smaller fraction of the fatigue lifetime compared to the crack initiation lifetimes (see Figures 5.30 and 5.31). Therefore, it is important to understand the effects of local conditions (mechanics and environment) around pits on crack initiation behaviour. This is discussed below.

#### **9.5.2.1 Influence of local mechanics**

In air, the early initiation of cracks indicates that the conditions for crack initiation were more favoured when pits were deeper and when stresses were higher. Since tests were carried out in air, these conditions mainly depend on local mechanics, although metallurgical variables can also facilitate the crack initiation event. For instance, the presence of inclusions in the localised strain field can result in interfacial debonding or further strain concentration [16, 334, 335] thereby leading to early crack nucleation compared to when the inclusions are absent. Nevertheless, this and other possible mechanisms that may be related to metallurgical factors were not observed in the tests. Moreover, such mechanisms are thought to be dominated by the plastic zone near the pit mouth when their relative length scales are considered. Although metallurgical variables may result in scatter of the experimental data, they should not undermine the dominance of the plasticity that is around the pit. Considering only local mechanics, FE analysis revealed that crack initiation lifetime behaviour is due to strain localisation as a result of the mechanical effects of pit geometry and applied stress. Here, damage can be described as a function of cycles-dependent mechanical fatigue. Increasing either the pit size or the stress level increases the magnitude of local strain and plasticity. According to mechanical models of fatigue crack initiation, an inverse relationship exists between plastic strain magnitude and the number of cycles required to initiate a crack [39, 43, 44].

#### **9.5.2.2 Influence of environment**

The results also indicate that a corrosive environment influences the conditions required for crack initiation and hence, the lifetimes to crack nucleation. In the presence of the test environment, it is proposed that strain-enhanced dissolution of slip steps occurs such that cracks initiated earlier than in air. To quantify the effect of the environment on pit-to-crack transition lifetimes, the ratios of crack initiation lifetimes in air to that obtained in brine were plotted as a function of pit size and applied stress (Figure 9.4). It can be



observed that since in-air tests reflect only local mechanical conditions, the ratio can be considered as the contribution of the environment where higher ratios indicate greater fatigue damage. The present results suggest that the effect of the environment is dependent on the local mechanical conditions, which in turn depend on applied stress and pit size. At high stress levels and for deeper pits, the contribution of the local environment, seen as a reduction in crack initiation lifetime, is minimal. In contrast, the reduction in crack initiation lifetime is more pronounced at lower stresses as a result of increase in the contribution of the local environment to damage. In summary, the present results reveal that, while the synergistic effect of mechanical damage and corrosion can reduce pit-to-crack transition lifetimes, the extent of reduction appears to depend on the applied stress ranges. However, no apparent relationship existed between pit-to-crack transition lifetime and pit size.

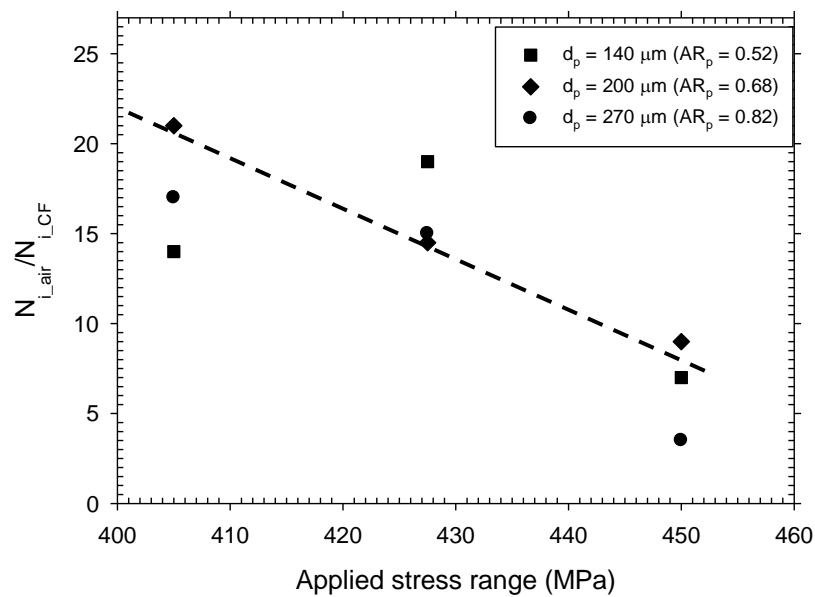


*Figure 9.4 Ratio of crack initiation lifetime in air to crack initiation lifetime in aggressive environment as a function of applied stress range at different pit depths.*

### 9.5.2.3 Influence of pit-to-pit proximity on crack initiation lifetime

Evidence from the present study reflects the significant influence of pit-to-pit proximity on determining crack nucleation behaviour and resistance of a material to fatigue failure. For instance, whereas no crack initiated up to  $10^7$  cycles from a single  $200 \mu m$  deep pit loaded at  $\Delta\sigma = 405$  MPa, cracks initiated when the centre of a pit of similar depth was

located 782  $\mu\text{m}$  from its centre ( $s_{cc} = 782 \mu\text{m}$ ) at the same stress range (see Figure 5.20). Decreasing the separation distance further to 693  $\mu\text{m}$  reduced the crack initiation lifetime by a factor of 10. The dependency between crack initiation lifetimes and proximity is attributed to the mechanical interaction between the strain fields associated with the pits. This interaction intensifies the level of local strains, which increases with decreasing separation distance (Figures 6.18 - 6.23). Considering the relationship between localised plasticity and the number of cycles required to initiate a crack, a decrease in the separation distance will increase susceptibility to early crack initiation and consequently shorter crack initiation lifetimes.

Another notable revelation from the present study is that the dependency between separation distance and crack initiation lifetimes exists only below certain threshold separation distances, which are also stress range and pit size dependent. This threshold can be interpreted as an allowable separation distance above which the detrimental effect of neighbouring pits on crack initiation lifetimes is mitigated. Below this 'safe' distance, a neighbouring pit has a tendency to facilitate crack initiation thus, reducing crack initiation lifetimes in a manner that increases with decreasing separation distance. It is noted that these results and discussions relate only to mechanical factors since the tests were carried out in air. In the presence of an aggressive environment, the results may be different due to the interaction that will occur between these mechanical and electrochemical factors. From operational and design perspectives, these findings will have implications. On one hand, isolated pits that seem to be non-damaging under certain loading conditions may become damaging when one or more pits develop near them, even under the same loading conditions. On the other hand, the crack initiation lifetimes of single pit from which cracks will normally initiate, can be further shortened significantly. In both cases, the total fatigue lifetimes will be shortened. However, the ranges of separation distance where this behaviour will or will not occur will depend on the applied stress range. Increasing the stress range will increase the safe allowable separation distance. Below this safe distance, the interactions between neighbouring pits should be considered.

## 9.6 Crack propagation behaviour

After initiation of stage I mode II cracks at the pit-to-crack transition stage, fatigue damage enters a mechanical regime that is cycles-dominated i.e. physically-short crack propagation stage. The propagation behaviour of fatigue cracks can be influenced by a number of factors, including stress level, local material microstructure and environmental conditions. In the present study, the effect of mechanical loading and local microstructure on the propagation behaviour of fatigue cracks emanating from pits was investigated in air and brine environment. The results are discussed further in this section with the purpose of elucidating the factors affecting and mechanisms contributing to damage i.e. crack propagation rates.

### 9.6.1 Growth of surface cracks from pits

In air, analyses of fractographic images and surface replicas show that the fatigue cracks predominantly initiated at two edges of a pit and propagated separately as corner cracks until their depth reaches that of the pit. At this point, the propagation rates of the two edge cracks can be said to have exceeded the pit propagation rate. In corrosion fatigue, the cracks grow in a similar way to that in air at high stress while at lower stresses, the corner cracks coalesce with those that initiated from the bottom. The resulting dominant surface cracks often have shapes that can be described as hemispherical (see Table 5.7). Assuming a growing pit, a point can also be defined where the crack growth rate will outrun the pit growth rate. A schematic illustrating crack initiation and propagation based on the experimental observations from the present study is shown in Figures 9.5 - 9.7.

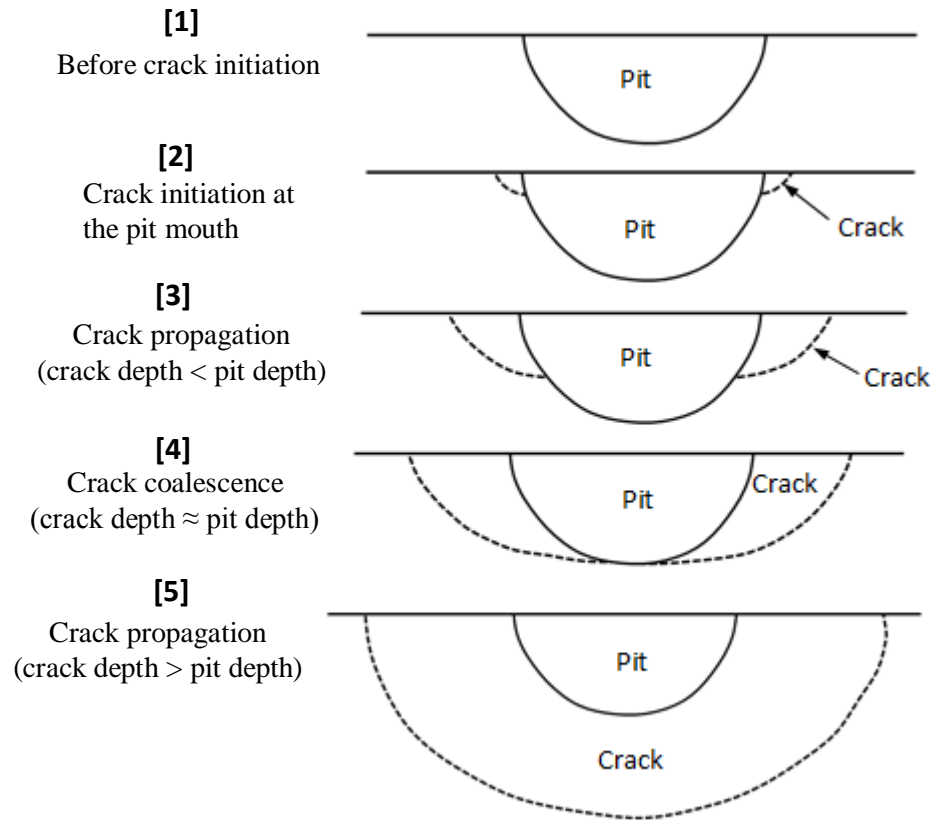


*Figure 9.5 Schematic illustrating initiation and subsequent propagation of crack emanating from single pits in air.*

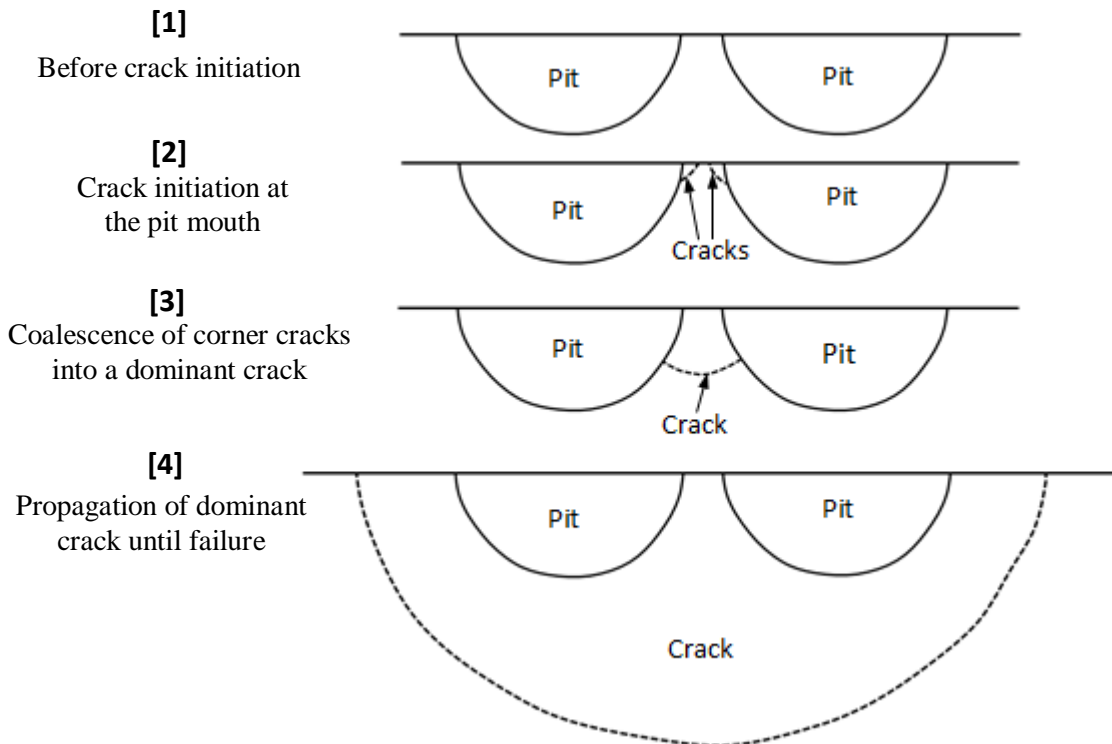


*Figure 9.6 Schematic illustrating initiation and subsequent propagation of crack emanating from double pits in air.*

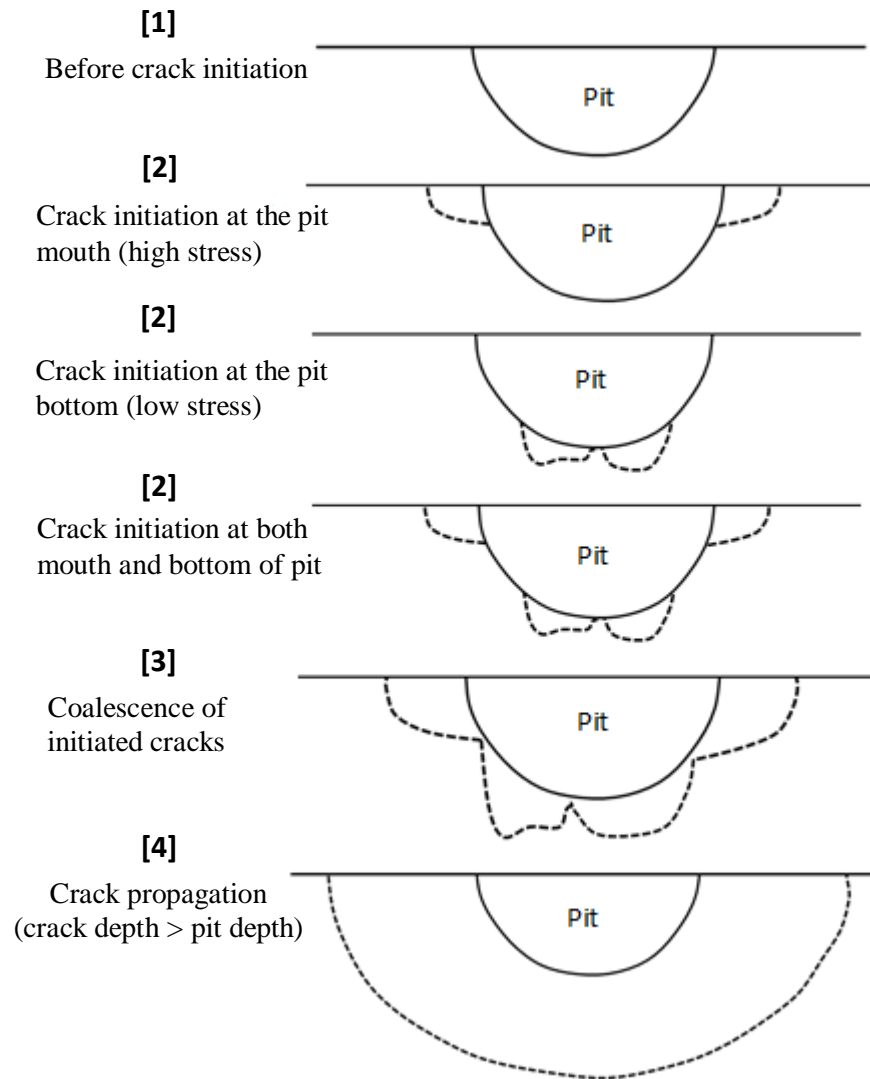


*Figure 9.7 Schematic illustrating initiation and propagation behaviour around a pit under corrosion fatigue conditions.*

### 9.6.2 Influence of microstructure on crack propagation

An important factor that influences crack development particularly in the early stages of crack development where crack lengths are short is the microstructure. The results obtained in this study reveal that the behaviour of cracks emanating from pits is dependent upon the local microstructure (see Figures 5.32 – 5.39). Stage I cracks, which initiated from the pit mouth in air continue their growth in mode II along planes of maximum shear stress. At low stress level, the cracks experienced retardations in growth rates and may be arrested at grain boundaries (see Figures 5.32 – 5.33). At higher stress level, the growth of the cracks was accelerated after experiencing retardations. As the

cracks became longer, the oscillations decreased to a minimum until the crack growth rates increased monotonically with crack length (see Figures 5.32 – 5.36).

This crack growth behaviour may be a result of a combination of several factors notably, distances between major barriers, grain orientation, grain size and barrier strength. In this steel, the tips of arrested cracks were observed at grain boundaries (see Figure 5.36). The average lengths (excluding the pit width) of the non-propagating cracks were different and it is not clear whether this length is related to variations in pit size, stress level, texture or any combination of these. Considering that stage I and stage II can be characterised as regimes where the influence of the local microstructure (notably perturbations in crack growth rates) is significant and minimum respectively, stage I – stage II transition crack lengths can be determined. For this study, this length was observed range between 200 – 300  $\mu\text{m}$  in air and brine environments.

### 9.6.3 Influence of environment on crack propagation

The results of crack propagation rates obtained in this study reveal the influence of the environment on the propagation behaviour of cracks emanating from pits and overall fatigue resistance. A notable role of the environment in the early stages cracking i.e. microstructural regime found in the present study, is the weakening of the resistance of the local microstructure to crack propagation so that the cracks, which initially arrested in air (see Figure 5.33), were able to re-propagate until failure of the specimen (see Figure 5.39). This indicates that the environment aids progress of the cracking process. The insight from this is that cracks that are deemed non-damaging as a result of crack arrest may become damaging when an aggressive environment is introduced. Some recent studies suggested that the growth rates of corrosion fatigue cracks emanating from pits can be retarded or become non-propagating due to the effect of microstructural barriers [286, 319]. In the present study, little or no perturbations in crack growth rates and no non-propagating cracks were observed in corrosion fatigue even at very low stress ranges. This behaviour may be attributed to the poor corrosion resistance of the material.

The present results indicate that the effect of the environment on crack growth rates is crack size and stress dependent. This effect, mainly seen as an additional contribution to mechanical damage via increase in crack growth rates compared to air, is particularly significant in the early stages of crack when crack lengths were short (see Figure 5.35) and

at lower stress levels (see Figure 5.36). An explanation for the sensitivity of the effect of the environment to stress level was discussed earlier (see Section 5.4.2). As noted in [172, 272, 336], crack length sensitivity may arise due to mass transport effects and a potential drop between crack tip and crack mouth. The rates of electrochemical reactions occurring within a crack will depend on the local chemistry, which is determined to a large extent, by the rate of mass transport of species between the bulk solution and that in the crack. That reactive species will have a less likelihood of getting to the crack tip in a longer crack, as shown for cracks under static stress [337, 338], is not fully supported because of the pumping action induced by cyclic displacement of crack walls. The greater displacement for a longer crack is expected to facilitate diffusion of the reactants thereby increasing dissolution rate. Hence, the reduction in contribution of the aggressive environment to damage at longer crack lengths, seen as decrease in crack propagation rates towards those in air, is thought to be a function of: potential drop down the crack and crack closure. Considering the solution potential down the crack, it is expected that the potential drop between the crack mouth and crack tip will depend on path length, conductivity of the solution within the crack and nature of oxide film formed on the crack walls. For long crack in the present material-environment system and test conditions, these factors will result in larger potential drop and hence, lower crack tip polarisation potential and lower crack growth rates than short cracks. The corrosion products observed on the fracture surfaces of specimens tested in corrosion fatigue (see Figure 5.47) provides evidence supporting the crack closure mechanism [170, 284, 339].

The convergence between the crack growth rates in air and corrosion fatigue when cracks were longer, particularly at higher stresses and where there is little effect of microstructure would suggest that the removal of the environment after a crack has reached certain lengths, notably in stage II regime, may not increase fatigue life significantly. Assuming this is true, the important stage in the damage process accounting for the actual reduction in the CF lifetime will then be the microstructural regime where the environment increases crack growth rates and weakens microstructural barriers compared to air. Akid *et al.* [2, 13] showed that the stage I to stage II transition crack length can be reduced in a corrosive environment compared to air. However, based on the observations from the current work, there appears no clear difference between the two environments.

## 9.7 Re-assessment of pit-to-crack transition criteria

Observations made in this study permit some comments on the assumptions and criteria for predicting pit-to-crack transition proposed by Kondo [169]. It is an implicit assumption in the model that cracks will initiate at the bottom of pits and that pit depth and crack depth at the point of transition are the same. Results from the present study however showed that cracks can initiate from the pit mouth and that crack depth and pit depth are not necessarily the same at the point of transition. The model also assumes linear elastic fracture mechanics i.e. no plasticity in order to evaluate the  $\Delta K$  associated with a pit. FEA results however, have shown that plasticity around pits can be significant, particularly at high stresses. Lastly, the model does not take into consideration any possible interactions that may occur between pits that are in close proximity. This study showed that such interactions are possible and can have substantial effects on pit-to-crack transition lifetimes. On this basis, it is sensible to suggest that existing corrosion fatigue lifetime models, which are based on the Kondo criteria, should be re-considered. In addition to a re-assessment of the underlying assumptions of the pit-to-crack transition criteria, the influence of local chemistry within and localised plasticity around pits must be accounted for in order to obtain realistic and more accurate predictive models.



---

---

# Chapter 10

## Conclusions

---

---

The fatigue and corrosion fatigue behaviour of API 5L X-65 HSLA linepipe steel has been investigated. The following conclusions may be drawn:

- The parent plate region of the pipe section is composed mainly of polygonal and equiaxed ferrite grains. An average grain size and average micro-hardness in this region are 15  $\mu\text{m}$  and 206 HV<sub>1.0</sub>.
- Under symmetric strain cycling, X65 steel showed a mixed-type cyclic behaviour.
- Fatigue lives were significantly reduced under corrosion fatigue compared to in air and the closer the pits, the shorter the fatigue life. Fatigue strength in air decreased with increasing pit depth. The fatigue strength for specimens with 140, 200 and 270  $\mu\text{m}$  deep pits was 87, 83 and 76%, respectively, of the fatigue strength of the smooth specimen.
- Application cyclic stress increased the rate of pit growth.
- In air, cracks were initiated predominantly from the pit mouth irrespective of stress level. A mechanics-based explanation for this was obtained from FEA of artificial pits, which indicated that, whereas stress is localised towards the pit bottom, strain is localised towards the pit mouth. In corrosion fatigue, cracks initiated from both the mouth and bottom of pits depending on stress level. Cracks tended to initiate at the pit base at low stress and at the pit mouth at higher stresses.
- For single and double pits in both air and an aggressive environment, crack initiation lifetime decreased with increasing pit size and stress level. Crack initiation lifetimes were shorter in corrosion fatigue compared to air. The effect of the environment on crack initiation lifetime was seen to be stress dependent.
- The dependency of crack initiation lifetime on pit-to-pit separation distance was seen at distances lower than a threshold separation distance, which increased with stress level and pit depth.
- The microstructure played a role in the crack growth behaviour particularly in the early stages when crack lengths were short. Crack growth rate perturbations observed in this regime were attributed to the influence of grain boundaries on crack growth mechanics. Cracks were sometimes arrested grain boundaries, particularly at relatively low stress levels, and thus became non-propagating. This

resistance of the grain boundaries to crack advance, appeared to be diminished or eliminated when the aggressive environment was introduced.

- Under corrosion fatigue conditions, crack growth rates were generally higher than in air. The environmental effect, which was seen to be both a function of stress level and crack length, was greater at lower stress levels and in the early stages when crack lengths were short. The effect of stress was attributed to the mechanical driving force dominating crack growth and little time is available for corrosion processes to contribute to crack-tip failure process.
- Results from CAFE simulations showed good agreement with experimental data i.e. (i) pit depth and pit aspect ratio increase with time, (ii) pit depth under stress was greater than when no stress was applied, (iii) localised stress and strain increase with pit depth and with time.
- Fatigue and corrosion fatigue lifetimes predicted based upon the developed model showed good correlation with the experimental fatigue lifetimes.

---

---

# **Chapter 11**

## **Future Work**

---

---

The following have been identified as potential future work:

### **11.1 Experimental work**

#### **Influence of hydrogen embrittlement on pit-to-crack transition**

Engineering components under cathodic protection or hydrogen-containing corrosive environments can be susceptible to hydrogen embrittlement. Corrosion pits, being regions of high stress/strain concentration compared to other regions of a component, can be preferred sites for preferred hydrogen trapping. This can in turn influence the initiation behaviour of cracks emanating from pits. A potential future work would be to investigate the effect of hydrogen embrittlement on the pit-to-crack transition behaviour in simulated operating condition.

#### **Corrosion fatigue testing in CO<sub>2</sub> and H<sub>2</sub>S environments**

The corrosion fatigue tests carried out in the present work were conducted in naturally aerated brine at room temperature, which do not simulate the real life operating conditions. An extension of this study would be to conduct similar tests in high-temperature high pressure brine/CO<sub>2</sub> and brine/H<sub>2</sub>S environments, which are more representative of the operating conditions. The results can then be juxtaposed with those obtained from the present work in order to understand damage evolution in more detail.

#### **Monitoring of evolution of cracks from pits**

The point when a pit transitions to a crack is important for corrosion fatigue lifetime modelling. Identifying this stage of the damage process experimentally and/or in-situ using conventional methods is challenging. Due to the limitations of the methods used for monitoring the evolution of cracks from pits in this work, only surface crack lengths could be detected; it was impossible to evaluate the transition stage accurately, measure crack depths and visualize the evolution of the cracks, all of which are important for a detailed understanding of pit-to-crack transition. A non-destructive technique that offers good prospect of allowing in-situ acquisition of this information is Synchrotron X-ray tomography. This technique allows 3-D visualisation of the interior structure of a solid material. An important future work that will elucidate the evolution of cracks from pits in

more detail would be to carry out continuous tomographic analysis of pre-pitted specimens during fatigue cycling.

### **TEM micro-analysis of dislocations around pits**

Plastic deformation is known to be due to the movement of dislocations through the lattice structure of metals. It was observed in the present work that plasticity around pits can be significant. Therefore, understanding how plastic strain and dislocation substructure evolve around the pit during fatigue cycling can provide insight into the damage mechanisms and controlling conditions that facilitate pit-to-crack transition. A useful series of tests would therefore be one which involves fatigue loading specimens with pre-determined pit size for different number of cycles. Since cracks can initiate from the mouth or base of pits, Focused Ion Beam technique can be used to obtain samples from these regions around the pit. The evolution of dislocation density and dislocation substructures can then be analysed on the TEM.

## **11.2 Modelling work**

### **Analysis of evolution of stress and strain under cyclic loading**

The FEA analysis investigations in this study focused on the application of static loads. Since corrosion fatigue is characterised by cyclic loading, understanding how this type of loading affects the conditions that facilitate cracking from pits can assist in development of lifetime models. A future work would be to investigate the evolution and distribution of stress and strain around pits as a function of number of cycles using an appropriate elastic-plastic cyclic material model.

### **3-D CAFE model development**

One of the objectives of the present work is to develop a 3-D cellular automata finite element model that offers a more accurate prediction of corrosion fatigue damage. A 3-D CA model has been developed and validated with experimental data; this model offers good predictions of the evolution of pit characteristics with time. Further work would be to develop the FE component of the model and validate the results from the complete 3-D CAFE model with experiments.

## REFERENCES

- [1] Cerit M., Genel K., Eksi S. *Numerical investigation on stress concentration of corrosion pit*. Engineering Failure Analysis, 2009. **16**, p. 2467-2472.
- [2] Papavinasam S., Friesen W., Revie R., Doiron A. *Predicting Internal Pitting Corrosion of Oil and Gas Pipelines: A Corrosion Engineering Approach* in NACE Corrosion 2005. 2005, NACE. p. 1-17.
- [3] Xia Z., Chou K.C., Szklarska-Smialowska Z. *Pitting corrosion of carbon steel in CO<sub>2</sub> - containing NaCl Brine*. Corrosion, 1989. **45**, p. 636-642.
- [4] Kresa G., Schutze M. *Corrosion Handbook: Corrosive Agents and Their Interaction with Materials, Volume 7: Sodium Chloride*. 2007: Wiley-Vch Verlag GmbH and Co.
- [5] Roberge P.R. *Corrosion Engineering: Principles and Practice*. 2008: McGraw-Hill.
- [6] *Natural Gas Pipeline Rupture and Fire Near Carlsbad, New Mexico, August 19, 2000.* , in Pipeline Accident Report NTSB/PAR-03/01. February 11,. 2003.
- [7] *Final Situation Report: The Prudhoe Bay oil spill*. Unified Command Joint Information Center. March 25, 2008.
- [8] Varma R., Varma D.R. *The Bhopal Disaster of 1984* Bulletin of Science, Technology & Society, 2005.
- [9] Schonbauer B.M., Stanzl-Tschegg S.E., Perlega A., Salzman R.N., Rieger N.F., Zhou S., Turnbull A., Gandy D. *Fatigue life estimation of pitted 12% Cr steam turbine blade steel in different environments and at different stress ratios*. International Journal of Fatigue, 2014. **65**, p. 33-43.
- [10] Sriraman M., Pidaparti R. *Crack Initiation Life of Materials Under Combined Pitting Corrosion and Cyclic Loading*. Journal of Materials Engineering and Performance, 2010. **19**, p. 7-12.
- [11] Liu X.F., Huang S.J., Gu H.C. *Crack growth behaviour of high strength aluminium alloy in 3.5%NaCl solution with corrosion inhibiting pigments*. International Journal of Fatigue, 2002. **24**, p. 803-809.
- [12] Akid R. *Effects of the Environment on the Initiation of crack growth*, W.A.V.D.S. at al, Editor. 1997, ASTM International, Philadelphia. p. 3-17.
- [13] Turnbull A. *Environment-assisted Fatigue in Liquid Environments*, in Comprehensive Structural Integrity, I.M.O.R. Karihaloo, Editor. 2003, Pergamon: Oxford. p. 163-210.
- [14] Ebara R. *Corrosion fatigue crack initiation behavior of stainless steels*. Procedia Engineering, 2010. **2**, p. 1297-1306.
- [15] Fontana M.G. *Corrosion Engineering*. 3rd Edition ed. 1987: McGraw-Hill.
- [16] Wang Y., Akid R. *Role of Nonmetallic Inclusions in Fatigue, Pitting, and Corrosion Fatigue*. Corrosion, 1996. **52**, p. 92-102.
- [17] Ovarfort R. *Critical pitting temperature measurements of stainless steels with an improved electrochemical method*. Corrosion Science, 1989. **29**, p. 987-993.
- [18] Wang J.H., Su C.C., Szklarska-Smialowska Z. *Effects of Cl<sup>-</sup> Concentration and Temperature on Pitting of AISI 304 Stainless Steel*. Corrosion, 1988. **44**, p. 732-737.
- [19] Laycock N.J., Newman R.C. *Localised dissolution kinetics, salt films and pitting potentials*. Corrosion Science, 1997. **39**, p. 1771-1790.
- [20] Frankel G. *Pitting corrosion*. 2003.
- [21] Karami M. *Review of Corrosion Role in Gas Pipeline and Some Methods for Preventing It*. Journal of Pressure Vessel Technology, 2012. **134**, p. 054501-054501.
- [22] Papavinasam S., Doiron A., Revie R. *Model to Predict Internal Pitting Corrosion of Oil and Gas Pipelines*. Corrosion, 2010. **66**, p. 1-11.
- [23] Papavinasam S., Demoz A., Omotoso O., Michaelian K., Revie R. *Further validation of an internal pitting corrosion model*, in NACE Corrosion Conference. 2008, NACE International. p. 1-31.
- [24] Han J., Yang Y., Nesic S., Brown B.N. *Roles of passivation and galvanic effects in localised CO<sub>2</sub> corrosion of mild steel*. in NACE Corrosion Conference and Expo. 2008. NACE International.
- [25] Han J., Brown B.N., Nesic S. *Investigation of the Galvanic Mechanism for Localized Carbon Dioxide Corrosion Propagation Using the Artificial Pit Technique*, in NACE Corrosion Conference and Expo. 2010, NACE International. p. 1-12.
- [26] Han J., Yang Y., Brown B., Nesic S. *Electrochemical Investigation of Localized CO<sub>2</sub> Corrosion on Mild Steel*. NACE Corrosion Conference 2007.

- [27] Palacios C.A., Shadley J.R. *Characteristics of Corrosion Scales on Steels in a Col-Saturated NaCl Brine*. Corrosion, 1991. **47**, p. 122-127.
- [28] Han J., Yang Y., Nesic S., Brown B.N. *Roles of passivation and galvanic effects in localized CO<sub>2</sub> corrosion of mild steel*, in NACE Corrosion Conference & Expo. 2008, NACE International. p. 1-19.
- [29] Han J., Nesic S., Yang Y., Brown B.N. *Spontaneous passivation observations during scale formation on mild steel in CO<sub>2</sub> brines*. Electrochimica Acta, 2011. **56**, p. 5396-5404.
- [30] Nesic S. *Key issues related to modelling of internal corrosion of oil and gas pipelines – A review*. Corrosion Science, 2007. **49**, p. 4308-4338.
- [31] Suresh S. *Fatigue of Materials*. 1998: Cambridge University Press.
- [32] Mughrabi H. *Introduction to the viewpoint set on: Surface effects in cyclic deformation and fatigue*. Scripta Metallurgica et Materialia, 1992. **26**, p. 1499-1504.
- [33] Miller K.J. *The behaviour of short fatigue cracks and their initiation Part II - A general summary*. Fatigue & Fracture of Engineering Materials & Structures, 1987. **10**, p. 93-113.
- [34] Brown M.W., Miller K.J. *Initiation and growth of cracks in biaxial fatigue*. Fatigue & Fracture of Engineering Materials & Structures, 1979. **1**, p. 231-246.
- [35] Miller K.J. *The behaviour of short fatigue cracks and their initiation. Part I - A review of two recent books*. Fatigue & Fracture of Engineering Materials & Structures, 1987. **10**, p. 75-91.
- [36] Murtaza G., Akid R. *Modelling short fatigue crack growth in a heat-treated low-alloy steel*. International Journal of Fatigue, 1995. **17**, p. 207-214.
- [37] Taylor D., Knott J.F. *Fatigue crack propagation behaviour of short cracks : Effect of microstructure*. Fatigue and Fracture of Engineering Materials and Structures, 1981. **4**, p. 147-155.
- [38] Brown M.W. *Aspects of Fatigue Crack Growth*. Proceedings of the Institution of Mechanical Engineers, Part C: Journal of Mechanical Engineering Science, 1988. **202**, p. 19-29.
- [39] Polák J. *Fatigue of Steels*, in Comprehensive Structural Integrity, I.M.O.R. Karihaloo, Editor. 2007, Pergamon: Oxford. p. 504-537.
- [40] Tanaka K. *Fatigue Crack Propagation*, in Comprehensive Structural Integrity, I.M.O.R. Karihaloo, Editor. 2003, Pergamon: Oxford. p. 95-127.
- [41] McIntyre P., Nesbitt J., Riley C.C. *Improved steels for non-magnetic electrical generator end rings*, in Materials Development in Turbo-machinery Design. 1989, The Institute of Metals: London. p. 193-203.
- [42] Basquin H.O. *The exponential law of endurance tests*, in Proceedings of the ASTM, 10. 1910, American Society of Testing for Materials. p. 625-630.
- [43] Coffin L.F. *A study of the Effects of Cyclic Thermal Stresses on a Ductile Metal*, in Transactions of American Society of Mechanical Engineers. 1954. p. 931-950.
- [44] Manson S.S. *Behavior of Materials Under Conditions of Thermal Stress*, in Technical Report No. 1170, National Advisory Committee for Aeronautics, NACA. 1953.
- [45] Anderson T.L., ed. *Flaw Characterisation*. Comprehensive Structural Integrity, ed. R.A. Ainsworth and K.H. Schalbe. Vol. 7. 2007. 227-242.
- [46] Paris P., Erdogan F. *A critical analysis of crack propagation Laws*. Journal of Basic Engineering, 1963. **85**, p. 528-534.
- [47] Donahue R.J., Mc H., Clark I., Atanmo P., Kumble R., McEvily A.J. *Crack opening displacement and the rate of fatigue crack growth*. International Journal of Fracture, 1972. **8**, p. 209-219.
- [48] Foreman R.G., Kearney V.E., Engle R.M. *Numerical Analysis of crack propagation in cyclic-loaded structures*. Journal of Basic Engineering, 1967. **89**, p. 459-464.
- [49] NASA *Fatigue crack growth computer programme "NASGRO" Version 3.0*, in Report JSC-22267B. 2002, NASA: Houston.
- [50] Zerbst U., Schwalbe K.H., Ainsworth R.A. *An Overview of Failure Assessment Methods in Codes and Standards*, in Comprehensive Structural Integrity, I.M.O.R. Karihaloo, Editor. 2003, Pergamon: Oxford. p. 1-48.
- [51] Anderson T.L. 7.06 - *Flaw Characterization*, in Comprehensive Structural Integrity, I.M.O.R. Karihaloo, Editor. 2003, Pergamon: Oxford. p. 227-243.
- [52] Ritchie R.O., Lankford J. *Small fatigue cracks: a statement of the problem and potential solutions*. Material Science and Engineering A., 1986. **84**, p. 11-16.



- [53] Akid R., Wang Y.Z., Fernando U.S. *The influence of loading mode and environment on short fatigue crack growth in a high tensile strength steel*, in Corrosion-Deformation Interactions, T.M.J.M. Gras, Editor. 1993, Les Editions de Physique Les Ulis: Fontainebleau, France. p. 659-670.
- [54] Hobson P.D., Brown M.W., les Rios E.R.D. *Two Phases of Short Crack growth in a Medium Carbon Steel*, K.J. Miller and E.R. De Los Rios, Editors. 1986, European Group on Fracture (EGF) Publication No.1. p. 441-459.
- [55] Brown M.W. *Interfaces between short, long and non-propagating cracks*. The Behaviour of Short Fatigue Cracks, 1986, p. 423-439.
- [56] Navarro A., de los Rios E.R. *A microstructurally-short fatigue crack growth equation* Fatigue & Fracture of Engineering Materials & Structures, 1988. **11**, p. 383-396.
- [57] Miller K.J. *The short crack problem*. Fatigue & Fracture of Engineering Materials & Structures, 1982. **5**, p. 223-232.
- [58] de los Rios E.R., Tang Z., Miller K.J. *Short crack fatigue behaviour in a medium carbon steel*. Fatigue & Fracture of Engineering Materials & Structures, 1984. **7**, p. 97-108.
- [59] Rodopoulos C.A., de los Rios E.R. *Theoretical analysis on the behaviour of short fatigue cracks*. International Journal of Fatigue, 2002. **24**, p. 719-724.
- [60] Pearson S. *Initiation of fatigue cracks in commercial aluminium alloys and the subsequent propagation of very short cracks*. Engineering Fracture Mechanics, 1975. **7**, p. 235-247.
- [61] Suresh S., Ritchie R.O. *Propagation of short fatigue cracks*. International Metals Reviews, 1984. **29**, p. 445-476.
- [62] Rosenberger A.H., Ghonem H. *High temperature elastic-plastic small crack growth behavior in a nickel-base superalloy*. Fatigue & Fracture of Engineering Materials & Structures, 1994. **17**, p. 509.
- [63] Soniak F., Remy L. *Behaviour of long and small cracks in a powder metallurgy superalloy at room and at high temperature*. in Fatigue 87-3rd International Conference on Fatigue and Fatigue Thresholds. 1987. Charlottesville: EMAS.
- [64] Miller K.J. *The short fatigue crack problem*. Fatigue & Fracture of Engineering Materials & Structures, 1972. **5**, p. 223-232.
- [65] Tokaji K., Ogawa T., Harada Y., Ando Z. *Limitations of the linear elastic fracture mechanics in respect of small fatigue cracks and microstructure*. Fatigue & Fracture of Engineering Materials & Structures, 1986. **9**, p. 1-14.
- [66] Miller K.J., Akid R. *The application of fracture mechanics to various metal surface states*. Proc Roy Soc Lond A 1996; 452:1411 – 1432. in Proceedings of the Royal Society. 1996. London.
- [67] Gangloff R.P., Ritchie R.O. *Environmental effects novel to the propagation of short fatigue crack*, in Fundamentals of deformation and fracture, K.J. Miller, Editor. 1985, Cambridge University Press: Cambridge. p. 529-558.
- [68] Lankford J. *Initiation and early growth of fatigue cracks in high strength steel*. Engineering Fracture Mechanics, 1977. **9**, p. 617-624.
- [69] Lankford J. *The influence of microstructure on the growth of small fatigue cracks* Fatigue & Fracture of Engineering Materials & Structures, 1985. **8**, p. 161-175.
- [70] de Los Rios E.R., Navarro A., Hussain K. *Mirostructural variations in short fatigue crack propagation of a C-Mn steel*, in Short fatigue cracks, K.J. Miller and E.R. De Los Rios, Editors. 1992, Mechanical Engineering Publications. p. 115-132.
- [71] Brown C.W., Hicks M.A. *A study of short fatigue crack growth behaviour in titanium alloy IM1685*. Fatigue & Fracture of Engineering Materials & Structures, 1983. **6**, p. 67-75.
- [72] Ray K.K., Narasaiah N., Sivakumar R. *Studies on short fatigue crack growth behavior of a plain carbon steel using a new specimen configuration*. Material Science and Engineering A., 2004. **372**, p. 81-90.
- [73] Tokaji K., Ogawa T. *The growth behaviour of microstructurally small fatigue cracks in metals*, in Short fatigue cracks, K.J. Miller and E.R. De Los Rios, Editors. 1992, Mechanical Engineering Publications.
- [74] Faber K.T., Evans A.G. *Crack deflection processes: I. Theory*. Acta Metallurgica, 1983. **31**, p. 565.
- [75] Tanaka K., Nakai Y., Yamashita K. *Fatigue growth threshold of small cracks*. International Journal of Fatigue, 1981. **17**, p. 519-533.

- [76] Suresh S. *Crack deflection: Implications for the growth of long and short fatigue cracks*. Metallurgical Transactions, 1983. **14A**, p. 2375-2385.
- [77] Lankford J. *The growth of small fatigue cracks in 7075-T6 aluminum*. Fatigue & Fracture of Engineering Materials & Structures, 1982. **5**, p. 233-248.
- [78] Zhai T., Wilkinson A.J., Martin J.W. *A crystallographic mechanism for fatigue crack propagation through grain boundaries*. Acta Materialia, 2000. **48**.
- [79] James M.R., Morris W.L. *Effect of fracture surface roughness on growth of short fatigue cracks*. Metallurgical Transactions, 1983. **14A**, p. 153-155.
- [80] Morris W.L. *The noncontinuum crack tip deformation behaviour of surface microcracks*. Metallurgical Transactions, 1980. **11A**, p. 1117-1123.
- [81] Breat J.L., Murdy F., Pineau A. *Short crack propagation and closure effect in a 508 steel*. Fatigue & Fracture of Engineering Materials & Structures, 1983. **6**, p. 349-358.
- [82] Miller K.J., de Los Rios E.R. *The behaviour of short fatigue cracks*. EFG Publication 1, ed. K.J. Miller and E.R. De Los Rios. 1986, London: Institute of Mechanical Engineering.
- [83] Miller K.J. *Initiation and growth of short fatigue cracks*. in IUTAM Eshelby Memorial Symposium. 1985. Cambridge University Press.
- [84] Miller K.J. *Fatigue at Notches: A review*. Journal of Marine Design and Operations, 2005. **Part B**, p. 49-62.
- [85] Ranganathan N., Aldroge H., Lacroix F., Chalon F., Leroy R., Tougui A. *Fatigue crack initiation at a notch*. International Journal of Fatigue, 2011. **33**, p. 492-499.
- [86] Verreman Y., Espinosa G. *Mechanically short crack growth from notches in a mild steel*. Fatigue and Fracture of Engineering Materials and Structures, 1997. **20**, p. 129-142.
- [87] Allery M.B.P., Birkbeck G. *Effect of notch root radius on the initiation and propagation of fatigue cracks*. Engineering Fracture Mechanics, 1972. **4**, p. 325-331.
- [88] Akid R., Murtaza G. *Environment Assisted short crack growth behaviour of high strength steel*, in Short fatigue cracks, K.J. Miller and E.R. de los Rios, Editors. 1992, Mechanical Engineering Publications. p. 193-207.
- [89] Murtaza G., Akid R. *Corrosion fatigue short crack growth behaviour in a high strength steel*. International Journal of Fatigue, 1996. **18**, p. 557-566.
- [90] Murtaza G., Akid R. *Empirical corrosion fatigue life prediction models of a high strength steel*. Engineering Fracture Mechanics, 2000. **67**, p. 461-474.
- [91] H. K., S. T. *Applicability of Fracture Mechanics to very Small Cracks or the Cracks in the Early Stages*. in Proceedings of the Second International Conference on Mechanical Behavior of Materials. 1976. Metals Park, OH: American Society for Metals.
- [92] El Haddad M., Topper T. H., N. T.T. *Fatigue Life Predictions of Smooth and Notched Specimens*. ASME Journal of Engineering Materials and Technology, 1981. **103**, p. 91-96.
- [93] Kruzic J.J., Ritchie R.O. *Kitagawa-Takahashi diagrams define the limiting conditions for cyclic fatigue failure in human dentin*. Technical Note: Journal of Biomedical Research 2006. **Part A**, p. 747-751.
- [94] Chapetti M.D. *Fatigue propagation threshold of short cracks under constant amplitude loading*. International Journal of Fatigue, 2003. **25**, p. 1319-1326.
- [95] Miller K.J. *The two thresholds of fatigue behaviour*. Fatigue & Fracture of Engineering Materials & Structures, 1993. **16**, p. 931-939.
- [96] Venkateswaran P., Ganesh R.S., Pathak S.D. *Generation of stress vs. crack length plots for a ferritic steel weld metal based on Kitagawa-Takahashi approach*. Materials Letters, 2005. **59**, p. 495-498.
- [97] Peters J.O., Boyce B.L., Chen X., McNaney J.M., Hutchinson J.W., Ritchie R.O. *On the application of the Kitagawa-Takahashi diagram to foreign-object damage and high-cycle fatigue*. Engineering Fracture Mechanics, 2002. **69**, p. 1425-1446.
- [98] Ciavarella M., Monno F. *On the possible generalizations of the Kitagawa-Takahashi diagram and of the El Haddad equation to finite life*. International Journal of Fatigue, 2006. **28**, p. 1826-1837.
- [99] Atzori B., Lazzarin P. *A three-dimensional graphical aid to analyze fatigue crack nucleation and propagation phases under fatigue limit conditions*. International Journal of Fracture, 2002. **118**, p. 271-284.

- [100] Rodopoulos C.A., Choi J.H., De Los Rios E.R., Yates J.R. *Stress ratio and the fatigue damage map - Part I: Modelling*. International Journal of Fatigue, 2004. **26**, p. 739-746.
- [101] Rodopoulos C.A., Yates J.R. *Fatigue damage tolerant analysis using the fatigue damage map*. in The 14th US National Congress of Theoretical and Applied Mechanics. 2002. Virginia.
- [102] McAdam D.J. *Stress-Strain relationships and the corrosion fatigue of metals*. in ASTM 26. 1926. American Society of Testing and Materials.
- [103] Pao P.S. *The Mechanisms of Corrosion Fatigue*. ASM Handbook: Fatigue and Fracture, 1996. **19**, p. 185-192.
- [104] Gerhardus H.K. *Stress Corrosion Cracking and Hydrogen Embrittlement*, in ASM Handbook, S.R. Lampman, Editor. 1996, ASM International.
- [105] Turnbull A., Horner D.A., Connolly B.J. *Challenges in modelling the evolution of stress corrosion cracks from pits*. Engineering Fracture Mechanics, 2009. **76**, p. 633-640.
- [106] Jones R.H. *Stress corrosion cracking*. Materials Performance and Evaluation. 1992: ASM International.
- [107] Kruger J. *Failure by stress corrosion cracking*, in Stress Corrosion Cracking, J. Yahalom and A. Aladjem, Editors. 1980, Freund Publishing House.
- [108] Swann P.R. *Dislocation substructure vs transgranular stress corrosion susceptibility of single phase alloys*. Corrosion, 1963. **19**, p. 102-112.
- [109] Logan H.L. *Film rupture mechanisms of stress corrosion*. Journal of Research, 1952. **48**, p. 99-105.
- [110] Ford F.P. *Current understanding of mechanisms of stress corrosion and corrosion fatigue*, in Environment-Sensitive Fracture, S.W. Dean, E.N. Pugh, and G.M. Ugiansky, Editors. 1984, ASTM. p. 32-51.
- [111] Puiggali M., Zielinski A., Olive J.M., Renauld E., Desjardins D., Cid M. *Effect of microstructure on stress corrosion cracking of an Al-Zn-Mg-Cu alloy*. Corrosion Science, 1998. **40**, p. 805-819.
- [112] Takano M. *Effect of Strain Rate on Stress Corrosion Cracking of Austenitic Stainless Steel in MgCl<sub>2</sub> Solutions*. Corrosion, 1974. **30**, p. 441-446.
- [113] Ruther W.E., Soppet W.K., Kassner T.F. *Effect of Temperature and Ionic Impurities at Very Low Concentrations on Stress Corrosion Cracking of AISI 304 Stainless Steel*. Corrosion, 1988. **44**, p. 791.
- [114] Angelova D., Akid R. *A normalization of corrosion fatigue behaviour: an example using an offshore structural steel in chloride environments*. Fatigue & Fracture of Engineering Materials & Structures, 1999. **22**, p. 409-420.
- [115] Brunella M.F., di Milano C.P. *Effect of Chloride Environments on Fatigue Behavior of AA6061-A1203 Particle Composite*. NACE International.
- [116] Thorpe T.W., Scott P.M., Rance A., Silvester D. *Corrosion fatigue of BS 4360:50D structural steel in seawater*. International Journal of Fatigue, 1983. **5**, p. 123-133.
- [117] Ebara R. *Corrosion fatigue crack initiation in 12% chromium stainless steel*. Materials Science and Engineering: A, 2007. **468-470**, p. 109-113.
- [118] Nan Z.Y., Ishihara S., Goshima T. *Corrosion fatigue behavior of extruded magnesium alloy AZ31 in sodium chloride solution*. International Journal of Fatigue, 2008. **30**, p. 1181-1188.
- [119] Akid R. *Corrosion Fatigue*, in Shreir's Corrosion, E. in Chief: Tony J.A. Richardson, Editor. 2010, Elsevier. p. 928-953.
- [120] Krishnan K.N. *Mechanism of Corrosion Fatigue in Super Duplex Stainless Steel in 3.5 percent NaCl Solution*. International Journal of Fracture, 1997. **88**, p. 205-213.
- [121] Horner D.A., Connolly B.J., Zhou S., Crocker L., Turnbull A. *Novel images of the evolution of stress corrosion cracks from corrosion pits*. Corrosion Science, 2011. **53**, p. 3466-3485.
- [122] Ahn S.-H., Lawrence F.V., Metzger M.M. *Corrosion fatigue of an HSLA steel*. Fatigue & Fracture of Engineering Materials & Structures, 1992. **15**, p. 625-642.
- [123] Zhou T.A. *Influence of pitting on the fatigue life of a turbine blade steel*. Fatigue and Fracture of Engineering Materials and Structures, 1999. **22**, p. 1083-1093.
- [124] Ishihara S., Saka S., Nan Z.Y., Goshima T., Sunada S. *Prediction of corrosion fatigue lives of aluminium alloy on the basis of corrosion pit growth law*. Fatigue and Fracture of Engineering Materials and Structures, 2006. **29**, p. 472-480.

- [125] Akid R., Miller K.J. *The Initiation and Growth of Short Fatigue Cracks in an Aqueous Saline Environment*, P.M. Scott and R.A. Cottis, Editors. 1990, Mechanical Engineering Publications. p. 415-415.
- [126] Akid R., Miller K.J. *Short fatigue crack growth behaviour of a low carbon steel under corrosion fatigue conditions*. *Fatigue & Fracture of Engineering Materials & Structures*, 1991. **14**, p. 637-649.
- [127] Akid R. *The role of stress-assisted localised corrosion in the development of short fatigue cracks*, in *Effects of the environment on the initiation of crack growth*, ASTM STP 1298, W.A. Van Der Sluys, R.S. Piascik, and R. Zawierucha, Editors. 1997, American Society of Testing and Materials. p. 3-17.
- [128] Akid R. *Modelling Environment-Assisted Short Fatigue Crack Growth*, in *Advances in Fracture Resistance and Structural Integrity*, V.V. Panasyuk, M.C. Pandey, O.Y. Andreykiv, J.F. Knott, P.R. Rao, R.O. Ritchie, and D.M.R. Taplin, Editors. 1994, Pergamon. p. 261-269.
- [129] Barsom J.M. *Mechanisms of Corrosion Fatigue below K<sub>ISCC</sub>*. *International Journal of Fracture*, 1971. **7**, p. 163-182.
- [130] Ford F.P. *Quantitative examination of slip-dissolution and hydrogen-embrittlement theories of cracking in aluminum alloys*. *Metal Science*, 1978. **12**, p. 326-334.
- [131] Gangloff R.P., Duquette D.J. *Corrosion fatigue of metals: A survey of recent advances and issues*, in *Chemistry and Physics of Fracture*, L.R. Latanision and R.H. Jones, Editors. 1987, Martinus Nijhoff Publishers: The Netherlands. p. 612-645.
- [132] Gangloff R.P., Wei R.P. *Small crack-environment interactions: The hydrogen embrittlement perspective*, in *Small Fatigue Cracks*, R.O. Ritchie and J. Lankford, Editors. 1986, TMS-AIME: Warrendale, PA.
- [133] Gangloff R.P. *Crack size effects on the chemical driving force for aqueous corrosion fatigue*. *Metallurgical Transactions A*, 1985. **16**, p. 953-969.
- [134] Wang Z.F., Li J., Wang J.Q., Ke W. *The influence of loading waveform on corrosion fatigue crack propagation*. *Corrosion Science*, 1995. **37**, p. 1551-1565.
- [135] Dong-Hwan Kang J.-K.L., Kim T.-W. *Corrosion Fatigue Crack Propagation of High-strength Steel HSB800 in a seawater environment*. *Procedia Engineering*, 2011. **10**, p. 1170-1175.
- [136] Komai K. *Corrosion Fatigue*, in *Comprehensive Structural Integrity*, I.M.O.R. Karimhaloo, Editor. 2003, Pergamon: Oxford. p. 345-358.
- [137] Oriani R.A. *The diffusion and trapping of hydrogen in steel*. *Acta Metallurgica*, 1970. **18**, p. 147-157.
- [138] Oriani R.A., Josephic P.H. *Equilibrium aspects of hydrogen-induced cracking of steels*. *Acta Metallurgica*, 1974. **22**, p. 1065-1074.
- [139] Akid R. *Corrosion Fatigue*, R.J. A. and et al., Editors. 2010, Elsevier Scientific Publishing Company, Amsterdam. p. 928-953.
- [140] Frankel G.S. *Pitting Corrosion of Metals A Review of the Critical Factors*. *Journal of the Electrochemical Society*, 1998. **145**, p. 2186-2198.
- [141] Szklarska-Smialowska Z. *Pitting Corrosion of Metals*. 1986: National Association of Corrosion Engineers (NACE).
- [142] Baker M.A., Castle J.E. *The initiation of pitting corrosion of stainless steels at oxide inclusions*. *Corrosion Science*, 1992. **33**, p. 1295-1312.
- [143] Grimes L. *A Comparative Study of Corrosion Pit Morphology in 7075-T6 Aluminium Alloy*. 1996.
- [144] Szklarska-Smialowska Z., Janik-Czachor M. *Pitting corrosion of 13Cr-Fe alloy in Na<sub>2</sub>SO<sub>4</sub> solutions containing chloride ions*. *Corrosion Science*, 1967. **7**, p. 65-72.
- [145] Evans V.R. *The Passivity of Metals. Part II: The breakdown of the protective film and the origin of corrosion currents*. *Journal of the Chemical Society*, 1929, p. 92-110.
- [146] Sato N. *Anodic Breakdown of Passive Films on Metals*. *Journal of the Electrochemical Society*, 1982. **129**, p. 255-260.
- [147] Hoar T.P. *The production and breakdown of the passivity of metals*. *Corrosion Science*, 1967. **7**, p. 341-355.
- [148] Burstein G.T., Pistorius P.C., Mattin S.P. *The nucleation and growth of corrosion pits on stainless steel*. *Corrosion Science*, 1993. **35**, p. 57-62.

- [149] Pistorius P.C., Burstein G.T. *Aspects of the effects of electrolyte composition on the occurrence of metastable pitting on stainless steel*. Corrosion Science, 1994. **36**, p. 525-538.
- [150] Pessall N., Liu C. *Determination of critical pitting potentials of stainless steels in aqueous chloride environments*. Electrochimica Acta, 1971. **16**, p. 1987-2003.
- [151] Pistorius P.C., Burstein G.T. *Growth of corrosion pits on stainless steel in chloride solution containing dilute sulphate*. Corrosion Science, 1992. **33**, p. 1885-1897.
- [152] Tang Y.M., Zuo Y., Zhao X.H. *The metastable pitting behaviors of mild steel in bicarbonate and nitrite solutions containing  $Cl^-$* . Corrosion Science, 2008. **50**, p. 989-994.
- [153] Gupta R.K., Sukiman N.L., Cavanaugh M.K., Hinton B.R.W., Hutchinson C.R., Birbilis N. *Metastable pitting characteristics of aluminium alloys measured using current transients during potentiostatic polarisation*. Electrochimica Acta, 2012. **66**, p. 245-254.
- [154] Davis B.W., Moran P.J., Natishan P.M. *Metastable pitting behavior of aluminum single crystals*. Corrosion Science, 2000. **42**, p. 2187-2192.
- [155] Hoeppe D.W., Arriscorreta C.A. *Exfoliation Corrosion and Pitting Corrosion and Their Role in Fatigue Predictive Modeling: State-of-the-Art Review*. International Journal of Aerospace Engineering, 2012. **2012**.
- [156] Jones K., Hoeppe D.W. *Pit-to-crack transition in pre-corroded 7075-T6 aluminum alloy under cyclic loading*. Corrosion Science, 2005. **47**, p. 2185-2198.
- [157] Frankel G.S., Stockert L., Hunkeler F., Boehni H. *Metastable Pitting of Stainless Steel*. Corrosion, 1987. **43**, p. 429-436.
- [158] Ebrahimi N., Moayed M.H., Davoodi A. *Critical pitting temperature dependence of 2205 duplex stainless steel on dichromate ion concentration in chloride medium*. Corrosion Science, 2011. **53**, p. 1278-1287.
- [159] Baumgartner M., Kaesche H. *Aluminum pitting in chloride solutions: morphology and pit growth kinetics*. Corrosion Science, 1990. **31**, p. 231-236.
- [160] Mizuno T. *In-situ analysis of chloride ion concentration within pits during pitting of iron*. Corrosion Science, 1990. **31**, p. 497-502.
- [161] Newman R.C. *The dissolution and passivation kinetics of stainless alloys containing molybdenum*<sup>1</sup>. Coulometric studies of  $Fe-Cr$  and  $Fe-Cr-Mo$  alloys. Corrosion Science, 1985. **25**, p. 331-339.
- [162] Inturi R.B., Szklarska-Smialowska Z. *Dependence of the pitting potential of Al alloys on solubility of alloying element oxides*. Corrosion Science, 1993. **34**, p. 705-710.
- [163] Sayed S.M., el Shayeb H.A. *The measurement of pitting corrosion currents of steel in neutral aqueous solutions*. Corrosion Science, 1988. **28**, p. 153-162.
- [164] R6 R.I. *Evaluation of fatigue and environmental assisted crack growth*, in Assessment of the integrity of structures containing defects. 2010.
- [165] Tanaka T., Wei R.P. *Growth of short fatigue cracks in HY130 steel in 3.5% NaCl solution*. Engineering Fracture Mechanics, 1985. **21**, p. 293-305.
- [166] Akid R. *The influence of environment upon the accumulation of damage under corrosion fatigue conditions*. Fatigue & Fracture of Engineering Materials & Structures, 1996. **19**, p. 277-285.
- [167] Piascik R.S., Willard S.A. *The growth of small corrosion fatigue cracks in alloy 2024*. Fatigue & Fracture of Engineering Materials & Structures, 1994. **17**, p. 1247-1259.
- [168] Nakai Y., Tanaka K., Wei R.P. *Short-crack growth in corrosion fatigue for a high strength steel*. Engineering Fracture Mechanics, 1986. **24**, p. 433-444.
- [169] Kondo Y. *Prediction of Fatigue Crack Initiation Life Based on Pit Growth*. Corrosion, 1989. **45**, p.7-11.
- [170] Suresh S., Zamiski G.F., Ritchie R.O. *Oxide-Induced Crack Closure: An Explanation for Near-Threshold Corrosion Fatigue Crack Growth Behavior*. Metallurgical and Materials Transactions A, 1981. **12**, p. 1435-1443.
- [171] Gangloff R.P. *The criticality of crack size in aqueous corrosion fatigue*. Research Mechanics Letters, 1981. **1**, p. 299-306.
- [172] Turnbull A. *The environmentally small/short crack growth effect: current understanding*. Corrosion Reviews, 2012. **30**, p. 1-17.
- [173] Jargelius-Pettersson R.F.A. *Electrochemical investigation of the influence of nitrogen alloying on pitting corrosion of austenitic stainless steels*. Corrosion Science, 1999. **41**, p. 1639-1664.

- [174] Gingell A.D.B., King J.E. *The effect of frequency and microstructure on corrosion fatigue crack propagation in high strength aluminium alloys*. Acta Materialia, 1997. **45**, p. 3855-3870.
- [175] Dawson D.B., Pelloux R.M. *Corrosion fatigue crack growth of titanium alloys in aqueous environments*. Metallurgical and Materials Transactions B, 1974. **5**, p. 723-731.
- [176] Tomohiro O., Yoshikazu N., Kenji H. *Effect of Sodium Chloride Concentration on Corrosion Fatigue Strength*. 2002. **77**, p. 1.19-1.20.
- [177] Yu J., Zhao Z.J., Li L.X. *Corrosion fatigue resistances of surgical implant stainless steels and titanium alloy*. Corrosion Science, 1993. **35**, p. 587-597.
- [178] Atkinson J.D., Chen Z. *The Effect of Temperature on Corrosion Fatigue Crack Propagation in Reactor Pressure Vessel Steels*.
- [179] Nakai Y., Alavi A., Wei R.P. *Effects of frequency and temperature on short fatigue crack growth in aqueous environments*. Metallurgical and Materials Transactions A, 1988. **19**, p. 543-548.
- [180] Jiashen Z., Jingmao Z. *Increasing the Fatigue Life of 40Cr Steel in Drilling Muds with Corrosion Inhibitors*. Corrosion, 1993. **49**, p. 256-263.
- [181] Stoltz R.E., Pelloux R.M. *Inhibition of Corrosion Fatigue in 7075 Aluminum Alloys*. Corrosion, 1973. **29**, p. 13-17.
- [182] Panasyuk V.V., Ratych L.V. *The methodology of estimating inhibitor effectiveness in corrosion fatigue crack propagation*. Corrosion Science, 1995. **37**, p. 391-412.
- [183] Angelova D., Akid R. *A note on modelling short fatigue crack behaviour*. Fatigue and Fracture of Engineering Materials and Structures, 1998. **21**, p. 771-779.
- [184] Beretta S., Carboni M., Conte A.L., Regazzi D., Trasatti S., Rizzi M. *Crack growth studies in railway axles under corrosion fatigue: Full-scale experiments and model validation*. in 11th International Conference on the Mechanical Behavior of Materials (ICM11). 2011. Como, Italy: Procedia Engineering.
- [185] Engelhardt G.R., Macdonald D.D. *Modelling the crack propagation rate for corrosion fatigue at high frequency of applied stress*. Corrosion Science, 2010. **52**, p. 1115-1122.
- [186] Jones W.J.D., Blackie A.P. *Effect of stress ratio on the cyclic tension corrosion fatigue life of notched steel BS970:976M33 in sea water with cathodic protection*. International Journal of Fatigue, 1989. **11**, p. 417-422.
- [187] Hilpert M., Wagner L. *Corrosion fatigue behavior of the high-strength magnesium alloy AZ 80*. Journal of Materials Engineering and Performance, 2000. **9**, p. 402-407.
- [188] Chen G.S., Wan K.C., Gao M., Wei R.P., Flournoy T.H. *Transition from pitting to fatigue crack growth modelling of corrosion fatigue crack nucleation in a 2024-T3 Aluminium Alloy*. Material Science and Engineering A., 1996. **219**, p. 1226-132.
- [189] Boukerrou A., Cottis R.A. *Crack initiation in the corrosion fatigue of structural steels in salt solutions*. Corrosion Science, 1993. **35**, p. 577-585.
- [190] Chen G.S., Duquette D.J. *Corrosion fatigue of a precipitation-hardened Al-Li-Zr alloy in a 0.5 M sodium chloride solution*. Metallurgical and Materials Transactions A, 1992. **23**, p. 1563-1572.
- [191] J. Congleton R.A.O., Parkins R.N. *Corrosion-fatigue Crack Nucleation in 1.5 Mn-0.5Si Steel*. Materials Technology, 1982. **9**, p. 94-103.
- [192] Fang B.Y., Eadie R.L., Chen W.X., Elboujdaini M. *Pit to crack transition in X-52 pipeline steel in near neutral pH environment Part 1 – formation of blunt cracks from pits under cyclic loading*. Corrosion Engineering Science and Technology, 2010. **45**, p. 302-313.
- [193] Palin-Luc T., Perez-Mora R., Bathias C., Dominguez G., Paris P.C., Arana J.L. *Fatigue crack initiation and growth on a steel in the very high cycle regime with sea water corrosion*. Engineering Fracture Mechanics, 2010. **77**, p. 1953-1962.
- [194] Burns J.T., Larsen J.M., Gangloff R.P. *Driving forces for localized corrosion-to-fatigue crack transition in Al-Zn-Mg-Cu*. Fatigue & Fracture of Engineering Materials & Structures, 2011. **34**, p. 745-773.
- [195] Masaki K., Ochi Y., Matsumura T. *Small crack property of austenitic stainless steel with artificial corrosion pit in long life regime of fatigue*. International Journal of Fatigue, 2006. **28**, p. 1603-1610.
- [196] Rokhlin S.I., Kim J.Y., Nagy H., Zoofan B. *Effect of pitting corrosion on fatigue crack initiation and fatigue life*. Engineering Fracture Mechanics, 1999. **62**, p. 425-444.

- [197] Dolley E.J., Lee B., Wei R.P. *The effect of pitting corrosion on fatigue life*. Fatigue & Fracture of Engineering Materials & Structures, 2000. **23**, p. 555-560.
- [198] Chen G.S., Wan K.C., Gao M., Wei R.P., Flournoy T.H. *Transition from pitting to fatigue crack growth—modeling of corrosion fatigue crack nucleation in a 2024-T3 aluminum alloy*. Materials Science and Engineering: A, 1996. **219**, p. 126-132.
- [199] Goto M., Nisitani H. *Crack initiation and propagation behaviour of heat-treated carbon steel in corrosion fatigue* Fatigue & Fracture of Engineering Materials & Structures, 1992. **15**, p. 353-363.
- [200] Akid R., Dmytrakh I.M., Gonzalez-Sanchez J. *Fatigue damage accumulation: Aspects of environmental interaction*. Materials Science, 2006. **42**, p. 42-53.
- [201] Cerit M. *Numerical investigation on torsional stress concentration factor at the semi elliptical corrosion pit*. Corrosion Science, 2013. **67**, p. 225-232.
- [202] Turnbull A., Wright L., Crocker L. *New insight into the pit-to-crack transition from finite element analysis of the stress and strain distribution around a corrosion pit*. Corrosion Science, 2010. **52**, p. 1492-1498.
- [203] Pidaparti R.M., Patel R.R. *Modeling the Evolution of Stresses Induced by Corrosion Damage in Metals*. Journal of Materials Engineering and Performance, 2011. **20**, p. 1114-1120.
- [204] R.M P., K K., A.S R. *Corrosion pit induced stresses prediction from SEM and finite element analysis*. International Journal of Computational Methods in Engineering Science and Mechanics, 2009. **10**, p. 117-123.
- [205] Pao P.S., Gill S.J., Feng C.R. *On fatigue crack initiation from corrosion pits in 7075-T7351 aluminum alloy*. Scripta Materialia, 2000. **43**, p. 391-396.
- [206] Wang Q.Y., Kawagoishi N., Chen Q. *Effect of pitting corrosion on very high cycle fatigue behavior*. Scripta Materialia, 2003. **49**, p. 711-716.
- [207] Turnbull A., Zhou S. *Pit to crack transition in stress corrosion cracking of a steam turbine disc steel*. Corrosion Science, 2004. **46**, p. 1239-1264.
- [208] Christman T.K. *Relationships Between Pitting, Stress, and Stress Corrosion Cracking of Line Pipe Steels*. Corrosion, 1990. **46**, p. 450-453.
- [209] Turnbull A., Zhou S., McCormick N., Lukaszewicz M. *An approach to measurement of environmentally assisted small crack growth*, in NACE Conference and Expo. 2013, NACE. p. 1-15.
- [210] BS7910 *Guide to methods for assessing the acceptability of flaws in metallic structures*. 2013: British Standard International.
- [211] Wei R.P., Landes J.D. *Correlation between sustained-load and fatigue crack growth in high strength steels*. materials Research and Standards, 1970. **9**, p. 25-27.
- [212] Wei R.P., Gao M. *Reconsideration of superposition model for environmentally assisted fatigue crack growth*. Scripta Metallurgica, 1983. **17**, p. 959-962.
- [213] Austen I.M., Walker E.F. *Corrosion fatigue crack propagation in steels under simulated offshore condition*. Fatigue 84, 1984, p. 1457-1469.
- [214] Lindely T.C., McIntyre P., Trant P.J. *Fatigue crack initiation at corrosion pits*. Metals Technology, 1982. **9**, p. 135-142.
- [215] Kawai S., Kasai K. *Considerations of allowable stress of corrosion fatigue: Focused on the influence of pitting*. Fatigue & Fracture of Engineering Materials & Structures, 1985. **8**, p. 115-127.
- [216] Hoepfner D.W. *Model for prediction of fatigue lives based upon a pitting corrosion fatigue process*. in Fatigue Mechanisms. 1979. American Society of Testing and Materials.
- [217] Harlow D.G., Wei R.P. *Probability modeling and material microstructure applied to corrosion and fatigue of aluminum and steel alloys*. Engineering Fracture Mechanics, 2009. **76**, p. 695-708.
- [218] ASTM ASTM E384 - 11e1 *Standard Test Method for Knoop and Vickers Hardness of Materials*. 2007, ASTM International.
- [219] Zhou S T.A. *Development of pre-pitting procedure for turbine disc steel*. British Corrosion Journal, 2000. **35**, p. 1-5.
- [220] Marcus P., Mansfeld F. *Analytical Methods In Corrosion Science and Engineering*. 2006, Boca Raton: CRC Press, Taylor & Francis Group.
- [221] Turnbull A. *Review of modelling of pit propagation kinetics*. British Corrosion Journal, 1993. **28**, p. 297-308.

- [222] Uniscan. <http://www.uniscan.com/electrochemistry-instruments/scanning-droplet-system/>. 2013.
- [223] ASTM ASTM E8 / E8M - 13a *Standard Test Methods for Tension Testing of Metallic Materials*. 2013, ASTM International.
- [224] ASTM ASTM E606 / E606M - 12, *Standard Test Method for Strain-Controlled Fatigue Testing*. 2012, ASTM International.
- [225] E466-07 A. *Standard practice for conducting force controlled constant amplitude axial fatigue tests of metallic materials* Vol. 03.01. 2007, West Conshohocken, PA: ASTM International.
- [226] ASTM *Standard practice for conducting constant amplitude axial fatigue tests of metallic materials*, in *Annual Book of ASTM Standards*, Section 3. 1994, ASTM International. p. 465-469.
- [227] Mughrabi H. *Cyclic slip irreversibilities and the evolution of fatigue damage*. Metallurgical and Materials Transactions A: Physical Metallurgy and Materials Science, 2009. **40**, p. 1257-1279.
- [228] Man J., Obrtlík K., Polak J. *Extrusions and intrusions in fatigued metals. Part 1. State of the art and history*. Philosophical Magazine, 2009. **89**, p. 1295-1336.
- [229] Polak J. *Cyclic deformation, crack initiation, and low-cycle fatigue*. Comprehensive Structural Integrity, 2003. **4**, p. 1-39.
- [230] Rajabipour A., Melchers R.E. *A numerical study of damage caused by combined pitting corrosion and axial stress in steel pipes*. Corrosion Science, 2013. **76**, p. 292-301.
- [231] ABAQUS *Analysis user's manual I-V. Version 6.13*. 2013, USA: ABAQUS Inc., Dassault Systemes
- [232] Python. *Python Scripting Language*. 2013; Available from: <https://www.python.org/>.
- [233] Moaveni S. *Finite Element Analysis - Theory and application with ANSYS*. Second ed. 2003: Pearson Education, Inc.
- [234] Cerit M., Genel K., Eksi S. *Numerical Investigation on stress concentration of corrosion pits*. Engineering Failure Analysis, 2009. **16**, p. 2467-2472.
- [235] Lazareva G.G., Mironova V.V., Omelyanchuk N.A., Shvab I.V., Vshivkov V.A., Gorpinchenko D.N., Nikolaev S.V., Kolchanov N.A. *Mathematical modeling of plant morphogenesis*. Numerical Analysis and Applications, 2008. **1**, p. 123-134.
- [236] Patel A.A., Gawlinski E.T., Lemieux S.K., Gatenby R.A. *A Cellular Automaton Model of Early Tumor Growth and Invasion: The Effects of Native Tissue Vascularity and Increased Anaerobic Tumor Metabolism*. Journal of Theoretical Biology, 2001. **213**, p. 315-331.
- [237] Emmerich H., Rank E. *An improved cellular automaton model for traffic flow simulation*. Physica A: Statistical Mechanics and its Applications, 1997. **234**, p. 676-686.
- [238] Berc L. *Techniques of spatially explicit individual-based models: construction, simulation, and mean-field analysis*. Ecological Modelling, 2002. **150**, p. 55-81.
- [239] Wolfram S. *Statistical mechanics of cellular automata*. Reviews of Modern Physics, 1983. **55**, p. 601.
- [240] Rajasankar J., Iyer N.R. *A probability-based model for growth of corrosion pits in aluminium alloys*. Engineering Fracture Mechanics, 2006. **73**, p. 553-570.
- [241] Chen H., Chen Y., Zhang J. *Cellular automaton modeling on the corrosion/oxidation mechanism of steel in liquid metal environment*. Progress in Nuclear Energy, 2008. **50**, p. 587-593.
- [242] Córdoba-Torres P., Nogueira R.P., de Miranda L., Brenig L., Wallenborn J., Fairén V. *Cellular automaton simulation of a simple corrosion mechanism: mesoscopic heterogeneity versus macroscopic homogeneity*. Electrochimica Acta, 2001. **46**, p. 2975-2989.
- [243] Saunier J., Dymitrowska M., Chaussé A., Stafiej J., Badiali J.P. *Diffusion, interactions and universal behavior in a corrosion growth model*. Journal of Electroanalytical Chemistry, 2005. **582**, p. 267-273.
- [244] Wang H., Han E. *Simulation of metastable corrosion pit development under mechanical stress*. Electrochimica Acta, 2013. **90**, p. 128-134.
- [245] Li L., Li X., Dong C., Huang Y. *Computational simulation of metastable pitting of stainless steel*. Electrochimica Acta, 2009. **54**, p. 6389-6395.
- [246] Lei L., Xiaogang L., Chaofang D., Kui X., Lin L. *Cellular automata modeling on pitting current transients*. Electrochemistry Communications, 2009. **11**, p. 1826-1829.
- [247] Lishchuk S.V., Akid R., Worden K., Michalski J. *A cellular automaton model for predicting intergranular corrosion*. Corrosion Science, 2011. **53**, p. 2518-2526.



- [248] Pidaparti R.M., Rao A.S. *Analysis of pits induced stresses due to metal corrosion*. Corrosion Science, 2008. **50**, p. 1932-1938.
- [249] Mathworks. MATLAB 2013a. 2013; Available from: [www.mathworks.com](http://www.mathworks.com).
- [250] Akid R., Dmytrakh I.M. *Influence of surface deformation and electrochemical variables on corrosion and corrosion fatigue crack development*. Fatigue & Fracture of Engineering Materials & Structures, 1998. **21**, p. 903-911.
- [251] Gutman E.M. *Mechanochemistry of Materials*. 1998, Cambridge: Cambridge International Science Publishing.
- [252] Gutman E.M., Solovioff G., Eliezer D. *The mechanochemical behavior of type 316L stainless steel*. Corrosion Science, 1996. **38**, p. 1141-1145.
- [253] ASTM *Standard Test Methods for Determining Average Grain Size*, in ASTM E112 - 13. 2013, American Standard Test Method.
- [254] Liu W., Cao F., Chen A., Chang L., Zhang J., Cao C. *Effect of Chloride Ion Concentration on Electrochemical Behavior and Corrosion Product of AM60 Magnesium Alloy in Aqueous Solutions*. Corrosion, 2012. **68**, p. 045001-1-045001-14.
- [255] Klesnil M., Lukas P. *Fatigue of metallic Materials*. 1980: Elsevier Scientific Publishing Company.
- [256] Ramberg W., Osgood W.R. *Description of Stress-Strain Curves by Three Parameters*. Technical Report No. 902, 1943.
- [257] Lefebvre D., Ellyin F. *Cyclic response and inelastic strain energy in low cycle fatigue*, *International Journal of Fatigue*, 6 (1984), pp.9-15. *International Journal of Fatigue*, 1984. **6**, p. 9-15.
- [258] Abilio M.J., Ribeiro A.S., Fernandes A.A. *Low and high cycle fatigue and cyclic elasto-plastic behaviour of the P355NL1 steel*. *Journal of Pressure Vessel Technology*, 2006. **128**, p. 298-304.
- [259] Plumtree A., Abdel-Raouf H.A. *Cyclic stress-strain response and substructure*. *International Journal of Fatigue*, 2001. **23**, p. 799-805.
- [260] Kruml T., Polák J. *Fatigue softening of X10CrAl24 ferritic steel*. *Materials Science and Engineering: A*, 2001. **319-321**, p. 564-568.
- [261] Roven H.J., Nes E. *The cyclic stress-strain response of a low alloyed steel. - plateau in the CSS-curve*. *Scripta Metallurgica*, 1987. **21**, p. 1727-1732.
- [262] Lemaitre J., Chaboche J.L. *Mechanics of Solid Materials*. Cambridge University Press.
- [263] Roven H.J., Nes E. *Cyclic deformation of ferritic steel—I. Stress-strain response and structure evolution*. *Acta Metallurgica et Materialia*, 1991. **39**, p. 1719-1733.
- [264] Polák J., Klesnil M. *The dynamics of cyclic plastic deformation and fatigue life of low carbon steel at low temperatures*. *Materials Science and Engineering*, 1976. **26**, p. 157-166.
- [265] Harb J.N., Alkire R.C. *The effect of fluid flow on growth of single corrosion pits*. *Corrosion Science*, 1989. **29**, p. 31-43.
- [266] Sun M., Xiao K., Dong C., Li X., Zhong P. *Effect of stress on electrochemical characteristics of pre-cracked ultrahigh strength stainless steel in acid sodium sulphate solution*. *Corrosion Science*, 2014. **89**, p. 137-145.
- [267] Zhang G.A., Cheng Y.F. *Micro-electrochemical characterization of corrosion of pre-cracked X70 pipeline steel in a concentrated carbonate/bicarbonate solution*. *Corrosion Science*, 2010. **52**, p. 960-968.
- [268] Van B.D., Farrington G.C., Laird C. *The interaction of simultaneous cyclic straining and aqueous corrosive attack in the behavior of persistent slip bands*. *Acta Metallurgica*, 1985. **33**, p. 1593-1600.
- [269] Horner D.A. *Assessing the Transition from Localised Corrosion to Environmentally Assisted Cracking in Structural Materials* in *Metalurgy and Material*, School of Engineering. 2007, The University of Birmingham.
- [270] Zhao W., Wang Y., Zhang T., Wang Y. *Study on the mechanism of high-cycle corrosion fatigue crack initiation in X80 steel*. *Corrosion Science*, 2012. **57**, p. 99-103.
- [271] Srivatsan S., Sudarshan T.S. *Mechanisms of fatigue crack initiation in metals: The role of aqueous environments*. *Journal of Materials Science*, 1988. **23**, p. 1521-1533.
- [272] Sudarshan T.S., Srivatsan T.S., Harvey D.P. *Fatigue processes in metals - The role of aqueous environments*. *Engineering Fracture Mechanics*, 1990. **36**, p. 827-852.
- [273] Pande C.S., Imam M.A., Srivatsan T.S. *Fundamentals of fatigue crack initiation and propagation: A review*. in *Fatigue of Materials: Advances and Emergences in Understanding*.

- [274] Soboyejo W.O., Knott J.F. *An investigation of crack closure and the propagation of semi-elliptical fatigue cracks in Q1N (HY80) pressure vessel steel*. International Journal of Fatigue, 1995. **17**, p. 577.
- [275] Soboyejo W.O., Knott J.F., Walsh M.J., Cropper K.R. *Fatigue crack propagation of coplanar semi-elliptical cracks in pure bending*. Engineering Fracture Mechanics, 1990. **37**, p. 323-340.
- [276] Kishimoto K., Soboyejo W.O., Knott J.F., Smith R.A. *A numerical investigation of the interaction and coalescence of twin coplanar semi-elliptical fatigue cracks*. International Journal of Fatigue, 1989. **11**, p. 91-96.
- [277] Leek T.H., Howard I.C. *An examination of methods of assessing interacting surface cracks by comparison with experimental data*. International Journal of Pressure Vessels and Piping, 1996. **68**, p. 181-201.
- [278] McComb T.H., Pope J.E., Grant Jr A.F. *Growth and coalescence of multiple fatigue cracks in polycarbonate test specimens*. Engineering Fracture Mechanics, 1986. **24**, p. 601-608.
- [279] Melin S. *Why do cracks avoid each other?* International Journal of Fracture, 1983. **23**, p. 37-45.
- [280] Forsyth P.J.E. *A unified description of micro and macroscopic fatigue crack behaviour*. International Journal of Fatigue, 1983. **5**, p. 3-14.
- [281] Soboyejo W.O., Knott J.F. *The propagation of non-coplanar semi-elliptical fatigue cracks*. Fatigue & Fracture of Engineering Materials & Structures, 1991. **14**, p. 37-49.
- [282] Plumtree A., O'Connor B.P. *The influence of microstructure on short fatigue crack growth*. Fatigue & Fracture of Engineering Materials & Structures, 1991. **14**, p. 171-184.
- [283] Akid R. *The effect of solution pH on the initiation and growth of short fatigue cracks*. 1990.
- [284] Vasudeven A.K., Sadananda K., Louat N. *A review of crack closure, fatigue crack threshold and related phenomena*. Materials Science and Engineering: A, 1994. **188**, p. 1-22.
- [285] Sivaprasad S., Tarafder S., Ranganath V.R., Tarafder M., Ray K.K. *Corrosion fatigue crack growth behaviour of naval steels*. Corrosion Science, 2006. **48**, p. 1996-2013.
- [286] Schönbauer B.M., Stanzl-Tschegg S.E. *Influence of environment on the fatigue crack growth behaviour of 12% Cr steel*. Ultrasonics, 2013. **53**, p. 1399-1405.
- [287] Murakami Y., Endo T. *Effects of small defects on fatigue strength of metals*. International Journal of Fatigue, 1980. **2**, p. 23-30.
- [288] Laird C. *The influence of metallurgical structure on the mechanisms of fatigue crack propagation*, in Fatigue Crack Propagation, STP 415. 1967, American Society for Testing and Materials: Philadelphia. p. 131-168.
- [289] Bhuiyan M.S., Mutoh Y., Murai T., Iwakami S. *Corrosion fatigue behavior of extruded magnesium alloy AZ61 under three different corrosive environments*. International Journal of Fatigue, 2008. **30**, p. 1756-1765.
- [290] Endo K., Komai K., Matsuda Y. *Mechanical Effects of Corrosion Products in Corrosion Fatigue Crack Growth of a Steel*, in Bulletin of Japan Society of Mechanical Engineers. 1981. p. 1319-1325.
- [291] Walker N., Beevers C.J. *A fatigue crack closure mechanism in titanium*. Fatigue & Fracture of Engineering Materials & Structures, 1979. **1**, p. 135-148.
- [292] McDowell D. *Basic issues in the mechanics of high cycle metal fatigue*. International Journal of Fracture, 1996. **80**, p. 103-145.
- [293] Guiraud F., Stevens R.N. *The nucleation and growth of short fatigue cracks both at plain surfaces and notches*. Fatigue & Fracture of Engineering Materials & Structures, 1990. **13**, p. 625-635.
- [294] Acuna N., Gonzalez-Sanchez J., Ku-Basulto G., Dominguez L. *Analysis of the stress intensity factor around corrosion pits developed on structures subjected to mixed loading*. Scripta Materialia, 2006. **55**, p. 363-366.
- [295] Newman Jr J.C., Raju I.S. *Stress-intensity factor equations for cracks in three-dimensional finite bodies*, in Technical Memorandum 83200. 1981, NASA.
- [296] Newman Jr J.C., Raju I.S. *Analyses of surface cracks in finite plates under tension or bending loads*, in NASA TP-1578. 1979, NASA.
- [297] Bar Massada A., Carmel Y. *Incorporating output variance in local sensitivity analysis for stochastic models*. Ecological Modelling, 2008. **213**, p. 463-467.
- [298] Campolongo F., Gabric A. *The parametric sensitivity of dimethylsulfide flux in the southern ocean*. Journal of Statistical Computation and Simulation, 1997. **57**, p. 337-352.

- [299] Van der Ween P., Zimer A.M., Pereira E.C., Mascaro L.H., Bruno O.M., De Baets B. *Modeling pitting corrosion by means of a 3D discrete stochastic model*. Corrosion Science, 2014. **82**, p. 133-144.
- [300] Liu H.-L., Yang F.-C., Huang C.-H., Fang H.-W., Cheng Y.-C. *Sensitivity analysis of the semiempirical model for the growth of the indigenous Acidithiobacillus thiooxidans*. Chemical Engineering Journal, 2007. **129**, p. 105-112.
- [301] Trethewey K., Chamberlain J. *Corrosion for Science and Engineering*. 1995: Addison Wesley Longman Limited.
- [302] Godard H.P. *The Corrosion of Light Metals*. 1967: John Wiley and Sons.
- [303] Song F.M., Kirk D.W., Graydon J.W., Cormack D.E. *Effect of Ferrous Ion Oxidation on Corrosion of Active Iron under an Aerated Solution Layer*. Corrosion, 2002. **58**, p. 145-155.
- [304] Stansbury E.E., Buchanan R.A. *Fundamentals of Electrochemical Corrosion*. 2000: ASM International.
- [305] Rollins V., Pyle T. *Strain enhanced dissolution effects in the corrosion fatigue failure of metals*. Nature, 1975. **254**, p. 322-323.
- [306] Mu Z.T., Chen D.H., Zhu Z.T., Ye B. *The stress concentration factor with different shapes of corrosion pits*. Advanced Materials Research 2011. **152-153**, p. 1115-1119.
- [307] Pidaparti R.M., Patel R.K. *Investigation of a single pit/defect evolution during the corrosion process*. Corrosion Science, 2010. **52**, p. 3150-3153.
- [308] Murakami Y., Endo M. *Effects of defects, inclusions and inhomogeneities on fatigue strength*. International Journal of Fatigue, 1994. **16**, p. 163-182.
- [309] McEvily A.J., Endo M., Yamashita K., Ishihara S., Matsunaga H. *Fatigue notch sensitivity and the notch size effect*. International Journal of Fatigue, 2008. **30**, p. 2087-2093.
- [310] Pilkey W.D., Pilkey D.F. *Peterson's Stress Concentration Factors*. 3rd ed. 2008: John Wiley & Sons.
- [311] Peterson R.E. *Notch Sensitivity*. Metal Fatigue. 1959: McGraw-Hill.
- [312] Nordberg H. *The effect of notches and non-metallic inclusions on the fatigue properties of high-strength steel*. in Swedish Symposium on Non-metallic Inclusions in Steel. 1981. Uddeholms AB: Swedish Institute for Metal Research.
- [313] Smith R.A., Miller K.J. *Prediction of fatigue regimes in notched components*. International Journal of Mechanical Sciences, 1978. **20**, p. 201-206.
- [314] Vallellano c., Navarro A., Dominguez J. *Fatigue crack growth threshold conditions at notches. Part I: theory*. Fatigue and Fracture of Engineering Materials and Structures, 2000. **23**, p. 113-121.
- [315] Konda Y., Wei R. *Approach on quantitative evaluation of corrosion fatigue crack initiation condition*. in International Conference on Evaluation of Materials Performance in Severe Environments. 1989. Kobe, Japan: The Iron and Steel Institute of Japan.
- [316] Kitagawa H., Takahashi S. *Applicability of fracture mechanics to very small cracks or the cracks in the early stage*. Proceedings of the 2nd International Conference on Mechanical behaviour of materials, Boston, 1976, p. 627-631.
- [317] Beretta S., Carboni M., Fiore G., Lo Conte A. *Corrosion-fatigue of A1N railway axle steel exposed to rainwater*. International Journal of Fatigue, 2010. **32**, p. 952-961.
- [318] Wu X.J. *Short Fatigue Crack Behaviour of a Submarine Hull Steel in Inert and Aggressive Environments*. 1995, PhD Thesis, The University of Sheffield.
- [319] Schonbauer B.M., Stanzl-Tschegg S.E., Perlega A., Salzman R.N., Rieger N.F., Zhou S., Turnbull A., Gandy D. *Fatigue life estimation of pitted 12% Cr steam turbine blade steel in different environments and at different stress ratios*. International Journal of Fatigue, 2014. **65**, p. 33-43.
- [320] Scully J.R., Moran P.J. *Influence of Strain on the Environmental Hydrogen-Assisted Cracking of a High-Strength Steel in Sodium Chloride Solution*. Corrosion, 1988. **44**, p. 176-185.
- [321] Esaklul K.A., Gerberich W.W. *Internal hydrogen degradation of fatigue thresholds in HSLA steel*. Fracture Mechanics: Sixteenth Symposium, ed. M.F. Kanninen and A.T. Hopper. Vol. STP 868. 1985, Philadelphia: ASTM.
- [322] Barsom J.M. *Effect of cyclic stress form on corrosion fatigue crack propagation below KISCC in a high yield strength steel*. Corrosion fatigue, ed. O.F. Devereux, A.J. McEvily, R.W. Staehle. 1971: NACE.
- [323] Seys A.A., Brabers M.J., Van Haute A.A. *Analysis of the Influence of Hydrogen on Pitting Corrosion and Stress Corrosion of Austenitic Stainless Steel in Chloride Environment*. Corrosion, 1974. **30**, p. 47.

- [324] Pickering H.W., Frankenthal R.P. *On the mechanism of localized corrosion of iron and stainless steel*. Journal of Electrochemical Society, 1972. **119**, p. 1297-1304.
- [325] Wilde B.E. *Mechanism of Cracking of High Strength Martensitic Stainless Steels in Sodium Chloride Solutions*. Corrosion, 1971. **27**, p. 326-333.
- [326] Fukuzumi T., Komazaki S., Misawa T. *Hydrogen Embrittlement and Corrosion Fatigue Caused by Pitting Corrosion of Spring Steels for Automobile with Improved Pitting Corrosion Resistance by Alloying Elements and Chemical Passivation Treatment*. Tetsu-to-Hagane, 2002. **88**, p. 81-87.
- [327] Suzuki T., Yamabe M., Kitamura Y. *Composition of Anolyte Within Pit Anode of Austenitic Stainless Steels in Chloride Solution*. Corrosion, 1973. **29**, p. 18-22.
- [328] Szklarska-Smialowska Z., Mankowski J. *Effect of temperature on the kinetics of development of pits in stainless steel in 0.5N NaCl + 0.1N H<sub>2</sub>SO<sub>4</sub> solution*. Corrosion Science, 1972. **12**, p. 925-934.
- [329] Pickering H.W. *The significance of the local electrode potential within pits, crevices and cracks*. Corrosion Science, 1989. **29**, p. 325-341.
- [330] Pickering H.W. *The role of electrode potential distribution in corrosion processes*. Materials Science and Engineering: A, 1995. **198**, p. 213-223.
- [331] Petersen C.W. *Solution Chemistry of Pitting of Iron in Artificial Seawater*. Galvanic and Pitting Corrosion - Field and laboratory studies, ed. R. Baboian, W. France, L. Rowe, and J. Rynewicz. Vol. STP 576. 1976, Philadelphia: ASTM.
- [332] Pyle T., Rollins V., Howard D. *The influence of cyclic plastic strain on the transient dissolution behavior of 18/8 stainless steel in 3.7 M H<sub>2</sub>SO<sub>4</sub>*. Journal of Electrochemical Society, 1975. **122**, p. 1445-1453.
- [333] Lukas P., Kunz L. *Role of persistent slip bands in fatigue*. Philosophical Magazine: Advances in Materials Plasticity, 2004. **84**, p. 317-330.
- [334] Murakami Y., Kodama S., Konuma S. *Quantitative evaluation of effects of non-metallic inclusions on fatigue strength of high strength steels. I: Basic fatigue mechanism and evaluation of correlation between the fatigue fracture stress and the size and location of non-metallic inclusions*. International Journal of Fatigue, 1989. **11**, p. 291-298.
- [335] Toyama K., Yamamoto M. *Relationship between fatigue properties and inclusion content of bearing steel* in 4th International Conference on Fatigue and Fatigue Thresholds, Fatigue '90 1990. Hawaii.
- [336] Turnbull A., Zhou S. *Electrochemical short crack effect in environmentally assisted cracking of a steam turbine blade steel*. Corrosion Science, 2012. **58**, p. 33-40.
- [337] Turnbull A., Thomas J.G.N. *A Model of Crack Electrochemistry for Steels in the Active State Based on Mass Transport by Diffusion and Ion Migration*. Journal of Electrochemical Society, 1982. **129**, p. 1412-1422.
- [338] Turnbull A., McCartney L.N., Zhou S. *A model to predict the evolution of pitting corrosion and the pit-to-crack transition incorporating statistically distributed input parameters*. Corrosion Science, 2006. **48**, p. 2084-2105.
- [339] Liaw P.K. *Mechanisms of near-threshold fatigue crack growth in a low alloy steel*. Acta Metallurgica, 1985. **33**, p. 1489-1502.

## APPENDIX A

*Appendix A - Yield stress versus plastic strain for isotropic hardening of X65 steel.*

Yield stress (MPa)	Plastic strain	Yield stress (MPa)	Plastic strain
527.87	0	659.32	0.0730
528.77	0.0001	661.95	0.0749
530.25	0.0013	664.00	0.0768
530.83	0.0039	666.23	0.0788
531.25	0.0070	667.99	0.0807
533.25	0.0104	670.02	0.0827
532.98	0.0139	671.20	0.0847
535.45	0.0170	674.15	0.0868
546.65	0.0181	675.30	0.0888
554.70	0.0200	677.37	0.0909
560.16	0.0218	679.94	0.0929
564.63	0.0235	680.21	0.0950
569.62	0.0251	682.11	0.0971
575.20	0.0267	684.27	0.0993
579.75	0.0284	685.83	0.1015
584.31	0.0300	687.28	0.1037
589.39	0.0317	689.57	0.1059
592.52	0.0334	689.592	0.1081
597.52	0.0351	692.32	0.1103
601.04	0.0368	693.26	0.1127
605.78	0.0385	695.50	0.1151
609.73	0.0402	697.14	0.1175
612.591	0.0420	697.77	0.1199
615.80	0.0437	699.51	0.1224
620.29	0.0455	701.90	0.125
622.94	0.0472	702.96	0.1276
626.15	0.0490	704.38	0.1303
629.95	0.0508	706.83	0.1330
631.64	0.0526	706.87	0.1358
635.18	0.0544	709.38	0.1387
637.81	0.0562	710.19	0.1417
641.18	0.0580	711.97	0.1447
643.50	0.0598	712.40	0.1478
645.86	0.0617	713.57	0.1510
648.03	0.0635	714.39	0.1543
651.82	0.0654	716.20	0.1576
653.23	0.0673	716.18	0.1610
655.47	0.0692	716.58	0.1645
658.36	0.0711	717.63	0.1679

## APPENDIX B

\* Prefix: SN – Stress-life tests under stress control; AF – Air fatigue; CF – Corrosion fatigue;

# Number of cycles ('000s); NPC – Non-propagating crack

*Appendix B1 - Summary of stress-life data for plain specimens tested in air ( $f = 15$  Hz;  $R = 0.1$ )*

Specimen*	$\Delta\sigma$ (MPa)	$N_f$ (cycles)#
SNAF05	495	932.00
SNAF06	486	115.95
SNAF16	468	737.90
SNAF21	450	8250.00
SNAF22	477	525.46
SNAF23	450	>10000
SNAF25	450	>10000
SNAF28	468	827.00
SNAF30	477	312.56
SNAF35	432	>10000

\* Prefix: SN – Stress-life tests under stress control; AF – Air fatigue # Number of cycles ('000s).

**Appendix B2 - Summary of stress-life data for single-pitted specimens tested in air ( $f = 15$  Hz,  $R = 0.1$ )**

Specimen*	$\Delta\sigma$ (MPa)	$d_p$ ( $\mu\text{m}$ )	$AR_p$	$N_i$ (cycles) <sup>‡</sup>	$N_p$ (cycles) <sup>‡</sup>	$N_f$ (cycles) <sup>‡</sup>
SNAF11	382.5	267	0.82	-	-	>10000
SNAF20	427.5	145	0.52	-	-	>10000
SNAF33	450	267	0.83	380	157.5	537.5
SNAF39	450	204	0.69)	1346	167.6	1513.6
SNAF40	450	274	0.82	504	180	684
SNAF42	382.5	274	0.82	8256	*NPC	>10000
SNAF43	414	198	0.68	7540	**NPC	>10000
SNAF45	369	272	0.82	-	-	>10000
SNAF46	360	267	0.81	-	-	>10000
SNAF47	427.5	202	0.67	4307	190	4497
SNAF48	427.5	271	0.82	3525	130	3655
SNAF49	405	265	0.81	5025	180	5205
SNAF50	382.5	274	0.82	8256	NPC	> 10000
SNAF54	450	197	0.68	1562	-	-
SNAF56	405	194	0.67	-	-	>10000
SNAF60	450	137	0.52	2296	124.1	2400.1
SNAF107	436.5	141	0.52	-	-	>10000
SNAF112	450	110	0.43	-	-	>10000

**Appendix B3 - Summary of stress-life data for single-pitted specimens tested in Forties brine ( $f = 2$  Hz,  $R = 0.1$ )**

Specimen*	$\Delta\sigma$ (MPa)	$d_p$ ( $\mu\text{m}$ )	$AR_p$	$N_i$ (cycles) <sup>‡</sup>	$N_p$ (cycles) <sup>‡</sup>	$N_f$ (cycles) <sup>‡</sup>
SNCF58	405	138	0.52	730	145	875
SNCF59	450	141	0.52	325	92	417
SNCF61	427.5	202	0.69	305	70	375
SNCF62	427.5	266	0.82	236	77	313
SNCF63	427.5	142	0.52	520	87	607
SNCF85	450	197	0.68	195	49	244
SNCF86	450	271	0.82	156	64	190
SNCF87	405	265	0.81	292	127	419
SNCF88	350	266	0.82	-	-	785
SNCF89	350	196	0.68	-	-	890
SNCF90	350	144	0.52	-	-	965
SNCF105	405	205	0.68	-	-	684
SNCF106	427.5	137	0.52	575	115	690
SNCF109	405	197	0.68	475	153	628

**Appendix B4 - Summary of stress-life data for double-pitted specimens tested in air ( $f = 15$  Hz;  $R = 0.1$ )**

Specimen*	$\Delta\sigma$ (MPa)	$d_p(1)$ ( $\mu\text{m}$ )**	$d_p(2)$ ( $\mu\text{m}$ )**	$AR_p(1)$ **	$AR_p(2)$ **	$S_{ee}$ ( $\mu\text{m}$ )	$S_{cc}$ ( $\mu\text{m}$ )	$N_i$ (cycles) <sup>‡</sup>	$N_p$ (cycles) <sup>‡</sup>	$N_f$ (cycles) <sup>‡</sup>
SNAF64	427.5	203	195	0.69	0.67	479	1066	4485	310	4795
SNAF65	427.5	274	265	0.83	0.79	398	1063	584	180	764
SNAF69	427.5	205	198	0.70	0.67	132	743	103	315	418
SNAF70	427.5	272	268	0.83	0.81	703	1364	3896	285	4181
SNAF71	427.5	269	265	0.83	0.80	207	857	186	320	506
SNAF72	427.5	198	203	0.68	0.70	686	1265	4265	360	4625
SNAF73	427.5	264	272	0.81	0.81	525	1188	1996	235	2231
SNAF74	405	270	272	0.81	0.83	165	829	205	355	560

SNAF75	405	265	273	0.80	0.83	212	877	796	400	1196
SNAF76	427.5	271	273	0.80	0.82	292	959	285	320	605
SNAF77	427.5	197	200	0.68	0.70	302	877	757	310	1067
SNAF78	427.5	195	200	0.67	0.69	386	965	1925	245	2170
SNAF80	427.5	192	207	0.68	0.70	210	790	546	355	901
SNAF81	427.5	268	274	0.81	0.83	116	776	70	315	385
SNAF82	405	272	268	0.81	0.81	316	983	1356	320	1676
SNAF83	405	206	197	0.69	0.68	202	782	1652	460	2112
SNAF91	405	196	198	0.68	0.69	105	693	170	380	550
SNAF94	360	268	267	0.81	0.81	122	782	687		

\*\* (1) represents values for first pit; (2) represents values for second pit

## APPENDIX C

*Appendix C1 - Summary of maximum pit depth obtained from 3 simulations of the CA model optimized for flowing condition.*

Time (s)	Experiment	Simulation 1	Simulation 2	Simulation 3	Mean	Std. Dev.
1800	--	70	70	65	68	3
3600	102	100	115	120	112	10
5400	--	160	160	155	158	3
7200	152	185	185	193	188	5
10800	--	255	243	243	247	7
14400	273	290	300	295	295	5
18000	--	337	340	340	339	2
21600	--	370	375	367	371	4
25200	--	408	410	400	406	5
28800	387	440	440	435	438	3
43200	537	550	550	525	542	14
57600	611	630	640	595	622	24
72000	685	685	700	670	685	15
86400	754	735	745	725	735	10

*Appendix C2 - Summary of maximum pit depth obtained from 3 simulations of the optimized CA model for stagnant (no flow) condition.*

Time (s)	Experiment	Simulation 1	Simulation 2	Simulation 3	Mean	Std. Dev.
1800	71	60	63	60	61	2
3600	112	100	108	106	105	4
5400	130	135	145	130	137	8
7200	147	160	162	167	163	4
10800	168	195	198	205	199	5
14400	199	222	217	227	222	5
18000	231	237	237	245	240	5
21600	239	243	245	257	248	8
25200	265	258	257	263	259	3
28800	272	265	265	275	268	6

**Appendix C3 - Summary of pit aspect ratio obtained from 3 simulations of the optimized CA model for stagnant (no flow) condition.**

Time (s)	Experiment	Simulation 1	Simulation 2	Simulation 3	Mean	Std. Dev.
1800	0.28	0.26	0.24	0.24	0.25	0.012
3600	0.46	0.4	0.38	0.38	0.39	0.012
5400	0.50	0.52	0.46	0.47	0.48	0.032
7200	0.58	0.72	0.57	0.55	0.61	0.093
10800	0.62	0.67	0.64	0.63	0.65	0.021
14400	0.68	0.73	0.70	0.69	0.71	0.021
18000	0.77	0.77	0.74	0.73	0.75	0.021
21600	0.78	0.79	0.75	0.77	0.77	0.020
25200	0.80	0.8	0.79	0.79	0.79	0.006
28800	0.82	0.8	0.80	0.81	0.80	0.006

## APPENDIX D

**Appendix D - Experimental and predicted crack initiation lifetimes for double pits in air.**

d (μm)	Aspect ratio	$\Delta\sigma$ (MPa)	Experiment (μm)	Equations 8.9/8.16
692	0.68	405	170000	223114
782	0.68	405	1652000	863267
950	0.68	405	10000000	10790297
743	0.68	427.5	103000	160932
790	0.68	427.5	546000	260053
877	0.68	427.5	757000	632210
965	0.68	427.5	1925000	1552726
1066	0.68	427.5	4485000	4354885
1264	0.68	427.5	4265000	3337356
828	0.82	405	205000	270574
876	0.82	405	796000	463859
983	0.82	405	1356000	1362820
770	0.82	427.5	70000	77195
857	0.82	427.5	186000	137985
960	0.82	427.5	285000	274451
1063	0.82	427.5	584000	545883
1188	0.82	427.5	1996000	1257535
1364	0.82	427.5	3896000	4072002

## APPENDIX E

**Appendix E1 – Input file for finite element analysis of 2-D pit geometry from CA model**

```

*Heading
** Job name: Job-1 Model name: Model-1
** Generated by: Abaqus/CAE Student Edition 6.13-2
**Preprint, echo=NO, model=NO, history=NO, contact=NO
**
** PARTS
**
*Part, name=Part-1
*End Part
**
** ASSEMBLY
**
*Assembly, name=Assembly
**
*Instance, name=Part-1-1, part=Part-1
**-----
*Node
*INCLUDE, INPUT=delNodes.inp

```



```

**
**-----
*Element, type=CPE4
*INCLUDE, INPUT=delMesh.inp
**
**-----
*Nset, nset=pset1, internal, generate
*INCLUDE, INPUT=NsetPart_del.inp
**
**-----
*Elset, elset=pset1, internal, generate
*INCLUDE, INPUT=ElsetPart_del.inp
**
**-----
** Section: Section-1
**Solid Section, elset=pset1, material=Material-1,

*End Instance
**
**
*Nset, nset=Set-1, instance=Part-1-1, generate
*INCLUDE, INPUT=NsetPart_del.inp
**
*Elset, elset=Set-1, instance=Part-1-1, generate
*INCLUDE, INPUT=ElsetPart_del.inp
**
*Nset, nset=pset2, internal, instance=Part-1-1, generate
*INCLUDE, INPUT=NsetBC_del.inp
**
*Elset, elset=pset2, internal, instance=Part-1-1, generate
*INCLUDE, INPUT=ElsetBC_del.inp
**
*Elset, elset=psurf1, internal, instance=Part-1-1, generate
*INCLUDE, INPUT=ElsetSurf_del.inp
**
*Surface, type=ELEMENT, name=psurf2, internal
psurf1, S3
*End Assembly
**
** MATERIALS
**
*Material, name=Material-1
*Elastic
210000., 0.3
*Plastic
*INCLUDE, INPUT=Plastic.inp
**
**-----
**
** STEP: Step-1
**
*Step, name=Step-1, nlgeom=NO, inc=100000
*Static
0.5, 1., 1e-40, 1.
**
** BOUNDARY CONDITIONS
**
** Name: BC-1 Type: Displacement/Rotation
*Boundary
pset2, 1, 1
**
** LOADS
**
** Name: Load-1 Type: Pressure
*Dload
psurf2, P, 100.
**
** OUTPUT REQUESTS
**
*Restart, write, frequency=0
**
** FIELD OUTPUT: F-Output-1
**
*Output, field, variable=PRESELECT
**
** HISTORY OUTPUT: H-Output-1
**
*Output, history, variable=PRESELECT
*End Step
=====

```

## Appendix E2 – Python subroutine for extracting stress tensor components from Abaqus output database (.odb files)

```

#-----
from odbAccess import *
from sys import argv, exit
#import sys

```

```
#from odbAccess import *
from types import IntType
#~~~~~
def rightTrim(input,suffix):
    if (input.find(suffix) == -1):
        input = input + suffix
    return input
#~~~~~
def resultadoFEM(odbName,elsetName):
    """ Print max mises location and value given odbName
        and elset(optional)
    """
    elset = elemset = None
    region = "over the entire model"
    """ Open the output database """
    odb = openOdb(odbName)
    assembly = odb.rootAssembly
    if elsetName:
        try:
            elemset = assembly.elementSets[elsetName]
            region = " in the element set : " + elsetName;
        except KeyError:
            print 'An assembly level elset named %s does' \
                'not exist in the output database %s' \
                % (elsetName, odbName)
            odb.close()
            exit(0)

    lastFrame = odb.steps['Step-1'].frames[-1]
    Stress = 'S'

    step=odb.steps.values()
    allFields = lastFrame.fieldOutputs
    stressSet = allFields[Stress]

    if elemset:
        stressSet = stressSet.getSubset(
            region=elemset)

    outFile = open(odbName + '_Stress.dat', 'w')

    format = '%6i %1i %19.10e %19.10e %19.10e %19.10e %19.10e %19.10e\n'

    for v in stressSet.values:

        a=v.elementLabel
        b=v.integrationPoint
        Mises = v.mises
        Mprin=v.maxPrincipal
        outFile.write(
            format % ((a,b,Mises,Mprin) + tuple(v.data)))
    outFile.close()

    odb.close()
#=====
# S T A R T
#
if __name__ == '__main__':

    odbName = None
    elsetName = None
    argList = argv
    argc = len(argList)
    i=0
    while (i < argc):
        if (argList[i][:2] == "-o"):
            i += 1
            name = argList[i]
            odbName = rightTrim(name,".odb")
        elif (argList[i][:2] == "-e"):
            i += 1
            elsetName = argList[i]
        elif (argList[i][:2] == "-h"):
            print __doc__
            exit(0)
        i += 1
    if not (odbName):
        print '**ERROR** output database name is not provided'
        print __doc__
        exit(1)
    resultadoFEM(odbName,elsetName)
```

---

---

---

---